Electromagnetic Form-Fit Joining

Zur Erlangung des akademischen Grades eines
Dr.-Ing.
von der Fakultät Maschinenbau
der Technischen Universität Dortmund
genehmigte Dissertation

vorgelegt von
Dipl.-Wirt.-Ing. Christian Weddeling
aus
Vreden

Dortmund, 2014

Vorsitzender der Prüfungskommission:	Prof. Dr.-Ing. A. Brümmer
Berichter:	Prof. Dr.-Ing. Dr.-Ing. E.h. A. E. Tekkaya
	Prof. G. S. Daehn Ph.D.
Mitberichter:	Prof. Dr.-Ing. A. Menzel
Tag der mündlichen Prüfung:	18. Dezember 2014

Dortmunder Umformtechnik

Band 81

Christian Weddeling

Electromagnetic Form-Fit Joining

D 290 (Diss. Technische Universität Dortmund)

Shaker Verlag
Aachen 2015

Bibliographic information published by the Deutsche Nationalbibliothek
The Deutsche Nationalbibliothek lists this publication in the Deutsche Nationalbibliografie; detailed bibliographic data are available in the Internet at http://dnb.d-nb.de.

Zugl.: Dortmund, Technische Univ., Diss., 2014

Copyright Shaker Verlag 2015
All rights reserved. No part of this publication may be reproduced, stored in a retrieval system, or transmitted, in any form or by any means, electronic, mechanical, photocopying, recording or otherwise, without the prior permission of the publishers.

Printed in Germany.

ISBN 978-3-8440-3405-9
ISSN 1619-6317

Shaker Verlag GmbH • P.O. BOX 101818 • D-52018 Aachen
Phone: 0049/2407/9596-0 • Telefax: 0049/2407/9596-9
Internet: www.shaker.de • e-mail: info@shaker.de

“Great visions not only need wings, but also a landing gear to land upon.”

Neil Armstrong, American astronaut, 1930 – 2012

To my parents

For their love, support, and patience

Acknowledgement

This thesis was written during my time as a research assistant at the Institute of Forming Technology and Lightweight Construction (IUL) at TU Dortmund University.

First of all, I would like to thank my academic advisor Prof. Dr.-Ing. Dr.-Ing. E.h. A. Erman Tekkaya for the opportunity to work under his guidance and for his scientific supervision. His vast passion for forming technologies and the intensive professional discussions with him were always very inspiring and encouraging for me. I sincerely appreciate his exceptional support and his great trust, which were essential for the successful completion of this work. I would also like to thank Prof. Glenn S. Daehn, Ph.D., from the Department of Materials Science and Engineering of the Ohio State University. His extensive knowledge about impulse forming and his elaborate advice were a tremendous help in finishing this dissertation. I did not only benefit professionally from his support, but also personally. Due to the given possibility of joining his research group for two extended research stays, I had the chance of experiencing a different working culture. Furthermore, I would like to thank Prof. Dr.-Ing. A. Brümmer and Prof. Dr.-Ing. A. Menzel for their willingness of being part of my dissertation committee and their insightful suggestions regarding my work.

For the development of the analytical models in this work, I was very fortunate to have the support of Prof. Dr.-Ing. Peter Haupt. I am extremely grateful for the fruitful discussions with him, for his extraordinary suggestions and for his inexhaustible patience. For their steady support and the excellent collegiality I would like to thank my colleagues from the IUL and especially the members of the Department of Non-Conventional Processes. It was a great honor for me to work with such a skilled, motivated, and intelligent group of people. In particular, I appreciate the assistance of Soeren Gies and Marlon Hahn. The intensive and sometimes provoking discussions with them were enormously helpful during the time of my research. Many thanks also to Koray Demir for his outstanding help with the Finite Element Simulations for this work. Additionally, I express my gratitude to Dr.-Ing. Nooman Ben Khalfia for the sincere discussions regarding my work and for his support during the final stage of writing this dissertation. For arousing my enthusiasm for research in general and for joining by forming in particular, I would like to thank Dr.-Ing. Michael Marré. I am also very grateful for the excellent guidance of Prof. Dr.-Ing. Alexander Brosius as well as my former group leaders Dr.-Ing. Verena Psyk and Dr.-Ing. Lukas Kwiatkowski. Cordial thanks to Dirk Hoffmann, Werner Feurer, Andreas Herdt, Daniel Jäger, and Benjamin Tarloff for their assistance with the experimental investigations of this work. Furthermore, I thank Volker Walter from the Institute for Applied Materials and Jens Nellesen from the Institute of Materials Engineering for performing the computer tomography analyses of this work. During my time at the

Ohio State University I experienced an exceptional support by Steven Woodward, Anupam Vivek and Geoffrey Taber. They made these stays extraordinarily inspiring and a once-in-a-life-time experience. My IUL-colleagues Andrea Hallen and Jeanette Brandt have been my English language counselors, many thanks for their excellent help. I would also like to thank Patrick Cramer for his creative support when designing this thesis' layout and cover.

For their trust and their love, I would like to thank my parents, Ludwig and Elisabeth Weddeling, as well as my siblings Florian and Sabine. This work would not have been possible without their unconditional support and patience during all stages of my life.

Finally, I would like to express my sincere gratitude to my companion Britta Kraczyk for her magnificent support, her encouragement, and her inexhaustible patience during the final stage of completing this dissertation.

Dortmund, January 2015 Christian Weddeling

Abstract

As a way to reduce a vehicle's weight, the application of space frame structures has been increasing. This innovative lightweight design concept is already commonly applied in the low volume production of cars. Due to the high stiffness and low mass, extruded aluminum profiles are particularly suitable for the manufacturing of such structures. But the potential for great weight reduction using space frames is curtailed by the difficulties associated with manufacturing the space frames. These structures have complex demands on joining technologies, and conventional processes often are pushed to their technological limits.

A promising alternative to connect extruded aluminum profiles without heating or penetration is joining by electromagnetic crimping. Compared to adhesive bonding and welding, the process also requires a less extensive preparation of the joining zone. This technique is characterized by the use of pulsed magnetic fields to form a profile made of an electrically conductivity material into form-fit elements, like grooves, of the other joining partner. Thereby, an interlock is generated which enables the load transfer. However, existing process and joint design methodologies require either sophisticated numerical modeling or extensive experimental studies. The influence of some major process and joining zone parameters, like the forming direction and the groove shape, on the joint strength is also still unknown. Additionally, it has not been analyzed how a mass reduction in the joining zone and the resulting change of the radial strength of the joining partners affects the crimping process and the transferable load.

Therefore, a fundamental process understanding of the manufacturing and the load transfer of form-fit connections manufactured by electromagnetic crimping is developed in this thesis. Based on analytical, experimental, and numerical studies, major parameters are identified and their influence on the joining process and the achievable joint strength is analyzed. For the analytical investigations a continuous approach describing the manufacturing of the connections as well as the load transfer is introduced here. This model also facilitates the process and joining zone design of electromagnetically crimped connections. Furthermore, a process window considering the influence of a mass reduction in the joining zone on the connection strength is developed based on the experimental results and the analytical approach.

Kurzzusammenfassung

Der Einsatz von Rahmenstrukturen aus stranggepressten Aluminiumprofilen bietet eine gute Möglichkeit zur Gewichtsreduktion im Fahrzeugbau. Besonders in der Fertigung von Kleinserienfahrzeugen findet diese Space-Frame-Bauweise bereits eine breite Verwendung. Aufgrund ihrer hohen Steifigkeit bei gleichzeitig geringem Gewicht sind stranggepresste Aluminiumprofile ausgezeichnet für leichte Rahmenstrukturen geeignet. Dem großen Leichtbaupotenzial dieser innovativen Bauweise stehen allerdings häufig komplexe Anforderungen an die einzusetzenden Fügetechnologien entgegen. So stoßen konventionelle und weitverbreitete Verfahren beim Fügen von Aluminiumprofilen oft an ihre technologischen Grenzen.

Eine vielversprechende Alternative zur Fertigung derartiger Rahmenstrukturen ohne eine temperaturbedingte Beeinflussung der Fügezoneneigenschaften oder zusätzliche Bohrungen für Hilfsfügeteile ist das elektromagnetische Krimpen. Zudem ist die Fügezonenvorbereitung bei diesem Verfahren wesentlich weniger aufwendig als zum Beispiel beim Kleben oder Schweißen. Beim elektromagnetischen Krimpen werden gepulste Magnetfelder genutzt, um ein Profil aus einem elektrisch leitfähigen Werkstoff in Formschlusselemente, wie zum Beispiel umlaufende Nuten, des anderen Fügepartners einzuformen. Aufgrund der komplexen Prozess- und Fügezonenauslegung, die momentan nur auf Basis aufwendiger experimenteller oder numerischer Untersuchungen möglich ist, fand das elektromagnetische Krimpen bisher keine große Verbreitung. Zudem ist der Einfluss einiger bedeutender Prozess- und Fügezonenparameter, wie zum Beispiel der Umformrichtung sowie der Nutform, auf die erzielbare Verbindungsfestigkeit noch unklar. Auch wurden die Auswirkungen einer Massenreduktion in der Fügezone und die sich hieraus ergebende Festigkeitsänderung der Fügepartner in radialer Richtung auf den Fügeprozess und die Kraftübertragung bislang noch nicht untersucht.

Daher wird im Rahmen dieser Arbeit ein grundlegendes Prozessverständnis zum Fügen mittels elektromagnetischen Krimpens entwickelt. Basierend auf analytischen, experimentellen und numerischen Untersuchungen werden bedeutende Prozess- und Fügezonenparameter identifiziert sowie ihr Einfluss auf den Fügeprozess und die erzielbare Verbindungsfestigkeit analysiert. Für die analytischen Untersuchungen wird im Rahmen der vorliegenden Arbeit ein durchgängiges Modell entwickelt, welches sowohl den Fügeprozess wie auch die Lastübertragung der Verbindung abbildet. Dieses Modell erlaubt zudem eine einfache Prozess- und Fügestellenauslegung. Abschließend wird ein Prozessfenster, das den Einfluss einer Massenreduktion in der Fügezone auf die Verbindungsfestigkeit berücksichtigt, vorgestellt. Dieses basiert auf den gewonnenen analytischen und experimentellen Erkenntnissen dieser Arbeit.

Content

Acknowledgement **IX**

Abstract **XI**

Kurzzusammenfassung **XIII**

Content **XV**

Symbols and Abbreviations **XVII**

1 Introduction **1**

2 State of the art **3**

2.1 Load transfer mechanisms 5
2.2 Mechanical and hydraulical crimping 9
2.3 Joining by rolling 11
2.4 Joining by die-less hydroforming 12
2.5 Joining by impulse forming 15
  2.5.1 Fundamentals of electromagnetic compression 15
  2.5.2 Determination of the acting loads 19
  2.5.3 Strength-affecting parameters and joint design strategies 20
  2.5.4 Tooling for electromagnetic compression 27
2.6 Summary and conclusion 29

3 Objective **31**

4 Experimental procedure **33**

4.1 Crimping parameter determination 33
  4.1.1 Experimental methodology 34
  4.1.2 Electromagnetic forming setup 35
  4.1.3 Specimens and investigated parameters 37
  4.1.4 Determination of forming velocity and deformation 41
4.2 Joint strength determination 42
  4.2.1 Joining equipment 43
  4.2.2 Specimens and investigated parameters 44
  4.2.3 Determination of the joining partner deformation 46
  4.2.4 Connection strength determination 48

5 Prediction of crimping parameters **51**

5.1 Analytical prediction 51
  5.1.1 Prediction of forming depth 52
  5.1.2 Determination of the charging energy 56
5.2 Verification of the analytical parameter prediction 60

5.3 Summary and conclusion ... 72

6 Influences on the achievable joint strength 75

6.1 Analytical joint strength determination ... 75
6.1.1 Compressed connections ... 76
6.1.2 Expanded connections ... 83
6.2 General parameters affecting the joint strength ... 86
6.2.1 Influence of the groove geometry on the joint strength ... 87
6.2.2 Analytical comparison of the forming direction ... 96
6.2.3 Joining gap influence on the joint strength ... 103
6.2.4 Charging energy variation ... 105
6.3 Strength of connections featuring hollow mandrels ... 107
6.3.1 Load transfer of hollow mandrels ... 108
6.3.2 Groove shape variation ... 110
6.3.3 Influence of mandrel material ... 112
6.4 Summary and conclusion ... 113

7 Manufacturing aspects for joints with hollow mandrels 115

7.1 Joining with support mandrels ... 115
7.2 Threshold diameter ratio of the mandrels ... 119
7.3 Deduction of a process window ... 122
7.4 Example joint design ... 126
7.5 Summary and conclusion ... 129

8 Summary and outlook 131

References 135

Appendix 147

Curriculum vitae 153

Symbols and Abbreviations

Symbols

Symbol	**Unit**	**Description**
A_C	mm²	Contact area
A_M	mm²	Cross-sectional area mandrel
$A_\mathrm{M,GB}$	mm²	Cross-sectional area mandrel at groove base
A_R	mm²	Cross-sectional area ring
$A_\mathrm{R,GB}$	mm²	Cross-sectional area ring at groove base
A_T	mm²	Cross-sectional area tube
a_0	mm	Joining gap
a_air	mm	Air gap between coil and workpiece
B	T	Magnetic flux density
C	F	Capacitance
C_C	1/s	Cowper-Symonds parameter
C_w	m/s	Longitudinal wave speed
c	m/s	Speed of light
D	mm	Outer diameter
D_M	mm	Outer diameter mandrel
D_R	mm	Outer diameter ring
D_T	mm	Outer diameter tube
d	mm	Inner diameter
d_M	mm	Inner diameter mandrel
d_R	mm	Inner diameter ring
d_T	mm	Inner diameter tube
Δd_M	mm	Change of the inner mandrel diameter
E	kJ	Charging energy
E_max	kJ	Maximum charging energy

Symbol	**Unit**	**Description**
F	N	Force
F_{ax}	N	Pull-out force
$\overrightarrow{F_L}$	N/mm³	Lorentz force
$F_{\mathrm{max,J}}$	N	Maximum pull-out force of the joint
$F_{\mathrm{y,J}}$	N	Yield force of the joint
$F_{\mathrm{y,T}}$	N	Yield force of the tube
$F_{\mathrm{y,M,GB}}$	N	Yield load of the smallest cross section of the mandrel
f	Hz	Discharge frequency
f^*	Hz	Short circuit frequency
f_0	Hz	Initial frequency
f_{b}	Hz	Beat frequency
f_{d}	Hz	Doppler-shifted frequency
H	A/m	Magnetic field intensity
H_{i}	A/m	Magnetic field intensity at the inner surface of the workpiece
H_{o}	A/m	Magnetic field intensity at the outer surface of the workpiece
h	mm	Groove depth
h_{B}	mm	Forming height at point B
h_{C}	mm	Forming height at point C
h_{d}	mm	Forming depth (groove center)
I	A	Current (primary current)
I_{e}	Ns/mm²	Total impulse
I_{max}	A	Maximum current
I_{w}	A	Workpiece current (secondary current, induced current)

Symbol	Unit	Description
I_0	A	Current amplitude
J	A/m²	Current density
k	MPa	Yield stress at pure shear
L_{coil}	H	Inductance of the tool coil
L_{i}	H	Inner inductance of the capacitor bank
L_{res}	H	Resulting inductance
$L_{\mathrm{res,d}}$	H	Resulting inductance considering the workpiece deformation
L_{w}	H	Inductance of the workpiece
$L_{\mathrm{w,d}}$	H	Inductance of the workpiece considering the workpiece deformation
l_0	mm	Initial gage length (tensile testing machine)
l_{c}	mm	Contact length at groove base
l_{coil}	mm	Coil length
l_{JZ}	mm	Length joining zone
l_{M}	mm	Mandrel length
l_{p}	mm	Pressurized length
l_{R}	mm	Length ring
l_{T}	mm	Tube length
M	H	Mutual inductance
M_{B}	Nm	Bending moment
m	kg	Mass
$m_{\mathrm{M,s}}$	kg	Mass solid mandrel
$m_{\mathrm{M,h}}$	kg	Mass hollow mandrel
Δm_{J}	%	Mass reduction under the groove
n	-	Number of turns

Symbol	**Unit**	**Description**
$p(t)$	MPa	Pressure
p_b	MPa	Boundary pressure, change of velocity field
p_C	-	Cowper-Symonds exponent
p_e	MPa	Effective pressure
p_f	MPa	Interference pressure
p_i	MPa	Hydraulic fluid pressure, internal pressure
p_im	MPa	Impact pressure
$p_\mathrm{m}(t)$	MPa	Magnetic pressure
p_M	MPa	Pressure acting on the mandrel
p_T	MPa	Pressure acting on the tube
p_y	MPa	Collapse pressure
Q_A	-	Cross-sectional area ratio
Q_J	-	Diameter ratio of the joint
Q_M	-	Diameter ratio mandrel
Q_R	-	Diameter ratio ring
Q_T	-	Diameter ratio tube
R_M	mm	Outer radius of the mandrel
R_coil	Ω	Electrical resistance of the tool coil
R_i	Ω	Inner electrical resistance of the capacitor bank
R_GE	mm	Groove edge radius
R_res	Ω	Resulting electrical resistance
R_r1, R_r2	mm	Principle radii of curvature
R_T	mm	Outer radius of the tube
$R_\mathrm{T,d}$	mm	Mean outer radius of the tube during the joining process
R_w	Ω	Electrical resistance of the workpiece

Symbol	Unit	Description
r	mm	Radius
r_A	mm	Tube radius at point A (center line)
r_B	mm	Tube radius at point B (center line)
r_C	mm	Tube radius at point C (center line)
r_{coil}	mm	Inner radius of the tool coil
r_D	mm	Tube radius at point D (center line)
r_T	mm	Inner radius of the tube
s	mm	Wall thickness
T	s	Period
t	s	Time
t_b	s	Time at first velocity field change (plastic hinge splits up into two)
t_c	s	Time at second velocity field change (the two plastic hinges are unified)
t_f	s	Time at which the forming process ends
t_{max}	s	Time at peak current
t_{mean}	s	Time interval between the onset of plastic deformation and the centroid of the pulse
t_y	s	Beginning of plastic deformation
t_0	s	Time at zero-crossing of the current
U	V	Charging voltage
$v(t)$	m/s	Velocity
v_d	m/s	Workpiece velocity (groove center)
v_C	m/s	Crossbar velocity (tensile testing machine)
v_{im}	m/s	Impact velocity
v_{max}	m/s	Maximum velocity

Symbol	**Unit**	**Description**
w	mm	Groove width
w'	mm	Adjusted groove width for charging energy variation
w_B	mm	Width at point B
α	°	Groove angle
β	°	Wrap around angle at groove edge
δ	1/s	Damping coefficient
δ_d	1/s	Damping coefficient considering the workpiece deformation
δ_s	mm	Skin depth
ε	-	Strain
$\dot{\varepsilon}$	1/s	Strain rate
γ_{GE}	°	Groove edge angle
κ	S/m	Electrical conductivity
λ	Nm	Wave length
σ_{ax}	MPa	Axial stress
$\sigma_{f,0}$	MPa	Initial flow stress
σ_f	MPa	Flow stress
$\sigma_{f,dyn}$	MPa	Strain rate-dependent flow stress
σ_r	MPa	Radial stress (in wall thickness direction)
σ_y	MPa	Yield stress (at 0.2 % plastic strain)
$\sigma_{y,0.01}$	MPa	Yield stress (at 0.01 % plastic strain)
$\sigma_{y,J}$	MPa	Yield stress of the joint
$\bar{\sigma}_{y,J}$	-	Specific joint strength
σ_z	MPa	Axial stress
σ_ϕ	MPa	Meridional stress

Symbol	**Unit**	**Description**
σ_θ	MPa	Circumferential stress
v	-	Poisson’s ratio
μ	H/m	Permeability
μ_0	H/m	Permeability of free space (vacuum)
μ_f	-	Coefficient of friction
μ_r	H/m	Relative permeability
ρ	kg/m^3	Density
ρ_A	kg/m^2	Surface density
ω	1/s	Angular frequency (damped)
ω_0	1/s	Angular frequency (undamped)

Physical constants

Symbol	**Value**	**Description**
c	299,792,485 m/s	Speed of light
μ_0	$4 \cdot \pi \cdot 10^{-7}$ H/m	Permeability of free space (vacuum)

Abbreviations

Abbreviation	**Description**
CNC	Computerized numerical control
CT	Computer tomography
DHF	Die-less hydroforming
EMF	Electromagnetic forming
FEA	Finite element analysis
HAZ	Heat-affected zone
MAPE	Mean absolute percentage error
MIG	Metal inert gas
PDV	Photonic-Doppler-Velocimetry
TIG	Tungsten inert gas

1 Introduction

In the past few decades, a growing need for individual mobility and an associated rise in annual mileage can be observed (Wegerdt et al., 2000) despite increasing public debates regarding air pollution and petroleum scarcities (Schmidt and Schneider, 2010). In response to the conflicting needs for mobility and environmental protection, automotive industries are moving toward more environmentally friendly designs while maintaining vehicle performance. Two major efforts have been seen so far. The first approach is the development of fuel-efficient vehicles that meet the stricter emission standards set forth by the European Union (N.N., 2009). The second approach revolves around designing and promoting electrically powered vehicles in the German market (N.N., 2011). But despite the differences in these two approaches, they both require innovative lightweight vehicle designs to increase fuel-efficiency or compensate for larger batteries.

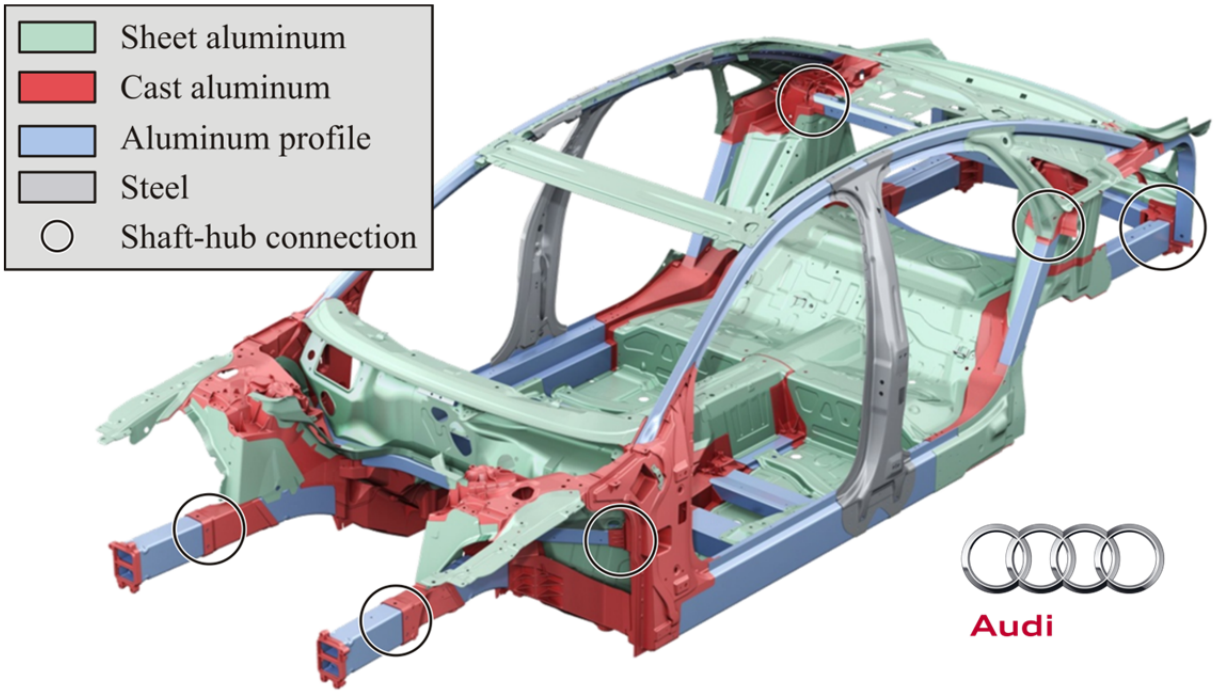

Figure 1-1: Audi A8 space frame

An innovative lightweight design concept, which is especially suitable for low volume production, is the so-called space frame design. An example of the application of this design concept for an automotive chassis is shown in **Figure 1-1**. Such frame structures are already commonly applied in conventional combustion engine vehicles, for example the Audi A8 (Friedrich, 2013). These frames are also increasingly used in electrically powered vehicles (Goroncy, 2011). Additionally, the automotive industry has been increasing its use of lighter metals such as aluminum and magnesium alloys in preference to of steel (Schürmann, 2007). Chatti (2004) states that extruded aluminum profiles are particularly suitable for manufacturing lightweight frame structures. A major advantage of these profiles is the high freedom in the cross-sectional designs. As a result, load-adapted and functional cross section shapes can be manufactured and parts with a high stiffness, but a low mass, can be achieved.

However, the potential for extensive weight reduction using space frame structures is stunted by the complex demands on current joining technologies to manufacture these structures. The most commonly applied joining techniques for the manufacturing of such frame structures are thermal welding processes. But Barnes and Pashby (2000) claim that some aluminum alloys tend to crack when welded without a proper filler material. For example, the 6000 series of aluminum alloys that are very well suited for space frame structures due to their mechanical properties have this tendency to crack. The welding failures can be prevented by applying a 4000 series alloy as filler, but since the 4000 series have lower strengths than the base material the achievable connection strengths are comparatively weak. Another effect of welding aluminum alloys that leads to weaker joints is the formation of a so-called heat-affected zone (HAZ). To achieve joint strengths in the range of the base material’s strength, an additional heat treatment of the joining zone is necessary (Barnes and Pashby, 2000). The industry conventions to create high strength connections include laser welding and its variants. But these processes often have very narrow joining tolerances and, therefore, an intensive preparation of the joining zone is required (Zäh and Trautmann, 2004). In addition, substantial and expensive equipment is needed to position and engender the necessary relative movement between workpieces and laser beam.

Alternative joining techniques, like mechanical fastening or adhesive bonding, also have significant disadvantages which exclude them from specific applications. For instance, mechanical fastening requires supplementary connection elements such as screws, bolts, or rivets, and often additional pre-punch operations are also necessary. The required cutting and penetration of the joining partners can lead to an inhomogeneous stress distribution and, therefore, to critical notch stresses. As a result, the transferable loads might be reduced. Adhesive bonding often requires intensive surface preparation and the working times are typically long (Schürmann, 2007).

A promising joining alternative to overcome some of these disadvantages, especially in the case of profile to profile connections, is the application of joining by forming processes (Mori et al., 2013). Due to its very homogenous bond characteristics and the ability to manufacture multi-material joints very rapidly without additional connection elements, electromagnetic form-fit joining is particularly suitable for this kind of connection. A major problem of this process is the very complex and expensive process and joint design. Therefore, a fundamental understanding of the manufacturing process and the load transfer of form-fit connections joined with this technique shall be developed within this work. Additionally, strategies for the joining zone and the process design shall be deduced from this knowledge.

2 State of the art

As stated by Mori et al. (2013), the term joining by forming covers techniques that are used to join two or more workpieces by deforming at least one part or an additional fastener plastically. Grote and Antonsson (2009) divide joining by forming into forming of wiry bodies (e.g. weaving, splicing, and knotting), forming of plates, tubes, and shapes, and procedures of riveting. Because forming of wiry bodies is not pertinent to the manufacturing of lightweight frame structures and since riveting procedures require additional connection elements, both subgroups are not considered within this thesis. For the same reasons, processes for joining sheet metal parts, like hemming or clinching, are also not covered here. Detailed information on these techniques can be found in the review of Groche et al. (2014). Since the focus of this work is on the manufacturing of space frame structures, techniques suitable for the joining of tubular workpieces and corresponding load transfer mechanisms are introduced in this section. These processes can be classified by their forming direction and by their forming energy input. **Table 2-1** indicates that two different forming directions are possible, expansion and compression. For the energy input, the processes can be divided into techniques with an energy transfer by mechanical tool contact, working media, or working energy.

Table 2-1: Classification of joining by forming processes for tubular workpieces

		Forming direction	
		Expansion	**Compression**
Energy input	**Mechanical**	Joining by rolling (**Section 2.3**)	Mechanical crimping (**Section 2.2**)
	Working media	Joining by die-less hydroforming (**Section 2.4**)	Hydraulical crimping (**Section 2.2**)
	Working energy	Electromagnetic expansion (**Section 2.5**)	Electromagnetic compression (**Section 2.5**)

Lange (1993) claims that the major advantage of joining by forming is its ability to join dissimilar metallic and non-metallic materials with each other. Due to different material properties of the joining partners, like melting temperatures and thermal conductivities, the manufacturing of such multi-material connections is very difficult or often not even possible by fusion welding. In addition, connections joined by a forming technique do not have a heat-affected zone that might cause a joint strength reduction (Mori et al., 2013). They also do not exhibit thermal distortion, which can lead to a geometrical inaccuracy of the joined component.

The main disadvantage of all joining by forming operations is that only overlap connections are possible. As a result, the connections have typically a higher mass than, for example, welded butt-joints. The manufactured connections are also typically non-detachable, which makes repairs more complex. Furthermore, only for a few processes calculation methods for the process and joint design are available. Further advantages and disadvantages of joining by forming processes are compiled by Mori et al. (2013) and shown in **Table 2-2**.

Table 2-2: Advantages and disadvantages of joining by forming processes in (Mori et al., 2013)

Advantages	Disadvantages
• Wide range of materials, including dissimilar ones (metallic/non-metallic), being joined • Less distortion, embrittlement and tensile residual stress • High process reliability and simple quality control • Environmental safety	• Mainly overlap joints • Geometrical unevenness of joining • More difficult correction and repair • Lack of standardization and calculation methods

Figure 2-1 shows a selection of components manufactured with joining by forming processes. Typical industrial applications of these techniques are joined camshafts, heat exchangers, and hose couplings (see **Figure 2-1**).

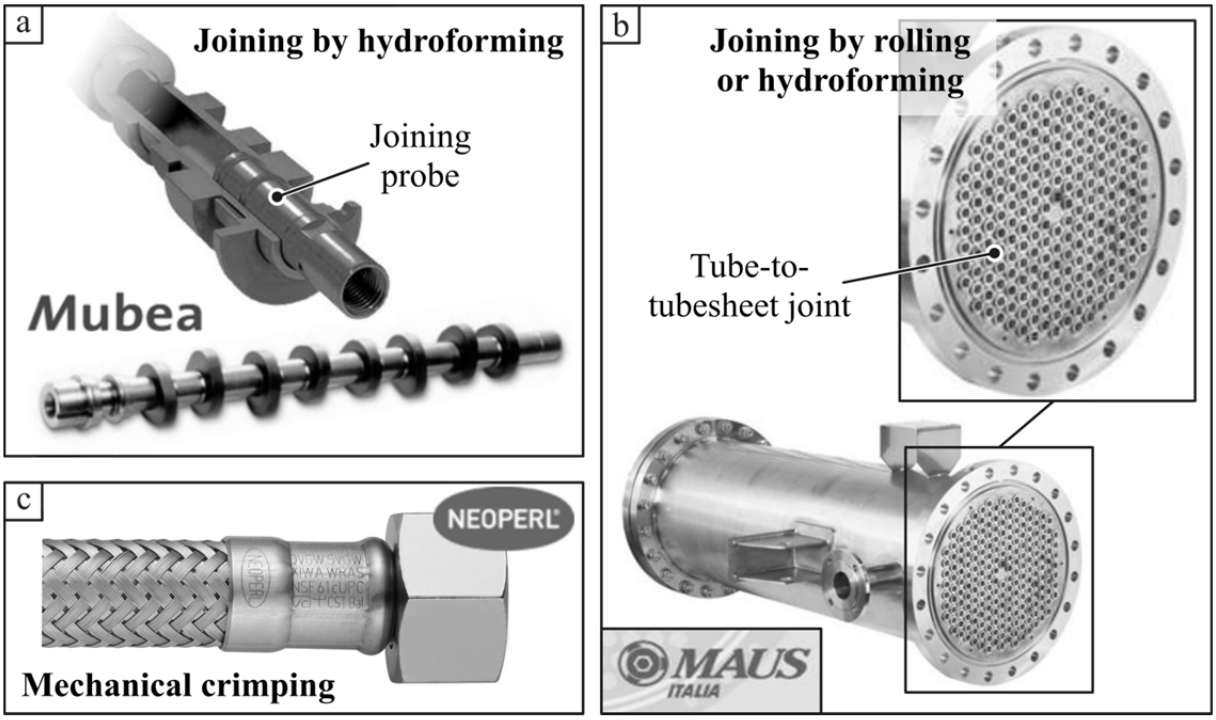
a
Joining by hydroforming
Joining probe
Mubea
b
Joining by rolling or hydroforming
Tube-to-tubesheet joint
MAUS ITALIA
c
NEOPERL
Mechanical crimping

Figure 2-1: Components joined by forming, a) camshaft, b) heat exchanger, and c) water hose coupling (Mori et al., 2013)

2.1 Load transfer mechanisms

In general, joining by forming allows the generation of three different types of joints: interference-fit joints, form-fit connections, and adhesive bonds (Mori et al., 2013). All three mechanisms and any combination of them can be used for tubular workpieces (Psyk et al., 2010). The selection of the load transfer mechanism is based on the requirements of the connection, for instance what materials have to be connected or what external loads are going to act on the joint. For profile-shaped parts, interference-fit and form-fit connections are the most common ones. They can be manufactured by all joining by forming techniques suitable for these workpiece geometries. Adhesive bonds of tubes and profiles are mainly generated with the impulse forming process magnetic pulse welding. Other processes which are able to generate this connection type as well, like roll bonding, are mainly used for sheet metal parts. In the following, all three bonding mechanisms are explained in detail.

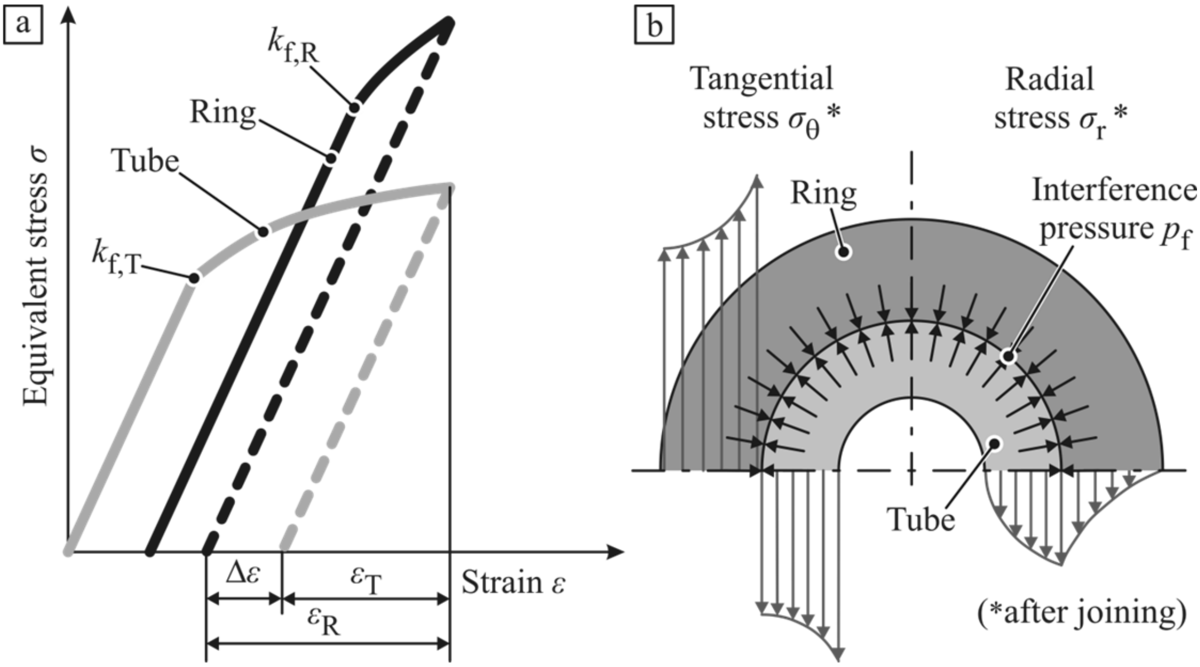

Figure 2-2: Principle of an interference-fit joint manufactured by expansion (Groche and Tibari, 2006), a) difference in elastic recovery strain of the tube ε_T and the ring ε_R, b) resulting stresses in the joint

An **interference-** or **force-fit joint** is based on a difference in the elastic recovery of the two components being joined, leading to an interference pressure p_f between the workpieces after the forming process (see **Figure 2-2a**). The difference in the elastic behavior can be achieved by using materials with different material characteristics, such as yield stress and Young's modulus for the workpieces. For example, in the case of joining by expansion and constant Young's moduli, the ring has to be machined of the material with the higher yield point (Pryzybylski et al., 2007). For compression, the yield stress σ_y of the inner joining partner has to be higher than the tube's value of

σ_y. It is also possible to connect two parts made of the same material by an interference fit. In this case, the difference in elastic deformability results only from the dissimilar geometries of ring and tube (Garzke, 2001) and the achievable joint strengths are typically very low. **Figure 2-3** shows the three general process stages of the manufacturing of an interference-fit connection. The actual joint generation starts after the gap between the joining partners is bridged. During forming, the tube is expanded elastic-plastically while the ring is only elastically deformed. After releasing the forming pressure, the parts recover elastically, but due to the higher elastic strain in the outer part, the tube stops the complete recovery of the ring and, as a result, tangential tensile stresses and tangential pressures remain in the ring and tube respectively (see **Figure 2-2b**). A radial interference pressure p_f at the interface between the partners is formed from these stresses and the optimal maximum forming pressure is achieved just before the outer partner begins to deform plastically (Marré, 2009). Since the interference pressure depends on the difference in elastic recovery of the two partners, a further increase of p_i increases p_f only minimally due to the strain hardening of the outer collar.

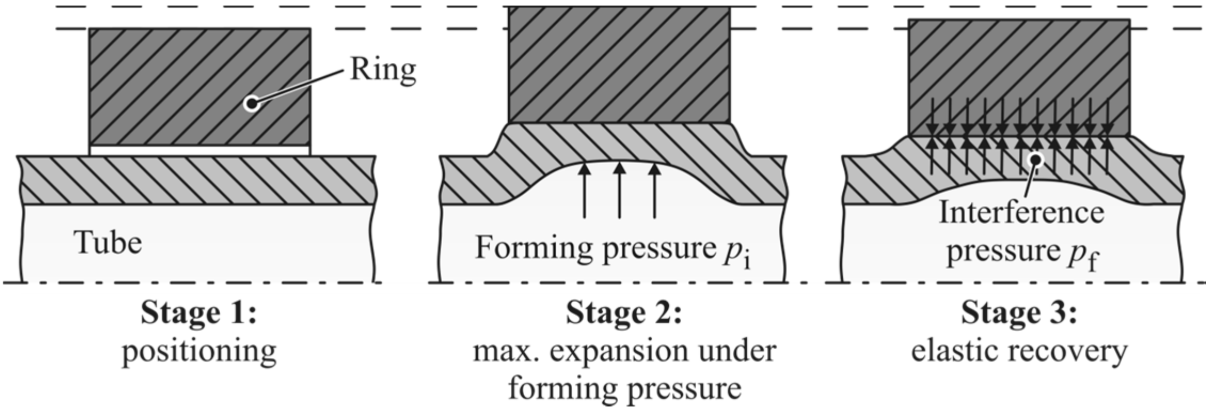
Ring
Tube
Forming pressure p_i
Interference pressure p_f
Stage 1: positioning
Stage 2: max. expansion under forming pressure
Stage 3: elastic recovery

Figure 2-3: Process stages the manufacturing of an interference-fit joint by expansion (Marré, 2009)

The joint strength of an interference-fit connection can be described using Coulomb's law of friction, where the joint strength depends on the interference pressure p_f, the coefficient of friction μ_f, and the area of the joining zone A_C.

$$F_{ax} = A_C \cdot \mu_f \cdot p_f \tag{2.1}$$

Since A_C is usually closely defined by design restrictions in industrial applications, the potential to increase the joint strength by increasing A_C is very limited (Brandes, 1998). The same applies for the material selection of the joining partners and the resulting interference pressure. Hence, it is far more effective to increase the value of μ_f. The coefficient of friction depends in general on the material combination, the surface condition and texture, the relative movement between the partners, and the contact pressure (Hölzl, 1998). For a given material combination, cleaning the contact areas of the joining partners and increasing the surface roughness in this area can increase the coefficient of friction (Marré, 2009). Shot peening and machining with different cutting parameters can be used to increase the surface roughness and the resulting joint strength, for example (Hammers et al, 2009).

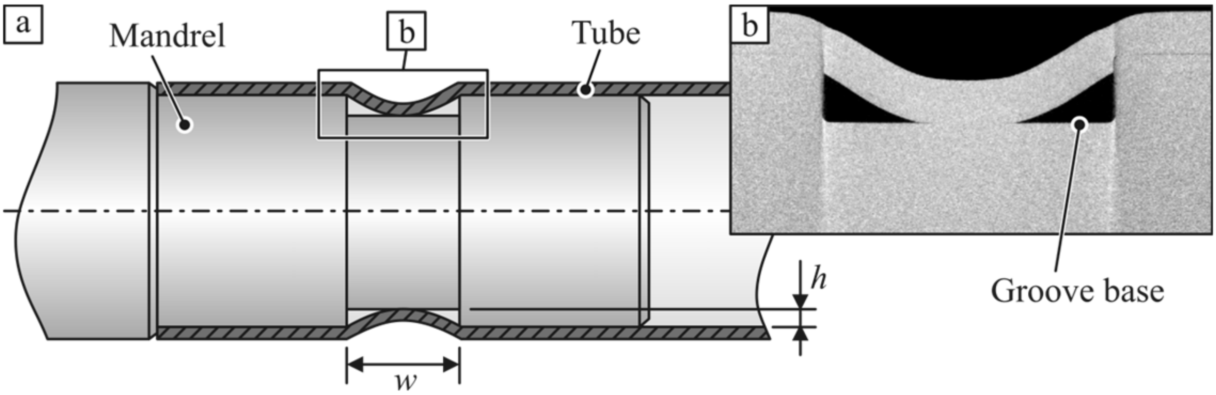

Figure 2-4: Form-fit connection, a) strength affecting parameters and b) tomographic images

In the case of **form-fit joints**, one of the joining partners has additional geometrical characteristics, such as circumferential grooves (see **Figure 2-4**) or knurled surfaces (Eguia et al., 2004). The connection is made by forming the tube material into these elements to produce an undercut (Bühler and von Finckenstein, 1968b). These joints can withstand high loads and provide a tight seal in the connection (Yokell, 1992). Bühler and von Finckenstein (1968b) show that the required push-out force increases with decreasing width w and increasing depth h of the groove (see **Figure 2-4a**). Increasing the number of grooves also strengthens the joints significantly (Park et al., 2005a). Since the manufacturing costs of such circumferential grooves are quite low, Podhorsky and Krips (1990) state that the cost-benefit ratio of this joint type is very high. Usually form-fit connections also allow the transfer of higher loads than interference-fit joints.

For **impulse-welded joints**, solid-state welds are generated from high impact velocities v_{im} up to several hundred m/s and impact pressures up to a few thousand MPa. To achieve such velocities over a short distance, one of the joining partners has to be rapidly accelerated (Lysenko, 1970). During the acceleration a jetting effect occurs in which a thin layer of material from the contact gap is exfoliated and ejected, leaving behind a chemically pure surface (see **Figure 2-5**). Shribman and Tomer (2006) claim that the formation of the weld is attributable to pressure, not heat, like in a traditional weld. During the collision the atoms of the two joining members experience forces large enough to overcome their repulsive forces and, as a result, they form a stable equilibrium due to electron sharing and exchanging. This prediction is supported by numerical investigations of electromagnetic pulse welding performed by Hisashi et al. (2009). However, for some cases there are indications of melting and solidification found in the microstructure of the welded seam (Brown et al., 1978). A wavy or rippled pattern can be seen at the interface of the weld (see **Figure 2-5**).

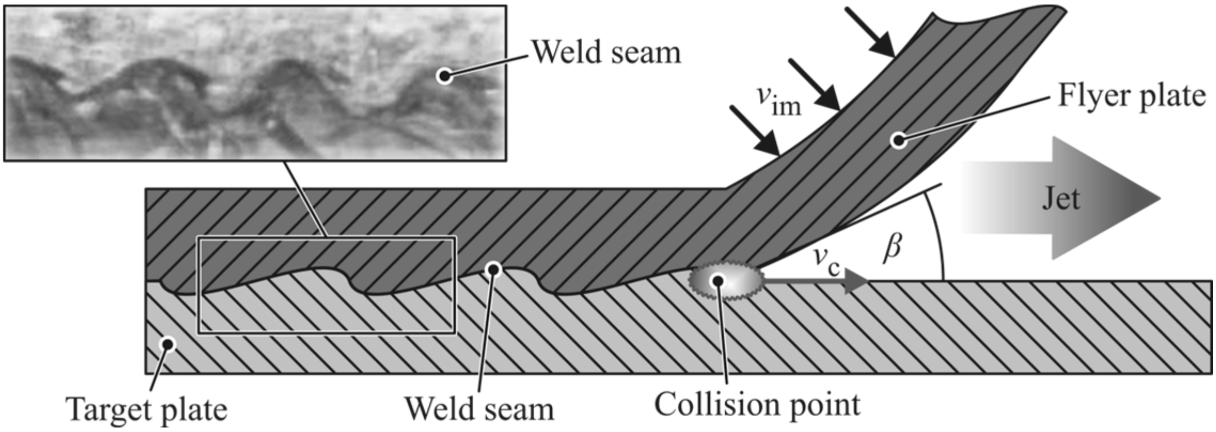

Figure 2-5: Principle of impulse welding (Ben-Artzy et al., 2010)

It is assumed that these waves are the result of the Kelvin-Helmholtz instability and the reflected shockwaves produce this pattern (Ben-Artzy et al., 2010). The major parameters that determine the weld quality are the collision velocity v_c, the collision angle β, and the material properties of the joining partners (e.g. density) (Cowan et al., 1971). Parameters v_c and β are dependent on the applied forming energy and the initial gap between the two joining members.

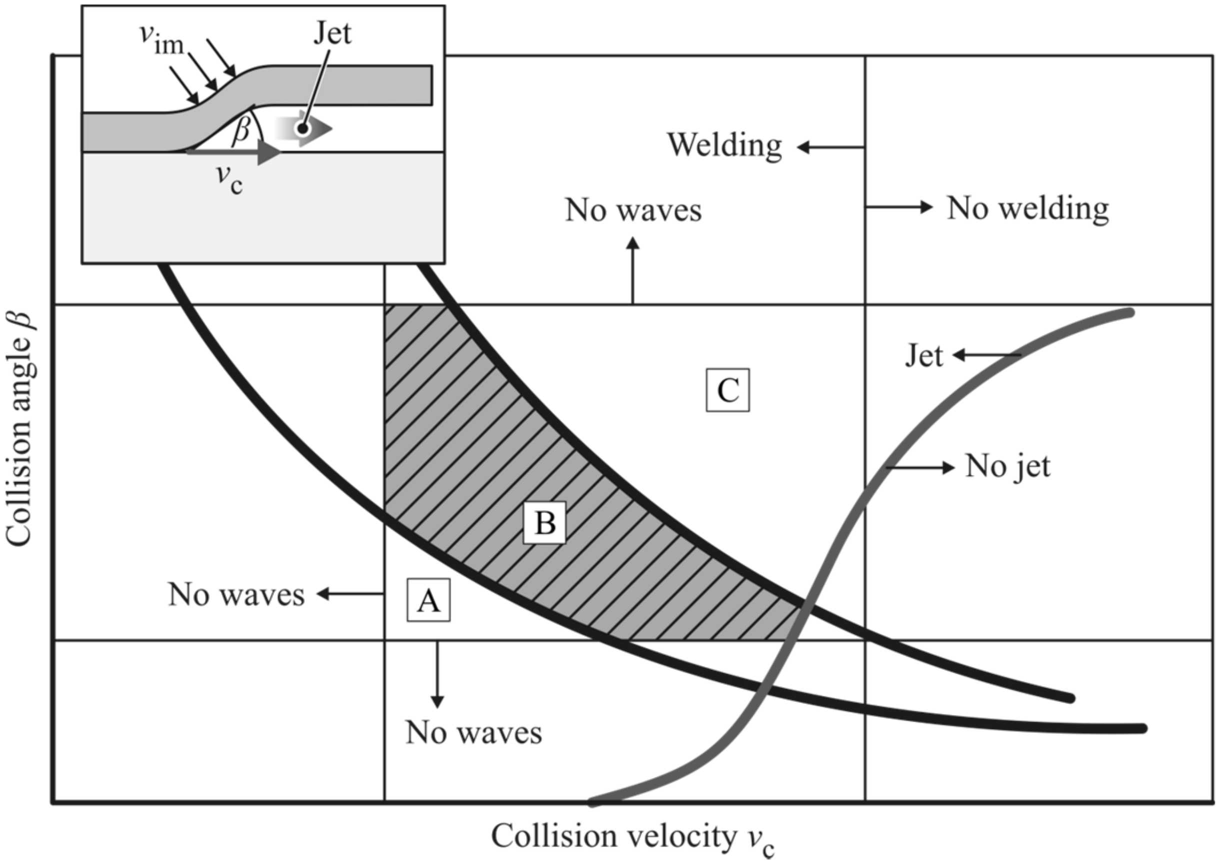

Figure 2-6: Process window impulse welding (Mousavi and Sartangi, 2009)

Okagawa and Aizawa (2004) state that the gap needs to be large enough to provide adequate room for the workpieces to accelerate and build up the needed kinetic energy. But the gap must not be too large as the moving part will decelerate and its kinetic energy will fall below the critical value necessary to generate a weld. A process window of impulse welding presented by Mousavi and Sartangi (2009) is shown in **Figure 2-6**. In zone A, no welding occurs since the values of v_c and β are not large enough. Zone C is characterized by large brittle intermetallic phases caused by the melting of the workpieces due to excessive impact energies. Proper welding can only be seen in Zone B. Impulse welding allows the combination of dissimilar metals, such as aluminum to steel (Kore et al., 2007), to magnesium (Kore, et al. 2009), to copper, and to nickel (Watanabe et al., 2006). The typical strength of impulse welded connections is within the range of the base material's strength, meaning that the base material fails and not the weld seam.

2.2 Mechanical and hydraulical crimping

Mechanical crimping was introduced in 1930 to join hydraulic couplings onto the corresponding hoses (Rasmussen, 1977). The manufacturing of hydraulic hose lines is still the major application of this process (Haisler, 1986). **Figure 2-1c** displays an example of such a connection. As shown in **Figure 2-7**, segmented tools are used for the manufacturing of the connection. These crimping dies are positioned around the outer workpiece. By a hydraulic drive, the tool segments are moved in the radial direction and the necessary forming pressure is applied to the outer workpiece. Typically, tools with four, six, eight, or even ten segments are used for the process. Compared to a process with only two semi-circular dies, the increased number of crimping dies leads to a more uniform distribution of the radial forming pressure. Since one tool set can cover a wider range of compression radii, the process flexibility is also increased (Rasmussen, 1977).

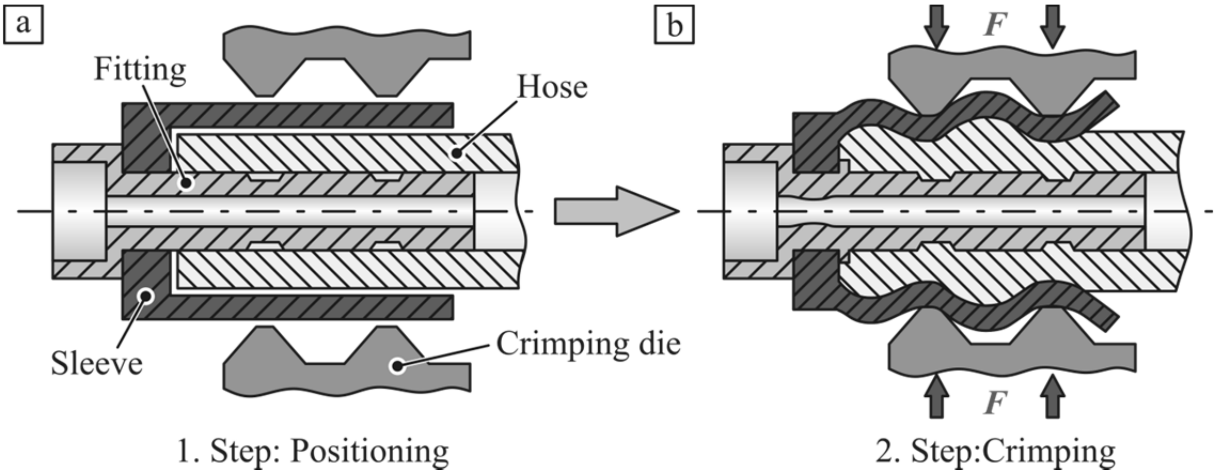

Figure 2-7: Process principle of mechanical crimping, a) positioning and b) crimping (Cho et al., 2005)

Mechanical crimping can be divided into three process steps. First, the three workpieces sleeve, hose, and fitting are loosely assembled before the compression (Cho et al., 2005).While the sleeve and the fitting are made of metal, the hose is made of plastic or rubber. It is also often reinforced with steel wires to resist high working media pressures. A force or displacement-controlled movement of the crimping segments starts in the second process step. This leads to an elastic-plastic compression of the sleeve. If the joining gap between the sleeve and the two inner partners, hose and fitting, is bridged, any further tool movement results in a mutual deformation of all workpieces. From the deformation of all three parts either an interference-fit or a form-fit joint is manufactured. In the last process step the crimping dies are retracted and the finished component is removed from the joining machine.

A detailed investigation of mechanical crimping is presented by Cho and Song (2007). In their numerical study the authors consider the elastic-plastic deformation of joining and the time-dependent relaxation of the rubber hose. It is found that the interference pressure between the joining partners is decreased significantly due to stress relaxation of the hose. It can be assumed that this reduction of interference pressure leads to a decrease of pull-out strength and connection tightness. The use of mechanical crimping for form-fit joining tubular parts without an intermediate plastic or rubber tube is treated by Shirgaokar et al. (2004a). The influence of workpiece positioning, press jaw movement, and tool geometry on the pull-out force and the material thinning in the joint zone is examined in this work.

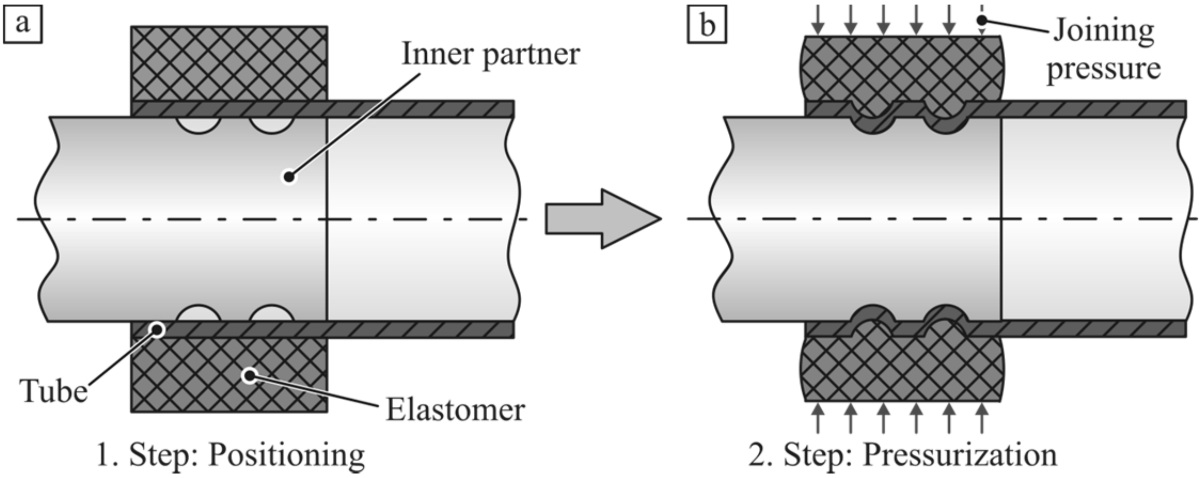

Figure 2-8: Process principle of hydraulical crimping, a) positioning and b) pressurization (Shirgaokar et al., 2004b)

In contrast to mechanical crimping, joining by hydraulic crimping uses an elastomer to apply the required forming pressure (Shirgaokar et al., 2004b). As shown in **Figure 2-8a**, the workpieces to be joined, which are typically a tube and a mandrel, are positioned inside the elastomer. Afterwards, the working media pressure is applied to the outer circumference of the elastic forming tool (see **Figure 2-8b**). The plastic deformation of the outer workpiece results from the reversible deformation of the elastomer. Thereby, the tube is bulged into grooves or an interference fit is created by an elastic-plastic deformation of both partners.

Shirgaokar et al. (2004b) identified by numerical studies the main parameters influencing the quality of hydraulically crimped connections. These are, for example, the coefficient of friction in the contact zone, the yield stress of the outer joining partner, and the difference between the diameters of tube d_T and mandrel D_M. An advantage of hydraulic crimping compared to the mechanical process variant is the more uniform pressure distribution over the circumference of the outer joining part. The resilient elastomer also allows for the filling of different groove geometries. In the case of mechanical crimping, each form-fit element requires a press jaw sets which is specifically pre-contoured to the groove's geometry.

2.3 Joining by rolling

During joining by rolling the workpieces are expanded due to the mechanical contact between the rolling element of a tool and the inner joining partner. The expansion of the tube is determined by the difference between the outer diameter of the motion of the rolling elements and the initial inner tube diameter. If this value is chosen properly, an elastic-plastic expansion of the inner workpiece and a purely elastic expansion of the outer part are achieved and an interference-fit connection can be created (Jantscha, 1929). Two basic variants of this joining process exist (Hagedorn, 2005). The first one, which is displayed in **Figure 2-9a**, is joining by rolling with an adjustable joining zone. In this variant, the expansion of the tube is defined beforehand and cannot be adjusted during process. The second basic variant, joining by rolling with an adjustable expansion, is shown in **Figure 2-9b**.

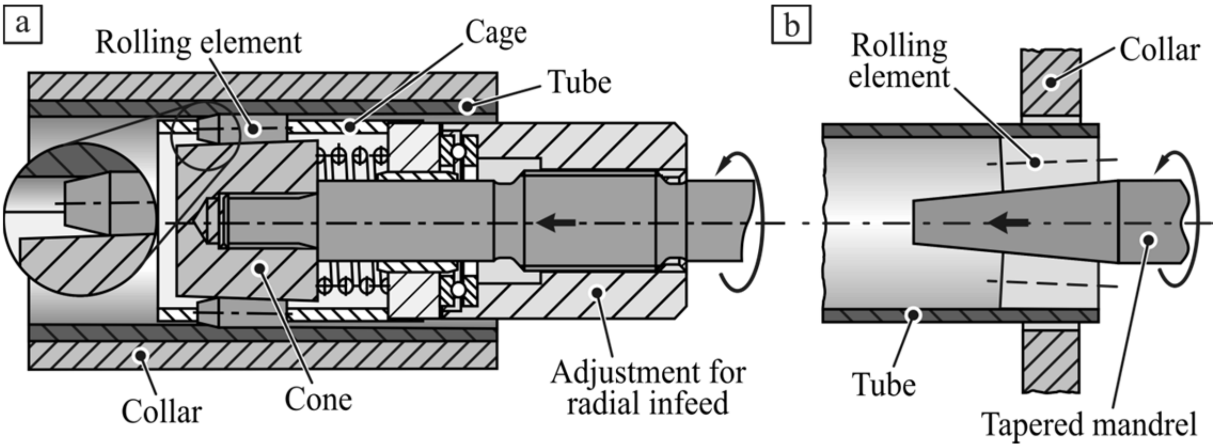

Figure 2-9: Process principles of joining by rolling with a) adjustable joining zone and b) adjustable expansion (Hagedorn, 2005)

Here, the axial position of the joining tool is fixed and the expansion can be adjusted as needed. By adding an additional CNC-axis, both basic variants can be combined

(Hagedorn, 2005). This CNC-axis is necessary to control the radial positioning of the rolling elements.

In early investigations on joining by rolling, Jantscha (1929) studied the influence of different material combinations on the achievable joint strength. The findings correspond to the general coherences for interference-fit connections described in **Section 2.1**. It is revealed that an increase of the yield stress difference between outer and inner joining partner increases the joint strength. The author also shows that the outer workpiece needs to have the higher yield stress to generate a sufficient joint.

A typical application of joining by rolling is the manufacturing of tube-to-tubesheet connections. For example, this joint type is applied in heat exchangers (see **Figure 2-1b**).

2.4 Joining by die-less hydroforming

Joining by hydroforming uses a pressurized hydraulic fluid to expand at least one of the joining partners to generate a joint between them. The process can either be performed within a die (Neugebauer, 2007) or die-less (Krips and Podhorsky, 1976). If a die holds the parts that are to be joined, the process is usually carried out parallel to additional forming operations (Neugebauer, 2005). Due to the need for dies and machines that provide the additional closing force during the process, this variant is only economically applicable for large quantities and a limited number of parts. These restrictions can be avoided by using joining by die-less hydroforming (DHF).

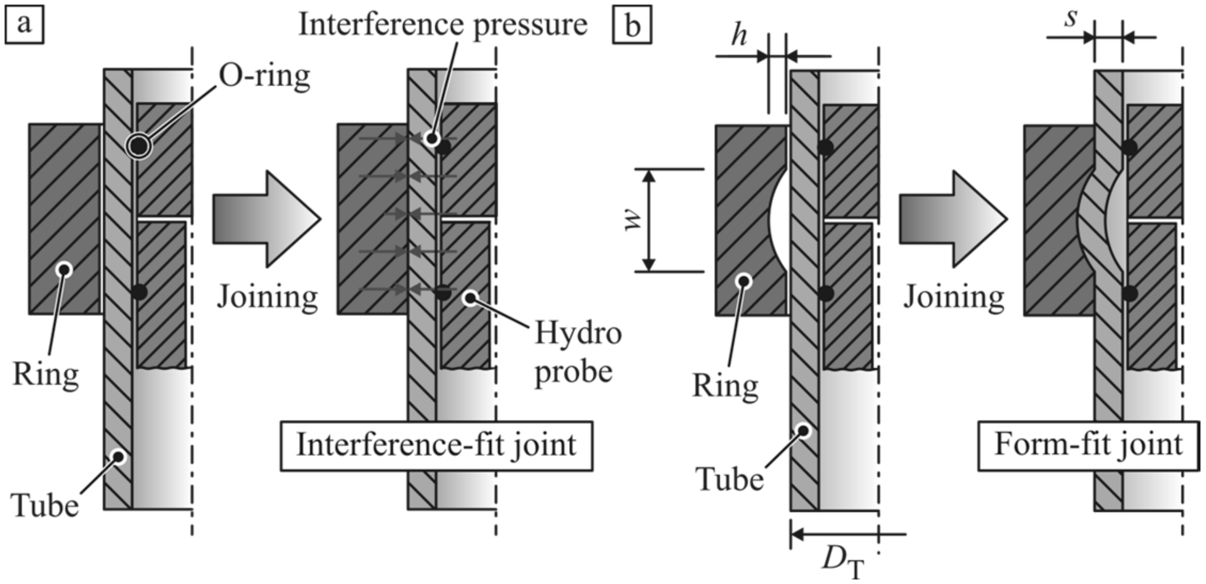

Figure 2-10: Process principle of joining by hydroforming, a) interference-fit joining and b) form-fit joining (Gies et al., 2012)

In the first process step, both joining partners are aligned in a typical shaft-to-collar configuration and a hydro-probe is positioned inside the inner joining partner (Marré, 2009). The probe is placed in the axial direction in the joining area underneath the outer collar (see **Figure 2-10**). In the next step, a pressurized fluid (e.g. water, oil) is applied to the joining area, which is sealed in axial direction. Therefore, the fluid pressure p_i can only act locally in this area. Plastic deformation of the inner tube occurs as soon as the stresses caused by p_i exceed the tube's yield stress (Yokell, 1990). After the gap between the two partners is closed, both parts are deformed together by the acting hydraulic pressure. In the last process step, the forming pressure is released and the parts recover elastically. As **Figure 2-10** shows, joining by DHF allows the manufacturing of interference-fit joints as well as form-fit connections (Krips and Podhorsky, 1976).

In Weddeling et al. (2011a), a combination of joining by hydroforming and adhesive bonding is analyzed. After generating a form-fit connection by DHF, an adhesive (DP490) is applied to the joining zone via a bore and a circumferential channel at the bottom of the circular grooves. The joint strength of the connections is increased tremendously compared to the pure form-fit joints. A combination of joining by hydroforming and adhesive bonding is very suitable in the case where the required joint strength cannot be achieved by interference-fit or form-fit connections due to design restrictions. Compared to pure adhesive bonds, this joint type reaches a handling strength right after the DHF process. Therefore, operational delays caused by the curing process of the adhesive can be avoided (Marré, 2009).

To determine the load transferable by an interference-fit joint and the forming pressure required to achieve this strength, Krips and Podhorsky (1976) developed an analytical model for the joining of tubes to tubular plates. They assumed plane stress and the yield criterion according to von Mises for their model. The authors also chose an elastic-ideal plastic material behavior for the tube and a pure elastic material behavior for the ring. Garzke (2001) also developed an analytical model for the calculation of the interference pressure with similar assumptions. Furthermore, he included possible differences in the Young's moduli of both joining partners. Both models show very similar results and correspond quite well to numerical and experimental results (Marré, 2009). They illustrate a linear relationship between forming pressure p_i and achievable interference pressure p_f, but both models do not consider the yield strength of the outer joining partner and its plastic deformation for the calculation of the p_f. Therefore, the interference pressure increases infinitely with an increasing hydraulic pressure according to both approaches. As a result, both models do not allow the determination of the technical upper limit of p_f. For this reason, Marré (2009) included the yield strength of the outer joining partner in his analytical approach. The numerical and experimental verifications of his model showed that the relationship between p_f and p_i is only linear until the a specific hydraulic pressure $p_{i,p,max}$ is reached and the ring starts to become plastically deformed. After exceeding $p_{i,p,max}$, the increase of the interference pressure is very minimal since it is only based on the strain hardening of the ring. All three models describe the influence of the geometry of the joining partners on the achievable interference pressure. Due to increasing stiffness with an increasing part thickness, a higher hydraulic pressure is required to generate the same interference pressure for a thicker ring (Garzke and Geuss, 2007). Therefore, a decrease in ring thickness at a constant forming pressure leads to a decrease in p_f. This relationship applies to the thickness variation of the tube as well.

For the manufacturing of form-fit connections, Gies et al. (2012) developed an analytical process parameter prediction based on membrane theory. This approach allows the determination of the forming pressure required to fill a specific groove geometry. It shows that the fluid pressure is affected by the groove's geometry, such as the groove width w and the groove depth h, the yield stress of the inner joining partner $\sigma_{y,T}$, the diameter D_T, and the thickness of the inner joining partner. The experimental investigations of Gies et al. (2013) also show that these are the main parameters influencing the required forming pressure.

Besides its ability to manufacture multi-material connections without any additional connection elements, Krips and Podhorsky (1976) state that the process monitoring for joining by DHF is very simple and requires no additional process steps after joining to ensure the joint strength. Due to high process stability, the achieved strength of the connection can be derived from the applied forming pressure. Compared to other joining techniques like welding or riveting, the process times for joining by hydroforming are fairly short. They usually range from a fraction of a second (Grünendick, 2002) up to a few seconds (Krips and Podhorsky, 1976), depending on the joining task.

Notable industrial applications of joining by hydroforming can be found in the fields of vehicle engineering and power plant design, specifically heat engineering. In the 1970s and 1980s, Krips and Podhorsky (1976) suggested the process for the manufacturing of tube to tubular plate joints for heat exchangers and for the joining of pipe sections (Krips and Podhorsky, 1976) in power plants. One of the first applications of DHF in the automotive industry is presented by Brandes (1998). In his work, the technique is used for the manufacturing of camshafts that consist of a tube with a joint on cams (see **Figure 2-1a**). He states that a weight reduction of up to 50% is possible with this design compared to a traditional forged camshaft. Brandes (1998) also introduces a joining probe that allowed the simultaneous generation of all joints in a part during one pressure cycle. Homberg et al. (2006) investigated the joining of extruded aluminum and magnesium profiles for the manufacturing of lightweight frame structures. To increase the industrial applicability of joining by die-less hydroforming, Marré et al. (2011) developed a probe that allows the joining of non-circular cross sections. Experimental investigations with a rectangular prototype of this joining probe concept show its suitability for the manufacturing of lightweight frame structures (Weddeling et al., 2011a).

2.5 Joining by impulse forming

Impulse forming methods allow the rapid manufacturing of multi-material joints without additional connection elements. With these techniques all three bonding mechanisms introduced in **Section 2.1** can be generated: interference-fit connections, form-fit joints, and adhesive bonds (Psyk et al., 2011). Examples of impulse joining processes are joining by electromagnetic forming (EMF) including magnetic pulse welding (Mori et al., 2013) and explosive welding (Zhang et al., 2011). Processes which are suitable for the joining of tubular workpiece are electromagnetic crimping (Marré et al., 2008) and vaporizing wire actuator forming (Vivek et al, 2014). In comparison to other widely used joining processes, like mechanical crimping, the connections achieved by impulse forming have very homogenous bond characteristics. This results from a uniform forming pressure distribution, which is typical for these techniques (Vivek et al., 2014). In addition, numerous materials show increased forming limits under impulse loading (Balanethiram and Daehn, 1995). Since deeper undercuts can be filled without damaging the deformed joining partner, this is particularly beneficial for form-fit joints (Bühler and von Finckenstein, 1968b). Compared to explosive welding, joining by electromagnetic forming can be applied in a factory environment without any safety concerns. Since the applied forces can be adjusted very accurately via the charging energy, electromagnetic forming is also highly reproducible (Daube et al., 1966). Another advantage of the process is that there is no physical contact between tool and workpiece during the joining operation (Bertholdi and Daube, 1966). This allows for the forming of a large variety of different profile cross sections. It also offers the possibility of joining an already coated workpiece without damaging the coating during the forming operation.

One of the major disadvantages of joining by electromagnetic forming is the complex and expensive process design. In many cases, only sophisticated numerical models lead to useful results because of the very intricate interactions between electromagnetic and mechanical mechanisms during the forming process (Psyk et al., 2011). These numerical calculations require a comprehensive knowledge in the field of multi-physical finite-element modeling. Additionally, the computation time of such models is typically quite long. Alternatively, very time-consuming experimental studies can be performed to determine the necessary process parameters (Bühler and von Finckenstein, 1971).

2.5.1 Fundamentals of electromagnetic compression

Electromagnetic forming (EMF) is an energy-based impulse forming process (Winkler, 1973). The technique uses pulsed magnetic fields to form highly conductive metals, such as aluminum. The process can be used for the compression or expansion of profiles with a closed cross section as well as for forming sheet metal (Harvey and Brower, 1958.). Although the first two process variants allow the joining of tubular workpieces, only electromagnetic compression is a promising technique for connecting such parts. The reason for this is that the mechanical strength of tool coils for electromagnetic expansion is relatively low and their lifetime is very limited (Belyy et al., 1977). Hence, only joining by electromagnetic compression is treated here.

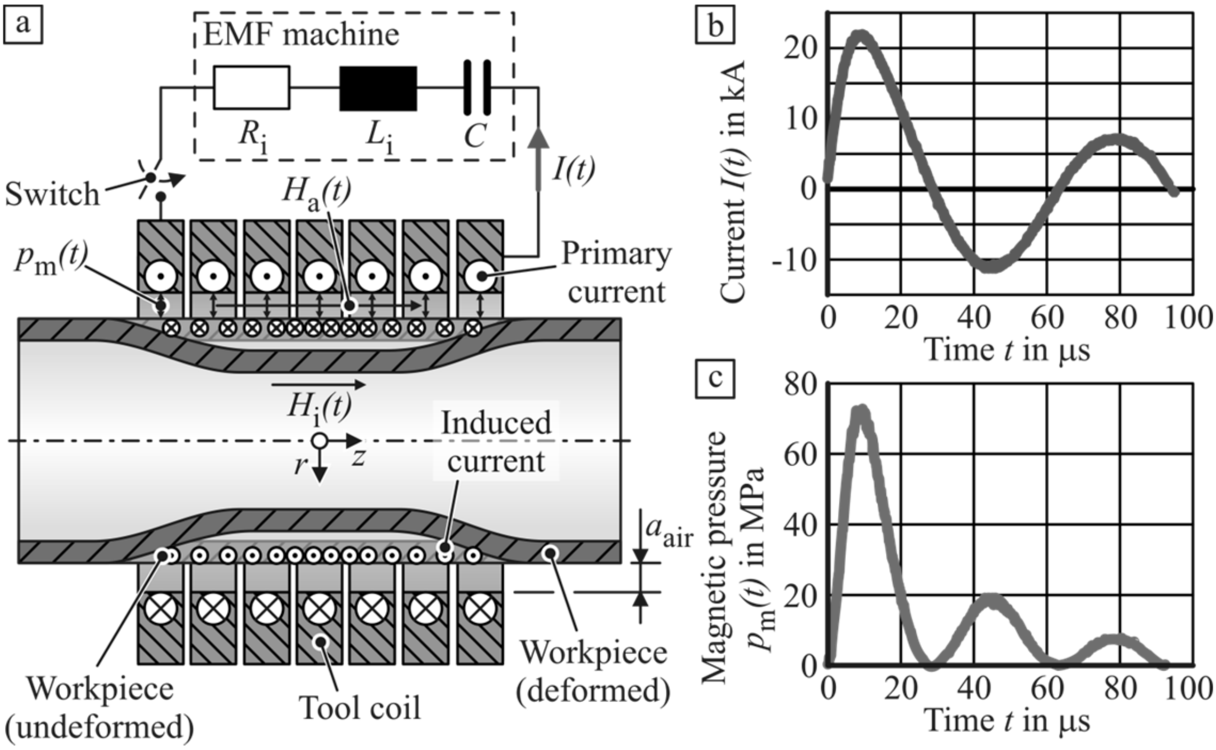
a
EMF machine
R_i
L_i
C
$I(t)$
Switch
$H_a(t)$
$p_m(t)$
Primary current
$H_i(t)$
Induced current
r
z
a_{air}
Workpiece (undeformed)
Tool coil
Workpiece (deformed)
b
Current $I(t)$ in kA
20
10
0
-10
0 20 40 60 80 100
Time t in µs
c
Magnetic pressure $p_m(t)$ in MPa
80
60
40
20
0
0 20 40 60 80 100
Time t in µs

Figure 2-11: a) Principle of electromagnetic compression b) discharge current c) magnetic pressure

Figure 2-11a shows the general setup of electromagnetic tube compression consisting of the EMF machine, the tool coil, and the workpiece. This setup can be represented by a *RLC* circuit in which the forming machine is symbolized by the inner resistance R_i, the inner inductance L_i, and the capacitance C. The combination of tool, coil, and workpiece is considered to be the consumer load of the circuit. The capacitance represents a number of capacitors which are used to store the energy need for the workpiece deformation before the discharge. This charging energy E can be calculated from the capacitance C and the applied charging voltage U.

$$E = \frac{1}{2} C \cdot U^2 \tag{2.2}$$

With a usual charging voltage of 3 to 25 kV, typical charging energies for electromagnetic forming systems range from 1 up to a 100 kJ (Beerwald, 2005). A sudden discharge of the capacitor generates a damped sinusoidal current *I(t)* through the coil (see **Figure 2-11b**). The values of the amplitudes of the primary currents running through the tool coil are typically between 10^4 - 10^6 kA, depending on the application and the parameters of the machine, coil, and workpiece (Daehn, 2011). The resulting magnetic field $H(t,r,z)$ around the coil induces a secondary current in the workpiece that opposes the primary current. Because of the so-called skin effect (Lamb, 1883), the induced currents run close to the surface of the workpiece. The skin depth δ_s is defined as the distance between the workpiece's surface and the point at which the current density is reduced to $1/e$ of its maximum value. The skin depth can be calculated based on the discharge frequency f, the permeability μ, and the electrical conductivity κ of the workpiece.

$$\delta_s = \sqrt{\frac{1}{\pi \cdot f \cdot \mu \cdot \kappa}} \tag{2.3}$$

Psyk et al. (2011) state that the permeability is defined as the magnetic permeability μ_0 in vacuum multiplied by the relative permeability μ_r of the workpiece material.

$$\mu = \mu_0 \cdot \mu_r \tag{2.4}$$

Due to the secondary current, the magnetic field is shielded from the inside of the tube and concentrated in the gap between coil and workpiece. Because of the high energy density between coil and profile, high Lorentz forces act orthogonally on the tube. As soon as the stresses in the tube reach the yield stress of the material, the profile is plastically deformed in the radial direction. Typically, the process takes between 10 and 100 µs. During this time the workpiece reaches strain rates of 10^4 s^{-1} and velocities of up to 250 m/s or more (Psyk et al., 2011).

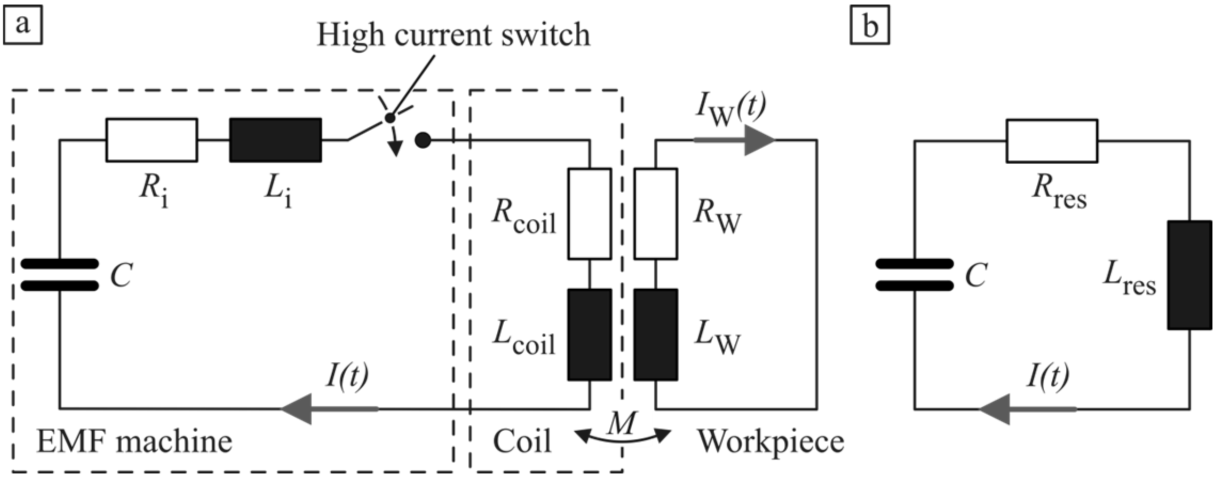

Figure 2-12: a) Equivalent circuit diagram of EMF (Bauer, 1967) b) simplified circuit diagram (Jablonski, 1976)

Figure 2-12a shows the equivalent circuit diagram of an electromagnetic forming application presented by Bauer (1967). For the determination of the discharge current

I(t), the inductances and the resistances of the *RLC* circuit can be aggregated. Jablonski and Winkler (1978) state that the resulting inductance L_{res} of the *RLC* circuit displayed in **Figure 2-12b** consists of the inner inductance L_{i}, the tool coil L_{coil}, and workpiece inductance L_{w} as well as the mutual inductance M between coil and tube.

$$L_{res} = L_i + L_{coil} - \frac{M^2}{L_w} \tag{2.5}$$

$$M = n \cdot L_w \tag{2.6}$$

For the calculation of the resulting resistance R_{res} the authors give the following expression:

$$R_{res} = R_i + R_{coil} + \frac{M^2}{{L_w}^2} R_w \tag{2.7}$$

The result of this is the simplified circuit diagram displayed in **Figure 2-12b**. If the capacitance C, the aggregated values of the inductance, and the resistance are known, the following differential equation can be applied to describe the oscillations of the simplified circuit:

$$L_{res} \frac{dI(t)}{dt} + R_{res} I(t) + \frac{1}{C} \int I(t) dt = 0 \tag{2.8}$$

By assuming no current and a capacitor voltage U at the beginning of the process as boundary conditions, a solution for the differential equation can be found as (Psyk et al., 2011):

$$I(t) = \frac{U}{\omega \cdot L_{res}} \cdot e^{-\delta t} \sin(\omega \cdot t) \tag{2.9}$$

In this solution, the variable ω represents the damped angular frequency of the discharge current.

$$\omega = 2 \cdot \pi \cdot f = \frac{2\pi}{T} \tag{2.10}$$

Its value can be determined by the difference of an ideal undamped frequency ω_0 and the damping coefficient δ of the simplified circuit.

$$\omega^2 = {\omega_0}^2 - \delta \tag{2.11}$$

The undamped angular frequency depends on the resulting inductance L_{res} and the capacitance of the simplified *RLC* circuit.

$${\omega_0}^2 = \frac{1}{L_{res} \cdot C} \tag{2.12}$$

For the calculation of the damping coefficient the resulting inductance and the resistance R_{res} have to be known.

$$\delta = \frac{R_{res}}{2 \cdot L_{res}} \tag{2.13}$$

For the equations above the inductance and the resistance of the combination of workpiece and tool coil are assumed to be constant. Due to the workpiece movement, both variables are indeed time-dependent. But a consideration of this dependence would inhibit an analytical solution of the differential Equation (2.8). Therefore, the workpiece movement is neglected for the calculation of the discharge current and both variables are assumed to be constant. The same applies for the following determination of the acting loads.

2.5.2 Determination of the acting loads

For the process design of electromagnetic forming and joining it is important to know the relevant parameters and their interactions. Of particular interest is the determination of the acting loads. Based on the current density $\vec{J}$ in the workpiece and the magnetic flux density $\vec{B}$, the volume forces $\overrightarrow{F_L}$ acting on the part can be determined by the expression introduced by Lorentz (1895):

$$\overrightarrow{F_L} = \vec{J} \times \vec{B} \tag{2.14}$$

Disregarding the radial component of the magnetic field intensity, the current density equals the derivative of the magnetic field intensity H with respect to the radius r of a tubular workpiece:

$$\vec{J} = -\frac{\partial H}{\partial r} \tag{2.15}$$

The magnetic flux density corresponds to the product of the magnetic field intensity and permeability μ. With this relationship, the forces acting on the workpiece in the radial direction can be described by the following equation (Bauer, 1967):

$$F_{L,r} = -\mu \cdot H \cdot \frac{\partial H}{\partial r} = -\frac{1}{2}\mu \frac{\partial (H^2)}{\partial r} \tag{2.16}$$

These volume forces can be converted mathematically into the so-called magnetic pressure p_{m}. Bühler and Bauer (1968) state that the pressure difference between two locations in the wall of the workpiece can be predicted by integrating the volume forces over the distance. Hence, the pressure p_{m} acting on the tube can be determined by applying the workpiece's inner r_{T} and outer radius R_{T} as integration limits:

$$p_m(t) = \int_{R_T}^{r_T} F(r,t)dr = \frac{1}{2}\mu\left(H_o{}^2(t) - H_i{}^2(t)\right) \tag{2.17}$$

In this equation H_{o} represents the magnetic field intensity between coil and tube or rather at the outer surface of the workpiece and H_{i} represents the field intensity inside the tube. The magnetic field inside the tube can be neglected if the skin depth δ_s is small compared to the workpiece's thickness:

$$p_m(t) = \frac{1}{2}\mu \cdot {H_o}^2(t) \tag{2.18}$$

The magnetic field intensity H_o in the gap between a direct acting compression coil and the workpiece can be determined with the following equation (Winkler, 1973):

$$H_o(t) = \frac{n \cdot I(t)}{l_{coil}} \tag{2.19}$$

This expression includes the number of turns n, the current running through electromagnetic actuator $I(t)$, and the coil length l_{coil}. **Figure 2-11c** shows a pressure curve which is calculated by the equations of this chapter in combination with the measured current in **Figure 2-11b**. It can be seen that the function of the acting magnetic pressure $p_m(t)$ is a damped, quadratic sinusoidal function (Beerwald, 2005).

2.5.3 Strength-affecting parameters and joint design strategies

In general, the highest strengths of electromagnetically joined connections are achieved either by pulse-welded adhesive bonds or crimped form-fit joints. Park et al. (2005a) and Weddeling et al. (2014b) showed that both bonding mechanisms can lead to joint strengths high enough to cause a failure in the base material and not in the joining zone. Since interference-fit connections are typically weaker than adhesive bonds and form-fit joints, they fail by the separation of the workpieces in the joining zone. Besides the manufacturing of high-strength bonds, magnetic pulse welding also allows the generation of gas-tight joints. This characteristic cannot be achieved with the two other connection types. But compared to form-fit or interference-fit joining, magnetic pulse welding typically requires higher workpiece velocities to cause the formation of a bond. Therefore, higher input energies and increased discharge currents are necessary to supply magnetic pressures high enough to reach the necessary impact velocities. Due to the increased acting pressures, reinforcements of the tool coils have to be stronger to ensure a sufficient tool lifetime. In addition, the wear of the EMF equipment is promoted by the increased discharge currents (Weddeling et al., 2014b).

Because of its lower tool loadings during the joining process and due to the fact that joint strengths similar to pulse-welded connections can be achieved, form-fit joining by electromagnetic crimping is a very promising technique for the production of lightweight frame structures. Therefore, the focus of this work is on this joint type. Since a form-fit joint often features an additional interference fit, this load transfer mechanism is included in the following state of the art on electromagnetic crimping.

In compression an interference fit is typically generated if the yield strength of the mandrel material is higher than the yield strength of the tube. Kleiner et al. (2006)

found an increasing connection strength with an increasing yield stress. This corresponds to the results of die-less hydroforming. The authors also observed that the strength of interference-fit connections joined by EMF depends on the impact velocity and the impact pressure of the tube onto the mandrel. Kleiner et al. (2006) show that higher impact velocities due to higher charging energies lead to an increased joint strength. To achieve a sufficient impact velocity, a gap between the partners in the initial condition is necessary. Additionally, the size of this gap is related to the achievable strength (see **Figure 2-13**). With a very small gap it is almost impossible to generate a significant connection strength. On the basis of recordings of workpiece velocities measured in free forming experiments, Kleiner et al. (2006) observe that the part is first accelerated up to a certain maximum velocity and afterwards it decelerates. In order to achieve the highest joint strength, the gap between the workpieces should be chosen considering the displacement at which the maximum velocity is reached. To achieve sufficiently high collision velocities for small gaps, increased charging energies are required.

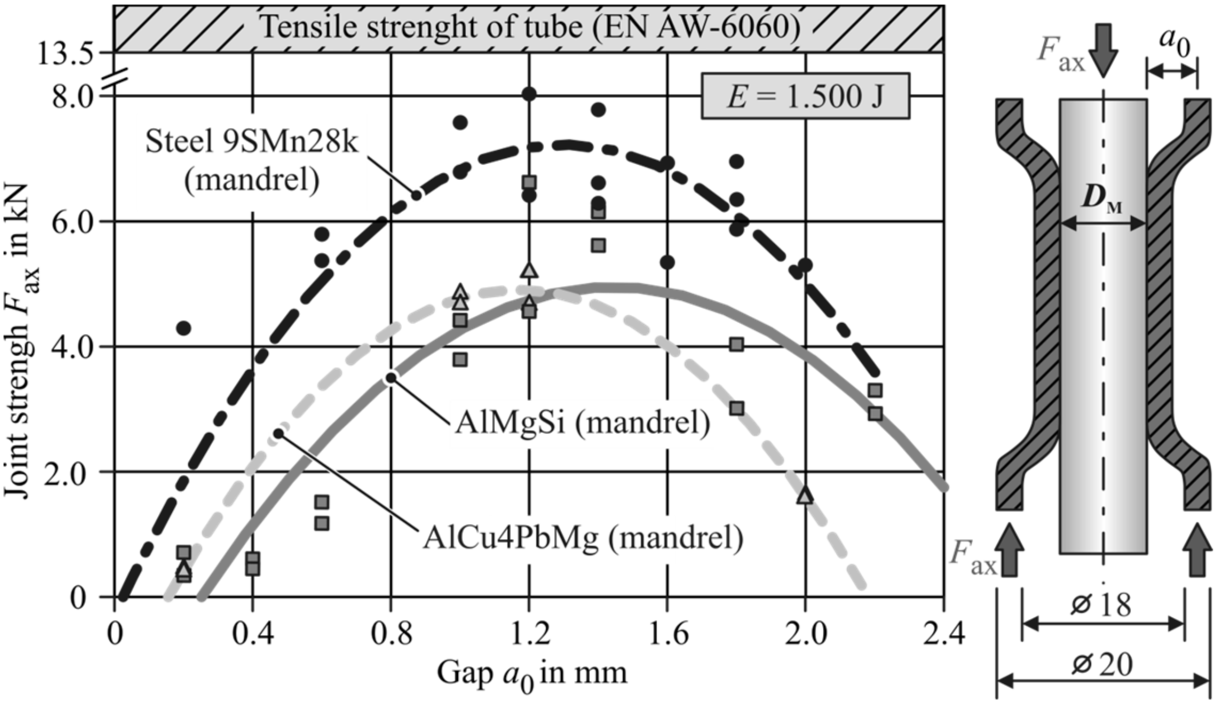

Figure 2-13: Joint strength versus joining gap a_0 and mandrel material (Barreiro et al. 2006)

Bühler and von Finckenstein (1968a) examine the influence of the compressive strength of the mandrels on the axial joint strength. This value is characterized by the ratio Q_M of the mandrel's inner diameter d_M and the outer diameter D_M. Therefore, a value of $Q_M = 0$ represents a solid mandrel with a high compressive strength and a ratio $Q_M \approx 1$ embodies a very thin-walled tube with an extremely low strength. To realize different diameter ratios, the wall thickness is varied. With regard to the achievable connection strength, the researchers identify three specific areas (see

Figure 2-14). A high compressive strength causes a very low deformation of the mandrel and, consequently, a low joint strength. Above a certain value the increase of Q_M causes a significant rise in the resulting pull-out force. If Q_M exceeds a critical ratio, the pull-out force drops severely. This is because the mandrel deformation becomes elastic-plastic instead of just elastic.

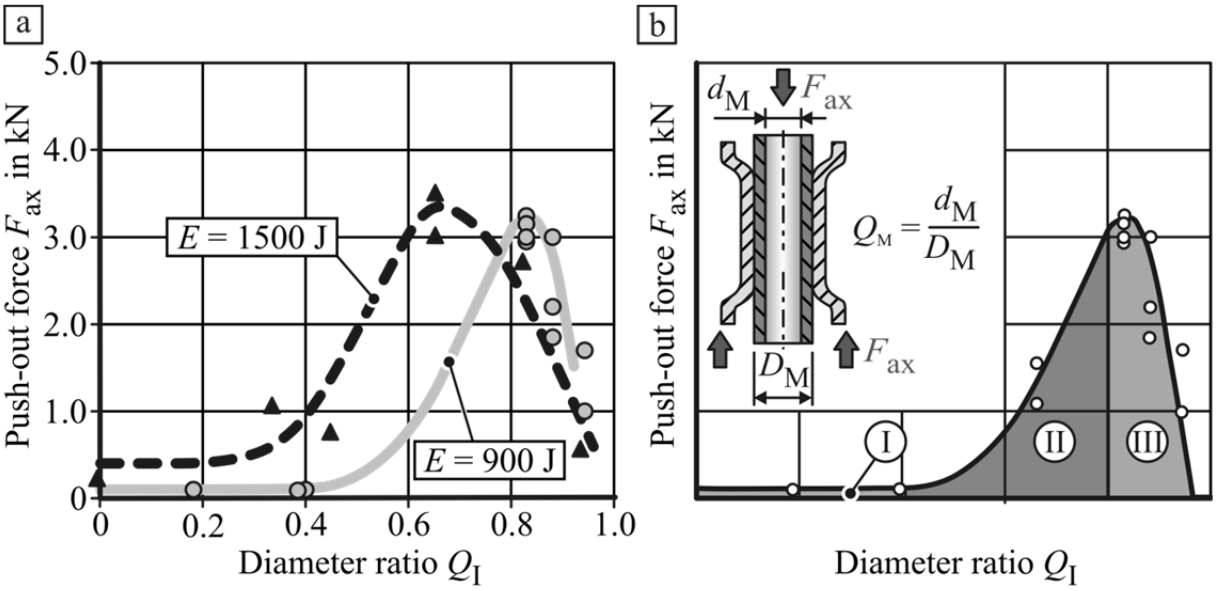

Material tube:	EN AW-6060	**Tube dimensions D_T x s:**	20 x 1 mm
Material mandrel:	9SMn28k	**Joining gap a_0:**	0.2 mm

Figure 2-14: Influence of the diameter ratio Q_M on the joint strength (Hammers et al., 2009)

As described above, in addition to the elastic-plastic bracing of the two partners, the joint strength depends on the coefficient of fiction in the joining zone and the size of this area. Hammer et al. (2009) show the influence of different surface properties on the achievable connection strength. To vary the surface roughness, the authors used different machining parameters when manufacturing the mandrels. They also applied shot peening to the mandrel surface to plastically deform it and thereby increase its hardness. Their work shows that both methods are suitable to increase the connection strength. The joining mechanism is particularly important if sensitive materials such as fiber-reinforced composites shall be joined and any damaging of the fibers by sharp edges has to be avoided. Interference-fit connections are also suitable if extensive deformation cannot be tolerated (Marré et al., 2007).

For form-fit joints one of the joining partners is featured with additional geometric elements such as circumferential grooves. **Figure 2-15** shows possible form-fit elements and the load cases for which they are suitable. The earliest studies on the manufacturing of these kinds of joints are performed by Bühler and von Finkenstein (1968b). They examine the influence of different geometries of circumferential grooves on the achievable push-out strength. Within their work the authors vary the groove width *w* and depths *h* of rectangular grooves. The charging energy is adjusted in such manner that the tube wall just touches the bottom of the groove. Their experiments show a significant effect of the grove geometry on the push-out strength. Bühler and von Finkenstein (1968b) observe an increase in push-out force with a decreasing groove width and an increasing groove depth. Golovashchenko (2001) performed similar experiments with circular grooves instead of rectangular ones. The findings are very similar to those generated by Bühler and von Finkenstein (1968b).

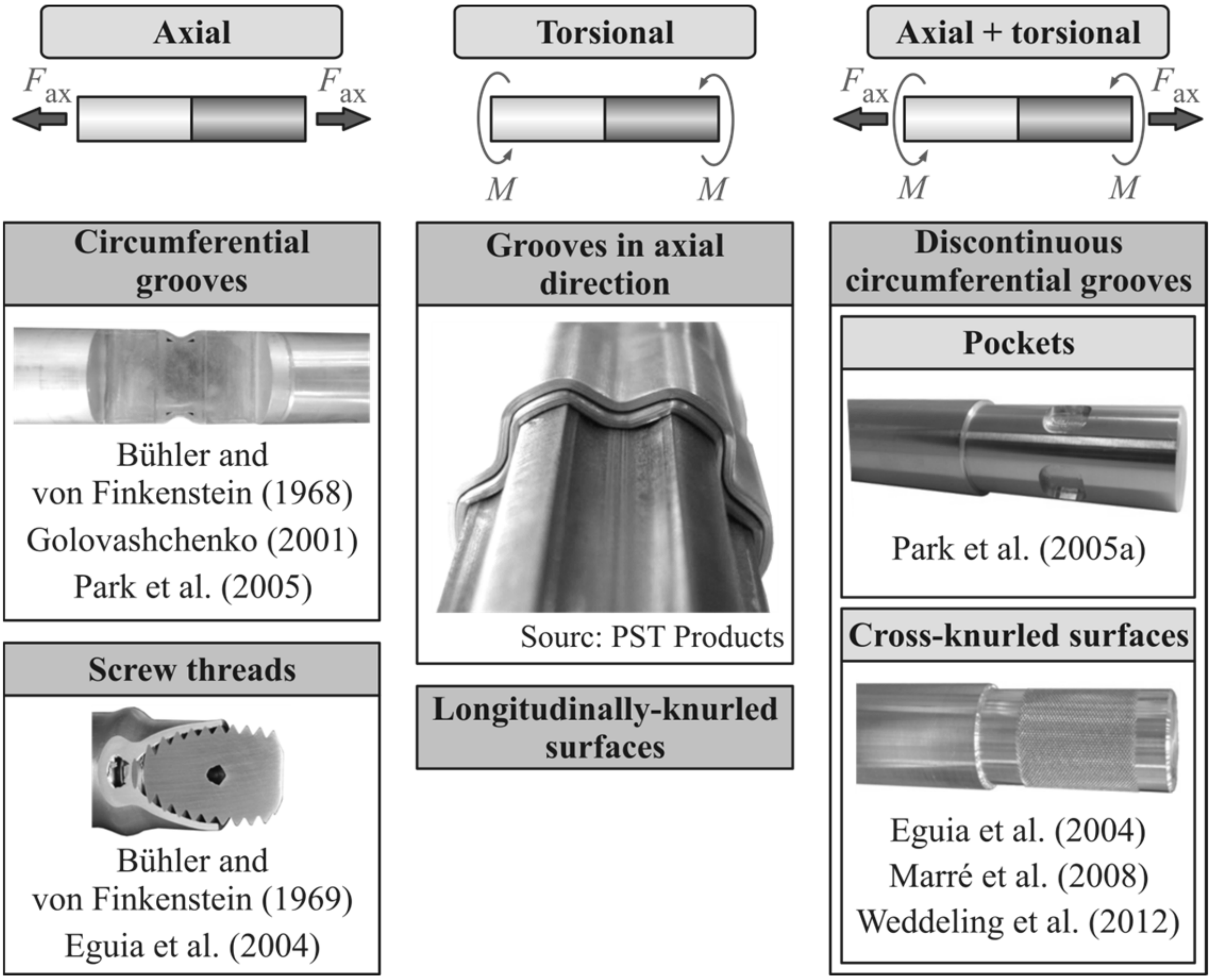
Axial
F_{ax}
F_{ax}
Torsional
M
M
Axial + torsional
F_{ax}
F_{ax}
M
M
Circumferential grooves
Bühler and von Finkenstein (1968)
Golovashchenko (2001)
Park et al. (2005)
Screw threads
Bühler and von Finkenstein (1969)
Eguia et al. (2004)
Grooves in axial direction
Sourc: PST Products
Longitudinally-knurled surfaces
Discontinuous circumferential grooves
Pockets
Park et al. (2005a)
Cross-knurled surfaces
Eguia et al. (2004)
Marré et al. (2008)
Weddeling et al. (2012)

Figure 2-15: Types of form-fit elements for tubular joints

Park et al. (2005a) perform another detailed study on form-fit joining by EMF. They investigated the influence of width and depth on the joint strength of rectangular grooves as well. However, the authors do not adjust the magnetic pressure with respect to the groove geometry like Bühler and von Finkenstein (1968b) and Golovashchenko (2001) do in their works. Park et al. (2005a) use the same forming pressure in all their experiments and they also applied several pulses in combination with an adjustment of the location to the joining zone. The authors observe a similar relationship between groove depth *h* and joint strength, as did the other researchers. They also found that if the depth exceeds a critical value, the joint strength starts to decrease due to a reduction of the tube's wall thickness and shearing at the groove edges. Concerning the groove width *w*, the results of Park et al. (2005a) differ from those generated by Bühler and von Finkenstein (1968b) and Golovashchenko (2001). They observe an increasing joint strength with wider grooves. Since they do not adjust the forming pressure with respect to the groove geometry and perform multiple pulses, they achieve a larger contact area at the bottom of the groove. This area increases with wider grooves as well. Due to residual stresses in this area, an additional interference-fit joint is generated which increased the overall connection strength. The researchers also observe that very large groove widths cause wrinkling, which affects the strength of the connection negatively.

Additionally, the authors examine how a groove edge radius R_{GE} affects the achievable connection strength. Park et al. (2005a) found an optimum of the groove edge radius with respect to the transferable load. The authors claim that it results from two opposing effects: Up to a certain limit a decreasing radius leads to an increase in joint strength, but when the edge radius becomes smaller than the optimal value, shearing at the edge is increased causing the strength to drop.

A significant joint strength increase can be achieved by the application of multiple grooves to the joining zone (Bühler and von Finkenstein, 1968b). Based on numerical simulations, Park et al. (2005a) suggest three grooves with different depths. They recommend an increase of the parameter *h* in the opposite direction of the acting load. Thereby, the authors achieved a joint strength of 88 % of the base material's strength. In the same work, Park et al. (2005a) also investigate the torsional loading of electromagnetically crimped joints based on numerical and experimental studies.

Based on their experimental findings, Golovashchenko (2001) and Park et al. (2005a) suggest the following guidelines for the design of circumferential grooves: Since narrower grooves need increased magnetic pressures to be filled, Golovashchenko (2001) suggested a minimal groove width of four times the tube wall's thickness. A further decrease of the form-fit element's width might affect the coil's lifetime negatively. Park et al. (2005a) recommend a groove depth bigger than the wall thickness of the tube to provide room for the material yield. For the maximal depth the authors give a value of 0.05 times the average tube diameter. This value is selected due to the observation of wrinkling, which reduces the joint strength at a certain groove depth. Park et al. (2005a) also suggest that the groove edge radius R_{GE} should not be smaller than the wall thickness of the tube to prevent a wall thickness reduction or shearing at the groove edge. To avoid joint separation by pulling the tube of the mandrel, the authors suggest that the value of R_{GE} shall not be larger than half the groove depth *h*.

To predict the required magnetic pressure and the charging energy for the manufacturing of a joint with a given groove geometry, Bühler and von Finkenstein (1971) introduce an semi-analytical model. This approach allows the analytical prediction of the minimal necessary magnetic pressure to initiate the plastic deformation with respect to groove width w, inner tube radius r_T, wall thickness s, and the workpiece's yield stress σ_y.

$$p_y = \sigma_y \left[3 \cdot \left(\frac{s}{w} \right)^2 + \frac{s}{r_T} \right] \tag{2.20}$$

The forming pressure required to ensure a filling of the groove can be determined based on design charts which show the relationship between the forming depth and the acting impulse integrated over the duration of the pressure pulse. These charts are developed on the basis of experimental studies and for each combination of groove width, tube geometry, and workpiece material a separate design chart is required.

Golovashchenko (2001) uses a combination of an analytical model and a finite element analysis to predict the charging energy required to manufacture a form-fit joint with a given circumferential groove geometry. In the first step, the author determines the appropriate mechanical pressure necessary to fill a specific groove by numerical calculations. Afterwards, Golovashchenko (2001) applies an analytical approach for the prediction of the required charging energy.

In his work, Golovashchenko (2001) also developed an analytical model to determine the ultimate joint strength based on the groove geometry. This approach is based on membrane theory and applies to circular grooves and conical form-fits at the tube's free end. Experimental investigations show a very good agreement between the calculated ultimate strength and the values measured in pull-out tests.

Instead of using circumferential grooves, Marré et al. (2008) use knurled surfaces as connection elements in their work (see **Figure 2-15**). The goal of this research is to join extruded aluminum profiles which are reinforced by embedding high-strength steel wires during the extrusion process. For these profiles the tangential deformation is restricted in order to avoid detaching of the aluminum matrix and the steel elements as well as necking of the reinforcement elements. Since the deformation required for filling the connection element is much smaller for knurled than for circumferential grooves, such surfaces were machined into the inner joining partner. With this design the researchers achieve pull-out forces on the order of the strength of the weakest joining partner. Weddeling et al. (2012) analyze the influence of the knurling pitch and the initial joining gap. Their study reveals that a coarse knurling leads to higher joint strength. For the initial joining gap the authors find an optimal value at which the highest connection strength is achieved. Similar to the interference-fit connections, the impact velocity is the highest at this optimal gap size, which corresponds to the findings of Eguia et al. (2004), who state that applying higher charging energies and, thus, higher impact velocities could increase the transferable load of a connection. The researchers attributed this relationship to a better engagement of the joining partner's surfaces. Besides the impact velocity, the connection strength is also influenced by the contact area in the joining zone. With an increasing gap, this area decreases and thereby the joint strength is affected negatively if the optimal gap size is exceeded.

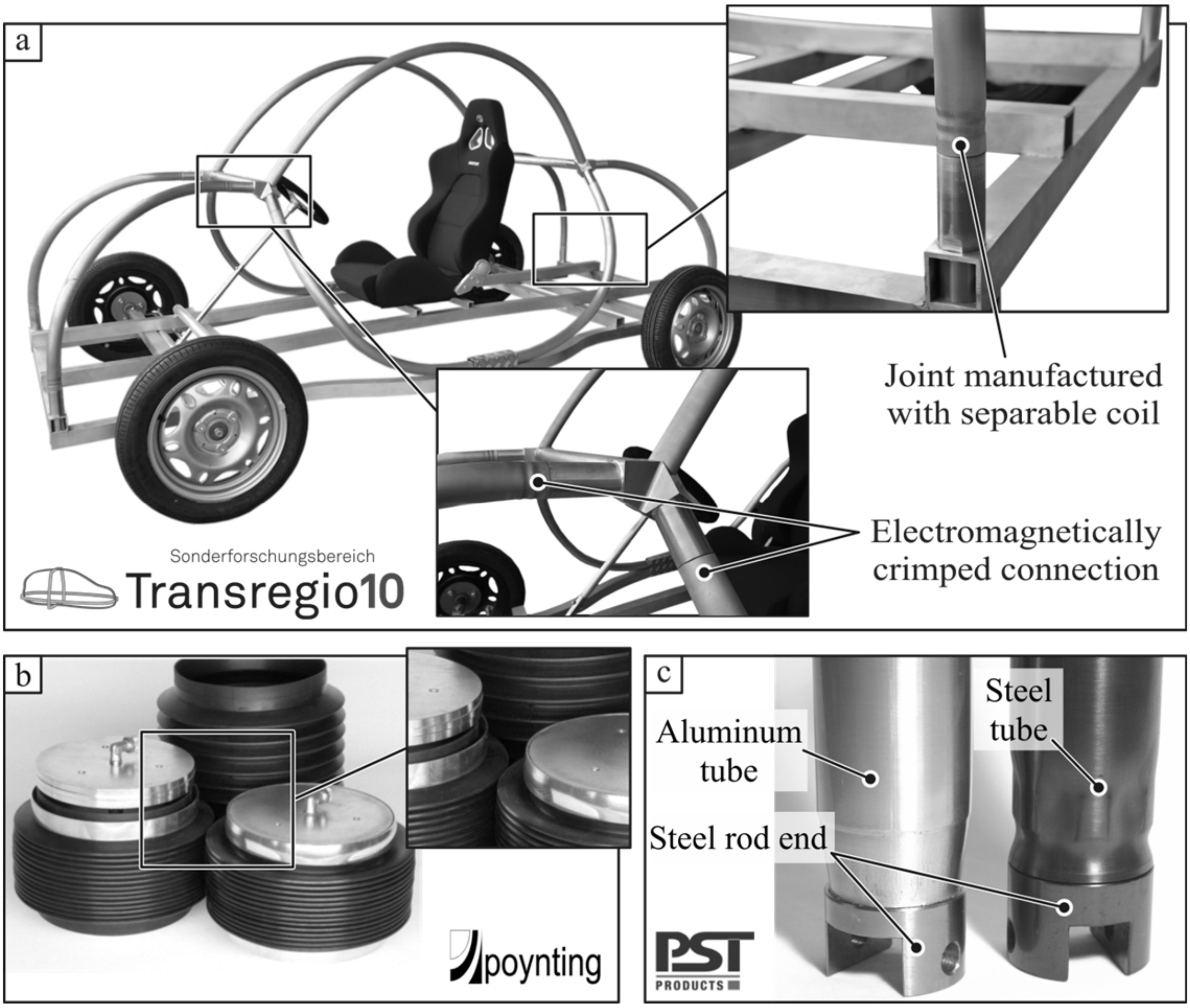
a
Joint manufactured with separable coil
Electromagnetically crimped connection
Sonderforschungsbereich
Transregio10
b
poynting
c
Aluminum tube
Steel tube
Steel rod end
PST PRODUCTS

Figure 2-16: a) Demonstrator space frame of the Collaborative Research Center SFB TR10, b) coil expansion vessel sealed by compressed aluminum ring, c) driveshaft with a welded (left) and crimped (right) joint

Weddeling et al. (2012) also analyzed the effect of the mandrel's compressive strength on the transferable loads. They observed a joint strength reduction with a decrease of this value. This influence can be attributed to a plastic deformation of the mandrel during the joining operation and a resulting decrease of the engagement of the joining partner's surfaces. Eguia et al. (2004) suggest the use of such surface patterning could also be applied for connections under torsional loads. They state that the torsional strength of the tube could be reached by using knurled mandrels.

Figure 2-16 shows some examples of joining by electromagnetic crimping. Further industrial applications of this process are reported from different fields. Some of the earliest reports are from the electrical industry, like swaging of copper tubes to coaxial cables (Birdsall et al., 1961), joining of metal fittings to ceramic insulators, and joining of high voltage cables (Rowland, 1967). Belyy et al. (1977) state that electrical connections manufactured by EMF have a 1.5 – 2 times lower contact resistance than connections produced by using a conventional hydraulic press. This correlates with an example introduced by Shribman and Tomer (2006). Rowland (1967) presents in his work some applications for the automotive industry, e.g. the sealing of rubber protective boots to ball joint housings and the assembly of air brake hoses. In his work, Sanderson (1967) mentions the electrical and automotive industry as fields of application for joining by electromagnetic forming. In addition, he reports the swaging of aluminum sheaths onto rods for nuclear reactors.

2.5.4 Tooling for electromagnetic compression

Besides directly acting compression coils, so-called field shapers are suitable tools for the manufacturing of electromagnetically crimped connections. The principle setup of such a tool is displayed in **Figure 2-17**. A field shaper is typically an axisymmetric component machined of an electrically conductive material. It features one or more axial slots and is placed inside a regular compression coil (see **Figure 2-17**).

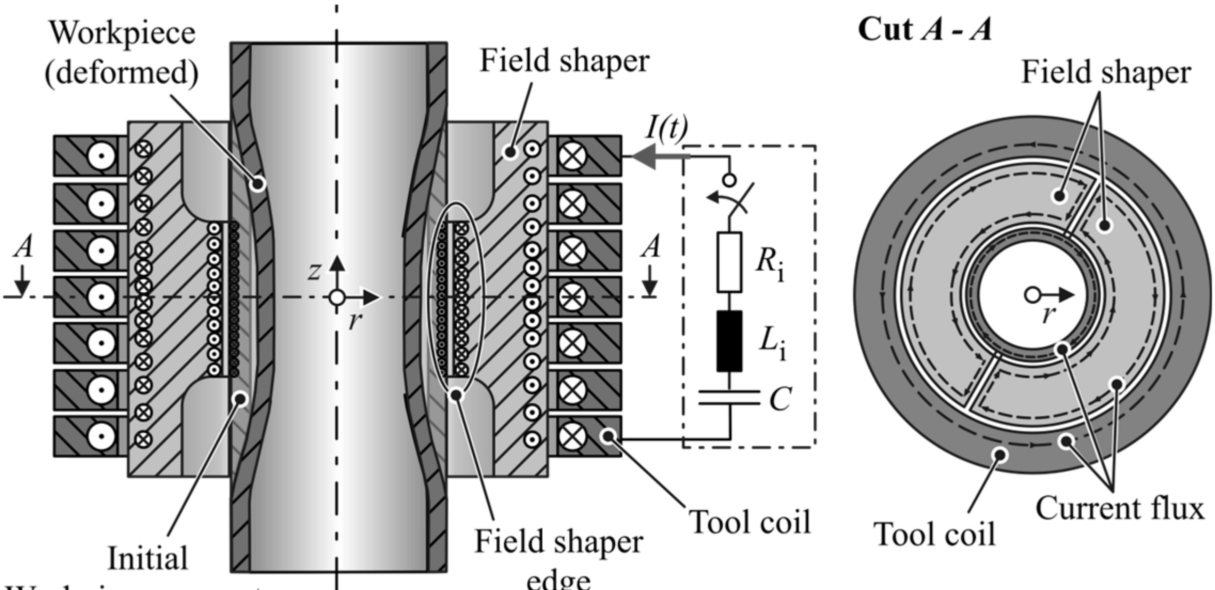

Figure 2-17: Process principle of electromagnetic compression with a field shaper (Dietz et al., 1967)

When the discharge current flows through the cylindrical coil, an opposing current is induced in the outer surface of the field shaper. At the axial slots the current is directed to the inner surface of the tool, which is also referred to as the field shaper edge. Since this surface is typically much smaller than the outer surface, the current density and the resulting field strength are increased here (Beerwald, 2005). Because of this concentrated magnetic field, a further electrical current is induced in the tubular workpieces in the region of the field shaper edge. Kim and Platner (1959) state that the coil lifetime can be increased by a field shaper, since the mechanical loading of the coil can be significantly reduced. This can be explained by the fact that the force between the field shaper and the workpiece are considerably higher than the forces acting between field shaper and tool coil. In addition, field shapers can be used in order to adjust the diameter and length of an existing compression coil to different workpiece and forming tasks (Rowland, 1967). Thereby, the flexibility of the process is significantly increased. A further advantage of separable field shapers with at least two axial slots is that they allow the manufacturing of parts with an overall geometry that would require coil diameters significantly larger than the workpiece geometry in the joining zone (Rowland, 1967). This is, for example, the case if the component features two relatively large fittings at both ends. The main disadvantage of this tool concept is the reduced process efficiency (Furth et al., 1957). The reasons for this are supplementary resistive losses in the additional tool component and losses of inductive energy because of an inefficient coupling between cylindrical coil, field shaper, and workpiece.

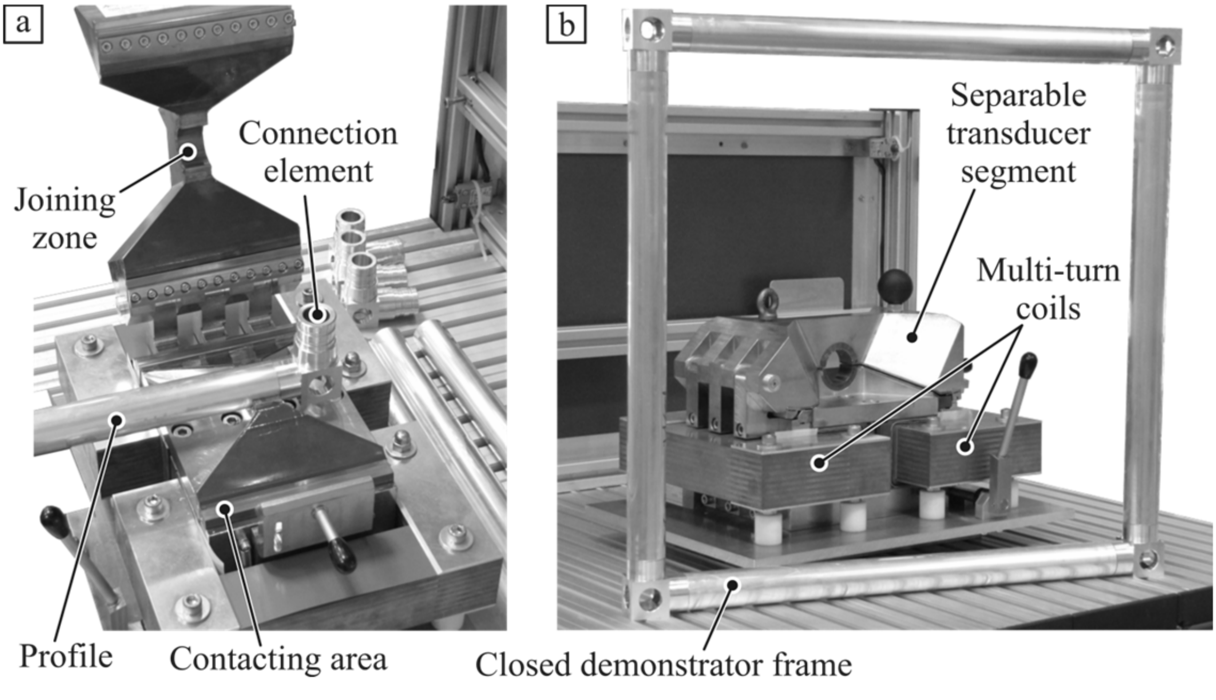

Figure 2-18: Separable tool coil for closing frame structures engineered by the Poynting GmbH, a) open tool and b) coil closed with frame

To manufacture space frame structures and, in particular, to close this kind of structures, a separable EMF tool is necessary. **Figure 2-18a** displays such a tool coil which is introduced in Henselek et al. (2004). The tool design is based on the so-called transducer principle, which is a specific field shaper. This component encloses the multi-turn coil and the workpiece each with a part of its surface. The frames displayed in **Figure 2-16a** and **Figure 2-18b** are manufactured with this tool concept. Another design for a separable coil is introduced by Golovashchenko (2005). This tool consists of two independent multi-turn windings which are connected in series and feature a concave working zone. For joining, the tubular workpiece is enclosed by these two segments and thereby a closed loop is formed. The practical application of this tool concept is presented in Golovashchenko (2005).

2.6 Summary and conclusion

The literature survey shows that joining by forming is applicable to the manufacturing of lightweight frame structures and multi-material connections. For example, the joining operation is characterized by a very uniform circumferential pressure distribution. As a result, the joint characteristics are typically fairly uniform. Additionally, the strain rates in impulse forming lead to increased formability of most materials (Balanethiram and Daehn, 1995). Therefore, compared to quasi-static forming processes, electromagnetic form-fit joining allows the generation of larger interlocks, which results in an increase in connection strength (Bühler and von Finckenstein, 1968b). With this joining process, connection strengths of up to about 90 % of the base material's strength can be achieved (Park et al. 2005a).

Although electromagnetic form-fit joining has several advantages compared to conventional joining techniques and other quasi-static joining by forming processes like mechanical crimping, the full potential of the process still cannot be exploited. This results from an incomplete fundamental understanding of the joining operation and the load transfer as well as the absence of suitable methodologies for the process and connection zone design:

1. So far, it has not been studied how the forming direction of the joining process affects the achievable connection strength. This means it is unclear if either an expanded or a compressed form-fit connection with identical groove geometry leads to the higher joint strength.
2. The component mass is an important factor for the design of lightweight frame structures. Hence, its influence on the structure's strength and stiffness needs to be known. But for connections with circumferential grooves it is still unclear how a mass reduction in the joining zone affects the crimping process and the transferable load. Possibilities to reduce the mass of a joint are the application of lightweight materials like aluminum and changing the mandrel geometry by inserting a hole in its center. While the effect of these design changes on the connection's mass can easily be determined, the joint's load transfer ability has not been studied until today. Although Bühler and von Finckenstein (1968b) and Park et al. (2005a) used

hollow mandrels within their investigations, they do not analyze the effect of a geometry or material change on the transferable loads.

3. Concerning the fundamentals of the load transfer, the effects of major groove characteristics like width and depth on the achievable joint strength are known. But the influences of several other joining zone properties have yet to be analyzed. For example, the effect of different groove shapes on the transferable loads has not been completely studied up to today. The joining gap a_0 between the two workpieces is another joining zone parameter which has not been the subject of a comparative study regarding form-fit connections. It is not clear how such a gap affects the achievable joint strength.

For the prediction of the joining process parameters, either complex numerical simulations (Golovashchenko, 2001) or experimental investigations (Bühler and von Finckenstein, 1971) are necessary. Both approaches are very time-consuming and do not describe the influence of certain parameters on the forming result. Numerical determinations also require a very profound knowledge of coupling electromagnetic with impulse mechanical calculations.

In contrast to the crimping parameter prediction there is the analytical approach by Golovashchenko (2001) available for the joint strength determination. Unfortunately, this model is only valid for circular groove geometries and conical form-fits at the tube’s free end. Additionally, it gives only the ultimate strength of a form-fit connection. When designing structural components, the elastic limit is typically the upper limit of the loads that can be applied. Since the ultimate strength includes already plastic deformations, this value is only suitable to a limited extent for a design process.

The literature survey shows that a detailed study on the parameters influencing the achievable joint strength is needed to complete the fundamental process understanding of electromagnetic form-fit joining. Based on this knowledge, a methodology or a process window needs to be developed to facilitate the process and connection design.

3 Objective

The objective of this work is the development of a fundamental process understanding of electromagnetic form-fit joining. To facilitate the process and joint design, the present fundamental process understanding shall include a convenient analytical model for the prediction of joining parameters and the achievable joint strength. Additionally, a process window considering the influence of a mass reduction in the joining zone on the connection strength shall also be provided (see **Figure 3-1**). Employing the knowledge presented in this work for the joining zone and process design shall allow the manufacturing of connections with strengths that are in the region of the strengths of the weakest joining partner. Consequently, the connection failure shall occur in the base material and not in the joining zone.

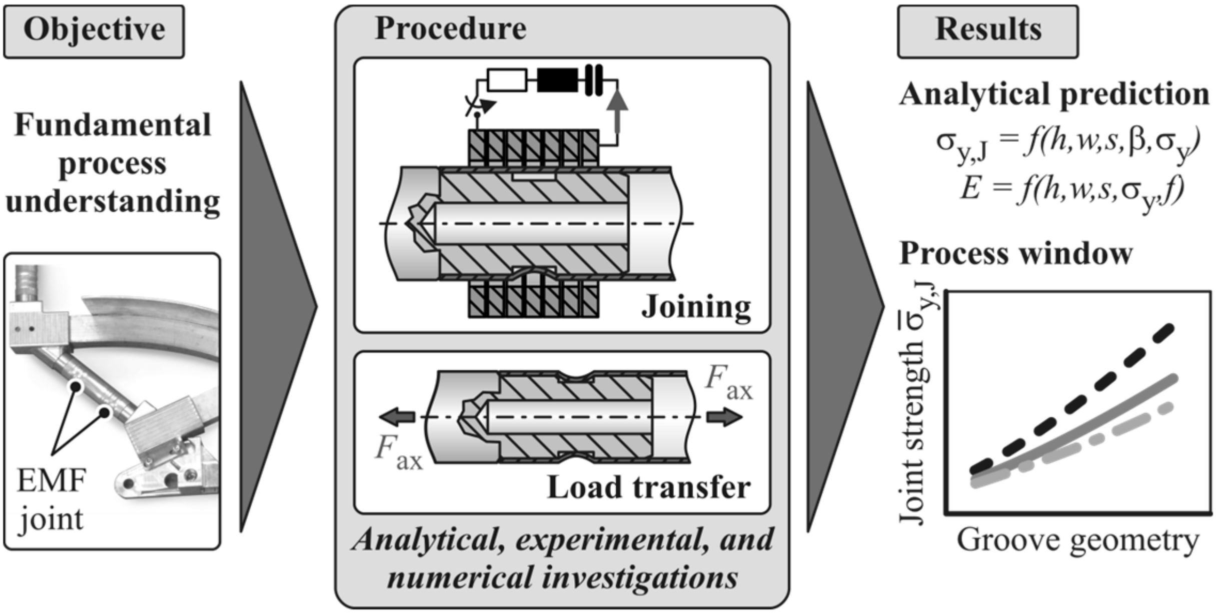
Objective
Fundamental process understanding
EMF joint
Procedure
Joining
F_{ax}
F_{ax}
Load transfer
Analytical, experimental, and numerical investigations
Results
Analytical prediction
$\sigma_{y,J} = f(h,w,s,\beta,\sigma_y)$
$E = f(h,w,s,\sigma_y,f)$
Process window
Joint strength $\bar{\sigma}_{y,J}$
Groove geometry

Figure 3-1: Overview of the objective, procedure, and results of this work

For the development of the fundamental process understanding the following questions have to be answered:

- Which parameters influence the groove filling and to what extend?
- What stress states appear during tensile loading of the form-fit connections?
- How does a mass reduction in the joining zone of connections featuring hollow mandrels affect the joining process and the resulting load transfer?

To answer these questions and to develop the desired fundamental understanding, analytical investigations of the joining process and the load transfer are performed (see **Figure 3-1**). Since the joining process as well as the load transfer shall be analyzed, the investigations are divided into two stages.

First, the crimping parameters are determined by an experimental methodology introduced in **Chapter 4**. Besides the determination of the necessary joining parameters, the generated results are also used to verify the analytical parameter prediction, which is introduced in **Chapter 5**. To allow a more detailed observation of the joining process, especially of the temporal sequence of the deformation, numerical investigations of the crimping process are performed. These investigations are also used for the verification of the analytical approach.

In the second stage, the load transfer of form-fit connections is analyzed. These investigations, which are presented in **Chapter 6,** include the analysis of the influence of general joining zone characteristics as well as the specific properties of hollow mandrels on the achievable joint strength. The aim of the investigations regarding the general joining zone characteristics is the determination of the influence of joint parameters which have not yet been discussed in the literature on the strength of electromagnetically crimped form-fit connections. The results generated within this experimental study are also used for the verification of an analytical joint strength determination, which is developed here. To analyze the influence of the forming direction on the connection strength, this model considers the specific characteristics of compressed and expanded joints. Subsequently, the load transfer of connections featuring hollow mandrels is analyzed. The objective of these investigations is the identification and analysis of specific parameters of such joints affecting the achievable connection strength. The joining behavior and its influence on the load transfer of connections with hollow mandrels are of peculiar interest in this section.

Conclusively, the analytical methodologies for the joining parameter prediction and for the connection strength determination are combined with the results on joints featuring hollow mandrels. Thereby, a process window considering the influence of a mass reduction in the joining zone on the connection strength is deduced (see **Chapter 7**).

4 Experimental procedure

The objective of the experimental investigations in this work is the determination of the joining process parameters as well as the evaluation of the achievable connection strengths depending on the joining zone characteristics and the process parameters. Because of these two major aims, the experimental procedure is divided into two parts. In the first part, the crimping parameters are predicted based on the properties of the joining partners and the joining zone. In the second part of the experimental procedure, these parameters are applied to manufacture form-fit connections with varying joining zone and process characteristics. Afterwards, the generated joints are tested in terms of their achievable tensile strength. **Table 4-1** gives an overview of the investigated parameters. All experiments are repeated at least three times.

Table 4-1: Investigated parameters

Joining zone parameters	
Groove	Dimensions (Width w, depth h, and edge radius R_{GE})
	Shape (rectangular, circular, and triangular)
Mandrel	Joining gap a_0 (outer diameter)
	Geometry of hollow mandrels (diameter ratio Q_{M})
	Material of hollow mandrels (yield stress)
Process parameters	
Pulse	Charging energy E
	Discharge frequency f
Forming operation	Stress state (compression and expansion)

4.1 Crimping parameter determination

For a successful process design of electromagnetic form-fit joining it is important to know what magnetic pressure pulse $p_{\mathrm{m}}(t)$, or rather which charging energy E is required to “fill” a given groove geometry. Bühler and von Finckenstein (1971) state that filling of the form-fit element is achieved, when the tube wall just touches the groove base in the center of the groove (see **Figure 2-4**).

Due to a significantly different stress state, higher forming pressures are required for the manufacturing of form-fit connections than for the free compression of tubes with the same radial displacement (Bühler and von Finckenstein, 1971). Hence, free compression tests of profiles without an inner joining partner are hardly suitable for the joining parameter determination. The disadvantage of a process parameter prediction involving the application of inner joining partners is that a new mandrel is required for each experiment. To lower the material consumption for the crimping parameter evaluation, a new experimental methodology is introduced in the following.

4.1.1 Experimental methodology

In this new approach to determine the required charging energy and the forming pressure, respectively, the mandrel is replaced by two steel cylinders (Weddeling et al., 2011b). These cylinders are connected by a threaded rod preventing a movement of the cylinders during the forming process. The rod also allows an accurate adjustment of the distance between the steel parts, which represents the groove width *w*. The tube with the steel cylinders is inserted into the tool coil (see **Figure 4-1**). Subsequently, the tube is electromagnetically formed into the gap between the steel cylinders and the resulting forming depth h_d is measured physically by a micrometer caliper and optically by a Photon Doppler velocimeter (see **Section 4.1.4**).

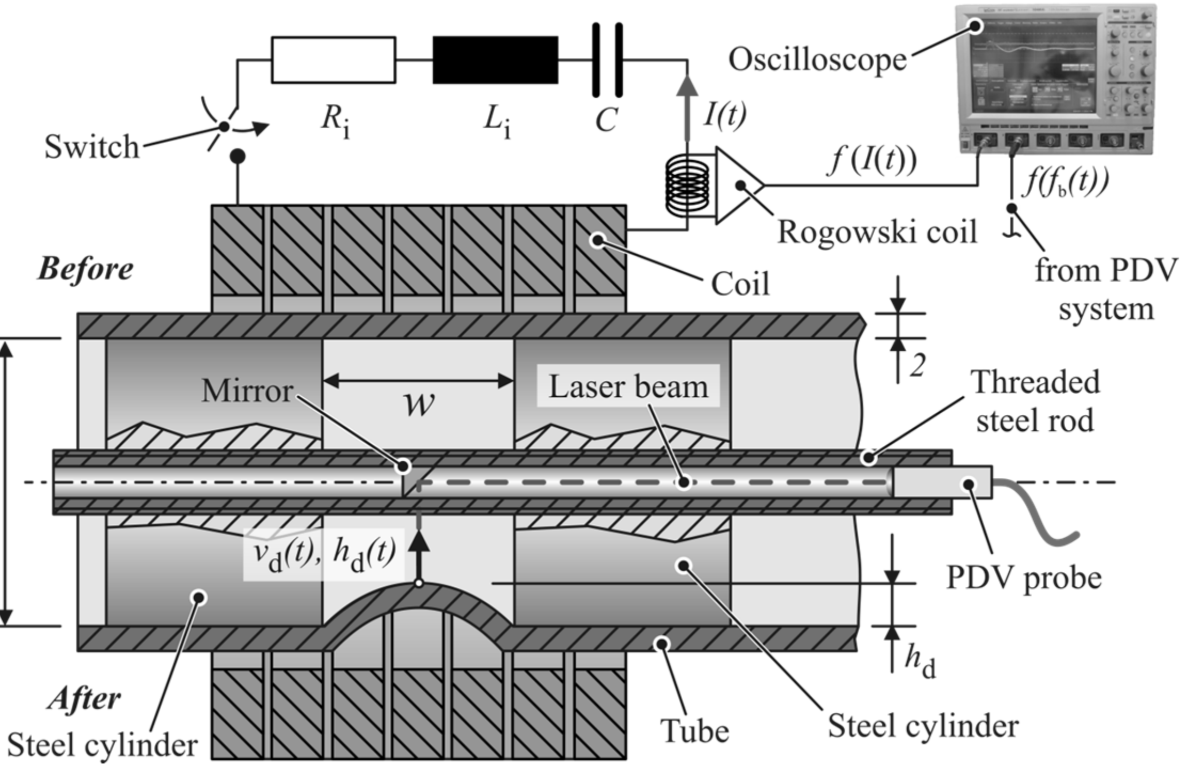
Oscilloscope
Switch
R_i
L_i
C
$I(t)$
$f(I(t))$
$f(f_b(t))$
Rogowski coil
from PDV system
Before
Coil
2
Mirror
w
Laser beam
Threaded steel rod
ø36
$v_d(t)$, $h_d(t)$
PDV probe
h_d
After
Steel cylinder
Tube
Steel cylinder

Figure 4-1: Setup of the experimental forming depth determination

Afterwards, the steel cylinders are unscrewed and extracted from the tube. To ensure an easy extraction of the cylinders from tube, it is recommended to slightly grease the steel parts before performing the forming operation. By repeating this procedure with at least three different energy values and displaying the charging energy over the resulting forming depth, a graph of the function $E(h_d)$ for a specific groove width *w* can be constructed. The resulting design chart for electromagnetic form-fit joining can be used for the prediction of the required charging energy with respect to the groove dimensions (see **Figure 4-2**).

To find an approximate start energy level of this experimental joinng parameter determination, Equation (2.20) is used to predict the yield pressure p_y of the tube. The value of p_y applied to the equations of **Section 2.5.1** and **2.5.2** gives the starting charging energy E.

Although the amount of specimens necessary for the parameter prediction is reduced with this methodology, it might still require a larger number of tests. Therefore, an analytical model for the process design which eases the process parameter determination and decreases the required expenditure is introduced in **Section 5.1**.

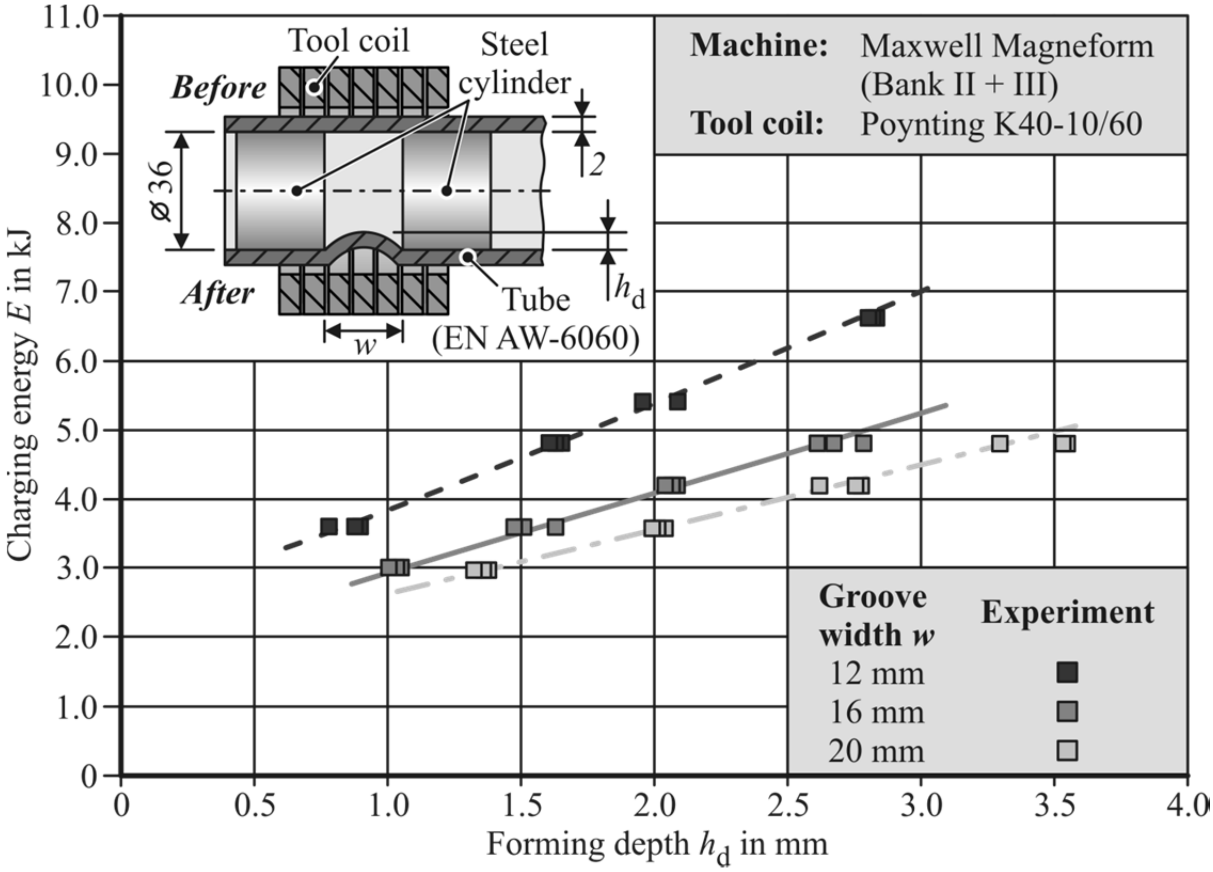

Figure 4-2: Design chart for the process design of electromagnetic form-fit joining

4.1.2 Electromagnetic forming setup

In this work a Maxwell Magneform (7000 Series) electromagnetic forming machine is used for the experimental joining parameter prediction. **Table 4-2** shows the properties of this EMF machine. The used Magneform machine offers the separate selection of different capacitor banks. This allows the incremental adjustment of the capacitance of the machine. This also influences the inner inductance L_i, the inner electrical resistance R_i, and the short circuit frequency f^* as well as the discharge frequency f (Psyk, 2010). As tool a K40-10/60 compression coil manufactured by Poynting GmbH is used for all experiments in this work (see **Table 4-3**).

For the measurement of the discharge current *I(t)* a Rogowski coil CWT-1500 from Power Electronic Measurements Ltd. is used. The basic shape of this gage is a helical coil. For the determination of the primary current the Rogowski coil is placed around one lead of the forming coil (see **Figure 4-1**). If a discharge current runs through the EMF coil, the generated magnetic field induces a voltage in the probe. This voltage is proportional to the change of the primary current.

Table 4-2: Machine properties of the used Maxwell Magneform (7000 Series)

No.	**Capacitor bank configuration**	**Maximal charging energy $E_{\max}$** (kJ)	**Maximal charging voltage $U_{\max}$** (kV)	**Capacitance C** (µF)	**Inner inductance L_i** (nH)	**Short circuit frequency f^*** (kHz)	**Inner resistance R_i** (mΩ)
1	**Bank I**	16	8.16	504	74	26	5.0
2	**Bank II**	8		237	98	32	6.9
3	**Bank III**	4		125	164	35	11.5
4	**Bank IV**			126			
5	**Bank II and III**	12		362	78	29	5.4
6	**Bank I, II, III, and IV**	32		992	50	22	3.3

Table 4-3: Tool coil properties

Type designation	K40-10/60	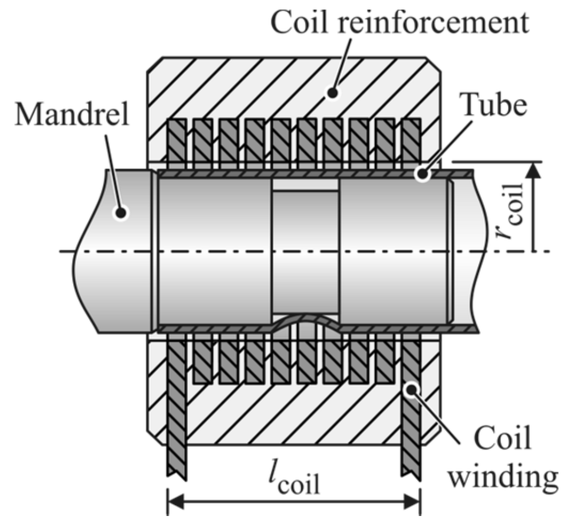 Coil reinforcement Mandrel Tube r_{coil} l_{coil} Coil winding
Coil type	Compression	
Manufacturer	Poynting GmbH	
Inner diameter r_{coil} (mm)	21.5	
Coil length l_{coil} (mm)	60	
Number of windings	10	
Winding material	Copper	

A WaveRunner 104MXi oscilloscope from LeCroy is used to display and record the measured signal. **Figure 4-3** shows a sample current curve. The following important values can be determined from these curves: the current maximum $I_{\max,1}$, the moment of this current $t_{\max,1}$, and the moment of the first zero-crossing $t_{0,1}$. The discharge frequency f can be approximated as (Psyk, 2010):

$$f = \frac{1}{2 \cdot t_{0,1}} \tag{4.1}$$

This prediction is used as an input value for the analytical process parameter determination introduced in **Section 5.1.2**.

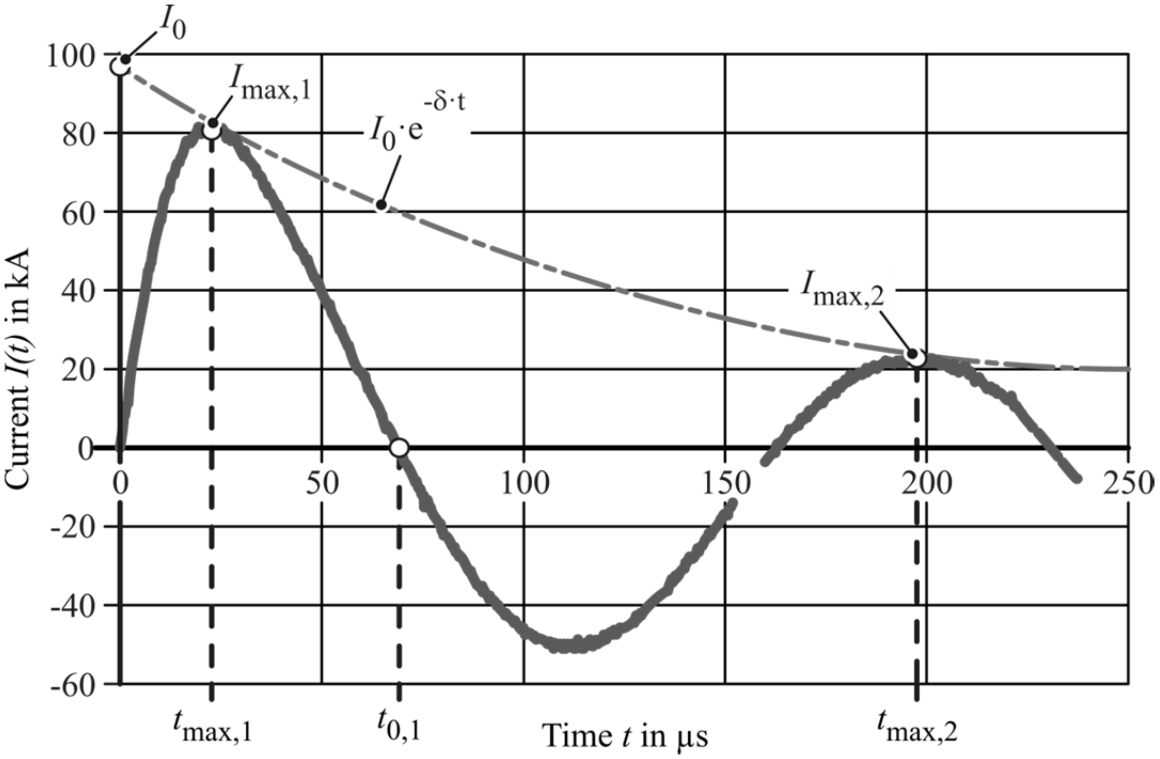

Figure 4-3: Recorded current curve

4.1.3 Specimens and investigated parameters

The distance between the steel cylinders *w* is chosen based on the groove widths of the joining experiments as: 12 mm, 16 mm, and 20 mm. In terms of the process parameters, the charging energy *E* and, therefore, the acting magnetic pressure amplitude is varied. To achieve forming depths h_d in the range of 0.5 to 4 mm, the range of the energy levels is chosen depending on the workpiece material and the groove width *w* (see **Table 4-4**).

Table 4-4: Charging energy levels and capacitor bank configurations

Material	**Groove width *w*** (mm)	**Charging energy levels *E*** (kJ)	**Capacitor bank configuration** (Table 4-2)
EN AW-1050A	12, 16 and 20	1.2, 1.8, and 2.4	5
EN AW-6060	12	3.6, 4.8, 5.4, and 6.4	2, 5 and 6
	16 and 20	3.0, 3.6, 4.2, and 4.8	2, 5 and 6
EN AW-2007	12, 16 and 20	3.6, 5.4, and 7.2	5

In addition to the variation of E, the discharge circuit characteristics are varied to analyze their influence on the forming depth h_d. Of particular interest are the effects of discharge frequency f and the resulting pressure pulse duration on h_d.

Barnes and Pashby (2000) state that the mechanical properties, in particular their relatively high strengths, make the 6000 series aluminum alloys a preferred material for lightweight space frame structures. Therefore, the common 6000 series alloy EN AW-6060 is chosen as tube material for the connections manufactured and analyzed in this work. Additionally, for the verification of the analytical model introduced in **Section 5.1**, experiments with EN AW-1050A and EN AW-2007 tubes are performed. All specimens have a length of 100 mm and an outer diameter D_T of 40 mm (see **Table 4-5**). The wall thickness s of the tubes is 2 mm.

For the yield stress determination of the specimen materials tube tensile tests based on the European standard EN 10002-1 (N.N., 2001) are performed. The determined material parameter σ_y corresponds to the initial flow stress $\sigma_{\mathrm{f},0}$ of the material. A universal tensile testing machine Zwick Z250 is used for these experiments. In accordance with the applied standard, a specimen length of 400 mm is chosen. To avoid a deformation of the ends of the tubes by the machine's grips, the ends are supported by steel plugs during the tests. The initial gauge length l_0 is set to 100 mm and 0.1 mm/s is chosen as pull or crossbar velocity v_c in the position-controlled tests. For the statistical validation the yield stress values deduced from the recorded stress-strain curve are averaged over at least 3 tensile tests per material batch (see **Table 4-5**). **Figure 4-4** shows the average stress-strain curves of the used tube materials.

Table 4-5: Material properties of the profiles

Material	**Chemical composition**	**Temper condition**	**Yield stress σ_y** (MPa)	**Deviation of σ_y** (MPa)
EN AW-1050A	Al 99.5	-	19	- 0.5 + 1.0
EN AW-6060	AlMgSi	T6	233	- 2.0 + 3.0
EN AW-2007	AlCu4PbMg	T4	263	- 0.5 + 1.5

Since the plastic flow of some materials is sensitive to the applied strain rates (Jones, 1997), a certain knowledge regarding the material behavior under high forming velocities is necessary for the numerical analysis of the electromagnetic crimping process in **Section 5.2**. For the determination of the strain rate-dependent material behavior an inverse engineering method (Brosius and Kleiner, 2004) is chosen here.

The basic idea of this approach is the adjustment of the parameters describing the dynamic material behavior in the finite element simulation until the calculated deformations match the experimentally measured ones.

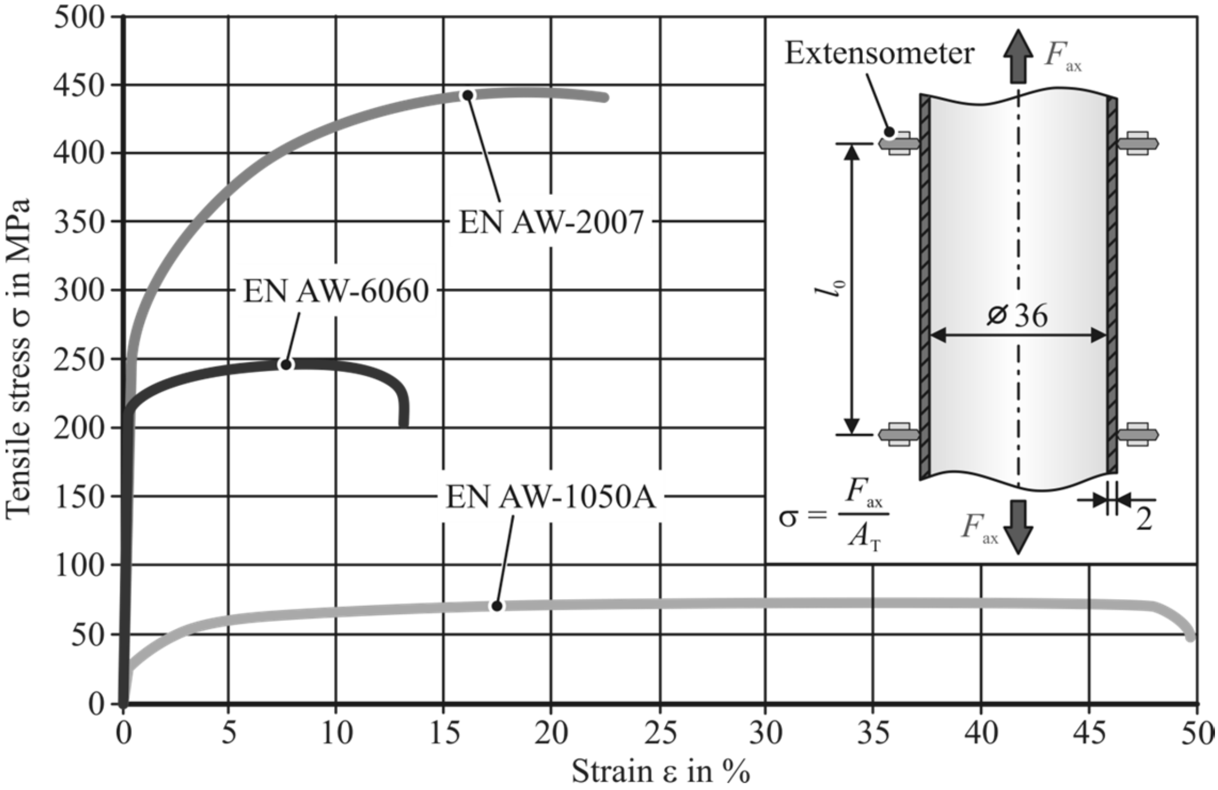

Figure 4-4: Average quasi-static stress-strain curves of the applied specimen materials

In this work, the deformation experiments of **Section 4.1** are numerically modeled. The input values of these analyses are the workpiece and tool properties as well as the experimentally measured current curves. The strain rate-dependent flow stress $\sigma_{\mathrm{f,dyn}}$ is described by the model of Cowper and Symonds (1957).

$$\sigma_{f,dyn} = \sigma_f \cdot \left[1 + \left(\frac{\dot{\varepsilon}}{C_C}\right)^{1/p_C}\right] \tag{4.2}$$

The two parameters of the Cowper-Symonds model, C_{C} and p_{C}, are optimized until the maximum tube compressions calculated by the finite element analysis match the experimental results. The necessary quasi-static flow curves of the tube materials are determined by the results of tube tensile tests described above in combination with the extrapolation approach by Voce (1948).

A staggered coupling approach between the electromagnetic and mechanical parts of the simulation is employed. Since the studied joining operation is rotationally symmetric, a two-dimensional model is constructed. The electromagnetic problem is solved by the finite element software ANSYS using an implicit time integration scheme. An explicit time integration scheme is used to solve the mechanical problem by the finite element software LS-DYNA. The electromagnetic model of ANSYS is updated at every microsecond according to the displacements calculated by LS-DYNA. The implicit electromagnetic solution has a time step of 0.5 microseconds, while the explicit mechanical solution has a time step of 0.005 microseconds. The inner joining partner or rather the steel cylinders are modeled as an insulator, so they do not have any effect on the electromagnetic solution. In the simulations the coil windings are represented by mechanically rigid concentric circles. Two-dimensional axisymmetric elements with four nodes and a single integration point are used to model all parts. To consider the skin effect, elements as thin as 0.125 mm are applied at the outer regions of the coil and the workpiece. Additionally, the specimen and the inner parts are meshed finely at the radius where the forming is concentrated, using elements of 0.1 mm edge length.

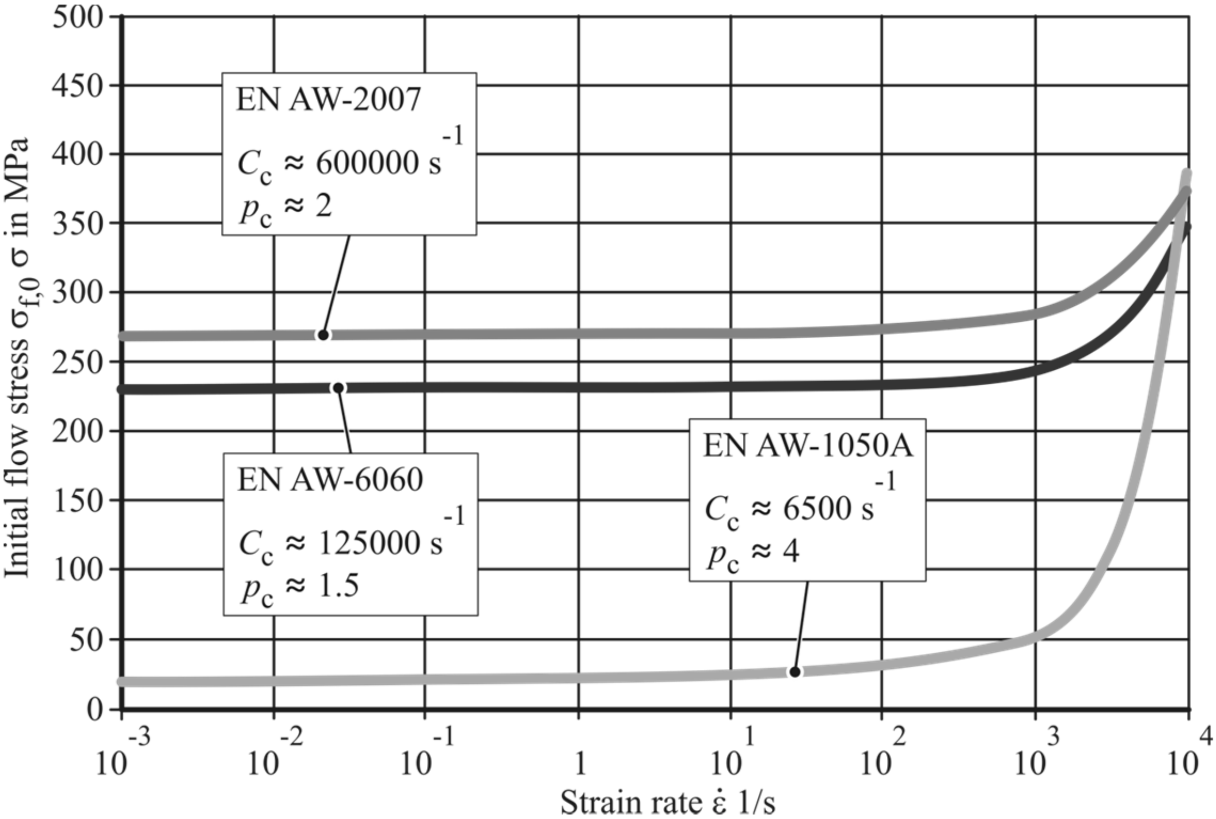

Figure 4-5: Strain rate dependency of the initial flow stress $\sigma_{f,0}$ of the used specimen materials

Figure 4-5 shows the obtained Cowper-Symonds parameters of the used materials and the resulting influence of the forming velocity on the plastic behavior of the specimen materials. The displayed relationship between strain rate $\dot{\varepsilon}$ and initial flow stress is determined by Equation (4.2) and the predicted parameters C_C and p_C. For the analyzed materials it is shown that $\dot{\varepsilon}$ has a significant influence on $\sigma_{f,0}$ for strain rates between $10^3\ s^{-1}$ and $10^4\ s^{-1}$, which are typical for electromagnetic forming (see

Section 2.5.1). The observation corresponds to the statement of Ostermann (2007) that aluminum alloys generally show an increased strain rate-dependent material behavior in this deformation velocity range. For EN AW-1050 and EN AW-6060 the relationship between $\dot{\varepsilon}$ and $\sigma_{\mathrm{f},0}$ agrees also with the findings of Tanimura et al. (1989) and Hockauf (2009). The highest strain rate sensitivity is found for EN AW-1050. The alloys EN AW-2007 and EN AW-6060 show a much lower effect of $\dot{\varepsilon}$ on the flow stress. This result corresponds to the comparison of the strain rate sensitivity of different aluminum alloys by Lindholm et al. (1971).

4.1.4 Determination of forming velocity and deformation

For the verification of the analytical model presented in **Section 5.1** the workpiece velocities $v_\mathrm{d}(t)$ and deformations $h_\mathrm{d}(t)$ in the groove center (see **Figure 4-1**) are measured during the experimental determination of the joining process parameters by a Photonic-Doppler-Velocimetry (PDV) system. This velocity measurement method was introduced by Strand et al. (2004) from Lawrence Livermore National Laboratories (LLNL). The physical principle of this system is based on the Doppler Effect. A laser beam with a narrow spectral line width is focused onto the surface whose speed is to be measured. Due to the movement of the surface, the frequency of the light is shifted. Considering the speed of light c, the Doppler shifted frequency f_d of the laser beam for a specific workpiece velocity $v(t)$ can be calculated by:

$$f_d = f_0 \cdot \left(1 + 2 \cdot \frac{v(t)}{c}\right) \tag{4.3}$$

The difference of this frequency to the initial frequency f_0 of the light signal is the beat frequency f_b.

$$f_b = f_d - f_0 \tag{4.4}$$

By inserting Equation (4.3) in (4.4) and taking into account the relation between wave length λ and frequency f_0

$$f_0 = \frac{c}{\lambda_0} \tag{4.5}$$

the workpiece velocity $v(t)$ is found:

$$v(t) = \left(\frac{\lambda_0}{2} \cdot f_b\right) \tag{4.6}$$

Hence, the part velocity is proportional to the beat frequency. **Figure 4-6** shows the schematic setup of the PDV system used for this work. The major component of the system is the erbium high power fiber laser with a wave length λ of 1550 nm. For the transport of the light within this system optical fibers are used. The light is focused onto the surface of the part by a focusing probe. It also collects the Doppler shifted light returning from the surface and sends it to the detector. At the photo detector the signal from the probe is combined with the incident signal to create the beat frequency. This frequency is displayed and recorded as amplitude over time plot by the same oscilloscope used to record the current curves. To transform the recorded amplitude over time data into a beat frequency over time curve, the MatLab function Spectrogram is used. This function performs a Fourier transformation with the recorded data and gives a frequency-time plot. An example of such a plot or spectrogram is shown in **Figure 4-6b**. Applying Equation (4.6) to the frequency values of this spectrogram leads to the desired velocity vs. time curve. By integration the deformation $h_d(t)$ over time can be gained from the velocity function $v_d(t)$.

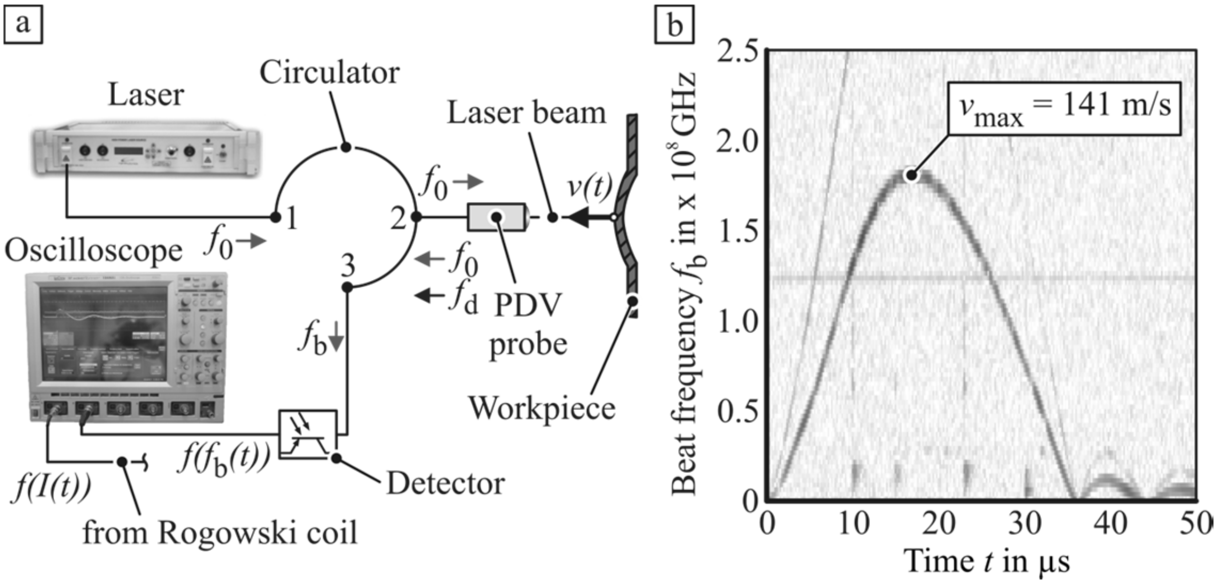

Figure 4-6: a) Principle of Photon Doppler velocimeter b) Spectrogram

The actual setup of the PDV probe for the experiments described in this section is shown in **Figure 4-1**. To avoid a collision of the workpiece with the probe, the sensitive measurement device is placed outside the forming zone. The laser beam is guided by steel tube with an angular gold-coated mirror at its end. Since the laser needs to shine perpendicular on the moving surface, this mirror is necessary to deflect the beam by 90 degrees.

4.2 Joint strength determination

The objective of the joining experiments is the identification and analysis of process, workpiece, and joining zone parameters which affect the achievable connection strength. An additional reason for the joining experiments is the verification of the analytical model for the connection strength prediction (see **Section 6.1**).

For the majority of joining experiments presented in this work electromagnetic compression is used to generate the form-fit connections (see **Figure 4-7**). Since only the effects of form-fit related parameters on the achievable joint strength are to be analyzed in this investigation regarding general joining zone characteristics, an additional interference fit needs to be suppressed. As this load transfer mechanism is based on a difference in elastic recovery of the two joining partners, a deformation of the mandrel during the joining operation needs to be avoided. To ensure this, solid mandrels are used (see **Figure 4-7a**). Additionally, both joining partners are manufactured from the same material to avoid or minimize a supplementary interference fit as well (Weddeling et al., 2011b). For the investigations regarding the influence of a mass reduction and the resulting change of the radial strength in the joining zone on the connection strength hollow mandrels are used (see **Figure 4-7b**).

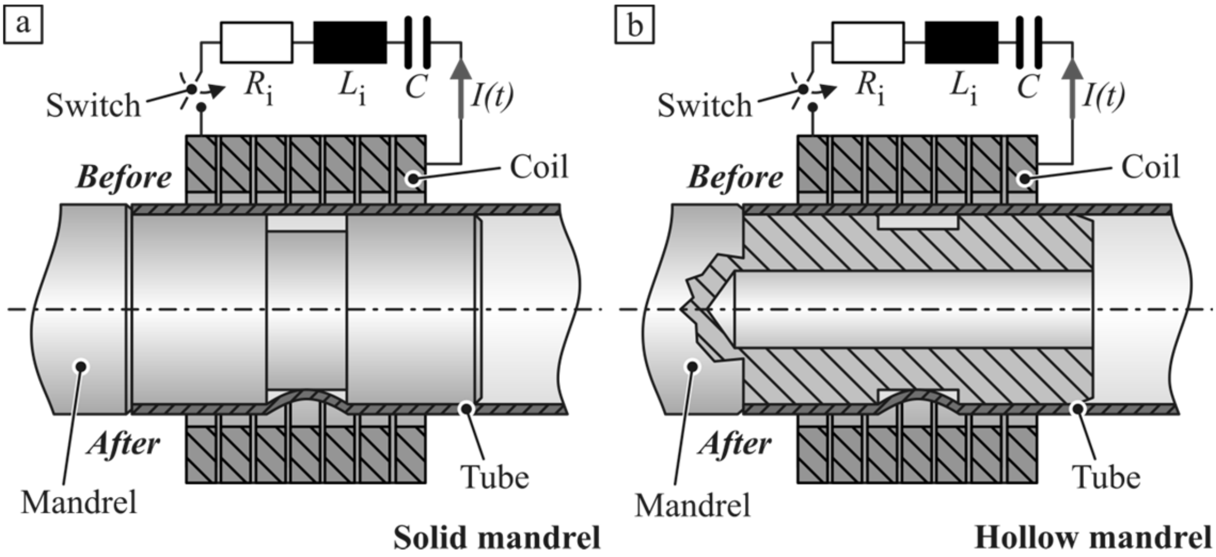

Figure 4-7: Electromagnetic form-fit joining of a) solid and b) hollow mandrels

4.2.1 Joining equipment

For the manufacturing of the form-fit connections the same EMF machine and tool coil are used as for the experimental process parameter determination described in **Section 4.1.2**. However, all joints are generated with the capacitor bank configuration number 5 (Bank II and III, see **Table 4-2**). The charging energies for the joining operations are selected based on the design chart in **Figure 4-2**, which results from the experimental process parameter determination. Due to process inaccuracies in the manufacturing of the specimens, the geometrical and material properties of the workpieces might vary in a certain range. To ensure filling of the grooves, even for joining partners with varying properties, the charging energies predicted from **Figure 4-2** are increased by 10 % for the joining operations.

Possible layers of lubricant or other contaminations on the surface of the workpieces change the coefficient of friction μ_f in the contact zone and, therefore, they might affect the connection strength. To remove potential contaminations from preceding manufacturing and handling processes from the specimen's surfaces, the tubes and mandrels are cleaned in an ultrasonic bath filled with Acetone for a minimum time of five minutes. This cleaning procedure ensures the same surface conditions for all specimens (compare Marré, 2009).

4.2.2 Specimens and investigated parameters

Figure 4-8 show the two general mandrel types which are used within this work. For the investigation of the influence of the basic joining zone and process parameters on the achievable connection strength, solid mandrels are manufactured from EN AW-6060. The total length of the specimens is 180 mm and the joining zone l_{JZ} is 80 mm long. To suppress an additional interference fit, EN AW-6060 is chosen as material for the outer joining partners as well. The respective tubes have an outer diameter D_T of 40 mm and a wall thickness s of 2 mm. The total specimen length is 300 mm. The properties of the specimen materials are shown in **Table 4-6**.

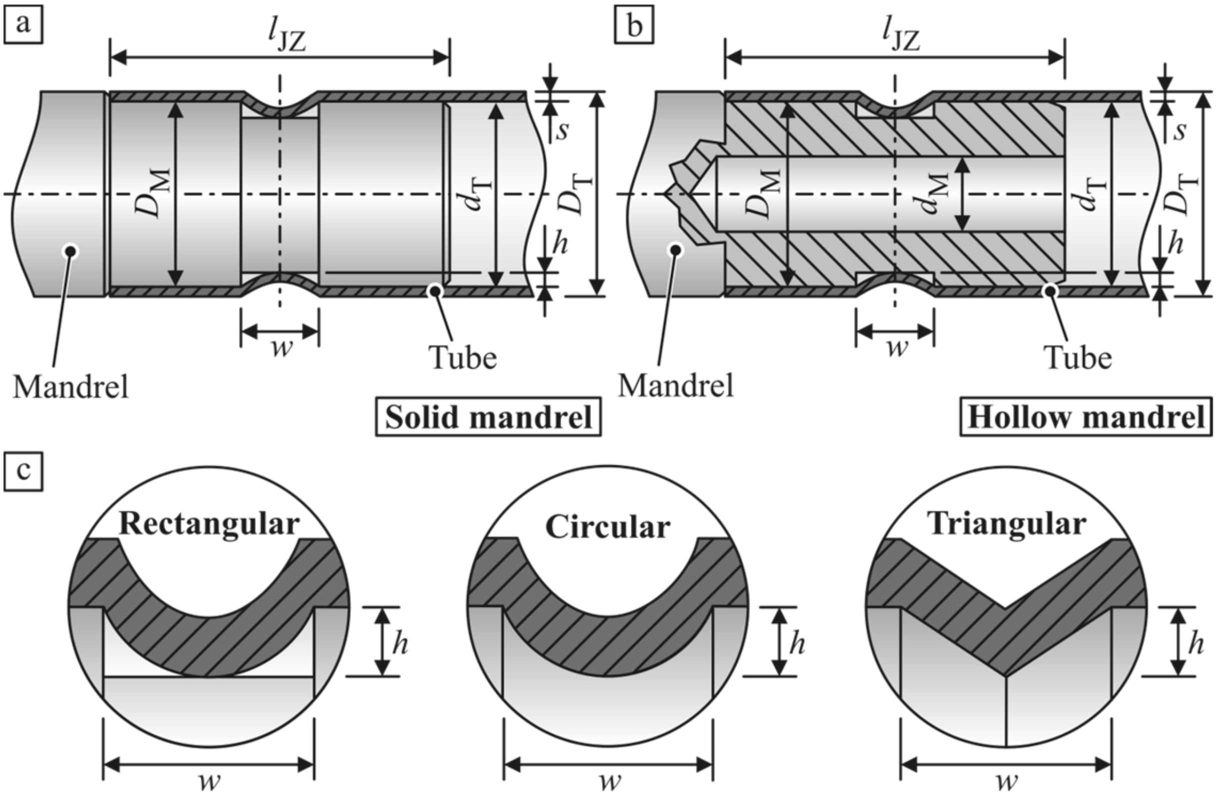

Figure 4-8: Specimens for joining by compression and applied groove shapes

The parameters varied in this analysis are the groove shape and its dimensions, the joining gap a_0, and the charging energy E. Also, the effect of an additional groove on the joint strength is examined. As shown in **Figure 4-8c**, three different groove shapes are analyzed: rectangular, circular, and triangular. In terms of the groove dimensions, the width w, the depth h, and the edge radius R_{GE} are varied. The groove widths considered here are 12, 16, and 20 mm. For the variation of the depth the values 1, 1.5 and, 3 mm are used. Additionally, 2.5 mm deep grooves are manufactured for the rectangular shapes. To investigate the influence of the groove edge radius R_{GE} on the joint strength, solid mandrels with the following radii are used: no radius, 0.5, and

1 mm. For the 3 mm deep grooves also mandrels with edge radii of 2 and 3 mm are manufactured. Mandrels with a rectangular groove shape are used for all experiments regarding the influence of the groove edge radius on the connection strength. **Table 4-7** gives an overview of all applied energies determined from the design chart in **Figure 4-2**.

By varying the mandrel's outer diameter D_M, the effect of a joining gap a_0 on the connection strength is investigated. In addition to the connections with no gap, the following gap sizes are treated: 1 mm, 2 mm, and 2.5 mm.

Table 4-6: Material properties of the components

Material	**Chemical composition**	**Temper condition**	**Components**	**Yield stress σ_y** (MPa)	**Yield stress $\sigma_{y,0.01}$ at 0.01 % plastic strain** (MPa)
EN AW-2007	AlCu4PbMg	T4	Mandrel	263	-
EN AW-6060	AlMgSi	T6	Mandrel, tube	233	212.5
EN AW-7075	AlZn5.5MgCu	T6	Mandrel	460[1]	-

Regarding the process parameters, only the effect of charging energy levels above the levels necessary to fill the grooves on the achievable joint strength is experimentally analyzed here. Therefore, connections with energy levels of 120 % and 140 % of the basic values from **Table 4-7** are manufactured. The specimens used for these tests have a rectangular groove shape and a width of 20 mm.

Table 4-7: Applied charging energies E (bank configuration 5 with E_{max} = 12 kJ)

	Charging energy E (kJ)		
Groove depth *h* (mm)	**Groove width *w* = 12 mm**	**Groove width *w* = 16 mm**	**Groove width *w* = 20 mm**[2]
1.0 mm	3.9	3.3	3.1 (3.7 and 4.3)
1.5 mm	4.7	3.8	3.5 (4.2 and 4.9)
3.0 mm	7.3	5.4	4.9 (5.9 and 6.8)

Subsequently to the basic investigation regarding the influence of the groove and process characteristics on the achievable joint strength, the behavior of hollow mandrels during the joining process and their load transfer is analyzed (see

---

[1] N.N. (2014a)

[2] The charging energy values written in parentheses are the values applied during the variation of *E*.

Figure 4-8b). Compared to solid mandrels, the geometry of hollow ones is changed by a drilled hole in the mandrel's center. The primary interest of this investigation is the effect of this change, which serves to reduce the mass in the joining zone, on the connection strength. A value that describes the general geometry of a hollow inner joining partner is the diameter ratio Q_M.

$$Q_M = \frac{d_M}{D_M} \tag{4.7}$$

A diameter ratio of zero stands for a solid mandrel and a value of Q_M close to one represents a very thin-walled one. This ratio is also a reference value for the mass and the compressive strength of a mandrel. To achieve different values of Q_M, the inner diameter d_M of the mandrel is varied within this work (see **Table 4-8**). The outer diameter of the mandrel is 36 mm for these investigations.

Table 4-8: Dimensions of hollow mandrels

Material	**Groove dimensions *w x h*** (mm)	**Diameter ratio Q_M**
EN AW-6060	12 x 1.0	0.59, 0.74, 0.78, 0.81
EN AW-6060	12 x 1.5	0.55, 0.69, 0.75, 0.78
EN AW-6060	12 x 3.0	0.43, 0.58, 0.64, 0.68
EN AW-6060	16 x 3.0	0.53, 0.58, 0.64, 0.68
EN AW-6060	20 x 3.0	0.56, 0.58, 0.64, 0.68
EN AW-2007	12 x 3.0	0.58, 0.64, 0.68
EN AW-7075	12 x 3.0	0.58, 0.64, 0.68

To analyze how an increased yield strength of the mandrel and the resulting additional interference fit affect the connection strength, joining experiments with mandrels manufactured from two supplementary aluminum alloys are also performed. These alloys are EN AW-2007 and EN AW-7075 (see **Table 4-8**). Furthermore, the effect of the groove shape on the joint strength of connections with hollow mandrels is investigated. As for the experiments regarding the general joining zone characteristics, mandrels with circular and triangular grooves are manufactured in addition to the inner joining partners with the basic rectangular form-fit elements. Three millimeter deep and 12 mm wide grooves are applied for these tests. As mandrel material EN AW-6060 is chosen and the three following inner diameters of this part are selected: 21 mm, 23 mm, and 24.5 mm.

4.2.3 Determination of the joining partner deformation

In order to determine the filling of the grooves and a potential plastic deformation of the mandrels, computer tomography (CT) and X-ray radioscopy investigations are carried out after the electromagnetic joining process (**Figure 4-9a**). These studies are performed at the Institute of Materials Engineering (LWT) of the TU Dortmund University and at the Institute for Applied Materials (IAM-WK) of the Karlsruher Institute of Technology.

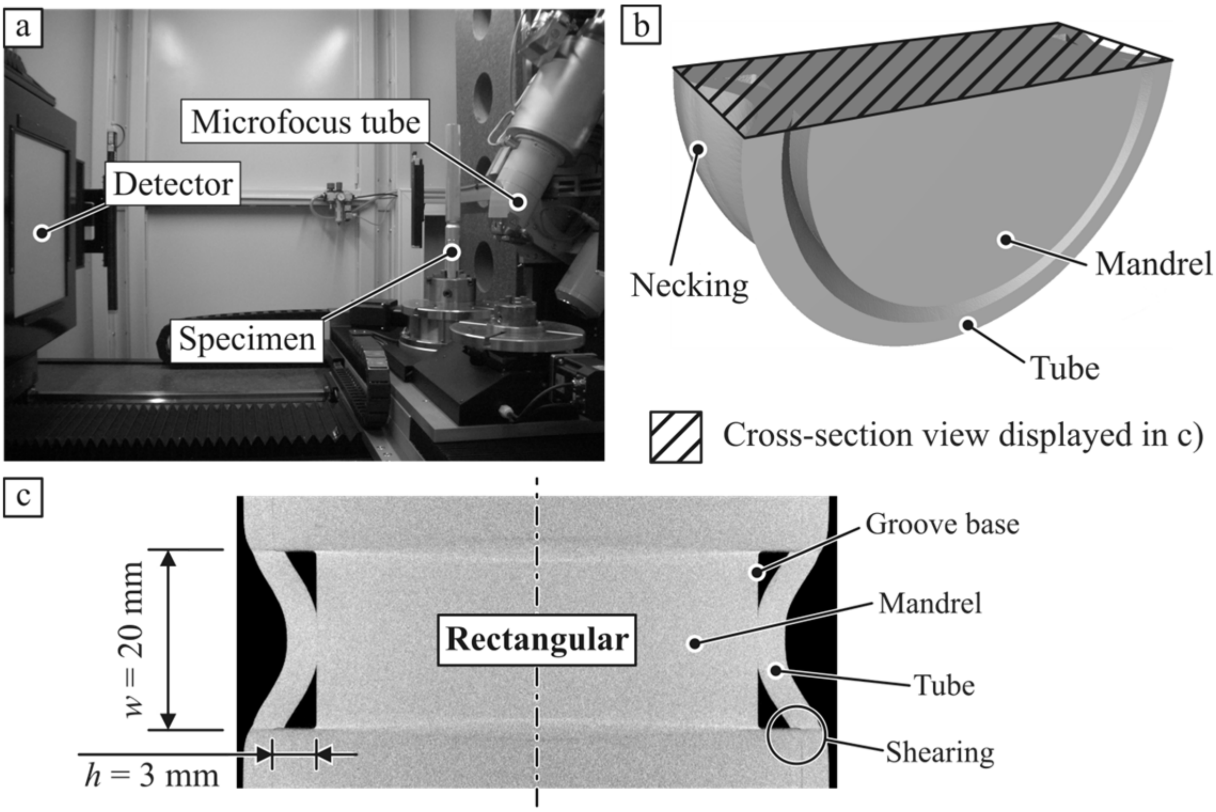

Figure 4-9: Computer tomography of joined specimens (Weddeling et al., 2011b) a) experimental setup b) 3D tomogram of a form-fit connection c) xy-slice extracted from the 3D tomogram

A computer tomography system v|tome|x L240 from phoenix|x-ray is used for the connections with solid mandrels. These investigations are performed at the Institute of Materials Engineering. For the joints featuring hollow mandrels, a Yxlon-CT Precision System is applied and the analyses are carried out at the Institute for Applied Materials. The specific properties of the two used CT systems and the detailed experimental parameters of these studies can be found in **Table 4-9**.

For the generation of the CT images the specimens are rotated stepwise around their longitudinal axis and an X-ray picture is recorded for each rotational increment. A total of 2200 and 2100 pictures, respectively, are taken for each specimen. Subsequently, these 2D images are reconstructed to a 3D tomogram of the joining zone (see **Figure 4-9b**). In **Figure 4-9c),** a 2D slice extracted from the three-dimensional CT image is shown. Since this procedure is quite time-consuming, regular 2D X-ray pictures are taken as well. The disadvantage of these images is that they also contain shadows of the areas surrounding the area of interest. This makes interpreting the images more complicated.

Table 4-9: Parameters of the applied computer tomography systems

Computer tomography system	**phoenix v|tome|x L240**	**Yxlon-CT Precision**
X-ray tube	Micro-focus tube with direct beam tungsten target	Micro-focus transmission tube with tungsten target
Acceleration voltage	230 kV	150 kV
Tube current	100 µA	40 µA
Prefilter	0.5 mm Cu	None
Focus-object-distance	131 mm	75 mm
Focus-detector-distance	1200 mm	690 mm
Magnification	~ 9.2	~ 9.2
Geometry	Cone beam	Cone beam
No. of angular positions	2200	2100
Angle increment	~ 0.164°	~ 0.171°
Detector typ	Flat panel-detector, 2048 x 2048 square pixels, active area: 409.6 x 409.6 mm	Flat panel-detector, 2048 x 2048 square pixels, active area: 409.6 x 409.6 mm

4.2.4 Connection strength determination

The achieved joint quality in terms of pull-out strength is tested using a universal tensile testing machine Zwick Z250, which is displayed in **Figure 4-10**. As pull-out rate of these tests 0.1 mm/s is chosen and the initial length l_0 between the extensometer gages is set to 100 mm. The tube ends are supported by steel plugs during the tests to avoid its deformation by the machine's grips. A load-displacement curve is recorded during the experiments and transformed into a load-strain curve afterwards (see **Figure 4-11**).

Based on the work of Bühler and von Finckenstein (1968b), the force $F_{\mathrm{y,J}}$ at which the first relative movement between the joining partners occurs and the plastic deformation of the whole specimen begins, respectively, is chosen as failure criterion of the connection. This value is characterized by a change in slope of the force-strain curve (see **Figure 4-11**). For the evaluation of $F_{\mathrm{y,J}}$ the force value at 0.01 % plastic strain is determined with the Zwick control and analysis software testExpert II. Instead of the commonly used 0.2 % plastic strain value for the yield stress determination, the 0.01 % value is chosen to receive a more accurate prediction of the joint failure. By dividing the yield force $F_{\mathrm{y,J}}$ of the connection by the cross section A_{T} of the weakest joining partner, which is generally the tube, the yield stress $\sigma_{\mathrm{y,J}}$ of the joint is found.

$$\sigma_{y,J} = \frac{F_{y,J}}{A_T} \tag{4.8}$$

To achieve a better comparability of the measured joint strength, the geometry and material independent specific joint strength $\bar{\sigma}_{\mathrm{y,J}}$ is introduced:

$$\bar{\sigma}_{y,J} = \frac{\sigma_{y,J}}{\sigma_{y,0.01,T}} \tag{4.9}$$

This value gives the joint failure in relation to the yield stress of the tube. Since 0.01 % plastic strain is selected as failure criterion of the connection, the yield stress $\sigma_{\mathrm{y,0.01,T}}$ of the profile material at this value is also determined by tube tensile tests (see **Table 4-6**).

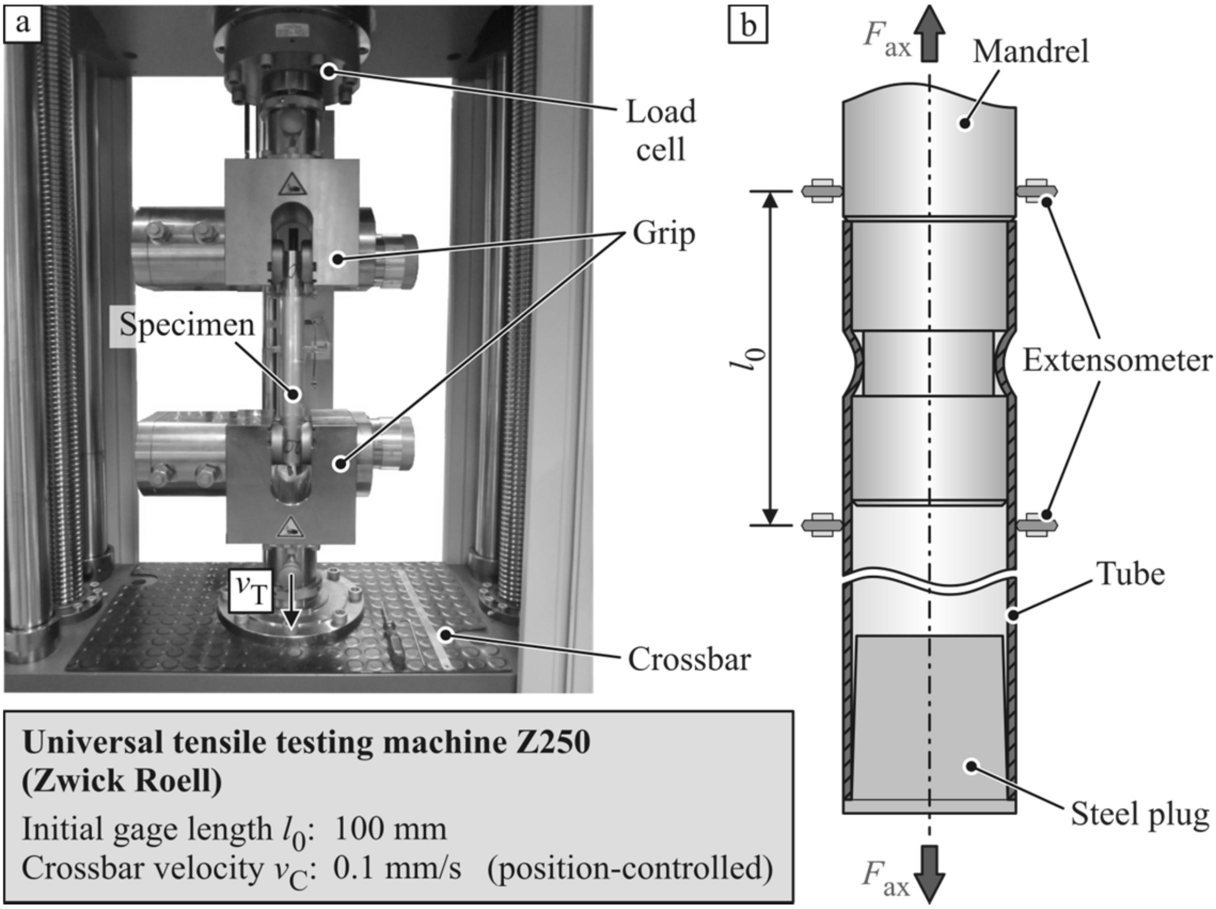

Universal tensile testing machine Z250 (Zwick Roell)

Initial gage length l_0: 100 mm

Crossbar velocity v_C: 0.1 mm/s (position-controlled)

Figure 4-10: Tensile testing of electromagnetic crimped connections

For the calculation of the yield stress $\sigma_{\mathrm{y,0.01,T}}$, the yield force $F_{\mathrm{y,T}}$ of the profile is divided by its cross-sectional area A_{T}.

$$\sigma_{y,0.01,T} = \frac{F_{y,T}}{A_T} \tag{4.10}$$

With this expression and Equation (4.8), the term of the specific joint strength $\bar{\sigma}_{\mathrm{y,J}}$ takes the following form:

$$\bar{\sigma}_{y,J} = \frac{F_{y,J}}{F_{y,T}} \tag{4.11}$$

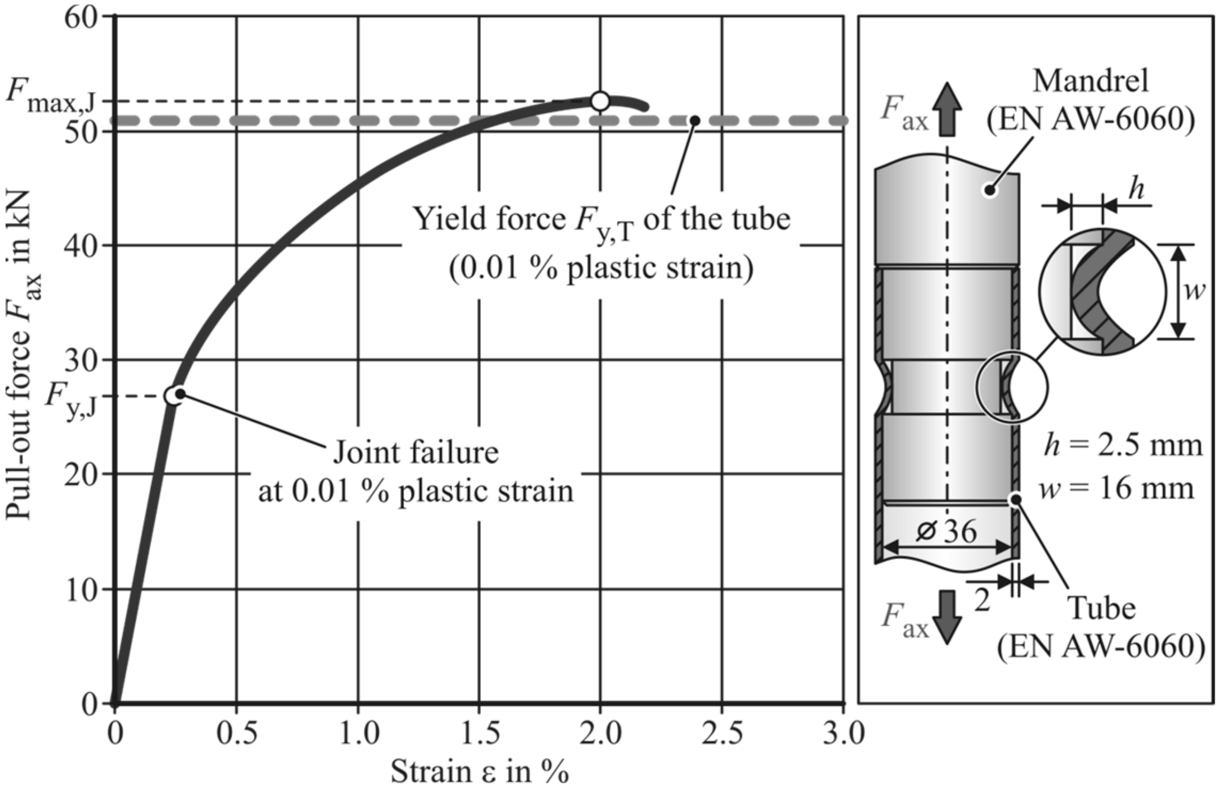

Figure 4-11: Typical pull-out curve of crimped specimens

5 Prediction of crimping parameters

As mentioned above, the experimental and numerical determination of the joining process parameters, critical for a sufficient process design, is very elaborate and expensive. Therefore, in the following section, an analytical approach is introduced which allows the prediction of the necessary charging energy to fill a specific groove geometry. For the evaluation of the charging energy *E*, the model considers the workpiece and groove dimensions as well as the *RLC* circuit characteristics like the discharge frequency *f* and the damping coefficient δ. The verification of this model is performed with the setup described in **Section 4.1**.

5.1 Analytical prediction

The model is divided in two parts. In the first part, the forming depths h_d resulting from various pressure pulses $p_m(t)$ are predicted based on an analytical approach for the prediction of the dynamic response of fully clamped cylindrical shells developed by Youngdahl (1970). **Figure 5-1** shows a schematic pressure curve of electromagnetic forming with the important characteristics. The significant pressure values are the amplitude of the function $p_{m,max}$ and the so-called collapse pressure p_y (Hodge, 1955). At this pressure, the plastic deformation of the shell element starts if the acting magnetic pressure p_m exceeds the value of p_y.

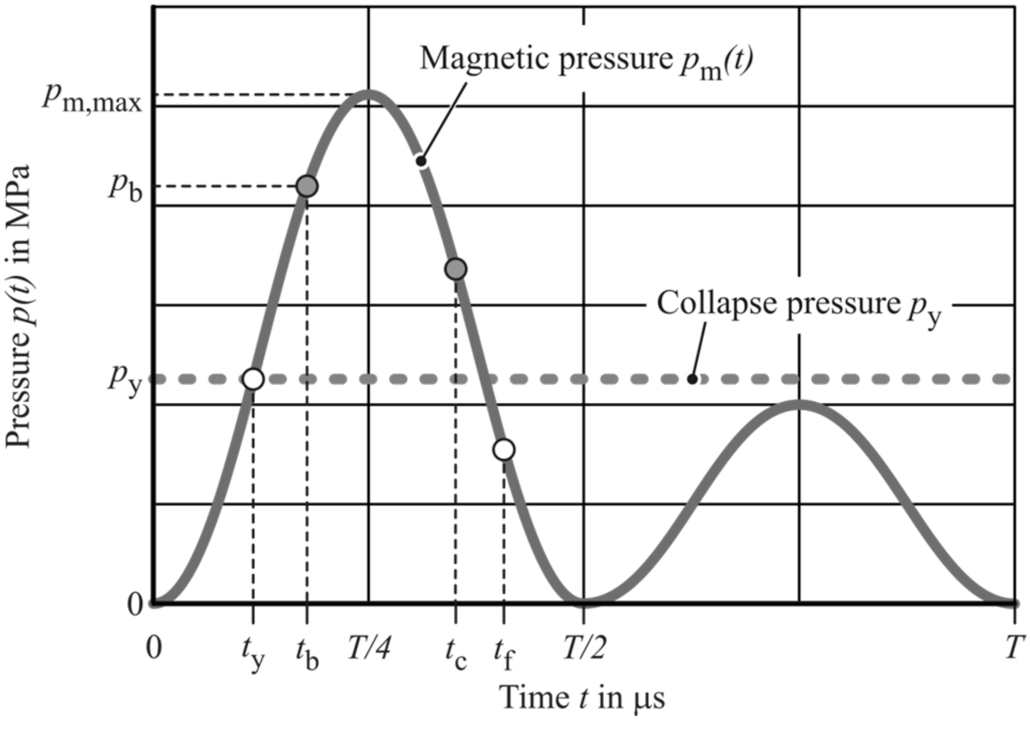

Figure 5-1: Schematic magnetic pressure curve

As described in **Section 2.5.2**, the actual function of the acting magnetic pressure $p_m(t)$ is a damped, quadratic sinusoidal function. Based on the work of Jablonski and

Winkler (1978), a quadratic sinusoidal function is assumed for the mechanical part of the model for simplification purposes. Beerwald (2005) shows that in tube compression, the deformation is usually completed during the first half-wave of the current, and respectively the pressure pulse. Hence, only the first half-wave of the pressure function is considered for the forming depth calculation. These assumptions lead to the following mathematical description of the magnetic pressure pulse:

$$p_m(t) = \begin{cases} p_{m,max} \cdot \sin^2(\omega \cdot t), & t \leq \dfrac{T}{2} \\ 0, & t > \dfrac{T}{2} \end{cases} \tag{5.1}$$

In the second part of the analytical model introduced in **Section 5.1.2**, the charging energies necessary to generate the forming pressure pulses are predicted. The calculations of this electrical part of the approach are influenced by the electrical resistance, the inductance and the capacitance of the *RLC* circuit. The angular frequency ω, which determines the pulse duration in **Section 5.1.1**, is also predicted in **Section 5.1.2.**

5.1.1 Prediction of forming depth

The first analytical approach for studying the dynamic plastic behavior of a fully clamped cylindrical shell was presented by Hodge (1955). **Figure 5-2** gives the dimensions of such a shell element. In this model, a rectangular pressure pulse is acting on the shell element. The axial-symmetric radial pressure distribution is constant in space. He also assumes an ideal plastic material behavior. Hence, the influence of strain hardening and of the strain rate on the yield strength of the material is neglected.

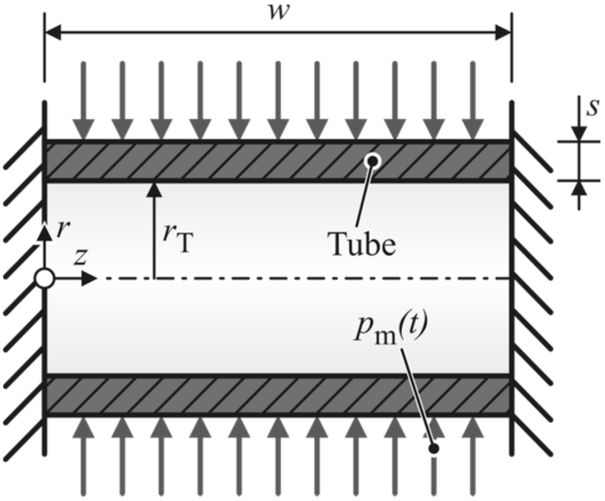

Figure 5-2: Fully clamped shell loaded by uniform pressure

The yield pressure p_y of the shell element can be calculated based on the geometrical parameters of the workpiece and its yield stress in pure shear k_T (Hodge, 1955):

$$p_y = \frac{2 \cdot k_T \cdot s}{r_T}\left(1 + \frac{2}{c^2}\right) \tag{5.2}$$

with

$$c^2 = \frac{w^2}{2 \cdot r_T \cdot s} \tag{5.3}$$

By replacing k_T in Equation (5.2) by the von Mises relationship between yield stress in pure shear and $\sigma_{y,T}$

$$k_T = \frac{\sigma_{y,T}}{\sqrt{3}} \tag{5.4}$$

the collapse pressure can be written as follows:

$$p_y = \frac{2 \cdot \sigma_{y,T} \cdot s}{\sqrt{3} \cdot r_T}\left(1 + \frac{2}{c^2}\right) \tag{5.5}$$

Compared to the work of Hodge, Youngdahl's (1970) model is valid for various pulse shapes. A rectangular pulse shape represents the simplest case of the dynamic plastic response determination of a structure. The basic idea of Youngdahl's approach is the transfer of an arbitrary pressure pulse into a rectangular pulse which leads to the same deflection. For this transformation, he developed three characteristic pulse parameters. If these parameters are equal for different pressure functions, the deflection resulting from these pulses is equal as well. The first of these parameters is the total impulse, which is defined as the integral of the pressure function from the beginning of the plastic deformation t_y to its end t_f.

$$I_e = \int_{t_y}^{t_f} p_m(t)dt \tag{5.6}$$

The second parameter is the effective pressure p_e. This specific value corresponds to the pressure magnitude of a rectangular pulse with the same total impulse as the treated pressure function $p_m(t)$ acting for two times the time t_{mean}.

$$p_e = \frac{I_e}{2 \cdot t_{mean}} \tag{5.7}$$

Youngdahl (1970) defines the t_{mean} as the interval between the onset of the plastic deformation and the centroid of the pressure pulse.

$$t_{mean} = \frac{1}{I_e}\int_{t_y}^{t_f} \left(t - t_y\right) \cdot p_m(t)dt \tag{5.8}$$

Since Youngdahl's basic idea is the transfer of any given pressure pulse into a rectangular pulse, he applies the equation of motion established by Hodge (1955) for a fully clamped cylindrical shell. Since this equation is not just time-dependent but also depends on the axial position z, assumptions for the occurring deformations and the resulting radial velocity field have to be made. For simplification purposes, Hodge (1955) assumes a linear velocity field. This assumption is based on the concept of the formation of plastic hinges (Szabó, 2001), which implies that not the whole shell becomes plastic when the pressure pulse exceeds the collapse pressure. Instead only certain areas, the so-called hinge bands, become plastic (see **Figure 5-3a**). The sections between these hinges remain rigid.

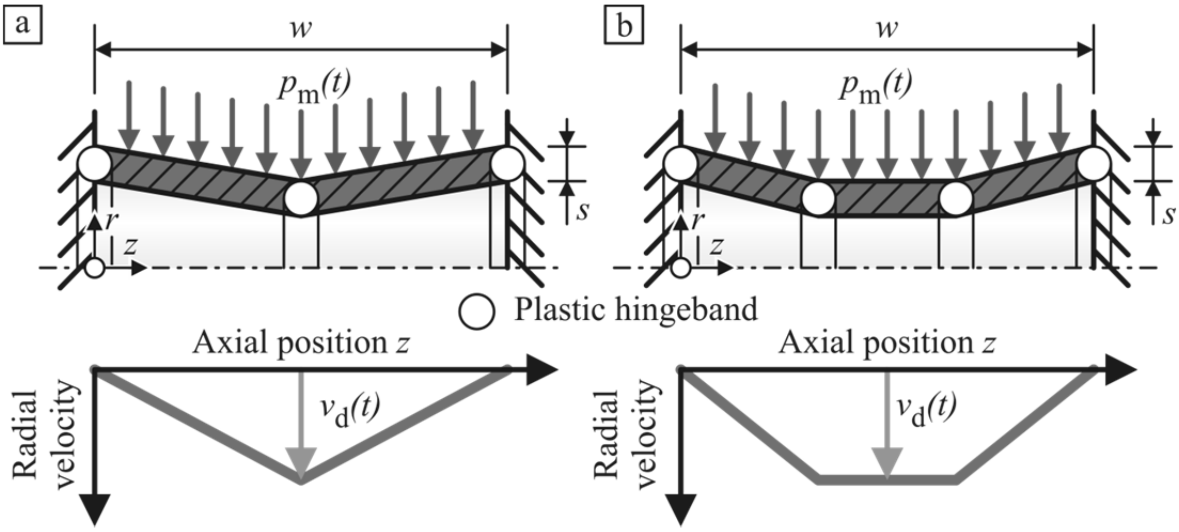

Figure 5-3: Assumed deformations and velocity fields for a) $p_y < p_m(t) < p_b$ and for b) $p_b \leq p_m(t)$

With these assumptions, Hodge (1955) obtains the following expression for the acceleration of the workpiece at its center ($z = w/2$):

$$\dot{v}_d(t) = \frac{3}{2 \cdot \rho_A}\left[p_m(\tau) - p_y\right] \tag{5.9}$$

The derivation of this equation by Hodge (1955) is presented in **Appendix A**. By integration of Equation (5.9), the following expressions for the workpiece velocity $v_d(t)$ and deformation $h_d(t)$ at the groove center are found (Youngdahl, 1970):

$$v_d(t) = \frac{3}{2 \cdot \rho_A}\left[\int_{t_y}^{t} p_m(\tau)d\tau - p_y\left(t - t_y\right)\right] \tag{5.10}$$

$$h_d(t) = \frac{3}{2 \cdot \rho_A}\left[t\int_{t_y}^{t} p_m(\tau)d\tau - \int_{t_y}^{t} \tau \cdot p_m(\tau)d\tau - \frac{1}{2}p_y\left(t - t_y\right)^2\right] \tag{5.11}$$

To determine the response time t_f, which is not known a priori, Youngdahl (1970) applied the boundary conditions $v_d(t_f) = 0$ and $t_f \neq t_y$ to Equation (5.10).

$$p_y\left(t_f - t_y\right) = \int_{t_y}^{t_f} p_m(t)dt \tag{5.12}$$

Since t_f is the only unknown variable in this term, it allows an exact calculation of the moment in time at which the plastic deformation of the cylindrical shell element ends. With the Equation (5.6) to (5.8), Youngdahl (1970) finds the expression for the final deformation in the center of a fully clamped cylindrical shell.

$$h_d\left(t_f\right) = \frac{3 \cdot {I_e}^2}{4 \cdot \rho_A \cdot p_y}\left(1 - \frac{p_y}{p_e}\right) \tag{5.13}$$

Hodge (1955) states that the assumption of a linear velocity field (see **Figure 5-3a**) for solving the mechanical problem of a fully clamped cylindrical shell is only valid if the acting pressure p_{m} is below the limit pressure p_{b}.

$$p_b = \frac{2 \cdot \sigma_{y,T} \cdot s}{\sqrt{3} \cdot r_T}\left(1 + \frac{6}{c^2}\right) \tag{5.14}$$

For acting pressures $p_{\mathrm{m}} \geq p_{\mathrm{b}}$, a new velocity field is introduced (see **Figure 5-3b)**. It is assumed that the plastic hinge band in the center of the shell splits up into two outward moving hinge bands if p_{m} exceeds the limit pressure p_{b} at $t = t_{\mathrm{b}}$. When the pressure pulse reaches its maximum value, the two hinge bands change their direction and move back to the center of the shell. At $t = t_{\mathrm{c}}$, they are recombined and form a single center hinge band again. Analogous to the pressure pulse parameters of Equation (5.6) to (5.8), Youngdahl (1970) introduced three equivalent characteristic values for the interval t_{b} to t_{c} (see **Figure 5-1**).

$${I_e}^* = \int_{t_b}^{t_c} p_m(t)dt \tag{5.15}$$

$$t_{mean}^* = \frac{1}{{I_e}^*}\int_{t_b}^{t_c} (t - t_b) \cdot p_m(t)dt \tag{5.16}$$

$${p_e}^* = \frac{{I_e}^*}{2 \cdot t_{mean}^*} \tag{5.17}$$

The time t_{c} can be determined in a similar manner as t_{f} (see Equation (5.12)). For the final deformation of a fully clamped cylindrical shell for a pressure amplitude $p_{\mathrm{m,max}}$ bigger than p_{b}, Youngdahl (1970) gives the following equation:

$$h_d\left(t_f\right) = \frac{{I_e}^2}{\rho_A}\left[\frac{3}{4}\left(\frac{1}{p_y} - \frac{1}{p_e}\right) - \frac{1}{4}\left(\frac{{I_e}^*}{I_e}\right)^2\left(\frac{1}{p_b} - \frac{1}{{p_e}^*}\right)\right] \tag{5.18}$$

5.1.2 Determination of the charging energy

Subsequent to the determination of the maximal deflection h_d resulting from a specific pressure pulse, the charging energy E necessary to generate this magnetic pulse has to be predicted. For this calculation, an analytical approach with respect to the workpiece, tool and machine properties is introduced in this section. The *RLC* circuit displayed in **Figure 2-12** provides the basis for the following determinations. As in the mechanical part of the model, it is assumed that the deformation ends before $t = T/2$. Therefore, only the first half-wave of the discharge current is considered as well. As mentioned in **Section 2.5.2**, the magnetic field generated by a current *I(t)* running through a long solenoid, can be expressed by Equation (2.19). On the assumption that the magnetic field is completely shielded from the inside of the tube, the acting magnetic pressure can be calculated by combining this formula with Equation (2.18). Substituting *I(t)* in the resulting pressure determination by the solution of the differential equation of the applied *RLC* circuit, which is given by Equation (2.9), leads to the following expression for p_m.

$$p_m(t) = \frac{1}{2}\mu \cdot \frac{n^2}{l_{coil}^2} \frac{U^2}{(\omega \cdot L_{res})^2} \cdot e^{-2\delta t} \sin^2(\omega \cdot t) \tag{5.19}$$

While a quadratic sinusoidal pressure function is applied to the forming depth determination in **Section 5.1.1**, a damped quadratic sinusoidal function is used for the calculation of the electrical parameters. The damping of Equation (5.19) is expressed by the coefficient δ. The damped function is chosen to consider the losses due to the inductance and the resistance of the *RLC* circuit for the approximation of the charging energy based on the maximum pressure.

The resulting inductance in Equation (5.19) can be determined with the Equations (2.5) and (2.6) from **Section 2.5.1**.The estimation of the tool coil inductance L_{coil} is based on the general equation for the inductance of a solenoid (Kazimierczuk, 2014). In this expression, L_{coil} depends on the inner radius r_{coil}, the length l_{coil}, and the number of turns n of the coil as well as the permeability μ. In contrast to the general equation, the term for the determination of L_{coil} is enhanced here by the influence of the skin depth δ_s (Al-Hassani, 1974). Therefore, the inner solenoid radius is increased by half the skin depth.

$$L_{coil} = \frac{\mu \cdot \pi \cdot \left(r_{coil} + 0.5 \cdot \delta_{s,coil}\right)^2 \cdot n^2}{l_{coil}} \tag{5.20}$$

The determination of the workpiece inductance L_w is adjusted in a similar way. Hence, the outer radius R_T of the tube is reduced by half the skin depth.

$$L_w = \frac{\mu \cdot \pi \cdot \left(R_T - 0.5 \cdot \delta_{s,T}\right)^2}{l_{coil}} \tag{5.21}$$

As mentioned in **Section 2.5.1**, the characteristics of the *RLC* circuit change during the forming process (Winkler, 1973). Due to the decrease of the workpiece radius in electromagnetic compression, the inductance of the system L_{res} increases. Thereby, the discharge current path *I(t)* and the resulting pressure pulse $p_{\mathrm{m}}(t)$ are influenced by the history of deformation (Beerwald, 2005). Since a consideration of this change in inductance would make a closed-form analytical analysis of the *RLC* circuit impossible, typically the influence of the deformation on L_{w} is neglected (Beerwald, 2005). To counteract the error resulting from this assumption, in this work, the initial tube radius R_{T} is replaced by the radius $R_{\mathrm{T,d}}$.

$$R_{T,d} = R_T - \frac{h_d}{2} \tag{5.22}$$

On the assumption of a nearly linear time gradient of the deformation, $R_{\mathrm{T,d}}$ represents the mean outer tube radius during the considered first half-wave of the pressure pulse. In case of form-fit joining, the tube radius R_{T} is not just time-dependent, but also related to the axial position. Since the largest deflection, which leads to the biggest increase of L_{res}, appears at the center of the groove, only the deformation at this position is considered for the adjustment of the workpiece inductance. With the adjustment of the tube radius, Equation (5.21) can be written as follows:

$$L_{w,d} = \frac{\mu \cdot \pi \cdot \left(R_T - 0.5 \cdot \left(\delta_{s,T} + h_d\right)\right)^2}{l_{coil}} \tag{5.23}$$

Inserting the workpiece inductance $L_{\mathrm{w,d}}$ with due regard to the deformation of the tube leads to an adjusted term for the resulting inductance L_{res}.

$$L_{res,d} = L_i + L_{coil} - \frac{\left(n \cdot L_{w,d}\right)^2}{L_{w,d}} \tag{5.24}$$

The electrical conductivities κ of the workpieces and the EMF tool in **Table 5-1**, which are necessary for the skin depths determination by Equation (2.3), are taken from literature (Psyk, 2010 and N.N., 2014a).

Table 5-1: Electrical conductivities from Psyk (2010) and N.N. (2014a)

Material	Copper (Coil)	EN AW-1050	EN AW-2007	EN AW-6060
Electrical conductivity κ (MS/m)	56	35	20	31

The damped angular frequency ω necessary for the mechanical (see **Section 5.1.1**) and the electrical part of the model is experimentally evaluated. Therefore, experiments at which the deformation of the tube is suppressed by a solid mandrel without a groove are performed. From the recorded currents curves, the discharge frequency f is evaluated by applying Equation (4.1). With Equation (2.10), the value of ω for the considered *RLC* circuit can be calculated afterwards. This experimental determination is chosen since a closed analytical prediction of the frequency is impossible. The reason for this is that f depends on the inductance of the EMF system and at the same time it influences L_{res} (see Equation (2.12), (5.20) and (5.21)). In **Table 5-2**, the experimental discharge frequencies with suppressed deformation for different materials and capacitor bank configurations are shown. The table also displays the average discharge frequencies of the forming experiments and their corresponding standard deviations. The standard deviation of the frequency depicts that the variation of f due to the workpiece movement is relatively small for all forming experiments. Also the deviations between the average frequencies of experiments with and without deformation are below 10 %. Therefore, it is acceptable to apply the experimentally measured discharge frequencies to the analytical process parameter prediction. The predicted values of ω are also used in Equation (5.1) for the mechanical part of the process parameter evaluation.

Table 5-2: Experimentally evaluated discharge frequency

Capacitor configuration (Table 4-2)	5	2	6	5	5
Maximal charging energy *E* (kJ)	12	8	32	12	12
Material	EN AW-6060	EN AW-6060	EN AW-6060	EN AW-2007	EN AW-1050A

Average frequency, with deformation (Hz)	**9957**	**12259**	**5831**	**9884**	**10776**
Standard deviation, with deformation (%)	1.46	1.47	1.58	2.53	5.52

Frequency *f*, suppressed deformation (Hz)	**9753**	**12111**	**5697**	**9527**	**9714**
Deviation to average frequency with deformation (%)	2.04	2.30	1.21	3.61	9.86

If the analytical approach presented in this section shall be used for the design of a new EMF system with respect to a specific joining operation, an experimental frequency determination cannot be applied. In this case an iterative approximation of f is a feasible alternative. In the first step, the inductance of the system and its resistance need to be predicted under neglection of the frequency and the resulting skin depth.

This can be done by the equations introduced by Jablonski and Winkler (1978). Afterwards, *f* can be determined with the expressions from **Section 2.5.1**. This allows a subsequent correction of the calculated inductance and resistance. By repeating this procedure, the values of *f*, L_{res}, and R_{res} can be approximated. But compared to the experimental approach, the iterative approximation is not as accurate.

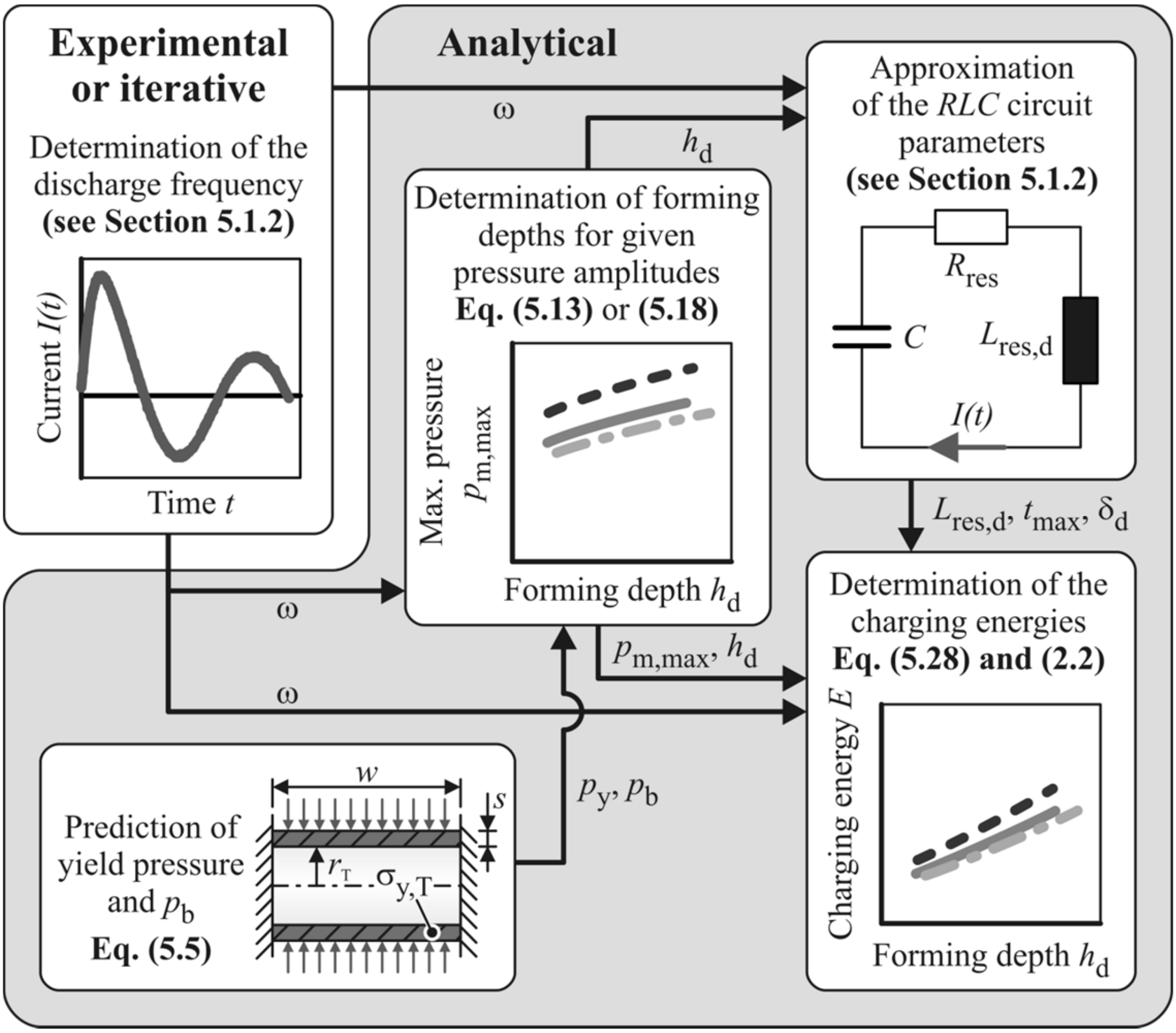
Experimental or iterative
Determination of the discharge frequency (see Section 5.1.2)
Current I(t)
Time t
Analytical
ω
h_d
Approximation of the RLC circuit parameters (see Section 5.1.2)
R_res
C
L_res,d
I(t)
L_res,d, t_max, δ_d
Determination of forming depths for given pressure amplitudes Eq. (5.13) or (5.18)
Max. pressure p_m,max
Forming depth h_d
ω
p_m,max, h_d
ω
Determination of the charging energies Eq. (5.28) and (2.2)
Charging energy E
Forming depth h_d
p_y, p_b
Prediction of yield pressure and p_b Eq. (5.5)
w
s
r_T
σ_y,T

Figure 5-4: Procedure of the analytical joining parameter prediction

Besides the aggregate inductance of the *RLC* circuit, the resulting resistance R_{res} and the damping coefficient δ also vary due to the workpiece movement. But it can be assumed that the change in the aggregated resistance is small and that it influences the charging energy required to generate the desired pressure pulse only to a minor degree. Therefore, R_{res} can be determined from the recorded current curves with suppressed deformation by the rearranged Equation (2.13).

$$R_{res} = 2 \cdot \delta \cdot L_{res} \tag{5.25}$$

In this term, the damping coefficient δ and L_{res} are also calculated from the measured current curves by Equations from **Section 2.5.1**. With the knowledge of resistance R_{res}

and $L_{\text{res,d}}$ for a specific deformation, the corresponding damping coefficient δ_{d} for the treated forming operation can be calculated.

$$\delta_d = \frac{R_{res}}{2 \cdot L_{res,d}} \tag{5.26}$$

Based on δ_{d} in combination with the angular frequency ω, the last unknown variable of Equation (5.19) can be determined. This is the time t_{max}, at which the pressure pulse reaches its maximum (Dietz et al., 1967).

$$t_{max} = \frac{1}{\omega} \cdot \arctan\left(\frac{\omega}{\delta_d}\right) \tag{5.27}$$

By applying the pressure amplitude $p_{\text{m,max}}$ required to fill a specific groove from the mechanical part of the model in **Section 5.1.1** and the corresponding values of $L_{\text{res,d}}$, δ_{d}, ω, and t_{max} to Equation (5.19), it takes the following form:

$$p_{m,max} = \frac{1}{2}\mu \cdot \frac{n^2}{l_{coil}^2} \frac{U^2}{\left(\omega \cdot L_{res,d}\right)^2} \cdot e^{-2\delta_d t_{max}} \sin^2(\omega \cdot t_{max}) \tag{5.28}$$

The charging voltage U necessary to generate this maximum magnetic pressure with respect to the *RLC* circuit characteristics can be found by rearranging this expression. To determine the charging energy E based on the predicted value of U and the capacitance C of the EMF machine, Equation (2.2) is applied. The complete procedure to determine the energy level necessary to fill a specific groove geometry with respect to the machine and workpiece properties is shown in **Figure 5-4**.

5.2 Verification of the analytical parameter prediction

In the following, the results of the experimental joining parameter identification and determination are presented. In combination with additional numerical calculations, these results are used to verify the analytical joining parameter prediction introduced in the previous section. The input parameters of this model can be found in **Section 4.1** and **5.1**. To illustrate the error of the analytical model with respect to the experiments, the mean absolute percentage error (MAPE) is determined (Armstrong, 1985). This value reflects the average deviation between calculated and measured results.

$$MAPE = \left[\frac{\sum_{i=1}^{N}\left(\frac{|A_i - F_i|}{A_i}\right)}{N}\right] \tag{5.29}$$

In this expression, A_{i} represents the actual or experimental result and F_{i} stands for the corresponding forecasted or analytically predicted value. The variable N represents the number of data points compared.

At first, the mechanical part of the model described in **Section 5.1.1** is evaluated. For this purpose, the analytical pressure values are compared to the values of $p_{m,max}$, acting during the experimental joining parameter determination. A possibility to determine the pressure amplitudes of the deformation tests is the measurement of the acting magnetic fields $H_o(t)$ and a subsequent calculation of the pressures by Equation (2.18). A corresponding measurement probe is introduced by Bauer (1965). The disadvantage of this approach is that the probe has to be very small to fit in the gap between coil and tube. This geometrical restriction leads to a very delicate probe design. Another possibility, which is chosen in this work, is to measure the discharge currents and calculate the pressures based on values of $I(t)$ by a numerical finite element analysis (FEA). For this purpose, the numerical model introduced in **Section 4.1.3** is applied here. The strain rate-dependent material behavior is considered in the model by Equation (4.5) in combination with the parameters from **Figure 4-5**. To determine the values of $p_m(t)$, the calculated Lorentz forces acting on the nodes in the center of the groove are aggregated (see **Figure 5-5**).

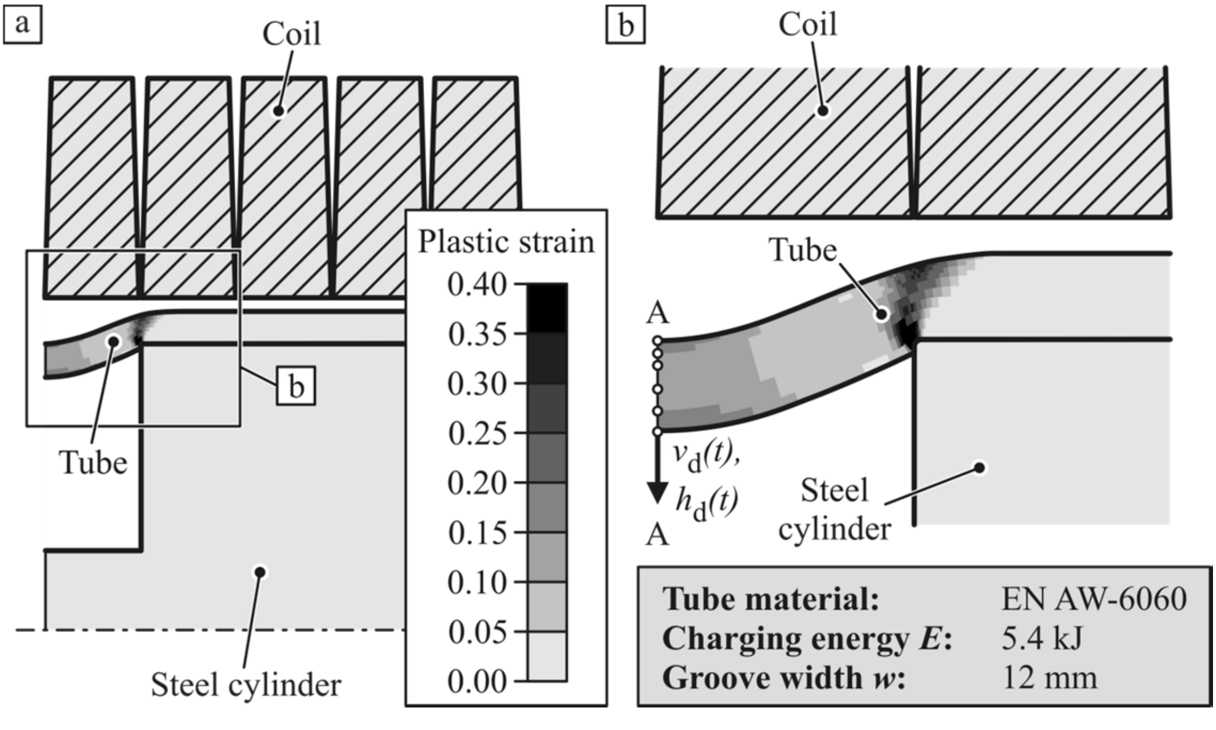

Figure 5-5: Numerical determination of forming velocity and forming depth

Due to the two-dimensionality of the model, the magnetic force values determined by the software have the unit force per radian. By dividing the sum of the Lorentz forces by a segment of the outer surface of the tube, the pressure in the center of the groove is evaluated. This segment is defined by the outer radius of the workpiece R_T and the element length in axial direction. The change of this length with time due to the deformation of the tube is also considered within the determination of the magnetic pressure.

The specific parameter variations which are considered in this numerical study are chosen in accordance with the experimental investigations of **Section 4.1**. A detailed list of the experiments, which are numerically modeled, is given in **Table 5-3**.

Table 5-3: Parameter variation of the finite element simulations

Tube material	**Capacitor bank configuration**	**Groove width** (mm)	**Charging energy E** (kJ)
EN AW-6060	5 (bank II + III)	12	3.6, 4.8, 5.4, and 6.6
		16	3.0, 3.6, 4.2, and 4.8
		20	3.0, 3.6, 4.2, and 4.8

Figure 5-6 shows the analytical and numerical results of the magnetic pressure prediction for a specific forming depth h_d. For these investigations, the combination of the capacitor banks II and III of the Maxwell Magneform EMF machine is used. The configuration has a maximum charging energy of 12 kJ. The average discharge frequency f of this capacitor bank setup with the K40-10/60 tool coil and an EN AW-6060 tube is about 9.75 kHz.

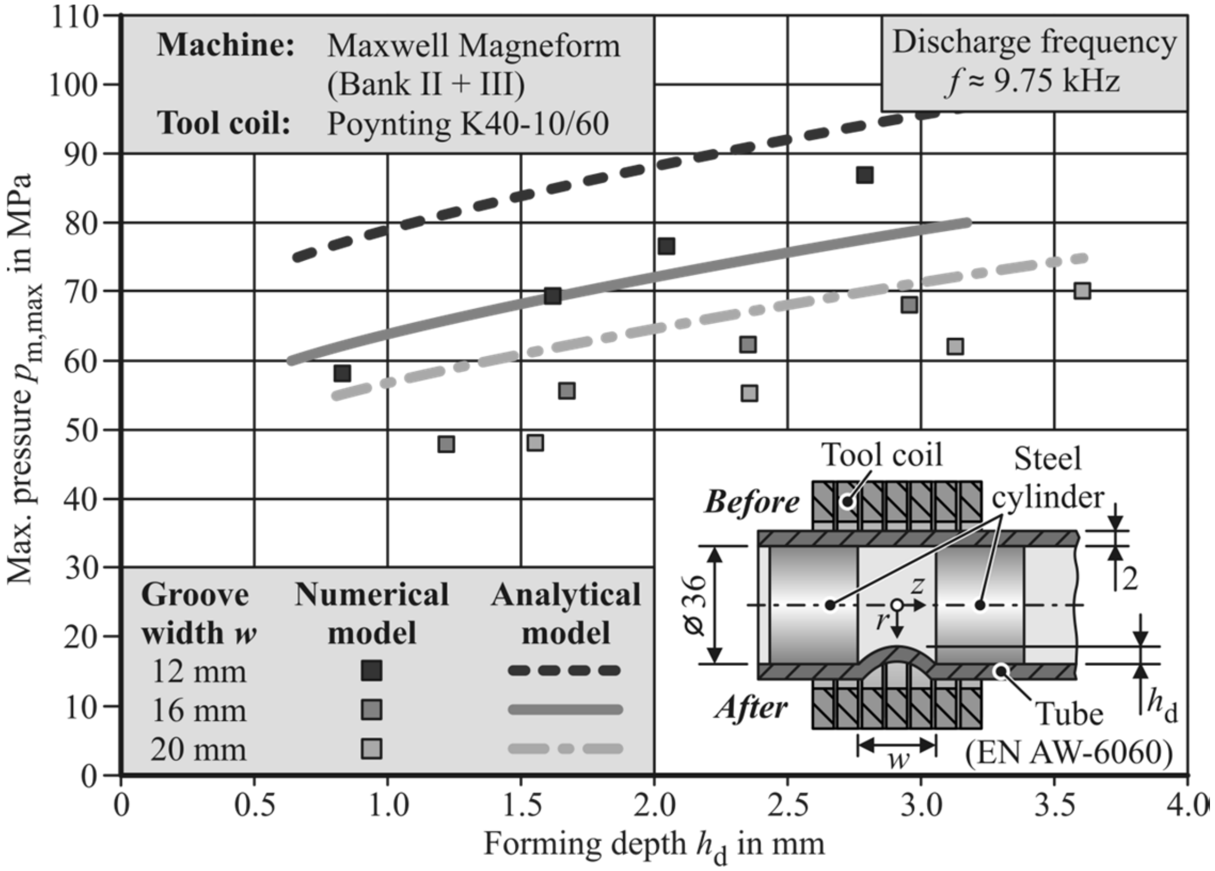

Figure 5-6: Analytical versus numerically determined pressure amplitude $p_{m,max}$

It can be seen that for each groove of width *w*, the required magnetic pressure rises with an increasing depth. The diagram also shows that higher energies are required to fill narrower grooves. The analytical and numerical results are qualitatively within good agreement, but quantitatively they differ noticeably with a maximum deviation of about 25 %. This difference between the calculations can be attributed to the simplifications of the analytical model (see **Section 5.1**). Especially, the assumption of a rectangular approximation of the yield domain and the simplified velocity fields make the analytical model more rigid. Hence, this approach supplies higher pressure values. Although the mechanical part of the analytical joining parameter prediction overestimates the required magnetic pressures, it is very valuable for the process design. It is particularly useful for the design of EMF crimping tools since the model gives an upper bound of the acting forces. Based on this knowledge, the winding material and geometry can be selected. It also allows the determination of the necessary coil reinforcements.

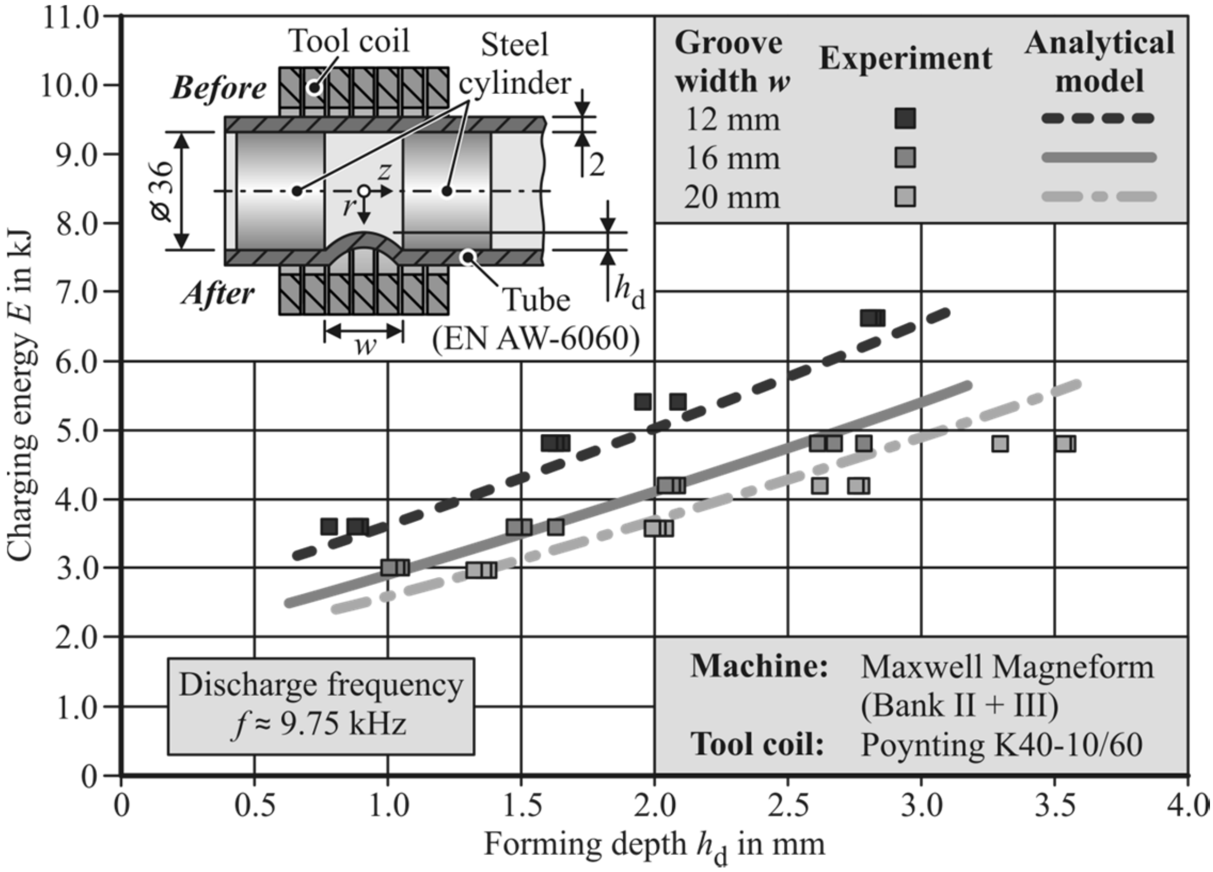

Figure 5-7: Comparison of experimentally and analytically determined charging energies

Subsequent to the verification of the mechanical part of the analytical process parameter prediction, the electrical part of the model is evaluated. To this end, the experimental and analytical charging energy values are plotted over the achieved forming depths h_d in **Figure 5-7**. Similar to the pressure versus forming depth plot, this diagram shows that increasing depth and decreasing width require higher charging energies. These findings correspond to the observations of Bühler and von Finckenstein (1971). The analytically predicted charging energies are in very good agreement with the experimental energy levels. The mean absolute percentage error or average deviation between model and experiments is approximately 5 %. The maximum divergence of this parameter combination is about 15 %.

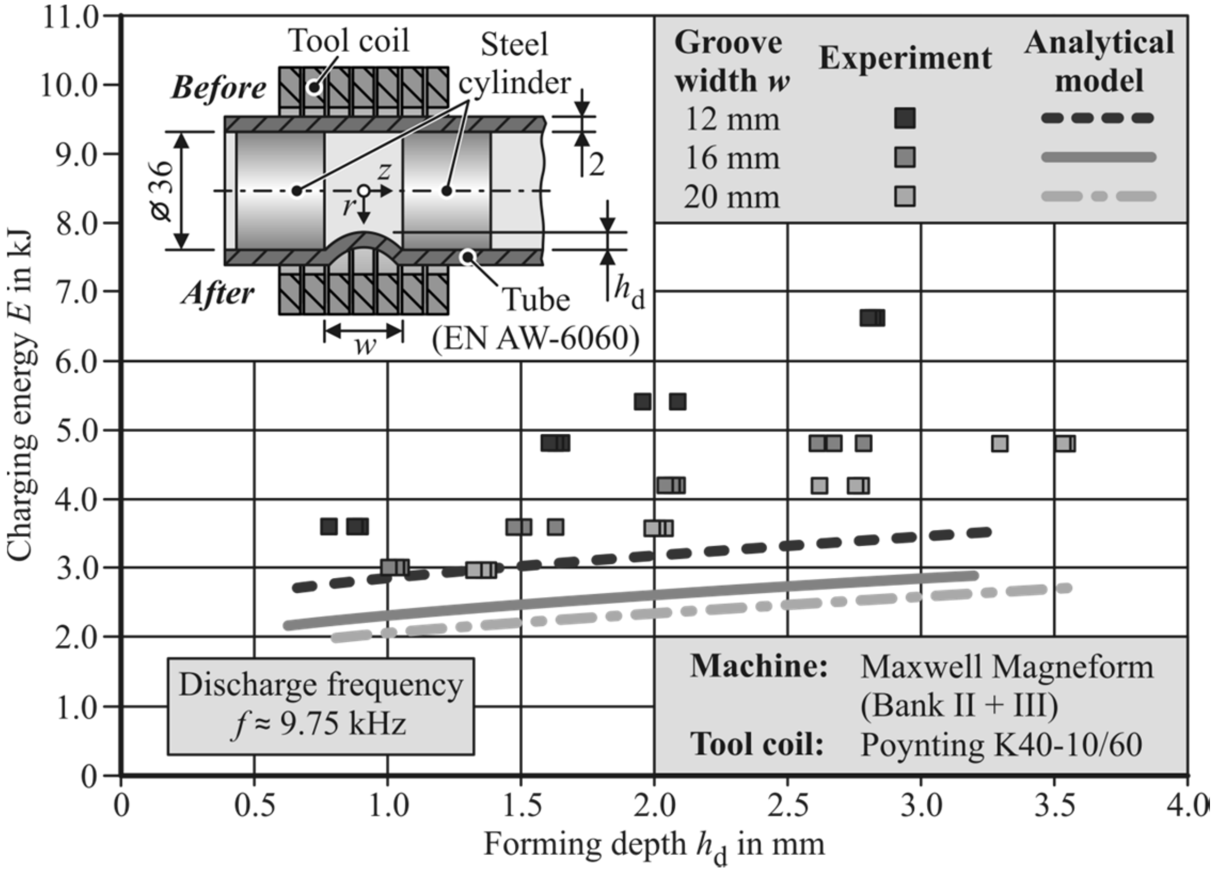

Figure 5-8: Charging energy levels selected for the experiments compared to the analytically determined values of E without inductance adjustment by Equation (5.22)

Figure 5-8 shows the comparison between the experimental charging energies and the values of E calculated without an adjustment of the system inductance by Equation (5.22). It can be seen that the analytical joining parameter prediction underestimates the selected energy levels significantly. The divergence between model and experiments ranges in this case from 22 % at the smallest deformations to about 50 % at the largest diameter changes. This observation can be attributed to the fact that the system inductance L_res is underestimated in the calculations without the consideration of the workpiece movement (see equations of **Section 5.1.2**). Equation (5.28) in combination with Equation (2.2) reveals that this leads to an underestimation of the charging voltage or the energy level necessary to generate the desired pressure pulse as well. The comparison of the results of **Figure 5-7** and

Figure 5-8 shows that the adjustment of the system inductance in the analytical model increases the accuracy of the approach significantly.

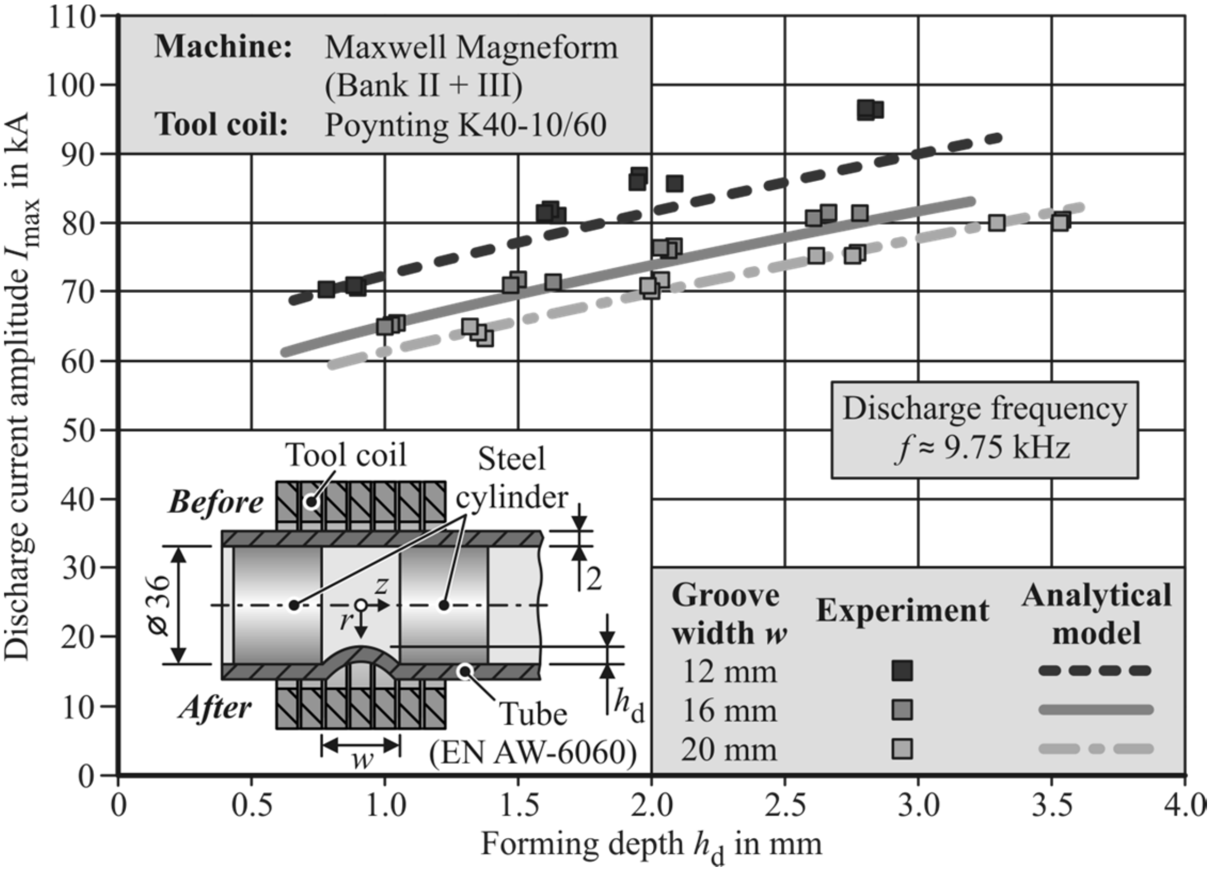

Figure 5-9: Analytically predicted current amplitude I_{max} versus experimental current

Besides the comparison of the calculated and measured charging energies for specific deformations, the current amplitudes I_{max} are determined for selected parameter variations and compared to the values of the corresponding experiments. The charging energies are not measured values, but energy levels that are selected at the EMF system. Due to outer influences or disturbances in the charging procedure, the selected levels might vary from the actual energies stored in the capacitors, and, therefore, this additional verification of the model is performed. The current amplitude I_{max} with respect to the predicted charging voltage can be approximated by the following equation (Dietz et al., 1967):

$$I_{max} = U \cdot \sqrt{\frac{C}{L_{res,d}}} \cdot e^{-\delta_d t_{max}} \tag{5.30}$$

The experimental values are determined from the measured current curves as described in **Section 4.1.2**. In **Figure 5-9**, the comparison of the maximum discharge current for different deformations h_d is displayed. It can be seen that the analytically calculated values agree very well with the experimentally measured ones. The largest deviation between model and experiments is less than 10 %. The knowledge of the maximum current is very important for the design of an EMF system and the necessary tooling since it gives an idea of the electrical loadings acting on the system. Hence, the electrical components of the system, like switches and wiring, can be selected or designed with respect to this knowledge.

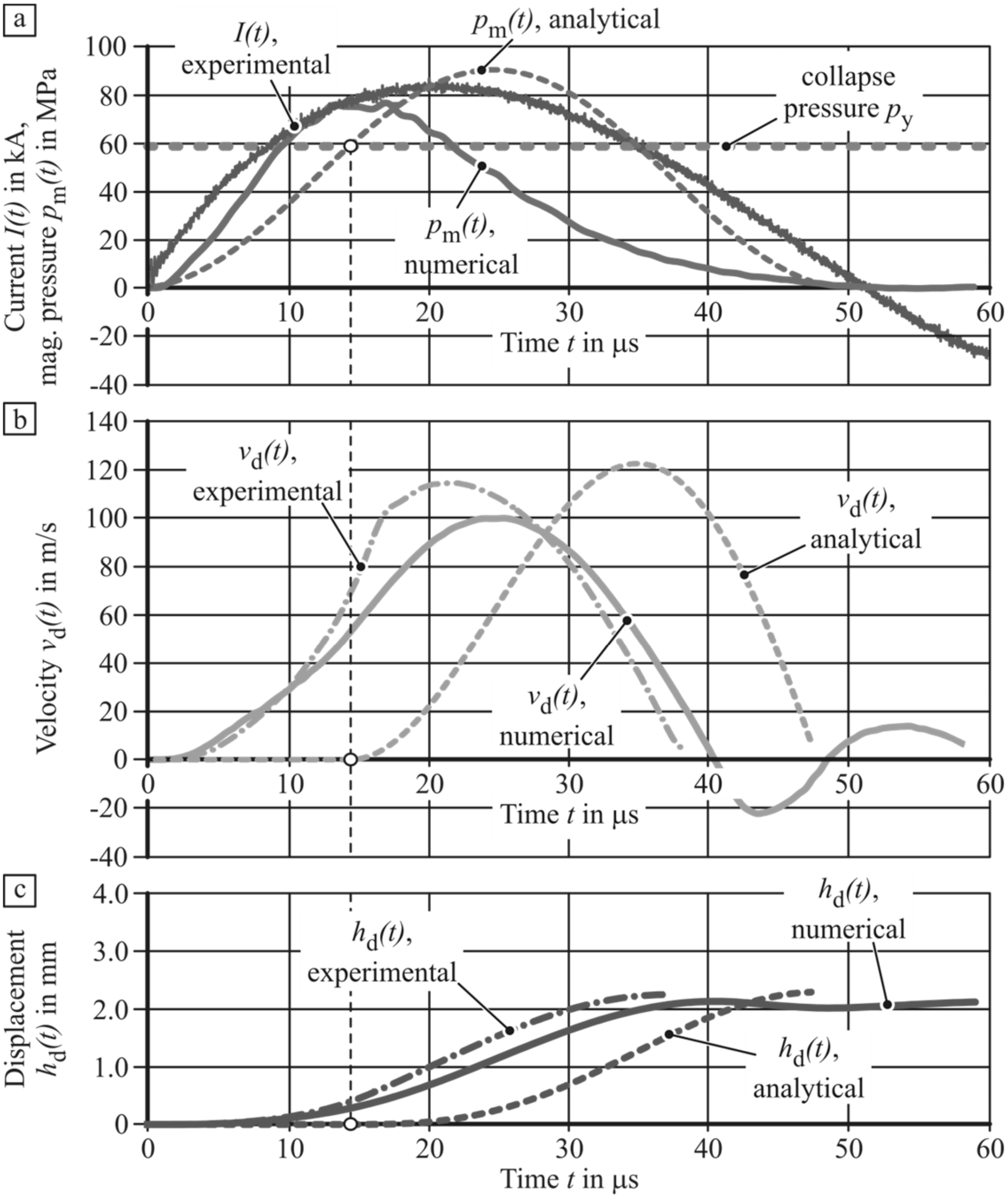

Machine: Maxwell (Bank II + III) **Energy *E*:** 5.4 kJ **Material:** EN AW-6060
Tool coil: Poynting K40-10/60 **Width *w*:** 12 mm

Figure 5-10: Analytical, numerical, and experimental deformation course

For a further verification of the analytical joining parameter prediction, the experimentally measured and numerically calculated time courses of forming velocity and deformation at the groove center are compared to the analytically approximated curves of $v_d(t)$ and $h_d(t)$. Thereby, it is analyzed if the model presented in **Section 5.1** only allows the prediction of the final deformations or if it is also able to map the forming process with respect to its time-dependent course. This comparison is performed for all parameter variations which are experimentally tested as well as numerically modeled (see **Table 5-3**). During the experiments, the discharge currents and the workpiece velocities at the groove center are recorded (see **Section 4.1**). The displacement curves are gained by integrating the velocity curve. As described above, the recorded currents $I(t)$ are used as input for numerical calculations of $p_m(t)$, $v_d(t)$, and, $h_d(t)$. The pressure amplitudes $p_{m,max}$ for the analytical model are also determined based on the recorded discharge currents by Equation (5.30) in combination with the approach of **Section 5.1.2**. To consider the change of inductance due to the workpiece movement for the pressure determination (see Equation (5.23)), the final forming depth h_d is predicted from the analytical values in **Figure 5-9**. This is done prior to the pressure amplitude calculation. Afterwards, the values of $v_d(t)$ and $h_d(t)$ are determined by Equations (5.10) and (5.11). The collapse pressure is also predicted analytically.

Figure 5-10 shows the analytically predicted, experimentally measured, and numerically calculated velocity and displacement curves for a forming operation with a charging energy of 5.4 kJ and a groove width of 12 mm. In terms of the peak values of velocity and displacement, all three approaches are in good agreement. The time course of the numerically determined velocity curve and of the one measured by PDV agree also very well. The same applies in the case of the deformation curves. In contrast to the numerical and experimental results, the analytical velocity curve has a shorter duration and a later starting point. The shorter analytical velocity curve can be attributed to the assumed ideal plastic material behavior of this approach. The later starting point of the analytically calculated deformation can be explained by the neglection of damping and elastic deformation in the mechanical part of this model.

The comparisons of the analytically, numerically, and experimentally determined deformation courses for the other treated parameter variations show the same analogies. This is indicated by the analytical, numerical, and experimental maximum workpiece velocities v_{max} displayed in **Figure 5-11**. The diagram shows that both mathematical models provide a good approximation of the maximum velocity at the groove center. The comparisons of the deformation course and the values of v_{max} imply that the numerical model approximates the experimental forming behavior very well. This supports the validity of the numerically calculated pressures in **Figure 5-6**. Additionally, the results provide a further validation of the analytical process parameter prediction due to its similarities to the velocity and displacement curves as well as to the maximum velocities determined numerically and experimentally.

Since the analytical joining parameter prediction shall not be limited to a specific EMF system and a particular workpiece material, a verification of the models validity with respect to the *RLC* circuit characteristics and the tube material is performed.

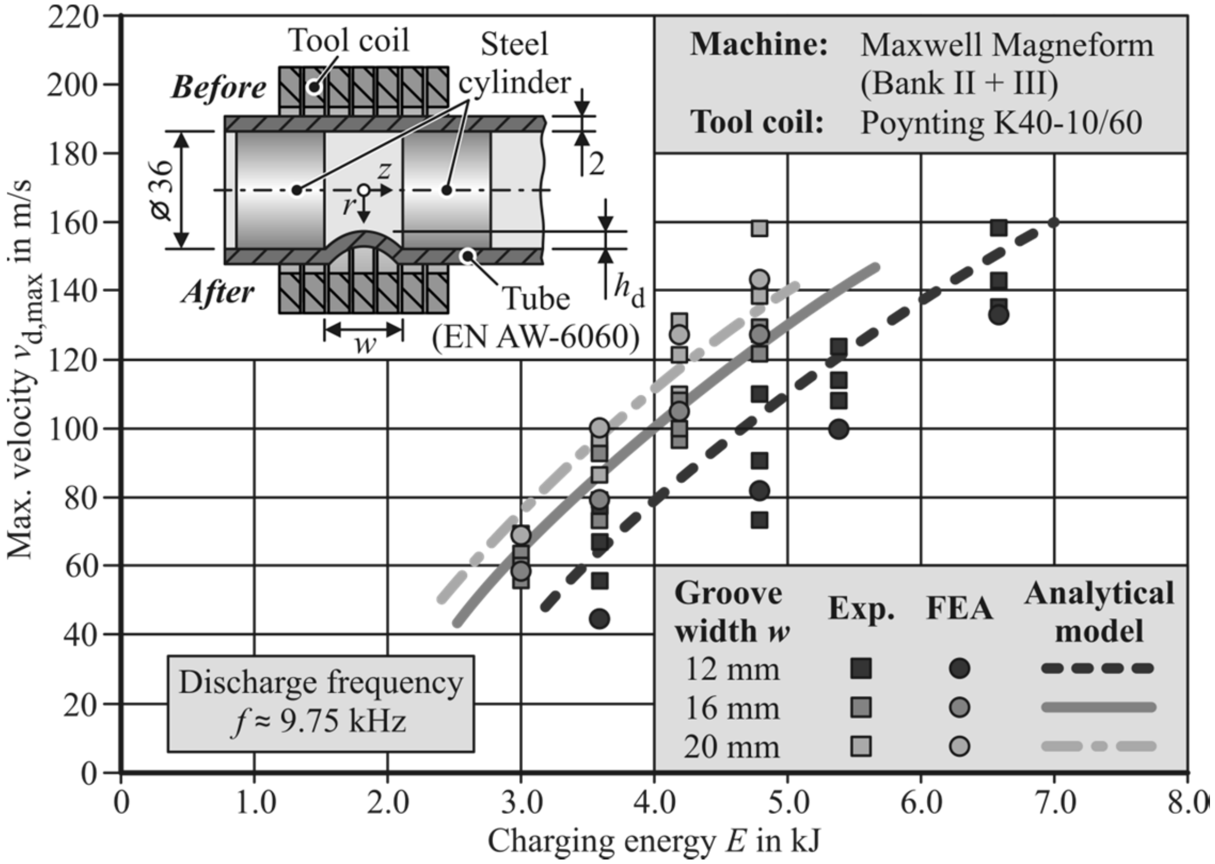

Figure 5-11: Comparison of the analytical, numerical, and experimental maximum workpiece velocity v_{max}

To identify the influence of the discharge frequency on the forming result, experiments with two capacitor bank configurations additional to the basic combination of bank II and III are performed (see **Section 4.1**). The experimental and analytical results are shown in **Figure 5-12**. Upon closer examination it can be seen that some of the applied charging energy values are not equal to the target values of the parameter variation in **Table 4-4**. For example, the lowest energies in **Figure 5-12a** are 4 % below the desired level of 3 kJ. These small deviations result from the type of the charging energy adjustment of the used Maxwell Magneform machine. At this system, the desired energy level is selected by a potentiometer with a scale of integer percentage values with respect to the maximum energy of the selected capacitor configuration. Therefore, an accurate adjustment of the desired level is not always possible.

The experimental results in **Figure 5-12** display an increased deformation with an increase in discharge frequency. For example, the different values of *f* lead to an average deviation in radial deformation Δh_d of about 0.43 mm for a groove width of 12 mm and an applied charging energy of 4.8 kJ. The observed increase in the process efficiency due to an increase of the discharge frequency can be attributed to an increased magnetic pressure amplitude $p_{\mathrm{m,max}}$.

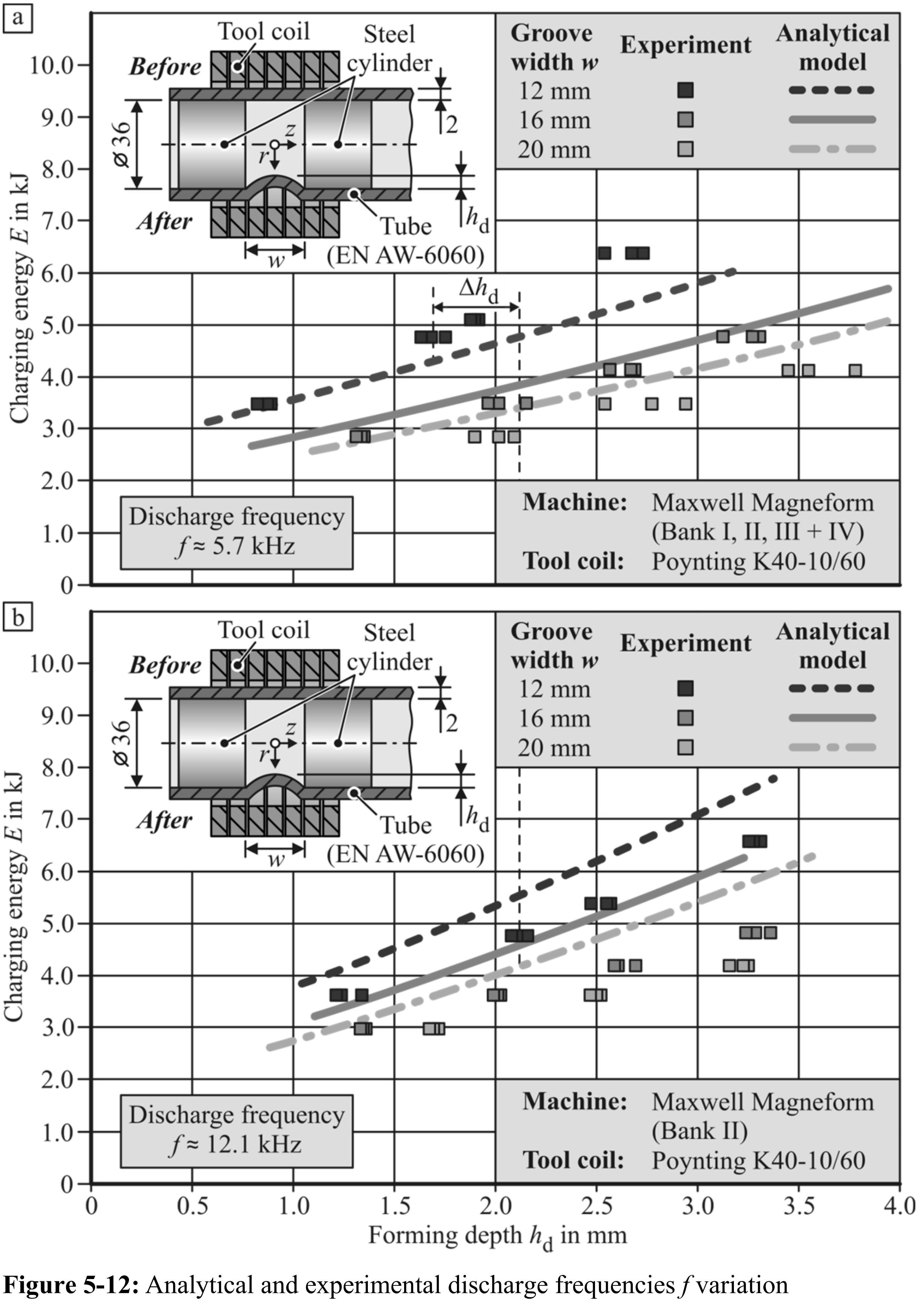

Figure 5-12: Analytical and experimental discharge frequencies *f* variation

Since higher frequencies lead to lower skin depths, the system inductance L_{res} is decreased as well (see Equations (2.5), (2.6), (5.20), and (5.21)). By combining Equation (5.30) and (2.2), it can be seen that a lower value of L_{res} leads to an increased current I_{max} for a constant charging energy.

$$I_{max} = \sqrt{\frac{2 \cdot E}{L_{res,d}}} \cdot e^{-\delta_d t_{max}} \tag{5.31}$$

Hence, the achieved magnetic pressure is also larger. Due to inertia effects, a more rapid rise of the acting pressure leads to a reduction of the workpiece deformation before the pressure maximum. Beerwald (2005) states that the system inductance decreases with a reduction of the gap a_{air} between coil and workpiece. Thereby, the pressure amplitude is increased further and a larger final deformation is achieved with shorter pressure rise times.

The approximated values for the lower discharge frequency (see **Figure 5-12a**) agree well with the energy levels of the experiments. The mean absolute percentage error between the selected charging energy values and the predicted ones is about 10 %. The maximum deviation is approximately 17 %. At the high discharge frequency (see **Figure 5-12b**), the model overestimates the experimentally determined values by a mean absolute percentage error of about 22 %. The maximal deviation between analytical prediction and experiments is 31 % in this case. This can be attributed to the replacement of the outer radius of the tube in the inductance determination by the mean outer radius $R_{\mathrm{T,d}}$ of the tube during deformation. This value, which can be calculated by Equation (5.22), is introduced based on the assumption that the deformation ends within the first half-wave of the pressure pulse. In case of the high frequency, the analytical calculations show that, especially for the larger deformations, the workpiece movement stops after the first half-wave. This observation can be explained by the fact that the deformation does not end if the magnetic pressure drops below the collapse pressure, but only when the inertia forces drop below this value. Since the final deflection is reached after $t = T/2$, the mean displacement during the first half-wave and the resulting system inductance are overestimated. This leads to the deviation between the calculated and experimentally applied charging energy values. Due to the fact that the analytical approach overestimates the necessary levels of E with increasing discharge frequencies, the filling of the grooves is ensured by the calculated values. Therefore, the model is still suitable for a process design, despite the quantitative deviations.

For the validation of the analytical joining parameter prediction regarding the tube material characteristics, experiments with three different aluminum alloys with varying yield stresses are performed. In addition to the EN AW-6060 tubes, workpieces manufactured of EN AW-1050A and EN AW-2007 are used. The comparison between the analytical model and the experiments regarding the influence of the material characteristics on the necessary charging energy is shown in **Figure 5-13**.

As expected, an increased yield stress requires a higher energy level to achieve the desired deformation in the center of the groove. The mean absolute percentage error for EN AW-2007 is about 11 % and for the alloy EN AW-1050A, this value is approximately 35 %. However, a significantly increasing deviation between calculated charging energy and the experimental value of E can be observed with an increase of the deformation for the alloys EN AW-2007 and EN AW-1050A. This observation can be attributed to the neglection of strain hardening and strain rate dependency in the analytical approximation. While the maximum deviation between model and experiment is about 18 % for EN AW-2007, EN AW-1050A shows a divergence of up to 40 %. It is assumed that the larger differences of EN AW-1050A result from the increased strain rate sensitivity of this alloy compared to the other two materials. Almost no increasing deviation between the predicted energies and the ones selected for the experiments with an increase of the deformation is observed for the alloy EN AW-6060. This finding can be explained by the fact that this material shows a relatively low effect of strain (see **Figure 4-4**) and strain rate (see **Figure 4-5**) on the material behavior.

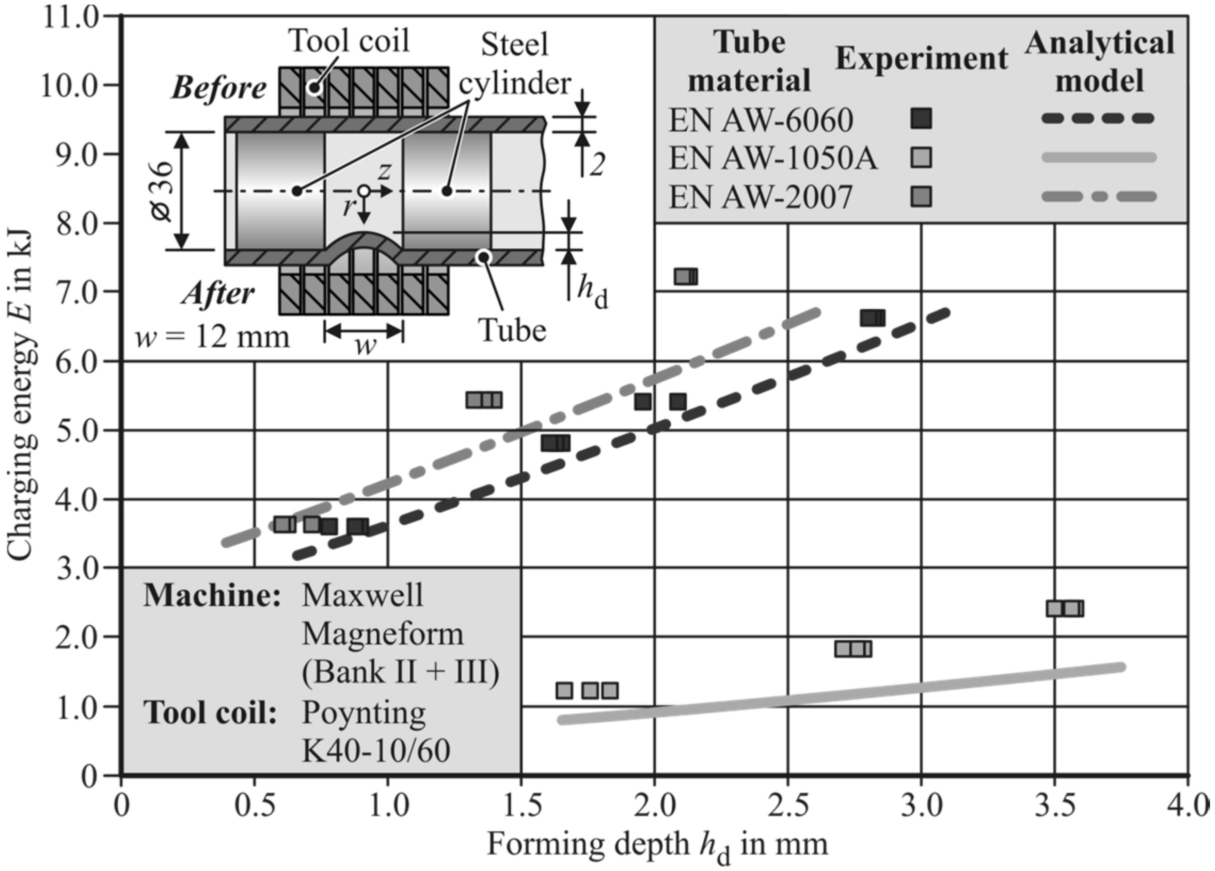

Figure 5-13: Comparison of experimentally and analytically determined charging energies for different materials (w = 12 mm)

Because the analytical model does not consider the increase in flow stress due to strain hardening and strain rate sensitivity, an additional experimental parameter determination (see **Section 4.1.1**) is suggested for materials sensitive to these effects. This investigation can be very limited since the analytical joining parameter prediction supplies a starting point for the tests which is already close to the exact energy level.

Table 5-4: Calculated skin depths for materials with different conductivities

Material	EN AW-1050	EN AW-2007	EN AW-6060
Electrical conductivity κ (MS/m)	35	20	31
Calculated skin depth δ_s (mm)	0.87	1.16	0.91

Besides different yield stresses, the applied materials have also dissimilar electrical conductivities. **Table 5-4** shows the values of the resulting skin depth δ_s, which are calculated by Equation (2.3). It can be seen that the determined values are significantly smaller than the wall thickness of the tube. Therefore, the assumption that the magnetic field is completely shielded from the inside of the tube is applicable (see **Section 5.1.2**).

5.3 Summary and conclusion

In this chapter, an analytical approximation of the joining parameters is introduced. It allows the prediction of the charging energy necessary to fill a specific groove geometry. Besides the joining zone characteristics, the model considers the major workpiece, tool, and machine properties.

By a combined analytical and experimental approach, significant process and workpiece parameters are identified and their influence on the joining operation is analyzed. In particular, it is found that the dimensions of the groove and the yield stress of the outer joining partner influence the energy level required for the joining task. In addition, the electrical characteristics of the EMF system and the resulting discharge frequency have a significant effect on the groove filling.

The experimental investigations of this chapter are also used for the verification of the analytical joining parameter prediction. For all experiments together, a mean absolute percentage error between the calculated charging energies and the experimentally applied ones of about 17 % is found. The largest deviations of up to 40 % are observed for the largest deformations. This finding can be attributed to the neglection of strain hardening and a strain rate sensitive material behavior in the analytical model. Furthermore, it is found that at high discharge frequencies, the joining parameter approximation overestimates the charging energies selected for the experiments. This divergence results from the assumption of the model that the forming process is completed within the first half-wave of the pressure pulse and the fact that the time t_f, at which the deformation ends, moves towards and beyond $T/2$ with increasing frequencies.

Despite the deviations between analytical model and experiments found in some cases, the presented approach is still a useful tool for the design of the joining process and the necessary EMF equipment. By applying the model in combination with the experimental methodology introduced in **Section 4.1.1**, the process parameters can be determined with a high accuracy. Due to the analytical approximation of the parameter range prior to the experiments, the number of tests can also be reduced significantly. Thereby, complex finite element simulations or extensive experimental studies can be avoided. This leads to a less expensive and time-consuming design process. Compared to numerical investigations and experiments, the approach also allows an isolated observation of the influence of selected EMF system properties on the forming result. Hence, it offers a valuable tool for an optimization of the electromagnetic forming equipment with respect to a specific joining task.

6 Influences on the achievable joint strength

The influence of several basic joining zone and process parameters on the achievable connection strength is still unclear. Examples of such parameters are the groove shape and the forming direction. Therefore, the objective of this chapter is the development of a fundamental understanding of the load transfer. To generate such knowledge about the effect of general parameters on the joint quality, an analytical connection strength prediction is developed here. The developed model shall also supply a simple joint design methodology. Additionally, the influence of the joining zone and process characteristics on the transferable loads is experimentally investigated. The conducted experiments also serve as verification of the introduced joint strength calculation.

Subsequent to the analysis regarding the influence of basic joining zone and process parameters on the connection strength, it is analyzed how a mass reduction in the joining zone and the resulting change of the radial strength of the components affects the crimping process and the transferable load. For these experimental investigations, the inner diameters of hollow mandrels are varied.

6.1 Analytical joint strength determination

The analytical model developed in this chapter shall allow an accurate determination of the achievable connection strength with respect to the properties of the joining partners, and namely the joining zone characteristics. Furthermore, it shall give a fundamental understanding of the stress state in the joining zone under quasi-static loading and how it affects the resulting connection strength. To compare the effect of the forming direction on the connection strength, a model for compressed and one for expanded joints are developed. Both analytical predictions are based on the same assumptions.

In contrast to the analytical approach developed by Golovashchenko (2001), the model introduced in this section shall provide a quantitative prediction of the elastic connection strength for groove geometries with different shapes. As described in **Section 4.2.4**, the axial force F_{ax}, at which the first relative movement between the joining partners occurs, is chosen as the failure criterion of the joints under tensional loads (Weddeling et al., 2011b). At this yield force $F_{\mathrm{y,J}}$, the connection starts to become plastic and the joint fails. Since only the elastic deformation of the joining partners is considered by this analytical methodology, strain hardening and wall thickness changes are neglected for the tube. The mandrel is assumed to be rigid. The yield force is defined as the axial stress $\sigma_{\mathrm{ax,D}}$ times the cross-sectional area A_{T} of the tube at point D in **Figure 6-1** (Weddeling et al., 2014a).

$$F_{y,J} = \sigma_{\mathrm{ax,D}} \cdot A_{T,D} \tag{6.1}$$

To determine $\sigma_{ax,D}$, a stress analysis approach for an axisymmetric cylindrical shell is performed. Storoschew and Popow (1968) give the following differential equation to describe the stress state in such shells:

$$r\frac{d\sigma_{\phi}}{dr} + \sigma_{\phi} - \sigma_{\theta} = 0 \tag{6.2}$$

Due to the assumption of thin-walled workpieces, plane stress is assumed in this approach. Hence, only the circumferential stress σ_θ and the meridional stress σ_ϕ are considered here. Furthermore, Equation (6.2) contains the tube radius r, which varies with the axial position (see **Figure 6-1**). It is assumed that the tensional loading of the connections leads to an upward bending of the tube (see **Figure 6-1**). Thereby, the contact surface of the joining partners is limited to the sections at the groove edges and the resulting frictional forces also act only at this interface between the workpieces.

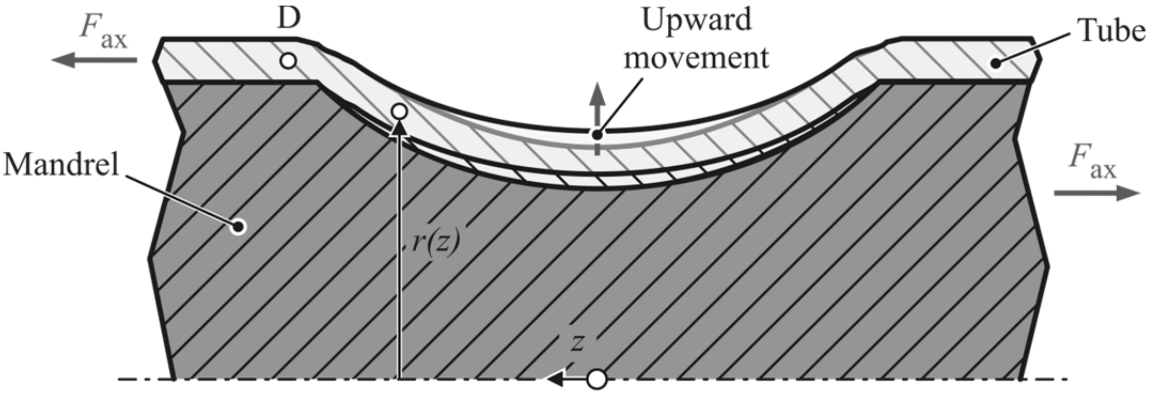

Figure 6-1: Assumed upward bending in the groove center during pull-out

Because this section is typically small compared to the whole deformation zone, it can be assumed that the influence of friction on the joint strength is small as well. For such cases, Storoschew and Popow (1968) propose the application of the Euler-Eytelwein equation for belt friction. Since the authors state that this approach for the approximation of the frictional influence on meridional stresses and the resulting connection strength entails only a minor error, it is applied here.

6.1.1 Compressed connections

In terms of compressed connections, three different basic groove shapes are considered. These shapes are circular, triangular, and rectangular. It is assumed that the connection strength results primarily from the expansion of the tube during pull out. Hence, only half of the tube geometry in pulling direction is considered for the following calculations (see **Figure 6-2a**).

The stress state in this tube segment is assumed to be tension in circumferential and meridional directions, with σ_θ bigger than σ_ϕ. With respect to Tresca, this stress state leads to the yield criterion below.

$$\sigma_\theta = \sigma_{y,T} \tag{6.3}$$

With this yield criterion, the circumferential stress can be eliminated in Equation (6.2).

$$r\frac{d\sigma_\phi}{dr} + \sigma_\phi - \sigma_{y,T} = 0 \tag{6.4}$$

Integration of this differential equation supplies:

$$\sigma_\phi = \sigma_{y,T} + \frac{K}{r} \tag{6.5}$$

The variable K is the constant of integration in this solution. By solving this equation for the deformed zone with respect to the corresponding boundary conditions, the value of the meridional stress $\sigma_{\phi,\mathrm{D}}$ at point D in **Figure 6-2a** is calculated. This value equals the axial stress $\sigma_{\mathrm{ax,D}}$ in Equation (6.1).

Circular grooves

The geometrical parameters of a circular groove are displayed in **Figure 6-2a**. The shape of the groove is described by the width w and the depth h (see **Figure 6-2b**). The forming zone is divided in three sections.

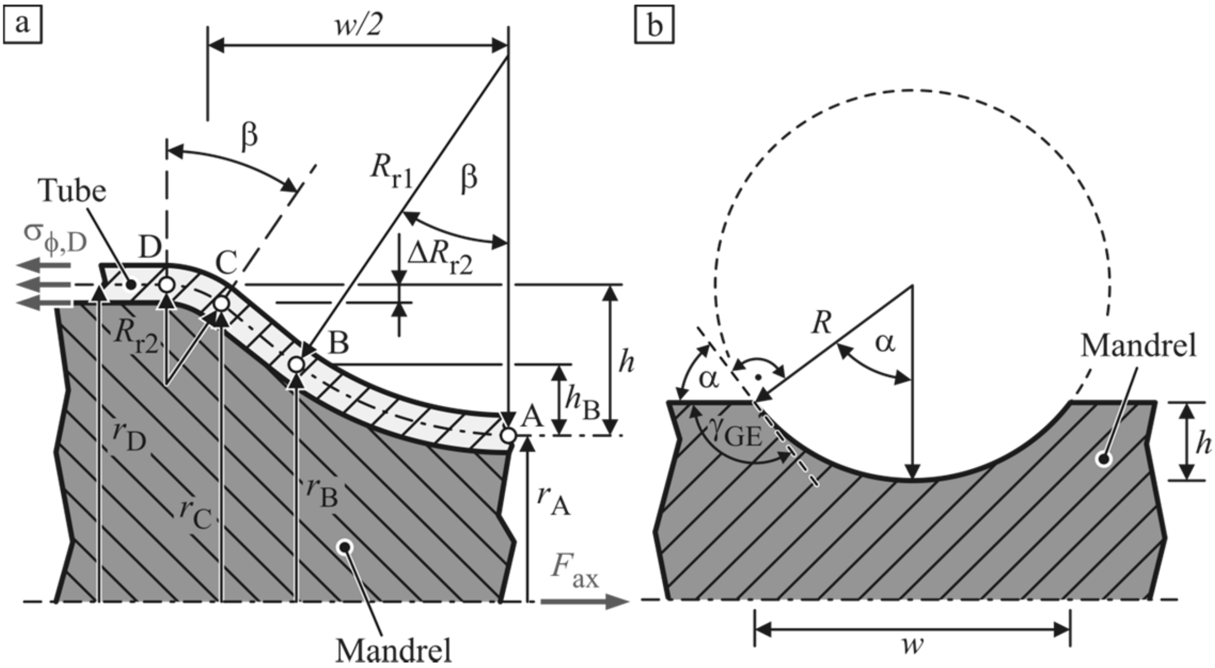

Figure 6-2: a) Crimped joint with circular groove b) groove geometry parameters

For the segment A-B it is assumed that the tube wall follows the bottom of the groove shape. The principle radius R_{r2} of the curvature in section C-D results from free bending of the tube wall at the groove edge during the joining operation (Golovashchenko, 2001). Its value can be determined based on the stress state at the edge of the form-fit element during generation of the joint and the tube properties. The straight section B-C is located between the two curved segments. It results from the groove geometry and the principle radius at the groove edge. To determine the meridional stress $\sigma_{\phi,\mathrm{D}}$, Equation (6.5) is solved successively for each of these sections.

Due to the assumption that the joint strength results primarily from the expansion of the tube during pull out, it is assumed that the meridional stress $\sigma_{\phi,\mathrm{A}}$ at point A with $r = r_\mathrm{A}$ equals zero.

$$0 = \sigma_{y,T} + \frac{K_A}{r_A} \tag{6.6}$$

This leads to the following expression for the constant of integration K_A at location A:

$$K_A = -\sigma_{y,T} \cdot r_A \tag{6.7}$$

Hence, the solution of Equation (6.5) for the segment A-B is found as:

$$\sigma_{\phi,\mathrm{A-B}} = \sigma_{y,T} - \sigma_{y,T}\frac{r_A}{r} \tag{6.8}$$

The meridional stress $\sigma_{\phi,\mathrm{B}}$ in point B with $r = r_\mathrm{B}$ is chosen as boundary condition for the solution of Equation (6.5) for the section B-C and the determination of the constant of integration K_B. At point B, $\sigma_{\phi,\mathrm{B}}$ equals the meridional stress caused by the radial expansion described by Equation (6.8) plus an additional term $\Delta\sigma_{\phi,\mathrm{B}}$ (Storoschew and Popow, 1968). This term is provoked by bending due to a change in curvature.

$$\sigma_{\phi,\mathrm{B}} = \sigma_{\phi,\mathrm{A-B}}(r_B) + \Delta\sigma_{\phi,\mathrm{B}} \tag{6.9}$$

Popow (1977) introduced the following equation for the determination of the meridional stress increase caused by the change of the principle radius of the curvature from R_ra to R_rb:

$$\Delta\sigma_{\phi} = \frac{1}{4} \cdot \sigma_{y,T} \cdot s \cdot \left(\frac{1}{R_{rb}} - \frac{1}{R_{ra}}\right) \tag{6.10}$$

A detailed derivation of this equation is presented in **Appendix B**. As shown in **Figure 6-2a**, the curvature radius changes from R_r1 to ∞ at the transition from section A-B to B-C. By introducing these two radii in Equation (6.10), the stress increase $\Delta\sigma_{\phi,\mathrm{B}}$ at point B can be predicted.

$$\Delta\sigma_{\phi,\mathrm{B}} = \frac{\sigma_{y,T} \cdot s}{4 \cdot R_{r1}} \tag{6.11}$$

With respect to **Figure 6-2b,** the principle radius R_r1 can be determined with the equation for the radius of a circular segment with respect to groove depth and width:

$$R_{r1} = R - \frac{s}{2} = \frac{4h^2 + w^2}{8h} - \frac{s}{2} \tag{6.12}$$

Introducing the term of the additional stress $\Delta\sigma_{\phi,\mathrm{B}}$ and Equation (6.8) into Equation (6.9) leads to the following function of the meridional stress in point B:

$$\sigma_{\phi,\mathrm{B}} = \sigma_{y,T} - \sigma_{y,T}\frac{r_A}{r_B} + \sigma_{y,T}\frac{s}{4\cdot R_{r1}} \tag{6.13}$$

With the value of $\sigma_{\phi,\mathrm{B}}$ as boundary condition in Equation (6.5), the constant of integration K_B is determined.

$$K_B = \left(\sigma_{y,T}\frac{s}{4\cdot R_{r1}} - \sigma_{y,T}\frac{r_A}{r_B}\right) r_B \tag{6.14}$$

With this constant, the function of the meridional stress for the section B-C with respect to the tube radius r takes the following form:

$$\sigma_{\phi,\mathrm{B-C}} = \sigma_{y,T} + \left(\sigma_{y,T}\frac{s}{4\cdot R_{r1}} - \sigma_{y,T}\frac{r_A}{r_B}\right)\frac{r_B}{r} \tag{6.15}$$

For the determination of the stress $\sigma_{\phi,\mathrm{C\text{-}D}}$, a similar boundary condition as in Equation (6.9) is applied to solve Equation (6.5) for the segment C-D of the deformation zone.

$$\sigma_{\phi,\mathrm{C}} = \sigma_{\phi,\mathrm{B-C}}(r_C) + \Delta\sigma_{\phi,\mathrm{C}} \tag{6.16}$$

Here, the term $\Delta\sigma_{\phi,\mathrm{C}}$ results from the curvature change in Point C. At this point, the principle radius changes from ∞ to $R_{\mathrm{r}2}$. Therefore, the strain increase $\Delta\sigma_{\phi,\mathrm{C}}$ can be calculated by

$$\Delta\sigma_{\phi,\mathrm{C}} = \frac{\sigma_{y,T}\cdot s}{4\cdot R_{r2}}. \tag{6.17}$$

As mentioned above, the principle radius $R_{\mathrm{r}2}$ results from free bending at the edge of the form-fit element during joining. For the calculation of $R_{\mathrm{r}2}$ with respect to the stress state of the joining operation at the groove edge, Golovashchenko (2001) gives the following expression:

$$R_{r2} = \frac{s}{4(1-\cos\beta)} \tag{6.18}$$

This equation for the determination of the principle groove edge radius is only valid in case of joining by compression. The detailed derivation of Equation (6.18) by Storoschew and Popow (1968) is presented in **Appendix C**.

To determine the wrap-around angle β at the groove edge, the groove angle α (see **Figure 6-2b)** has to be calculated first. For a circular segment, it can be determined by the equation below:

$$\alpha = 2\arctan\left(\frac{2\cdot h}{w}\right) \tag{6.19}$$

As shown in **Figure 6-2b**, the value of α conforms to the angle between the surface of the mandrel and the tangent at the edge of the groove. But since the tube is fully clamped at the edges of the groove (see **Section 5.1.1**), it can be assumed that its shape in axial direction is similar to the shape of a fully clamped beam (Grote and Antonsson, 2009). Therefore, the wrap-around angle at the edge has to be smaller than α. For this analytical connection strength prediction, it is assumed that β equals half the angle α.

$$\beta = \frac{1}{2}\alpha \tag{6.20}$$

After the derivation of the meridional stress increase $\Delta\sigma_{\phi,\mathrm{C}}$ and the geometrical characteristics of the curvature of the tube, the Equations (6.15) and (6.17) are introduced in Equation (6.16) to determine the meridional stress $\sigma_{\phi,\mathrm{C}}$ at point C.

$$\sigma_{\phi,\mathrm{C}} = \sigma_{y,T} + \left(k_{f,T}\frac{s}{4\cdot R_{r1}} - \sigma_{y,T}\frac{r_A}{r_B}\right)\frac{r_B}{r_C} + \sigma_{y,T}\frac{s}{4\cdot R_{r2}} \tag{6.21}$$

As for section B-C, the value of $\sigma_{\phi,\mathrm{C}}$ is used as boundary condition in Equation (6.5) to determine the constant of integration K_{C}.

$$K_C = \left[\left(\sigma_{y,T}\frac{s}{4\cdot R_{r1}} - \sigma_{y,T}\frac{r_A}{r_B}\right)\frac{r_B}{r_C} + \sigma_{y,T}\frac{s}{4\cdot R_{r2}}\right]r_C \tag{6.22}$$

With this constant, the function of the meridional stress for the section C-D with respect to the tube radius r takes the following form:

$$\sigma_{\phi,\mathrm{C-D}} = \sigma_{y,T} + \left[\left(\sigma_{y,T}\frac{s}{4\cdot R_{r1}} - \sigma_{y,T}\frac{r_A}{r_B}\right)\frac{r_B}{r_C} + \sigma_{y,T}\frac{s}{4\cdot R_{r2}}\right]\frac{r_C}{r} \tag{6.23}$$

Similar to the evaluation of the meridional stresses at the points B and C, a stress increase $\Delta\sigma_{\phi,\mathrm{D}}$ resulting from the curvature change in point D has to be considered for the determination of $\sigma_{\phi,\mathrm{D}}$.

$$\sigma_{\phi,\mathrm{D}} = \sigma_{\phi,\mathrm{C-D}}(r_D) + \Delta\sigma_{\phi,\mathrm{D}} \tag{6.24}$$

As **Figure 6-2a** shows, the curvature radius changes from R_{r2} to ∞ at point D. This leads to the following expression for the meridional stress increase at this position:

$$\Delta\sigma_{\phi,\mathrm{D}} = \frac{\sigma_{y,T}\cdot s}{4\cdot R_{r2}} \tag{6.25}$$

As mentioned above, it is assumed that tube and mandrel are only in contact at the edge of the groove. Therefore, the Euler-Eytelwein approach for belt friction is used to determine the influence of the frictional force at the groove edge (section C-D) on the joint strength. It considers the friction by an exponential function.

$$\sigma_{\phi,\mathrm{D}} = \left[\sigma_{\phi,\mathrm{C-D}}(r_D) + \Delta\sigma_{\phi,\mathrm{D}}\right]\cdot e^{\mu_f\beta} \tag{6.26}$$

For a further simplification, only the first two terms of the corresponding power series are applied to the model.

$$e^{\mu_f\beta} \approx \left(1 + \mu_f\beta\right) \tag{6.27}$$

The coefficient of friction is selected in accordance with the VDI[3] standard "Systematic calculation of high duty bolted joints" (N.N., 2003). This standard gives a value of 0.21 for μ_f for the combination of aluminum to aluminum, which is treated in this work. By combining Equations (6.23), (6.25), (6.26), and (6.27), the equation for the determination of the meridional stress $\sigma_{\phi,\mathrm{D}}$ at point D is found.

$$\sigma_{\phi,\mathrm{D}} = \sigma_{y,T}\left[1+\left[\left(\frac{s}{4\cdot R_{r1}}-\frac{r_A}{r_B}\right)\frac{r_B}{r_C}+\frac{s}{4\cdot R_{r2}}\right]\frac{r_C}{r_D}+\frac{s}{4\cdot R_{r2}}\right]\left(1+\mu_f\beta\right) \tag{6.28}$$

The expression of the specific joint strength $\bar{\sigma}_{\mathrm{y,J}}$ of form-fit connections with circular grooves is achieved by dividing this expression by the yield stress of the tube $\sigma_{\mathrm{y,T}}$.

$$\bar{\sigma}_{\mathrm{y,J}} = \left[1+\left[\left(\frac{s}{4\cdot R_{r1}}-\frac{r_A}{r_B}\right)\frac{r_B}{r_C}+\frac{s}{4\cdot R_{r2}}\right]\frac{r_C}{r_D}+\frac{s}{4\cdot R_{r2}}\right]\left(1+\mu_f\beta\right) \tag{6.29}$$

By comparing the approximated values of $\bar{\sigma}_{\mathrm{y,J}}$ for given tube and joining zone parameters to the experimentally measured connection strengths, this analytical prediction of the transferable loads is verified (see **Section 6.2.1**). To solve Equation (6.29) for given groove and tube dimensions, the tube radii at the observation points A, B, C, and D have to be determined. All values are calculated with respect to the geometrical conditions of the joined section shown in **Figure 6-2a**.

$$r_A = \frac{D_M}{2} - h + \frac{s}{2} \tag{6.30}$$

$$r_B = r_A + h_B = r_A + R_{r1}(1-\cos\beta) \tag{6.31}$$

$$r_C = r_D - \Delta R_{r2} = r_D - R_{r2}(1-\cos\beta) = r_D - \frac{s}{4} \tag{6.32}$$

$$r_D = \frac{D_T}{2} - \frac{s}{2} \tag{6.33}$$

Triangular grooves

The analytical joint strength prediction for connections with triangular grooves is very similar to the one for circular grooves. For the prediction of the elastic connection strength with respect to a specific groove geometry, Equation (6.29) is applied. **Figure 6-3a** gives an overview of all geometrical parameters of the triangular geometry. The principle radius R_{r2} at the groove edge and the tube radii r_C and r_D are determined in a similar way as for the circular grooves. Only the tube radii r_A and r_B and the principle radius R_{r1} are different for this joining zone shape. For the triangular joining zone shape, it is anticipated that the tube wall follows the groove geometry in section B-C instead of A-B. Hence, the wrap-around angle β is equal to the gradient angle of the shoulder of the groove.

---

[3] Association of German Engineers (Verein deutscher Ingenieure)

$$\beta = \arctan\left(\frac{2 \cdot h}{w}\right) \tag{6.34}$$

As for the round grooves, the segment at the bottom of the groove is assumed to be circular. Due to this shape, the tube wall does not touch the groove base at point A.

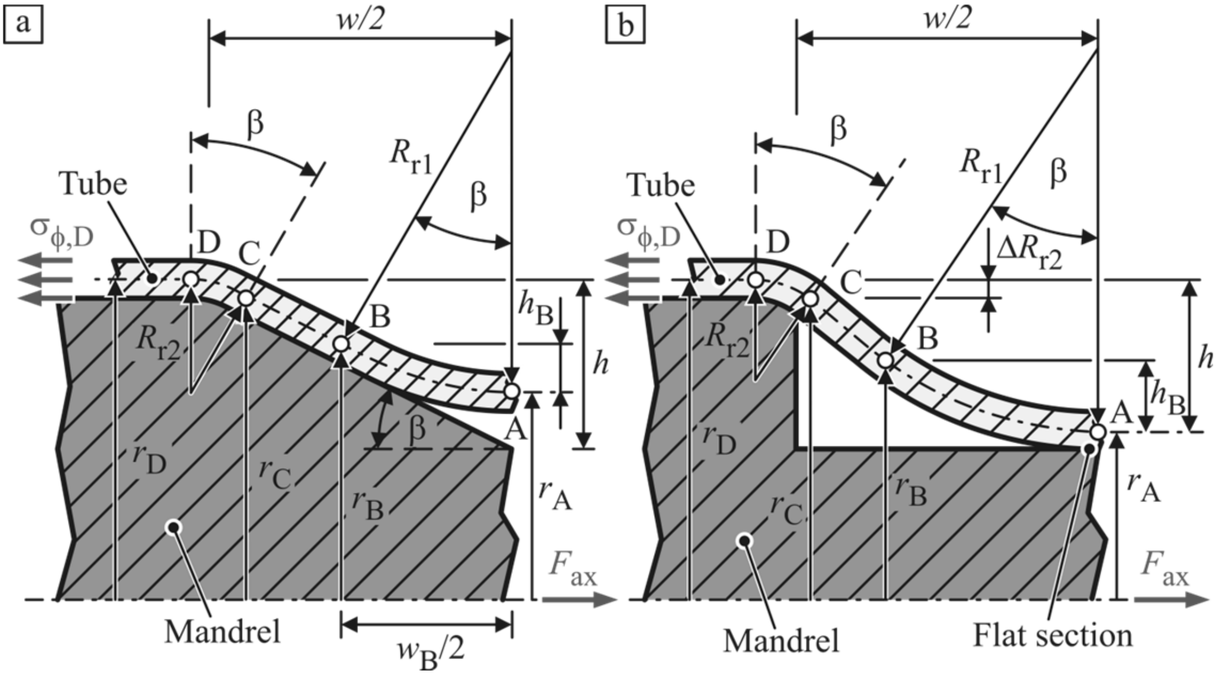
a
w/2
β
Tube
$\sigma_{\phi,D}$
D
C
R_{r1}
β
B
h_B
h
R_{r2}
β
A
r_D
r_C
r_B
r_A
F_{ax}
Mandrel
$w_B/2$
b
w/2
β
Tube
$\sigma_{\phi,D}$
D
R_{r1}
β
ΔR_{r2}
C
B
R_{r2}
h
A
h_B
r_D
r_C
r_B
r_A
F_{ax}
Mandrel
Flat section

Figure 6-3: a) Triangular and b) rectangular connection joined by compression

In addition, it is assumed that point B is located at the center of the shoulder of the groove. This leads to the following expression for the calculation of its axial position.

$$w_B = \frac{w}{2} \tag{6.35}$$

Based on this assumption about the location of B, the radius of the tube at this point can also be determined.

$$r_B = r_D - \frac{h}{2} \tag{6.36}$$

The radius R_{r1} of section A-B can be calculated based on a circular segment as follows:

$$R_{r1} = \frac{w_B}{2 \cdot \sin\beta} = \frac{w}{4 \cdot \sin\beta} \tag{6.37}$$

With the values of the angle β as well as the two radii r_B and R_{r1}, the radius of the tube at position A can be determined.

$$r_A = r_B - h_B = r_B - R_{r1}(1 - \cos\beta) \tag{6.38}$$

Rectangular grooves

For the determination of the transferable loads for connections with a rectangular groove shape, all geometrical parameters illustrated in **Figure 6-3b** are calculated in the same way as for the basic model with circular grooves. The only difference between the two approaches is the boundary condition for the meridional stress in point A. Due to the flat base of the rectangular grooves, the deformation of the tube wall at the bottom of the groove is not as geometrically restrained as for the circular joining zones. Therefore, it is assumed that the principle radius R_{r1} is not continuous for this geometry at the center of the groove. Instead, it is supposed that a very small section of the tube wall at position A is parallel to the groove base. This straight section implies that the curvature of the workpiece changes from ∞ to R_{r1} at this location. Hence, the following boundary condition is applied to the solution of Equation (6.5) for section A-B.

$$\sigma_{\phi,\mathrm{A}} = \Delta\sigma_{\phi,\mathrm{A}} = \frac{\sigma_{y,T} \cdot s}{4 \cdot R_{r1}} \tag{6.39}$$

The further determination of the meridional stresses in the other sections of the deformation zone follows the same pattern as the joint strength prediction of the circular groove shape. In this way, the following solution for the meridional stress in point D with respect to a rectangular groove shape is obtained:

$$\sigma_{\phi,\mathrm{D}} = \sigma_{y,T}\left[1 + \left[\left[\left(\frac{s}{4R_{r1}} - 1\right)\frac{r_A}{r_B} + \frac{s}{4R_{r1}}\right]\frac{r_B}{r_C} + \frac{s}{4R_{r2}}\right]\frac{r_C}{r_D} + \frac{s}{4R_{r2}}\right]\left(1 + \mu_f\beta\right) \tag{6.40}$$

By dividing the stress $\sigma_{\phi,\mathrm{D}}$ by the yield stress of the tube $\sigma_{\mathrm{y,T}}$, the specific joint strength $\bar{\sigma}_{\mathrm{y,J}}$ of connections with this groove shape is found.

$$\bar{\sigma}_{\mathrm{y,J}} = \left[1 + \left[\left[\left(\frac{s}{4R_{r1}} - 1\right)\frac{r_A}{r_B} + \frac{s}{4R_{r1}}\right]\frac{r_B}{r_C} + \frac{s}{4R_{r2}}\right]\frac{r_C}{r_D} + \frac{s}{4R_{r2}}\right]\left(1 + \mu_f\beta\right) \tag{6.41}$$

6.1.2 Expanded connections

To evaluate the influence of the forming direction on the transferable loads, an analytical joint strength prediction for expanded connections with circular grooves is developed as well. The geometrical parameters of this joint type are displayed in **Figure 6-4a**. The basic assumptions of the model for expanded form-fit connections are the same as for the compressed joints and the approach is also based on the Equation (6.2) (Weddeling et al., 2014a).

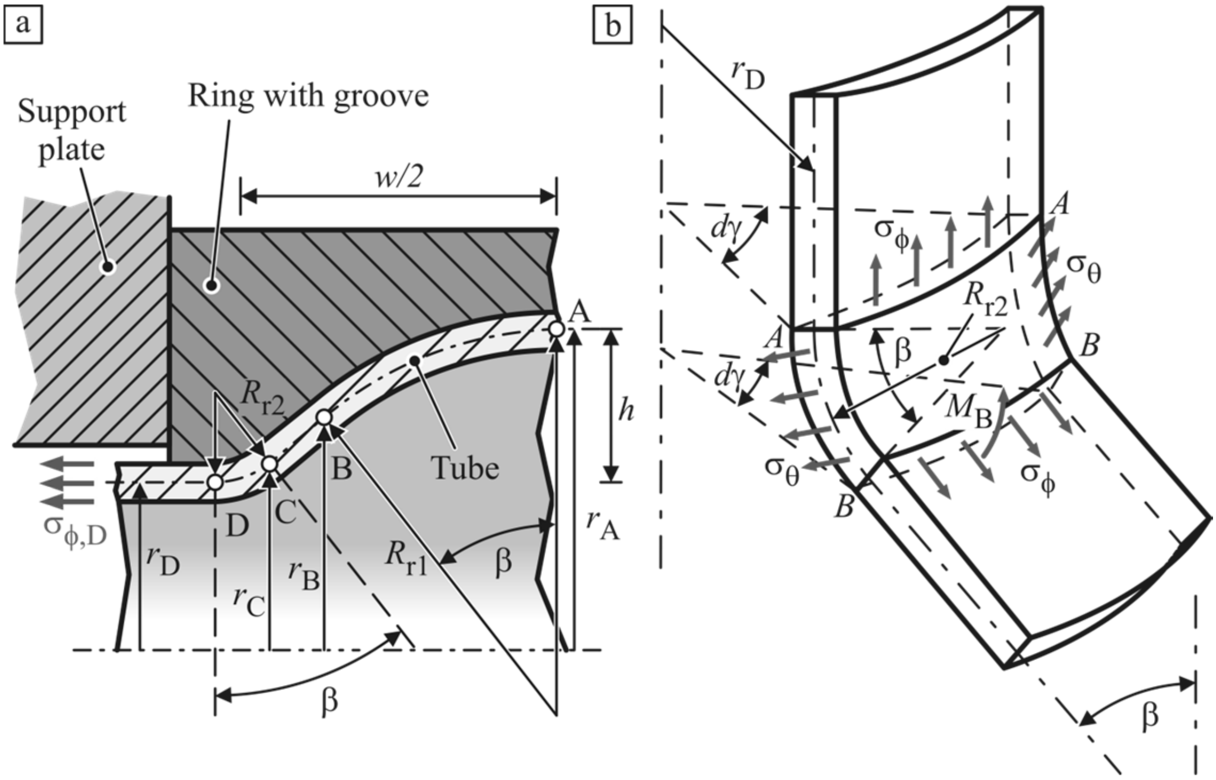
a
Support plate
Ring with groove
w/2
A
h
R_{r2}
B
Tube
$\sigma_{\phi,D}$
D
C
r_D
r_C
r_B
R_{r1}
β
r_A
β
b
r_D
dγ
σ_ϕ
A
σ_θ
R_{r2}
A
β
B
dγ
M_B
σ_θ
σ_ϕ
B
β

Figure 6-4: a) Expanded joint with circular groove b) assumptions for the determination of the groove edge radius R_{r2} for expanded connection

The major difference between these two analytical approaches is the stress state during pull-out. For the expanded connections, the stress state in the tube is assumed to be compression in the circumferential direction and tension in the meridional direction. With respect to Tresca, the yield criterion below is achieved for this stress state.

$$\sigma_{y,T} = \sigma_\phi - \sigma_\theta \tag{6.42}$$

Combining this yield criterion with Equation (6.2) leads to the following differential equation for the stress state of expanded connections during pull-out:

$$r\frac{d\sigma_\phi}{dr} + \sigma_{y,T} = 0 \tag{6.43}$$

The general solution of this differential equation is gained by integration.

$$\sigma_\phi = -\sigma_{y,T} \cdot \ln(r) + K \tag{6.44}$$

By applying the same pattern and the same boundary conditions as for the joint strength prediction of compressed connections with circular groove shapes, the expression for meridional stress $\sigma_{\phi,D}$ in point D is found (Weddeling et al., 2014a).

$$\sigma_{\phi,D} = \sigma_{y,T}\left[\ln\left(\frac{r_A}{r_D}\right) + \frac{s}{4 \cdot R_{r1}} + \frac{s}{2 \cdot R_{r2}}\right](1 + \mu_f \beta) \tag{6.45}$$

As for the previously introduced analytical models, the specific joint strength $\bar{\sigma}_{\mathrm{y,J}}$ is obtained by eliminating the yield strength $\sigma_{\mathrm{y,T}}$ of the tube.

$$\bar{\sigma}_{\mathrm{y,J}} = \left[\ln\left(\frac{r_A}{r_D}\right) + \frac{s}{4 \cdot R_{r1}} + \frac{s}{2 \cdot R_{r2}}\right]\left(1 + \mu_f \beta\right) \tag{6.46}$$

Expanded connections do not only feature a different stress state than compressed joints during pull-out, but the reversed forming direction also leads to a different stress condition during the manufacturing process. Hence, Equation (6.18) cannot be applied to calculate the bending radius R_{r2} at the groove edge of expanded joints. Based on a shell element curved in two planes and exposed to pure bending, the equation for the determination of this principle radius for connections joined by expansion is developed in the following (Storoschew and Popow, 1968). For such an element, which is shown in **Figure 6-4b**, the following equilibrium of moments can be established (see **Appendix C**):

$$-\sigma_\phi r_D s\, d\gamma (1 - \cos\beta) R_{r2} + \sigma_\theta s\, {R_{r2}}^2 \sin\beta\, d\gamma \frac{\sin\beta}{2} = \frac{1}{4}\sigma_{y,T} s^2\, r_D d\gamma \tag{6.47}$$

By canceling and rearranging, this equilibrium is transformed into the quadratic equation below:

$$\sigma_\theta \sin^2\beta\, {R_{r2}}^2 - 2\sigma_\phi r_D (1 - \cos\beta)\, R_{r2} - \frac{1}{2}\sigma_{y,T} s\, r_D = 0 \tag{6.48}$$

The value of R_{r2} is achieved by using the positive square root of the quadratic formula.

$$R_{r2} = \frac{\sqrt{4\sigma_\phi^2 r_D^2 (1 - \cos\beta)^2 + 2\sigma_\theta \sigma_{y,T} s\, r_D \sin^2\beta} + 2\sigma_\phi r_D (1 - \cos\beta)}{2\sigma_\theta \sin^2\beta} \tag{6.49}$$

For tube expansion, the circumferential stress σ_θ and the meridional stress σ_ϕ are tension. Marciniak and Duncan (2002) state that a circumferential stress twice as large as the meridional one can be assumed in this case. By applying this stress state to Equation (6.49), the following term for the determination of R_{r2} is achieved:

$$R_{r2} = \frac{\sqrt{r_D^2 (1 - \cos\beta)^2 + 2 \cdot s\, r_D \sin^2\beta} + r_D (1 - \cos\beta)}{2\sin^2\beta} \tag{6.50}$$

Due to the logarithmic solution of the differential Equation (6.43), only the tube radii at point A and D, r_{A} and r_{D}, have to be determined for this analytical strength prediction of expanded connections. Both radii can be calculated based on the outer diameter D_{T} of the tube, the groove depth h, and the wall thickness of the workpiece.

$$r_A = \frac{D_T}{2} + h - \frac{s}{2} \tag{6.51}$$

$$r_D = \frac{D_T}{2} - \frac{s}{2} \tag{6.52}$$

6.2 General parameters affecting the joint strength

The effect of basic joining zone characteristics and process parameters on the achievable joint strength is studied experimentally in this section and the analytical joint strength prediction is verified. As in **Section 5.2**, the accuracy of the model is illustrated by the mean absolute percentage error (see Equation (5.29)), which gives the average deviation between calculated and measured results. Although the influence on the transferable load of some parameters investigated here is already known from literature, these parameters have to be included in this study to validate the analytical model. Such parameters are the edge radius R_{GE} (Park et al. 2005a), the groove width w, and its depth h (Bühler and von Finckenstein, 1968b). The general joining zone and process parameters, which influences on the connection strength are still unknown, are the shape of the groove (Weddeling et al., 2011b), the forming direction, the joining gap a_0, and the applied charging energy E.

The energy levels required for the joining operations are determined with respect to the groove geometry by the experimental methodology described in **Section 4.1.1** and the resulting design chart in **Figure 4-2**. To ensure filling of the groove independent of any possible inhomogeneous workpiece properties, the predicted energies are increased by 10 %. Due to its higher accuracy, the experimental process parameter prediction is chosen instead of the analytical determination described in **Section 5.1**.

To analyze only the influence of form-fit related joining zone and process characteristics on the transferable loads, an additional interference fit needs to be avoided (see **Section 4.2**). Therefore, solid mandrels are used for these investigations on the general joining zone characteristics and both joining partners are manufactured of the same material. To confirm that no additional interference fit is generated during joining and that only the influence of the form-fit related parameters on the joint strength are analyzed, additional experiments with mandrels not featuring a groove are performed. After forming, all tubes can be pulled off the mandrels by hand. Hence, these preliminary tests confirmed that, even for the highest applied forming pressures, no interference fit is produced and that an additional joint strength proportion due to this load transfer mechanism is avoided (Weddeling et al., 2011). Subsequent to the joining operation, the connection quality is determined by pull-out tests (see **Section 4.2.4**). **Figure 6-5** shows the two typical modes of final failure that are observed for solid mandrels in this study (Weddeling et al., 2011b). For the shallow and wide grooves, the tubes are typically pulled off the mandrel. Compared to this, the deeper and narrower groove geometries show tearing of the tube, which is the weaker joining partner. In general, these connections show higher specific joint strengths and higher ultimate strengths than the ones failing without fracture. In addition, their final separation occurs very rapidly with less elongation before failure.

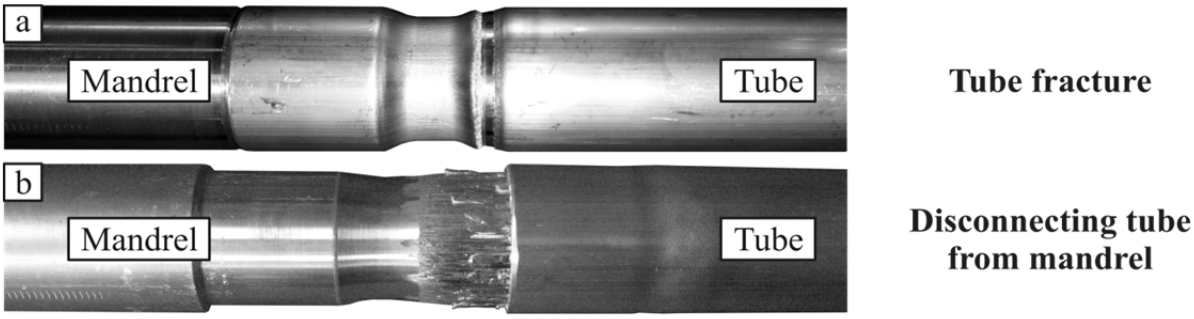

Figure 6-5: Modes of final failure at tensile tests: a) tearing b) pull off

6.2.1 Influence of the groove geometry on the joint strength

The influence of the basic groove geometry, which includes the shape and the dimensions of the form-fit element, on the achievable joint strength is analyzed in this section. In **Figure 6-6**, the experimentally determined specific strength $\bar{\sigma}_{y,J}$ of the connections with circular grooves is plotted versus groove depth *h* for each of the three groove width *w*. It can be seen that the joint strength increases with an increasing depth and a decreasing width. This finding corresponds to the results of Bühler and von Finckenstein (1968b). A very small deviation of the measured values is observed for all parameter variations. This implies a high repeatability and process stability.

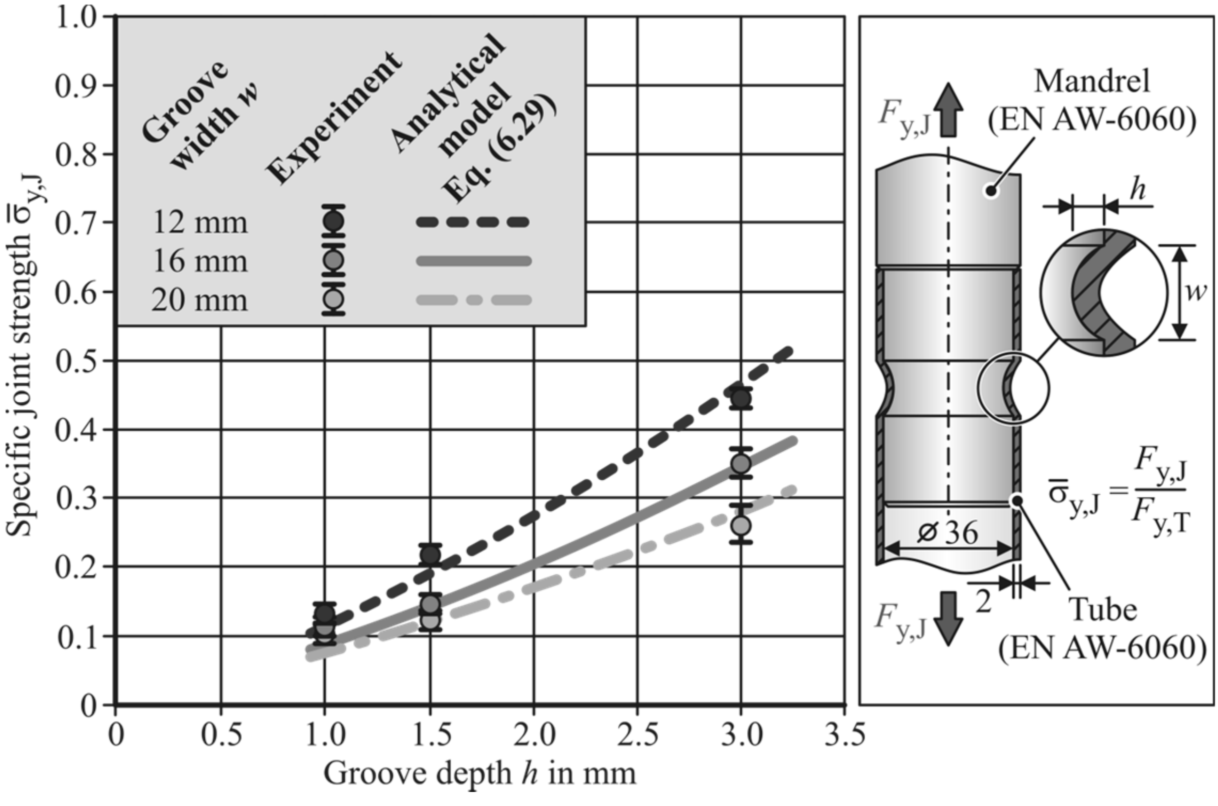

Figure 6-6: Comparison of analytically predicted and experimentally determined specific joint strength for circular grooves joined by compression

Figure 6-6 also shows that the joint strengths predicted analytically by Equation (6.29) are within good agreement with the measured values of the experiments. The mean absolute percentage error between the experimentally determined strengths and the calculated ones is 13 %. This denotes a good suitability of the model for the joining zone design process. Based on the analytical model, the joint strength rise with increasing groove depths can be attributed to a higher degree of radial expansion necessary to pull the tube off the mandrel. This increased deformation results from the decrease of the tube radius r_A at the groove center with increasing depth. The principle radii R_{r1} and R_{r2} are smaller at deeper grooves as well. This leads to a rise of the additional meridional stress in the tube wall, which results from increased bending due to a curvature change. The effect of the joint strength increase with a decreasing groove width can be attributed to a higher gradient of deformation in the forming zone. The analytical model considers this effect also by a decrease of R_{r1} and R_{r2}. Additionally, both geometrical groove parameters influence the wrap around angle β. With increasing depth and decreasing width, β rises as well. This leads to an increase of the frictional term in Equation (6.29) and, therefore, to a rise of the strength.

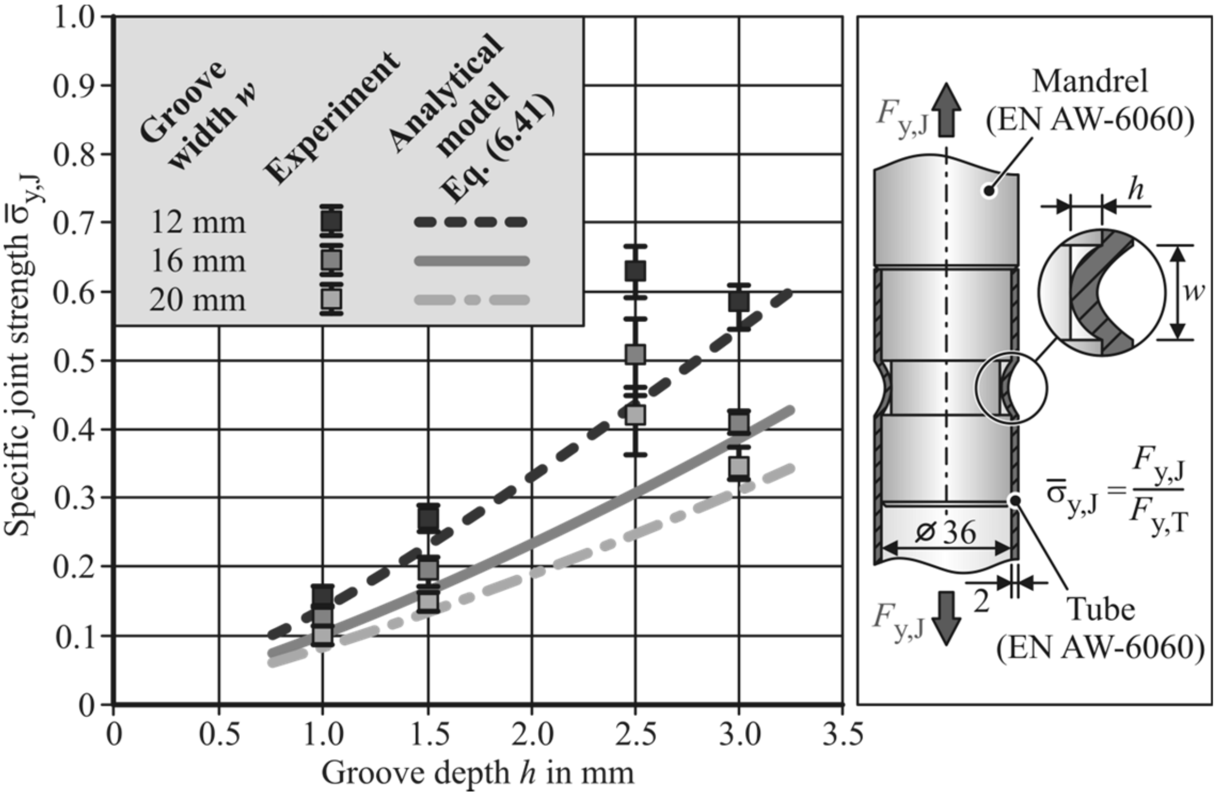

Figure 6-7: Comparison of analytically predicted and experimentally determined specific joint strength for rectangular grooves joined by compression

The results of the joining and pull-out experiments for connections with a rectangular groove shape are shown in **Figure 6-7**. It can be seen that the influence of groove depth and width on the joint strength is similar to those of circular grooves. But compared to the results of the circular groove geometry, the results of the rectangular grooves feature a maximum joint strength value. **Figure 6-8a** shows that this observation can be attributed to the tube being partially sheared at the groove edges. As **Figure 6-9** shows, the amount of shearing at this location increases with deeper grooves since higher magnetic pressures have to be applied to fill such geometries. This increase of shearing with increasing groove depth is found for all treated groove widths. The shearing causes an additional interlock at the edge of the form-fit element. Thereby, the groove edge angle γ_{GE} (see **Figure 6-2b**) is decreased locally. Due to the significantly reduced angle γ_{GE}, a larger deformation of the tube is necessary at this location so that the material can flow around the groove edge under loading. This leads to higher meridional stresses in the tube wall and the connection strength is increased. Up to the maximum, the extra interlock increases the joint strength. Eventually, the thinning of the tube due to shearing at this edge will weaken the connection more than the strength increase by the extra interlock. As a result, the overall joint strength decreases (Weddeling et al., 2011b). Although shearing can lead to a partial quasi-static joint strength increase, it shall be avoided since it could lead to the development of fatigue cracks.

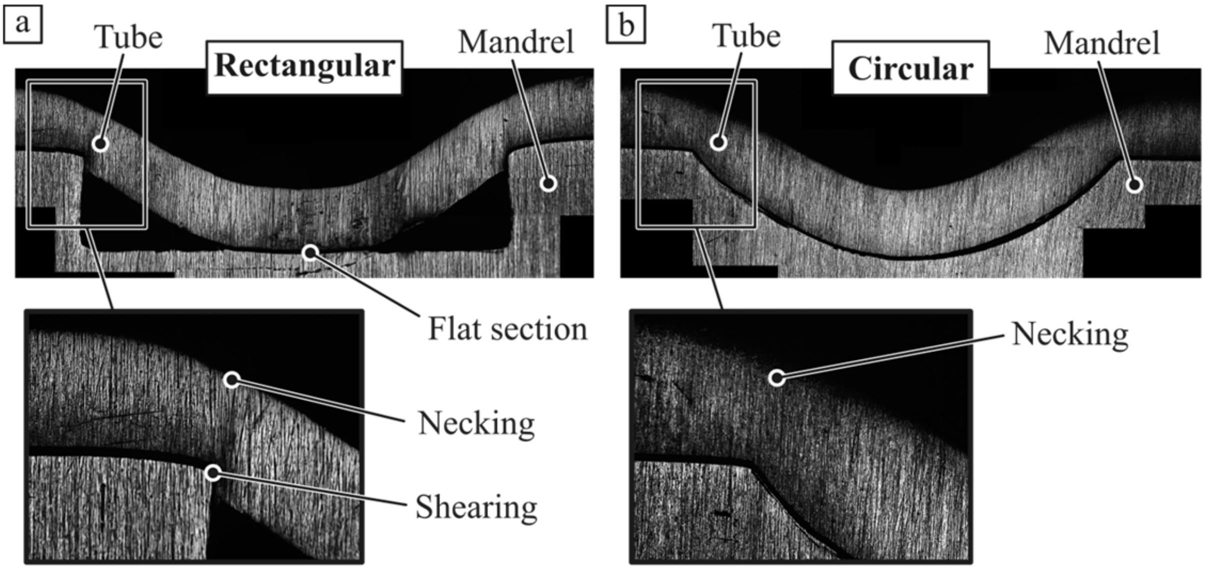

Material tube:	EN AW-6060	**Groove width *w*:**	12 mm
Material mandrel:	EN AW-6060	**Groove depth *h*:**	3 mm

Figure 6-8: Shearing and necking at the groove edge (Weddeling et al., 2011b) a) rectangular groove b) circular groove

A possibility to counteract shearing is the application of circular grooves. **Figure 6-8b** shows that this effect does not even occur at the deepest and narrowest groove of this shape. The figure only indicates necking at the groove edge for the circular grooves. This also leads to a reduction of the wall thickness of the tube. Therefore, it can be assumed that a maximum joint strength exists for circular grooves as well. But since the thinning of the tube wall is much smaller in this case, the joint strength maximum must be located at a much bigger groove depth.

Besides the experimentally determined joint strength, **Figure 6-7** also shows the values of $\bar{\sigma}_{\mathrm{y,J}}$ predicted analytically by Equation (6.41) for connections featuring rectangular grooves with respect to the dimensions of the form-fit element. The mean absolute percentage error of the model is about 19 %. The assumption that the shearing of the tube causes a local interlock at the edge, which leads to a joint strength increase, is also supported by the analytical approach. For the shallower grooves, the model is in good agreement with the experimental results since the amount of shearing is low at these depths (see **Figure 6-9a** and **b**). The maximal deviation between model and experiments is below 20 % for 1.0 mm and 1.5 mm deep form-fit elements. With increasing depth h, the divergence between analytically predicted joint strengths and experiments increases. For the 2.5 mm deep grooves, the deviation between model and the measured strengths is up to 41 %. This behavior can be attributed to the fact that the model does not consider shearing.

At the deepest grooves, model and experiments are also within good agreement. The deviation between calculated and measured strength is maximally 10 %. It can be assumed that the joint strength increase due to the additional interlock at the edge is opposed by a strength decrease due to a reduction of the tube wall thickness.

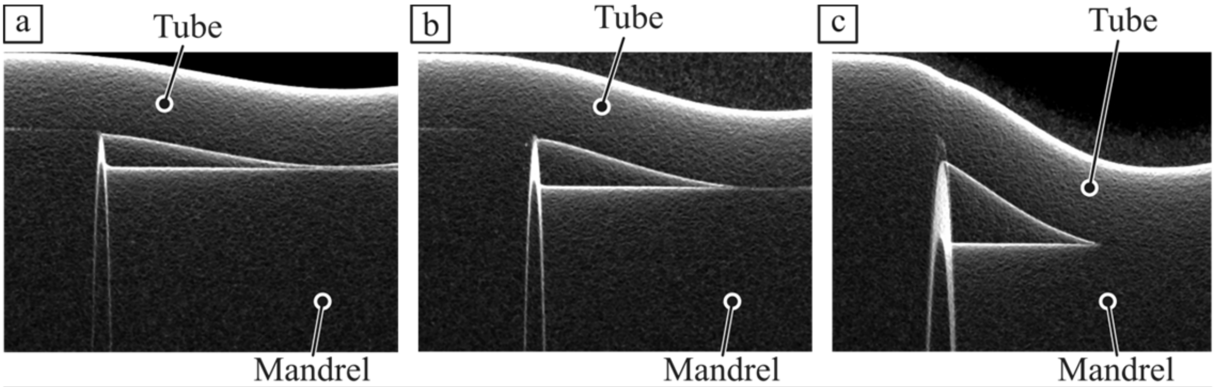

Material tube:	EN AW-6060	**Groove width *w*:**	12 mm
Material mandrel:	EN AW-6060	**Groove shape:**	rectangular

Figure 6-9: Increase of shearing with increasing groove depth a) $h_1 = 1.0$ mm b) $h_2 = 1.5$ mm c) $h_3 = 3.0$ mm

Even though the analytical model does not consider the effect of shearing on the transferable loads of joints featuring rectangular grooves, it is still a valuable tool for the design of the joining zone. Since it underestimates the specific strength, the model allows a conservative approximation of this value.

The last groove shape considered in this work is a triangular geometry, shown in **Figure 6-10a**. The relationship between achievable joint strength and groove depth for this shape is given by **Figure 6-11**. It can be seen that the influence of groove depth and width on the transferable load is very similar to that of circular grooves. The X-ray picture of the deepest and narrowest triangular groove in **Figure 6-10a** displays the absence of shearing at the groove edge. Therefore, a higher fatigue strength compared to rectangular grooves can be assumed for the triangular shaped form-fit elements. By comparing **Figure 6-10a** and **b**, it is observed that the triangular shape shows a lower amount of necking at the groove edge than the circular form-fit element. This can be attributed to the fact that the triangular groove is not completely filled at the center. For this reason, a tube formed into this shape is stretched less in the meridional direction than a profile formed into a circular form-fit element. Since the circumferential strain at the groove edge is about zero after the forming operation for both shapes and due to volume constancy, the triangular grooves show a reduced degree of deformation in wall thickness direction at the edge. This leads to decreased necking at this location for triangular grooves compared to circular ones.

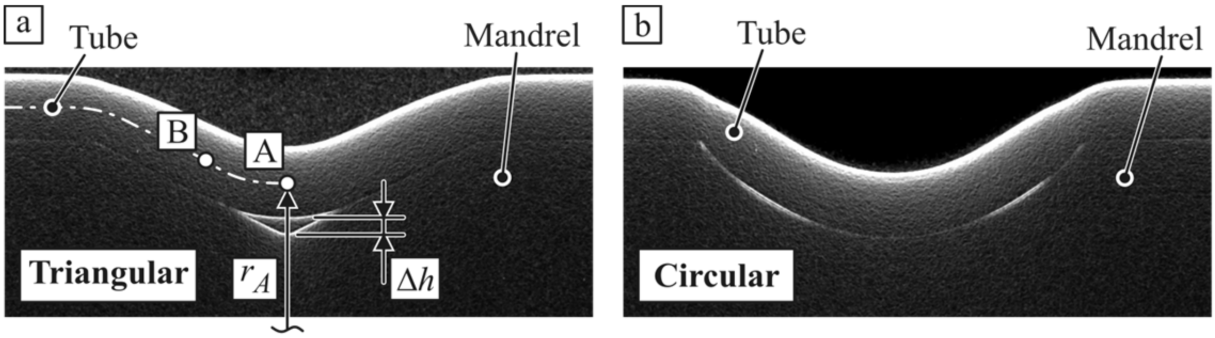

Material tube:	EN AW-6060	**Groove width *w*:**	12 mm
Material mandrel:	EN AW-6060	**Groove depth *h*:**	3 mm

Figure 6-10: X-ray pictures of a) triangular groove and b) circular groove

Figure 6-11 shows also the joint strengths analytically determined by Equation (6.29). The mean absolute percentage error between model and experimental values is about 24 %. To consider the incomplete filling of triangular form-fit elements in the analytical model, it is assumed that the tube wall does not follow the groove geometry in section A-B and that this workpiece segment ranges from the center of the groove to the center of the groove shoulder (see **Section 6.1.1**). For the verification of this assumption and the model in general, the calculated tube radii r_A at point A are compared to the experimental values for this radius, which are determined from the X-ray pictures of the different parameter variations (see **Figure 6-10a**). The results of this comparison are shown in **Table 6-1** and it can be seen that the calculated values are in good agreement with the experimental radii. Therefore, the geometrical assumptions for this groove shape are proven reasonable for the model.

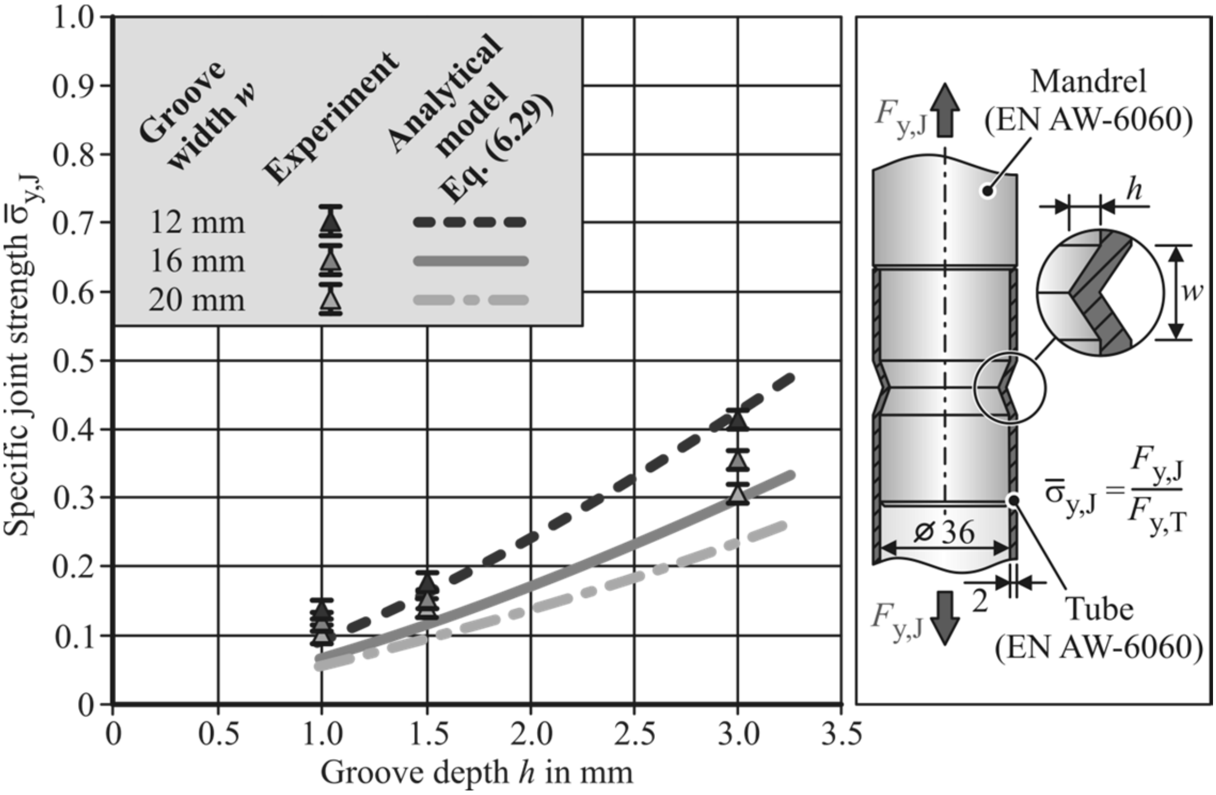

Figure 6-11: Comparison of analytically predicted and experimentally determined specific joint strength for triangular grooves joined by compression

Subsequent to the determination of the effect of the groove dimensions on the achievable joint strength for the three different groove shapes, these shapes are directly compared. **Figure 6-12** displays the influence of rectangular, circular, and triangular grooves with a width of 12 mm and various depths on the specific connection strength.

Table 6-1: Calculated and measured tube radius r_A for triangular grooves

Groove dimensions ***w* x *h*** (mm)	**Measured tube radius r_A** (mm)	**Calculated tube radius r_A** (mm)	**Difference** Δr_A (mm)	**Deviation** (%)
12 x 1.0	18.40	18.25	0.15	**0.79**
12 x 1.5	17.78	17.88	-0.10	**0.55**
12 x 3.0	16.55	16.79	-0.24	**1.44**
16 x 1.5	17.77	17.88	-0.10	**0.58**
16 x 3.0	16.45	16.77	-0.32	**1.96**
20 x 1.0	18.28	18.25	0.03	**0.14**
20 x 1.5	17.74	17.88	-0.14	**0.76**
20 x 3.0	16.45	16.77	-0.32	**1.94**

The diagram shows that the highest loads can be transferred by joints with a rectangular geometry and that the connections with triangular grooves always exhibit the lowest strengths. As mentioned above, the high strength of the rectangular geometries result partially from shearing at the edge of the groove. Although the analytical joint strength prediction does not consider this effect, it also gives the highest strength for the rectangular grooves. This is attributed to the assumption of an additional curvature change at point A and the resulting meridional stress increase at this point (see **Section 6.1.1)**. The flat section that causes the curvature change at the groove center can be seen in **Figure 6-8a**. In agreement with the analytical model, the lower strength of connections with triangular grooves compared to those with circular grooves can be attributed to the bigger tube radius r_A at point A. Therefore, the tube needs to be expanded less when pulling it off the mandrel.

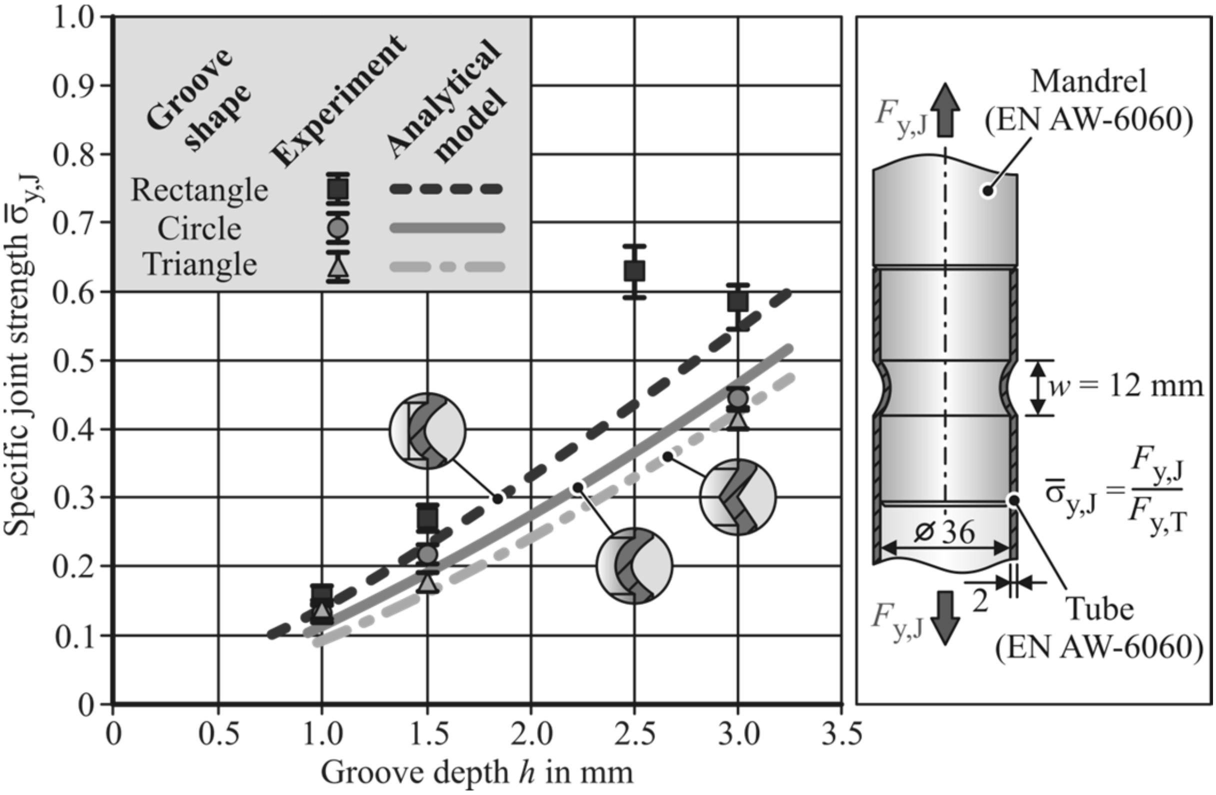

Figure 6-12: Analytical and experimental comparison of different groove shapes on the achievable specific joint strength

The third geometrical parameter being investigated for its influence on the joint strength is the groove edge radius R_{GE}. This parameter is particularly important with regard to shearing at the groove edge. Since this effect only occurs at the rectangular geometries, this groove type is applied for the investigation in the following. **Figure 6-13** shows the experimentally determined specific joint strengths with respect to the edge radius R_{GE} for selected combinations of width and depth. For this analysis, R_{GE} is varied between no radius and a maximum, which equals the groove depth. A variation of the edge radius for different depths and widths does not exhibit a significant effect on the achievable joint strength.

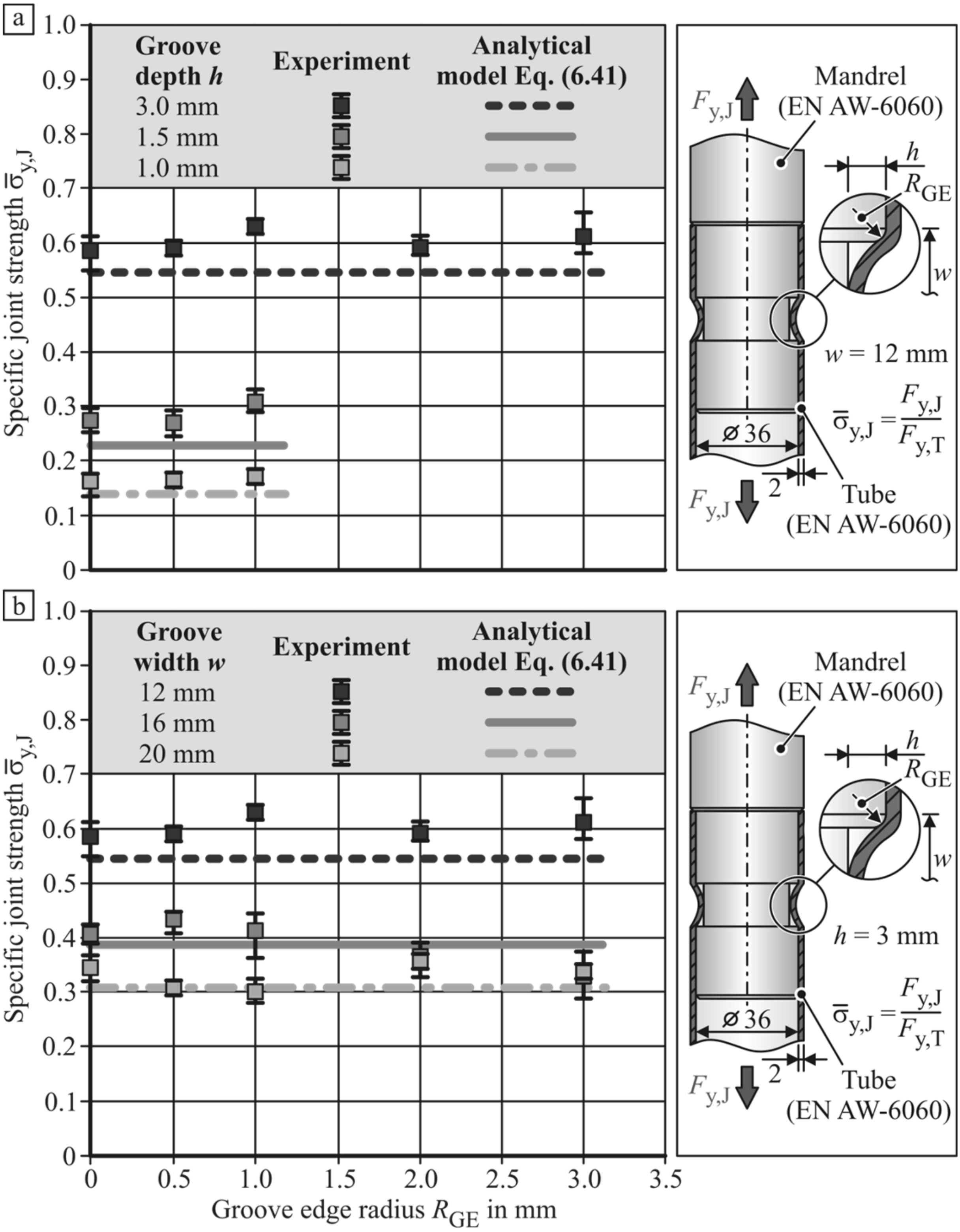

Figure 6-13: Specific joint strength over edge radius for different groove dimensions: a) groove depth variation b) groove width variation

This finding differs from the results of Park et al. (2005), who found an optimum of R_{GE} with respect to the joint strength (see **Section 2.5.3**). To explain the difference to the results of Park et al. (2005a), computer tomography pictures of the joining zone are made. **Figure 6-14** displays the effect of an increasing edge radius on the deformation of the tube in this area. It can clearly be seen that shearing at the groove edge decreases with an increasing radius R_{GE}. For increasing values of R_{GE}, it can be assumed that the decreasing additional interlock at the edge is opposed by a connection strength increase resulting from larger wall thicknesses. These contrary effects lead to the observed constant specific joint strength.

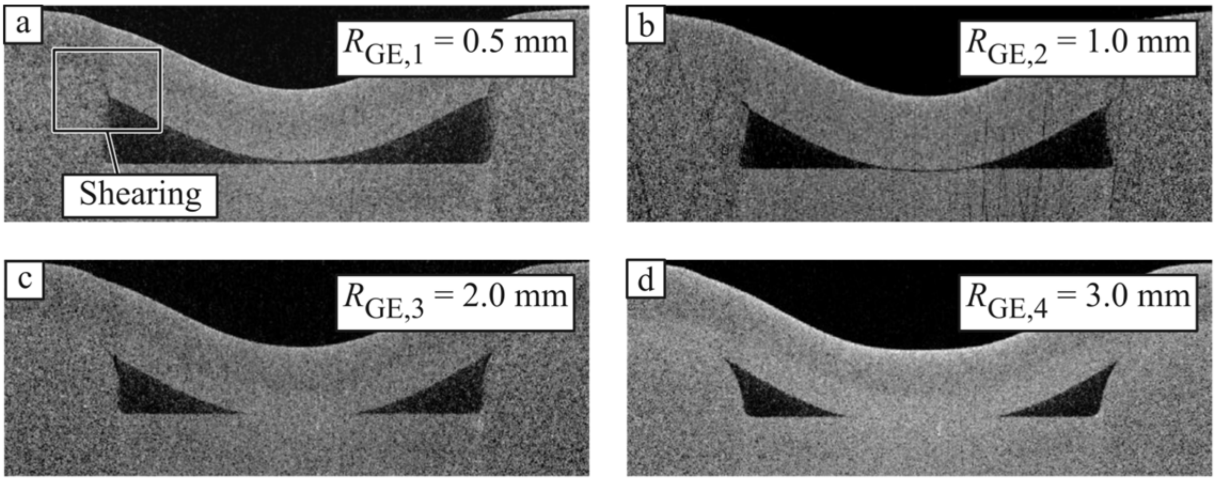
a
$R_{\mathrm{GE},1}$ = 0.5 mm
Shearing
b
$R_{\mathrm{GE},2}$ = 1.0 mm
c
$R_{\mathrm{GE},3}$ = 2.0 mm
d
$R_{\mathrm{GE},4}$ = 3.0 mm

Material tube:	EN AW-6060	**Groove geometry:**	12 x 3 mm
Material mandrel:	EN AW-6060	**Mandrel diameter D_{M}:**	36 mm

Figure 6-14: Groove edge radius variation

At edge radii of 2.0 mm and 3.0 mm in **Figure 6-14c** and **d,** shearing does not occur. The constancy of the joint strength in these cases can be explained with respect to the analytical model. The radius R_{r2} of the tube wall at the groove edge calculated by Equation (6.18) is bigger than the edge radius R_{GE} for all considered parameter variations. This implies that the tube wall does not fully abut on the groove edge radius (see **Figure 6-15a**). Therefore, the calculated values of R_{r2} are applied to the analytical strength prediction as tube radius at the groove edges instead of the machined values of R_{GE}. This leads to an elimination of the influence of R_{GE} on the analytically determined joint strengths for the connections treated in this work. The tomography pictures in **Figure 6-14c** and **d** also show that R_{r2} is larger than R_{GE}. So, it can be assumed that the achievable joint strength does not necessarily depend on the machined groove edge radius. It depends in fact on the radius of the tube wall at this location, which is influenced by the stress state at the groove edge during the joining process and perhaps by R_{GE}. The good agreement between the analytical and experimental results in **Figure 6-13** implies that this assumption is reasonable.

This assumption also allows the explanation of the divergent findings of Park et al. (2005a) regarding the influence of the edge radius. While, in this work, the magnetic pressure is adjusted with respect to the groove geometry, Park et al. (2005a) applied always the same pressure independently from width and depth. They also performed several pulses and adjusted the forming location during the manufacturing of one connection. Due to the application of this different joining procedure, Park et al. (2005a) achieve a larger contact area between tube wall and groove surface (see **Figure 6-15b**). This applies to the area of the groove edge as well. Hence, it can be assumed that, in their work, R_{r2} and R_{GE} are about equal (see **Figure 6-15c**). Since the tube radius at the groove edge equals the mandrel radius at this location, R_{GE} determines R_{r2} and thereby influences the joint strength in the research of Park et al. (2005a).

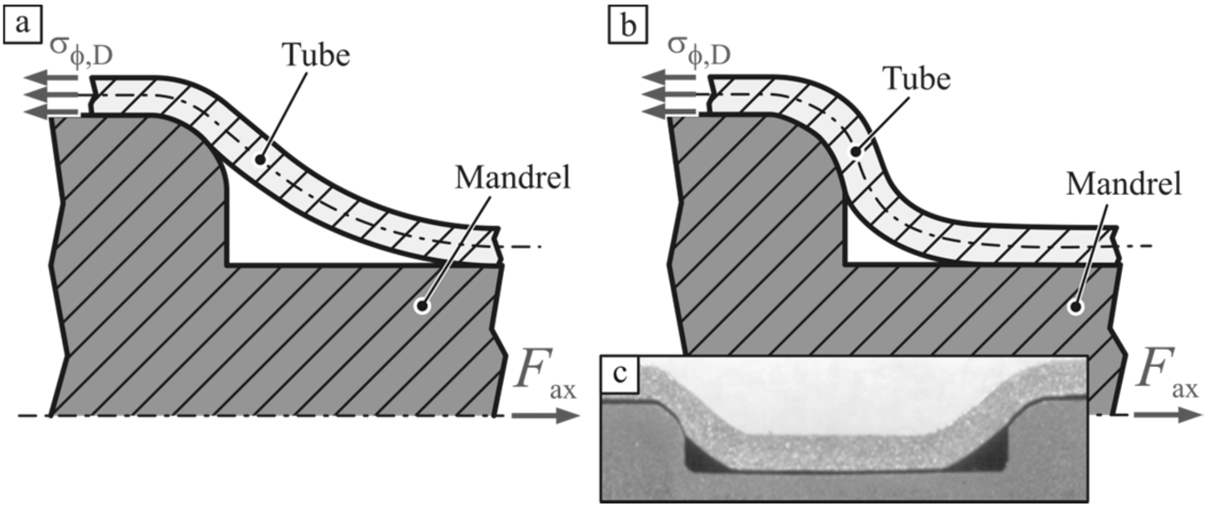

Figure 6-15: a) Principle radius R_{r2} of the tube wall bigger than edge radius R_{GE} b) radius R_{r2} equal to R_{GE} c) cross section of a connection joined by Park et al. (2005b)

Based on the results regarding the influence of the groove edge radius on the connection strength, it is suggested that the value of R_{GE} shall be as large as possible to avoid shearing of the tube. But the edge radius shall also not exceed the principle radius R_{r2} of the tube wall, which is established by the joining operation and can be determined by Equation (6.18) since this would reduce the connection strength.

The fact that the analytical results match the experimental ones in case of prevented shearing at the groove edge quite well also supports the assumption of an additional curvature change in point A for the rectangular geometries (see **Figure 6-3b**). As mentioned in **Section 6.1.1**, this change and the resulting meridional stress increase lead to the generally higher joint strengths of this groove geometry compared to the other two shapes.

6.2.2 Analytical comparison of the forming direction

In this section, the influence of the forming direction on the achievable strength of form-fit connections is examined. An analytical approach is chosen since it allows the comparison of the two connection types considering only workpiece and joining zone properties. Process-related effects on the achievable joint strength, like the strain rates of the joining operation and the resulting form filling characteristics, can be neglected. Therefore, the comparison is universally valid for all connections with the treated joining zone characteristics independent of the manufacturing process. The analytical prediction of the achievable joint strength for expanded connections with respect to different groove geometries is introduced in **Section 6.1.2**. Instead of electromagnetic expansion, joining by die-less hydroforming (DHF) is chosen to manufacture the connections for the experimental model verification. This process is selected since the mechanical strength of tool coils for electromagnetic expansion is quite low and they begin to deform plastically already after a few joining operations (Belyy et al., 1977). Hence, the reproducibility of the experiments is insufficient. Additionally, the coil lifetime is very short and it cannot be assured that the tool lasts the manufacturing of all necessary experiments. Compared to electromagnetic expansion, the tools used in joining by die-less hydroforming are much more reliable and have a longer lifetime. This results from the simpler design of the joining probes and the more favorable quasi-static mechanical loads acting on the tools. Since this work focuses on form-fit joining by electromagnetic crimping, the experimental verification of the model for DHF itself is not part of it. Hence, the experimental results from Gies et al. (2013) are used for the validation of the analytical approach developed in **Section 6.1.2**. For a better understanding, the procedure applied by the researchers is briefly reviewed in the following.

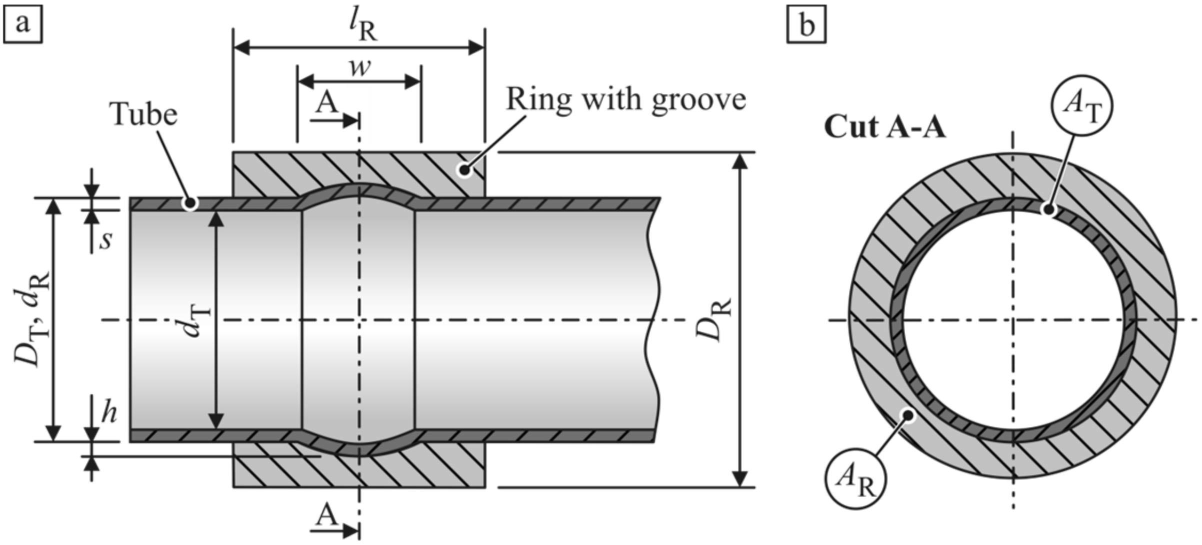

Figure 6-16: Specimen for joining by expansion (Gies et al., 2013)

Gies et al. (2013) use EN AW-6060 tubes with the same dimensions and the same material properties for their DHF investigations like the profiles applied for the joining by compression tests (see **Section 4.2.2**). But instead of mandrels, the authors use rings as outer joining partners. Both workpiece types illustrated in **Figure 6-16** are manufactured of the same aluminum alloy to minimize supplementary connection strength resulting from an additional interference fit.

For the expansion experiments, only grooves with a circular shape are used. While the groove widths are the same as for the investigations of electromagnetic form-fit joining, 1.0, 1.5, and 2.0 mm deep circumferential grooves are used in the DHF experiments. The depth of 2.0 mm is chosen because in pre-tests, the tubes fail during joining by expansion of the narrowest of the 3.0 mm deep grooves. This behavior can be attributed to the reduction in wall thickness during the forming process. To ensure a similar resistance against plastic deformation of the outer partner with varying depth h, the ratio of the cross-sectional area of the rings at the groove base $A_{\mathrm{R,GB}}$ corresponds to 1.5 times the cross-sectional area A_{T} of the tubes for all specimens (Gies et al., 2013).

$$Q_A = \frac{A_{R,GB}}{A_T} = \frac{\left(\frac{D_R}{2}\right)^2 - \left(\frac{d_R}{2} + h\right)^2}{\left(\frac{D_T}{2}\right)^2 - \left(\frac{d_T}{2}\right)^2} = 1.5 \tag{6.53}$$

A detailed overview of the dimensions of the rings is given in **Table 6-2**.It can be seen that the outer diameter D_{R} of the rings increases with increasing groove depth.

Table 6-2: Dimensions of the rings (Gies et al., 2013)

Material	**Groove depth *h*** (mm)	**Outer diameter D_{R}** (mm)	**Inner diameter d_{R}** (mm)	**Diameter ratio Q_{R}**	**Cross-sectional area ratio $Q_{\mathrm{A,R}}$**
EN AW-6060	1	47.1	40	0.85	1.5
EN AW-6060	1.5	48.0	40	0.83	1.5
EN AW-6060	2	48.9	40	0.82	1.5

Gies et al. (2013) use a hydraulic pressure unit manufactured by Maximator GmbH to supply the forming pressure p_{i} to the joining zone. The pressure unit is able to supply forming pressures of up to about 150 MPa. The joining system uses distilled water as working medium. The length of this pressurized area is limited by O-rings to 29 mm (see **Figure 6-17a**). Before the joining operation, both partners were placed in an ultrasonic acetone bath for five minutes to remove all surface contaminations. During the joining process, the hydraulic forming pressure p_{i} is increased linearly up to its maximum value, which is determined from the corresponding design chart. This pressure level is held for about five seconds before p_{i} is completely released and the finished connection is unloaded from the joining station (see **Figure 6-17b**).

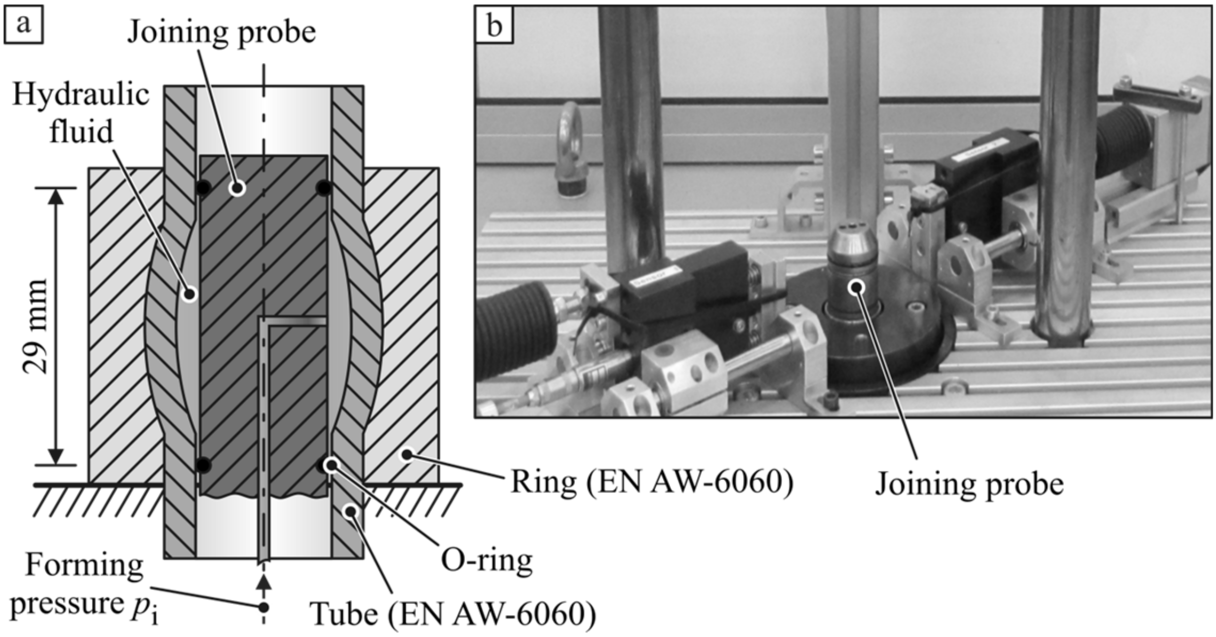
a
Joining probe
Hydraulic fluid
29 mm
Forming pressure p_i
O-ring
Tube (EN AW-6060)
Ring (EN AW-6060)
b
Joining probe

Figure 6-17: a) Setup of joining by die-less hydroforming (Gies et al., 2013) b) DHF joining station

Figure 6-18 shows the results of the pull-out tests and the analytically predicted connection strengths. The specific connection strength for different groove widths is plotted versus the groove depth in this figure.

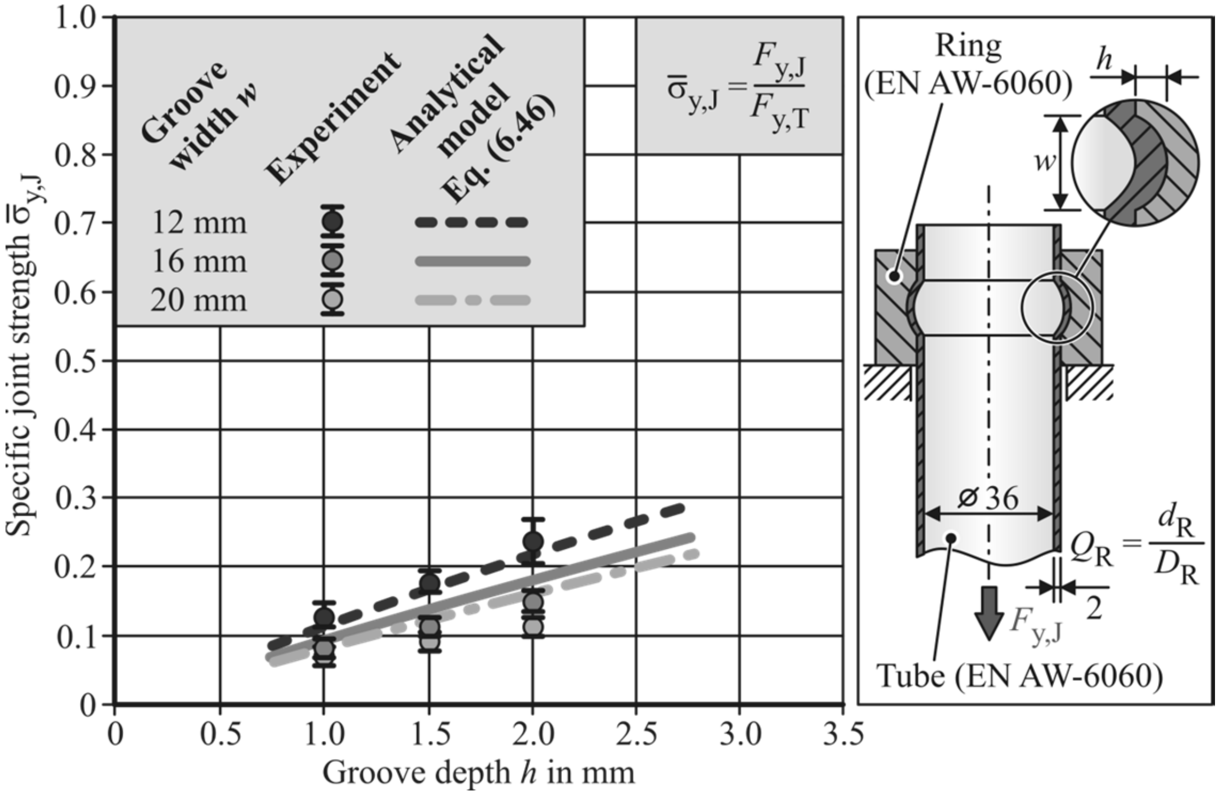

Figure 6-18: Comparison of analytically predicted and experimentally determined specific joint strength for circular grooves joined by expansion

As for the compressed joints, it is observed that an increasing depth *h* and a decreasing width *a* yield an increase in strength (Weddeling et al., 2014a). The experiments of Gies et al. (2013) also revealed two final failure modes of the connections at ultimate force. While the joints with the wider and shallower grooves failed by pulling the rings of the tubes, the narrowest and deepest grooves failed due to fracture of the tubes. To analyze the groove filling, the author machined pockets with an opening angle of 90° into additional joined specimens, which were not pulled (see **Figure 6-19**). Afterwards, pictures of the joining zone are taken with a digital microscope type KEYENCE VHX-500F. An example of such a microscopy image is shown in **Figure 6-19b**.

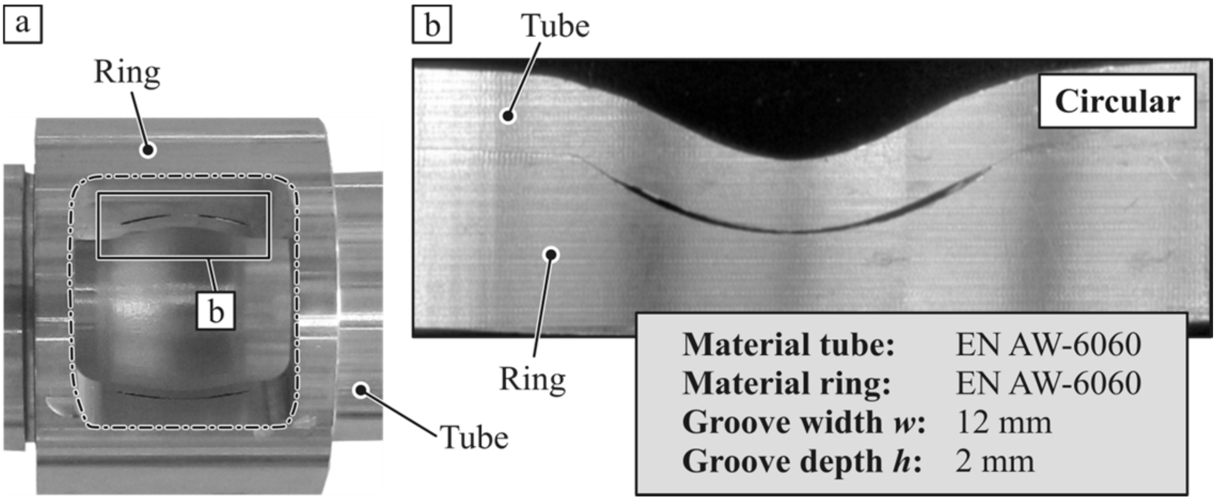

Figure 6-19: Cross section of hydroformed joints (Gies et al., 2013)

Besides the analyses of the groove filling behavior, these pictures are also used to determine the wrap-around angle β at the groove edge of the joined specimens. This is done to verify the assumption of the analytical model that the wrap-around angle β equals half of the groove angle α (Weddeling et al, 2014a). **Table 6-3** shows that the values of β calculated by Equation (6.19) and (6.20) are similar to the measured values of α. This implies that the assumption of Equation (6.20) is reasonable for the analytical model.

As shown in **Figure 6-18**, the calculated joint strengths agree well with the experimentally measured ones in terms of the trend of the plot. The mean absolute percentage error of the model is about 19 % in this case. It follows that the approach is well suited for the prediction of the effects of major joint parameters, e.g. groove depth and width, on the transferable loads. The lowest mean absolute percentage error of about 10 % between analytically calculated joint strengths and experimentally acquired results is found for connections with $w = 12$ mm. The largest average deviation of approximately 27 % between model and experiments is observed for the widest grooves. This can be attributed to an overestimation of the wrap-around angle β at the groove edges and, as a result, the frictional force at the groove edge is increased.

For the connection featuring a groove width of 16 mm, a mean absolute percentage error of about 19 % between calculated and measured values of $\bar{\sigma}_{y,J}$ is found.

Table 6-3: Comparison of measured and calculated wrap-around angles β of expanded connections (Weddeling et al., 2014a)

Groove dimensions *w* x *h* (mm)	**Measured angle *α*** (°)	**Calculated angle *β*** (°)
12 x 1.0	10.9	9.5
12 x 1.5	16.9	14.0
12 x 2.0	24.0	18.4
16 x 1.0	8.4	7.1
16 x 1.5	13.4	10.6
16 x 2.0	19.3	14.0
20 x 1.0	7.1	5.7
20 x 1.5	10.1	8.5
20 x 2.0	13.8	11.3

The comparison of experiments and model in **Figure 6-18** shows that the approach presented in **Section 6.1.2** provides a basic understanding of the load transfer of connections joined by expansion. Therefore, it allows an analytical joint strength comparison of this joint type to connections manufactured by compression.

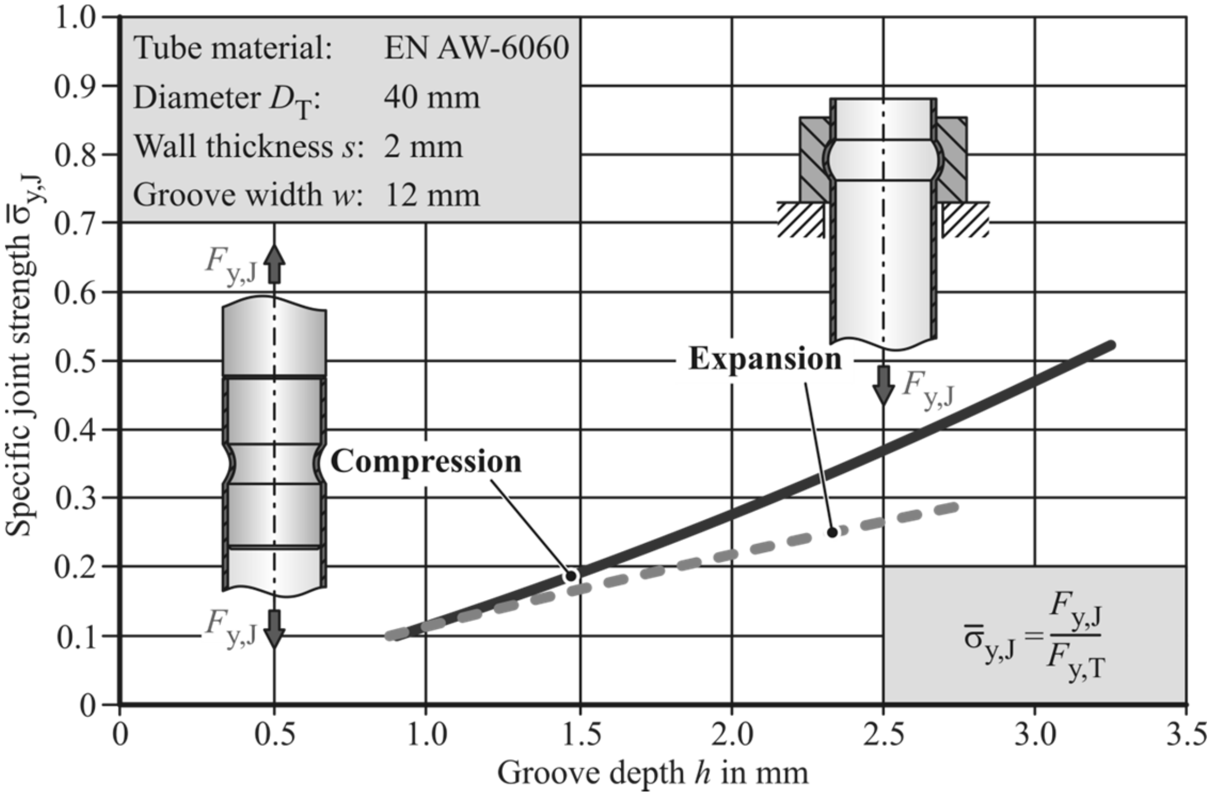

Figure 6-20: Comparison of the analytical approach for compression and expansion

Figure 6-20 shows the results of this evaluation for a groove with a circular shape and a width of 12 mm. It can be seen that a higher specific strength is achieved by compressed connections. This can be attributed to the different stress states of compressed and expanded joints during pull-out. In **Figure 6-21**, the distribution of the meridional and circumferential stresses for these connection types under tensional loading are displayed schematically with respect to the axial position *z*. While for compressed connections a stress state of pure tension with σ_θ larger than σ_ϕ is assumed, the expanded joints experience meridional tension and circumferential compression during pull-out (see **Section 6.1.1** and **6.1.2**). With respect to the Tresca yield criterion, the yielding of a workpiece occurs when the difference between the maximum and the minimum stress equals the yield stress σ_y. In case of pull-out of compressed connections, the maximum stress is σ_θ. Since it is assumed that σ_r is about zero, σ_r has to be the minimum stress. For expanded joints, the maximum stress is the one in meridional direction and the minimum stress is σ_θ, which is compression. Due to the fact that the meridional stress cannot be higher than the circumferential stress plus σ_y, the strength of this connection type is affected by the value of σ_θ. At compressed joints, the meridional stress and the resulting strength are independent of the other two stresses. Therefore, it can be assumed that in general these connections are able to transfer higher loads.

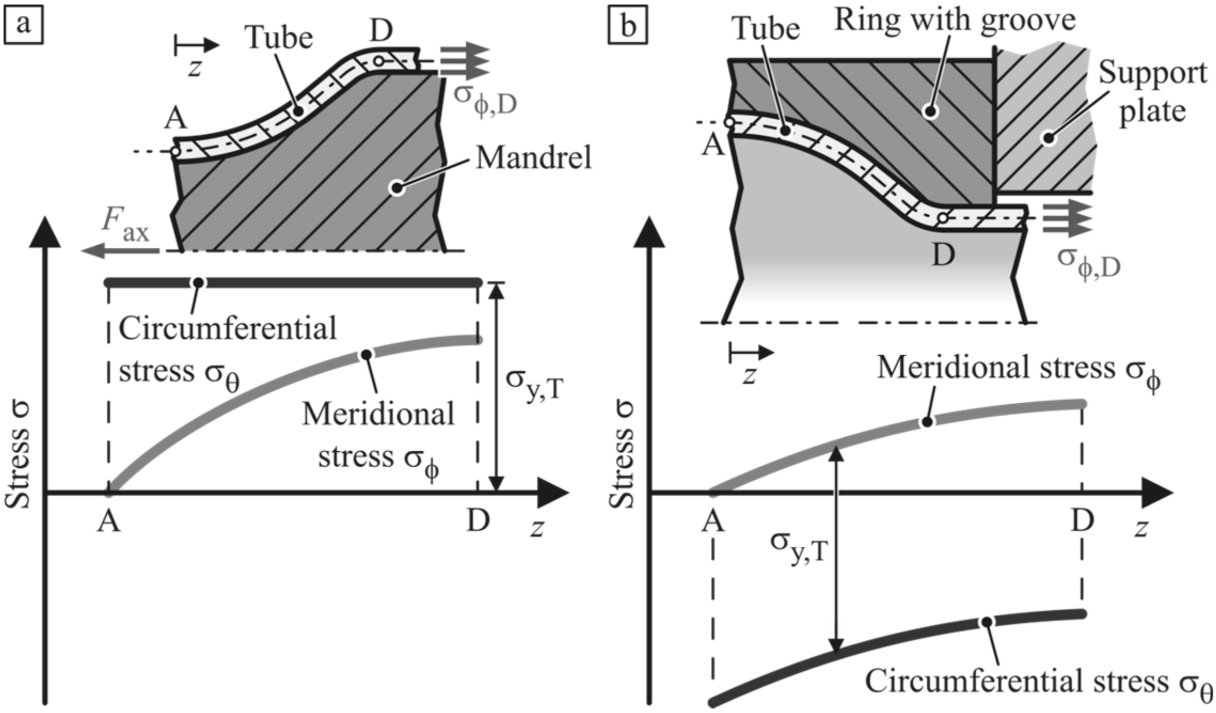

Figure 6-21: Stress state during pull-out in a) compressed and b) expanded joints

This finding implies that form-fit joints of tubular workpieces should be designed as compressed connections. Since process related effects on the transferable loads are eliminated in the connection strength comparison by the analytical model, it can be assumed that this recommendation is generally valid for most form-fit joints. But there are structures that require connections manufactured by expansion. An example of such parts are built camshafts or heat exchangers (Weddeling et al., 2014a)

6.2.3 Joining gap influence on the joint strength

A parameter which is particularly important for the achievable strength of interference-fit connections generated by electromagnetic forming is the joining gap a_0 between the workpieces (Kleiner et al., 2006). Since the influence of a joining gap on the strength of form-fit connections has not been analyzed yet, the necessary investigation is part of this work. In **Figure 6-22**, the specific joint strength for different groove depths is plotted versus the joining gap a_0. The diagram shows a maximal specific strength increase of about 30 %. It also illustrates that there is an optimal gap size with respect to the transferable load.

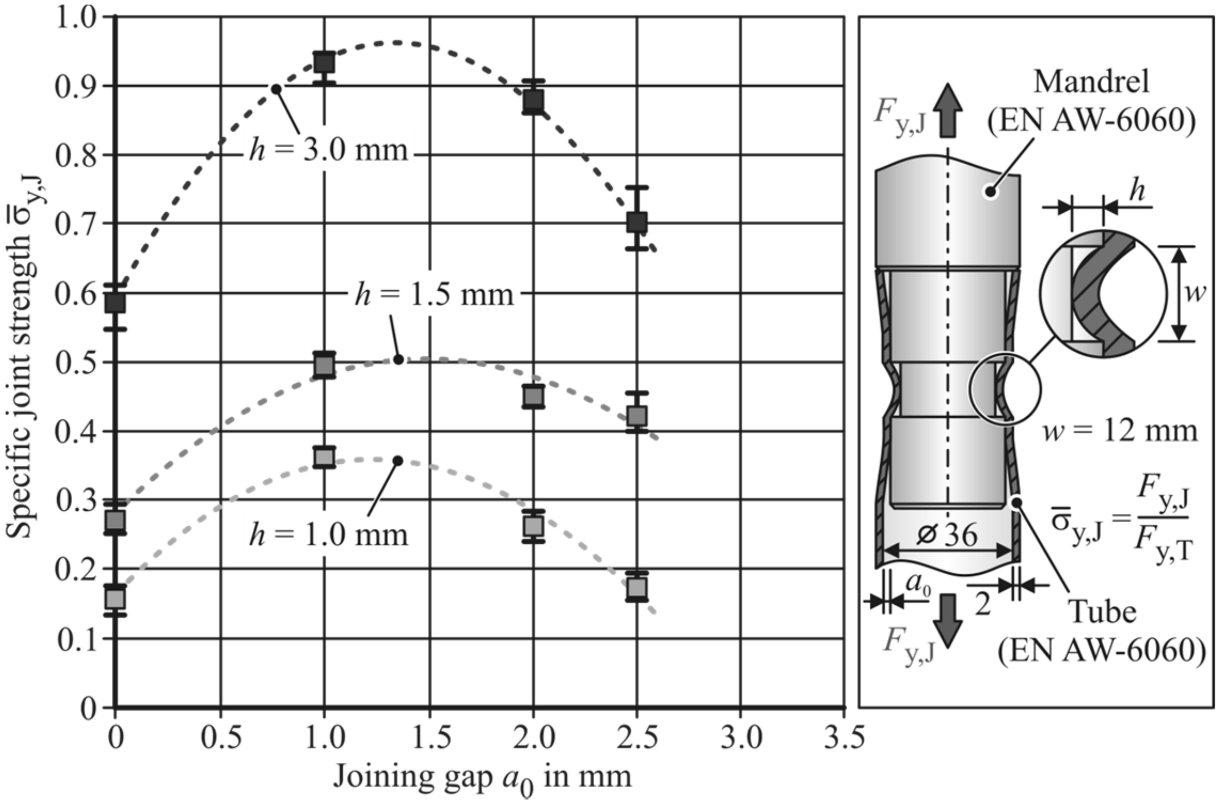

Figure 6-22: Specific joint strength over joining gap a_0

The general joint strength increase can be explained by an additional interference fit. Although it is mentioned above that this joint type can be avoided or minimized by applying solid mandrels and using the same material for both joining partners, it is possible to manufacture an interference fit with solid inner workpieces if there is a gap between the workpieces (Kleiner et al., 2006). Without such a gap, the acting magnetic pressure is generally not high enough to generate a sufficient elastic deformation of the mandrel. In contrast to this, a gap allows the acceleration of the workpiece up to very high velocities, which range typically from 50 to 250 m/s. When the outer workpiece impacts on the mandrel at such high speeds, very high impact pressures are generated. Johnson (1970) states that the impact pressure p_{im} which is developed when two semi-infinite elastic bodies (index 1 and 2) collide with an impact velocity v_{im} can be expressed as follows:

$$p_{im} = \frac{\rho_1 \cdot \rho_2 \cdot C_{w,1} \cdot C_{w,2}}{\rho_1 \cdot C_{w,1} + \rho_2 \cdot C_{w,2}} \cdot v_{im} \tag{6.54}$$

The material density is represented by ρ_{i} and $C_{\mathrm{w,i}}$ is the longitudinal wave speed. For most structural materials, this speed is of the order of about 7000 m/s. In case of aluminum, Bruno (1968) gives a value of about 6370 m/s for the longitudinal wave speed. This leads to an impact pressure of about 850 MPa for an aluminum-aluminum couple at a collision velocity of 100 m/s. This is a significant pressure increase compared to the typical forming pressures in **Section 5.2**. Due to the high impact pressures, the mandrel material close to its surface is elastically, probably even plastically, deformed and an interference-fit joint is generated.

The occurrence of an optimal joining gap size can be explained by the work of Kleiner et al. (2006). In their work, the authors show that there is an optimal value of a_0 with respect to the joint strength for interference-fit connections. They state that the part is first accelerated by the magnetic forces to a certain maximum velocity. Afterwards, when these forces are not acting anymore, the workpiece is decelerated as the kinetic energy of the workpiece is transformed into deformation energy. In order to achieve the highest connection strength, the gap shall be selected so that the impact velocity corresponds to the maximum speed of the workpiece. Thereby, the highest possible impact pressure and the largest deformation leading to the maximum joint strength are achieved.

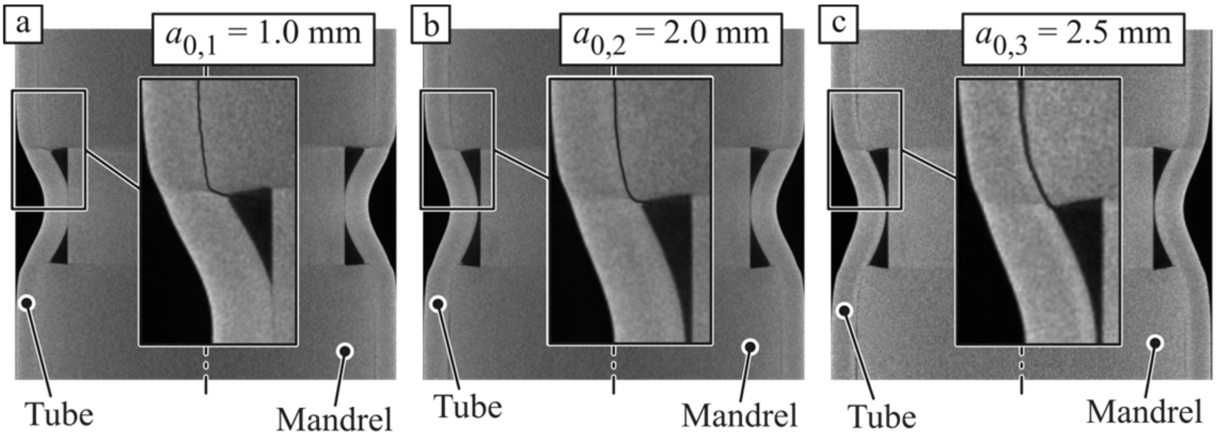

Material tube: EN AW-6060 **Groove geometry:** 12 x 3 mm
Material mandrel: EN AW-6060 **Mandrel diameter D_M:** 36 mm

Figure 6-23: Tomography images of joints manufactured with different gap width a_0

The drop in joint strength after its maximum can be assumed to be caused by a reduction in the diameter D_M of the mandrel due to an increasing gap width a_0. A decrease of this diameter leads to a smaller contact area A_C between the joining partners. Therefore, the total pull-out force F_{ax} is also decreased since it is proportional to A_C as Equation (2.1) shows. A reduction in wall thickness due to intensive shearing at the groove edge caused by high impact pressures can be precluded as a reason for the joint strength decrease from its maximal value. Instead, a reduction of shearing is actually observed with an increasing gap width a_0 in **Figure 6-23**. This can be attributed to the fact that the tube wall impacts on the surface of the mandrel at an angle and therefore the pressure at the groove edge does not only act in the radial direction, but also in axial direction. Since the impact angle increases with larger gaps, the value of the axial pressure component rises as well. This leads to an increase of rounding at the groove edge and thereby the amount of shearing is reduced (see **Figure 6-23**). It can be assumed that the elimination or minimization of the additional interlock at the edge of the groove causes at least some of the tensional strength decrease.

The disadvantage of a gap between the workpieces prior to the joining operation is that an accurate coaxial positioning of the components requires additional tooling, which might be quite complex, particularly for larger frame structures. An exact design is important because even a small mispositioning at the joint can lead to a much greater inaccuracy of the structure at a different location. Therefore, a joint design without a joining gap between the workpieces is preferred if the desired connection strengths can be achieved by other features.

6.2.4 Charging energy variation

In existing research works regarding form-fit joining by electromagnetic crimping, the charging energy levels are either adjusted with respect to the groove geometry (Golovashchenko, 2001) or kept constant (Park et al. 2005a). Therefore, it is hardly possible to predict how this process parameter affects the achievable connection strength when the energy exceeds the level required to ensure the filling of a specific groove geometry. To determine the effect of E on the achievable connection strength, additional joining experiments with 120 % and 140 % of the charging energy required for groove filling are performed (Weddeling et al., 2011b). Since the 20 mm wide grooves show minimized shearing at the groove edge (see **Figure 6-9**), this width is chosen to reduce the influence of an additional interlock on the connection strength. The corresponding results for grooves with three different depths are presented in **Figure 6-24**. It can be seen that the specific strength increases with a rising charging energy level. This increase can be partly explained on the basis of the analytical joint strength prediction. If a charging energy level which ensures a filling of the groove is selected, the velocity of the tube is approximately zero at the moment when it touches the groove base. In case of an energy higher than this value, the tube wall impacts the bottom of the form-fit element at a certain velocity. Hence, the length l_c of the straight section at the groove center increases with increasing charging energy (see **Figure 6-25**) leading to a decrease of the principle radius R_{r1}. Due to this change of the curvature, a higher meridional stress is necessary for the deformation of the tube during pull-out. Therefore, the joint strength is increased (see **Section 6.1.1**). Additionally, the wrap-around angle β at the groove edge also increases. As a result, the value of the friction term in Equation (6.41) rises as well. Besides the explanations for the joint strength increase given by the analytical model, it can also be assumed that for the highest magnetic pressures, a small shear interlock at the groove edge is generated, which can lead to a strength increase. Since shearing can have a devastating effect on the fatigue strength of a connection, the charging energy level has to be selected with special care.

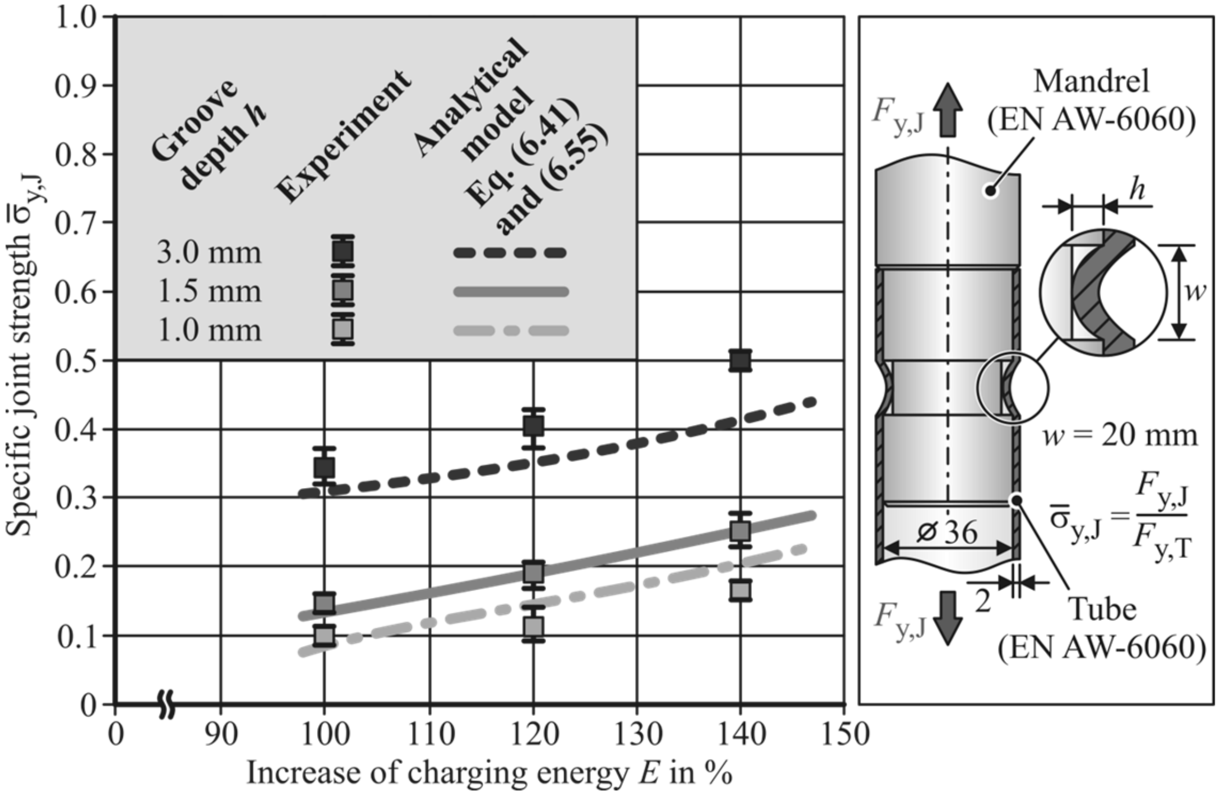

Figure 6-24: Specific joint strength over increase of charging energy

The analytical approach introduced in **Section 6.1** gives an explanation for the charging energy influence on the transferable load, but it does not allow the quantitative prediction of the achievable connection strength with respect to the joining zone and process parameters. To facilitate this determination, the effective groove width *w'* is introduced. It is assumed that the straight section in the center of the groove has no effect on the joint strength since during pull-out, no deformation occurs in this part of the tube. Therefore, the effective width is defined as groove width *w* minus the length of the straight segment. This implies that a connection joined with a charging energy higher than necessary for groove filling has the same tensional strength as one with a narrower groove, which is manufactured without an increased energy level. It is assumed that the length of the straight section is proportional to the charging energy increase. Hence, for the determination of the effective width, the following expression is found:

$$w'(E) = w - \frac{h}{h_d(E)} \tag{6.55}$$

The item $h_\mathrm{d}(E)$ in Equation (6.55) represents the forming depth which can be achieved for a specific groove width by the increased energy level with an unrestricted deformation in radial direction. For its determination, the analytical approach of **Section 5.1** is applied.

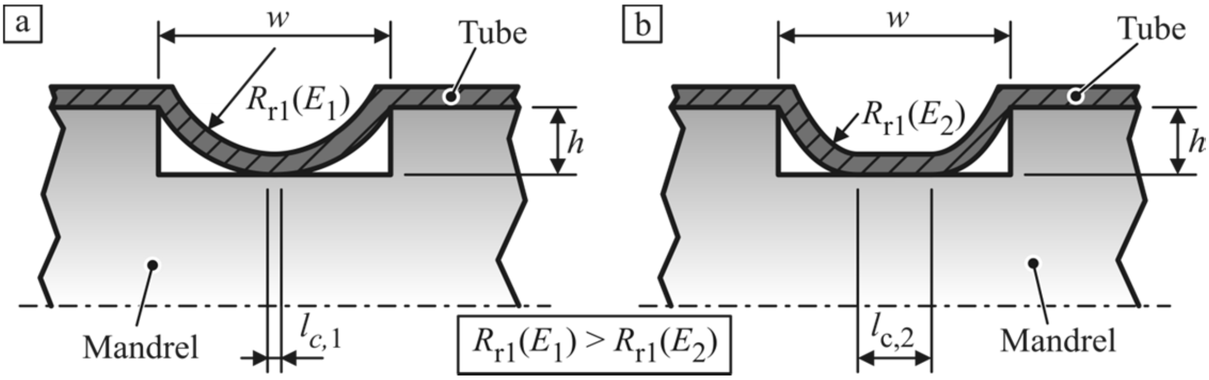

Figure 6-25: Groove filling for different energy levels (Weddeling et al., 2011b)

To predict the joint strength analytically, the width w is substituted by this value in Equation (6.41). Thereby, the effect of an increased charging energy on the transferable load is considered. **Figure 6-24** shows that the joint strengths predicted with this modification are in good agreement with the experimental values. The mean absolute percentage error between model and experimental strength values is approximately 13 %. The largest absolute difference of about 0.1 is observed for the deepest groove joined at the highst energy level. This difference can be attribuded to shearing at the groove edge and the resulting additional interlock, which is not considerd by the analytical joint strength prediction.

6.3 Strength of connections featuring hollow mandrels

As mentioned in **Chapter 3**, it is of particular interest how a mass reduction in the joining zone affects the joining behavior and the resulting load transfer behavior. Without changing the material, the only possibility to reduce the mass of a connection is to apply joining partners with a lower volume. The part that offers the highest potential for a mass reduction is the mandrel. This can be achieved by drilling a hole into the joining partner. But this leads also to a reduction of the compressive strength of the mandrel. To determine the effect of this resistance against plastic deformation on the achievable connection strength, the inner diameter d_M and thereby the diameter ratio Q_M of the mandrel is varied in the following experimental investigations (see Equation (4.7)). Additionally, the groove shape is varied during these tests to analyze its influence on the joining behavior and the transferable loads. To consider only the form-fit related effects on the specific strength and avoid an additional interference fit, the same material is used for both joining partner in these experiments. Subsequently, investigations are performed to evaluate the potential of a higher strength mandrel material and a resulting interference fit on the joint strength.

In terms of the final joint failure during pull-out, a third mode is observed for the experiments with hollow inner partners. If the inner diameter of the mandrel is increased up to a value at which the cross section at the groove base is similar to the cross section of the tube, fracturing of the mandrel is seen. **Figure 6-26** shows an example of a joint failed at this mode. For inner partners with smaller diameters d_M, the same failure modes as for the solid mandrels occurred (see **Figure 6-5**).

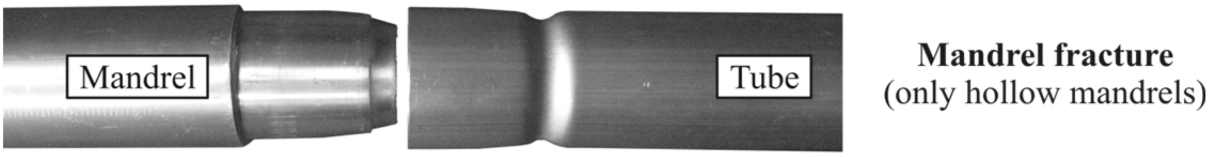

Figure 6-26: Additional failure mode of hollow mandrels

6.3.1 Load transfer of hollow mandrels

The experimentally determined joint strengths of hollow mandrels with different groove depths and widths are plotted in **Figure 6-27** over the diameter ratio Q_M. For this initial investigation on the strength of connections with hollow mandrels, a rectangular groove shape is selected. The diagram shows an optimal value of Q_M for all groove dimensions with respect to the specific strength. First, the joint strength rises with an increasing diameter ratio up to its maximum value. This can be attributed to an additional interference fit due to a decreased stiffness and an increasing elastic deformation of the inner workpiece. Although both joining partners are manufactured of the same material, the different geometrical dimensions of the inner and the outer part lead to a dissimilar elastic recovery of the workpieces and thereby a relatively small interference fit is generated (Marré, 2009). A similar correlation between joint strength and the ratio Q_M is shown by Kleiner et al. (2006) in their work regarding interference-fit connections manufactured by electromagnetic compression. The authors also reveal that the joint strength drops significantly if the inner diameter d_M is increased above its optimal value. This behavior can be observed for the experimental results in **Figure 6-27** as well. Kleiner et al. (2006) assume that this decrease in strength is caused by an elastic-plastic deformation of the inner partner. A reduction of the additional interference fit for thinner mandrels describes the significant joint strength decrease seen here only partly. It gives no explanation for the drop of the transferable load below the value of solid mandrels, which do not include an additional interference fit. This substantial strength reduction compared to connections with solid mandrels can be attributed to the different deformation behavior of hollow inner workpieces during joining.

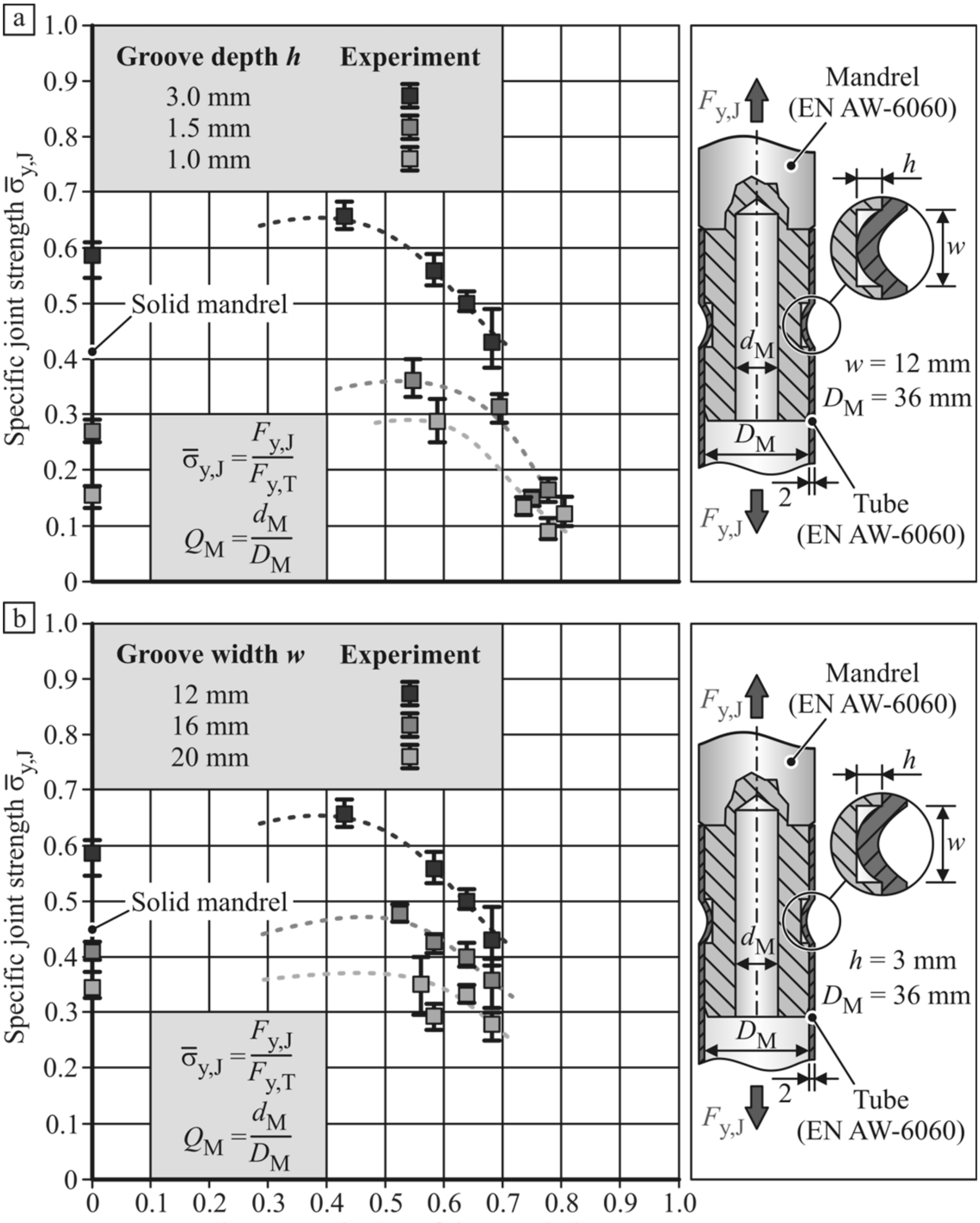

Figure 6-27: Influence of the diameter ratio Q_M on the strength of joints with hollow mandrels under a variation of a) groove depth and b) groove width

The computer tomography images in **Figure 6-28** display that the deformation of the mandrel increases with larger values of d_M due to a decrease of its compressive strength. This leads to an increase of the groove edge angle γ_{GE} (Weddeling et al., 2010). As a result, the principle radii R_{r1} and R_{r2} of the tube contour become larger and the curvature changes of the outer partner in the joining zone are less distinct compared to connections with solid mandrels. Since this yields a lower amount of bending during pull-out, the additional meridional stresses and, thereby, the total joint strength are decreased. Additionally, the CT images in **Figure 6-28** show a reduction of shearing at the edge of the groove with decreasing compressive strength of the mandrel, which leads to a further drop of the quasi-static joint strength.

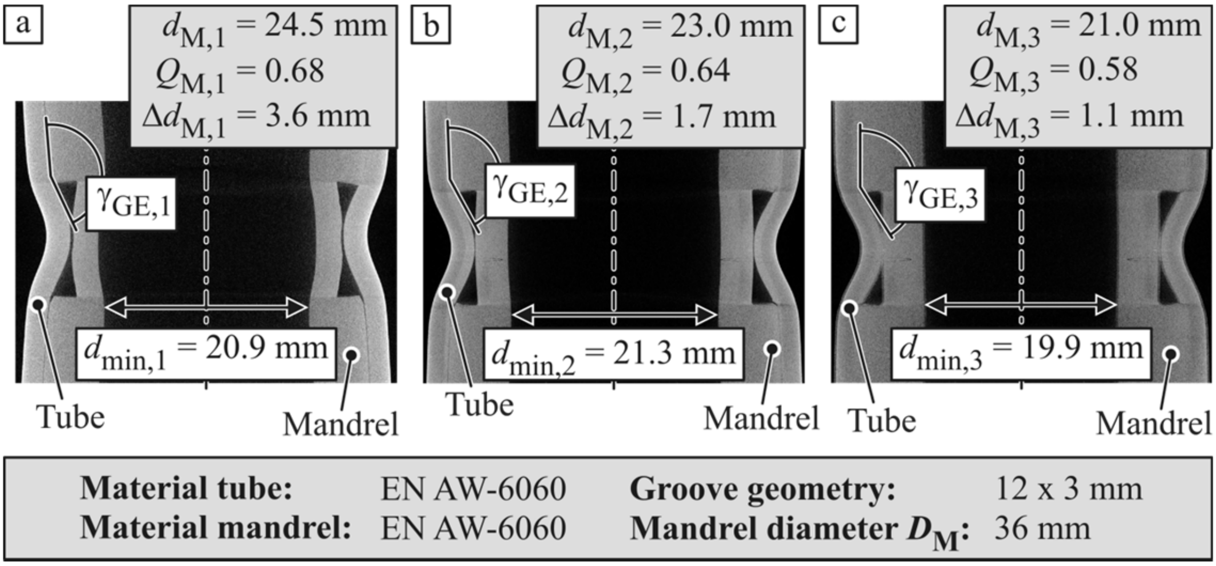
a
$d_{M,1}$ = 24.5 mm
$Q_{M,1}$ = 0.68
$\Delta d_{M,1}$ = 3.6 mm
$\gamma_{GE,1}$
$d_{min,1}$ = 20.9 mm
Tube
Mandrel
b
$d_{M,2}$ = 23.0 mm
$Q_{M,2}$ = 0.64
$\Delta d_{M,2}$ = 1.7 mm
$\gamma_{GE,2}$
$d_{min,2}$ = 21.3 mm
Tube
Mandrel
c
$d_{M,3}$ = 21.0 mm
$Q_{M,3}$ = 0.58
$\Delta d_{M,3}$ = 1.1 mm
$\gamma_{GE,3}$
$d_{min,3}$ = 19.9 mm
Tube
Mandrel
Material tube: EN AW-6060
Material mandrel: EN AW-6060
Groove geometry: 12 x 3 mm
Mandrel diameter D_M: 36 mm

Figure 6-28: Joining zone deformation of hollow mandrels

6.3.2 Groove shape variation

To analyze the influence of the groove shape on the strength of connections featuring hollow mandrels, joints with triangular and circular grooves are also manufactured and tested. **Figure 6-29** illustrates the strength of connections with these shapes compared to joints with rectangular grooves. The triangular and circular geometries also show an optimum of Q_M with respect to the specific strength. But the transferable loads of these groove types are higher than the strengths achieved by rectangular grooves. As illustrated in **Figure 6-30**, this can be attributed to a smaller plastic deformation of mandrels with triangular and circular form-fit element shapes during electromagnetic crimping. **Figure 6-28** depicts that the largest joining related diameter reduction of the inner partner with rectangular grooves occurs at the groove edges. While the magnetic pressure is transferred by the tube directly to the mandrel at this location, $p_m(t)$ acts in the groove center only on the outer workpiece. Additionally, the cross-sectional area of the mandrel changes at this position very rapidly from its largest to its smallest value. Hence, the full forming pressure acts at the groove edge on the smallest cross section of the mandrel. This leads to the largest deformation of the inner joining partner at this location.

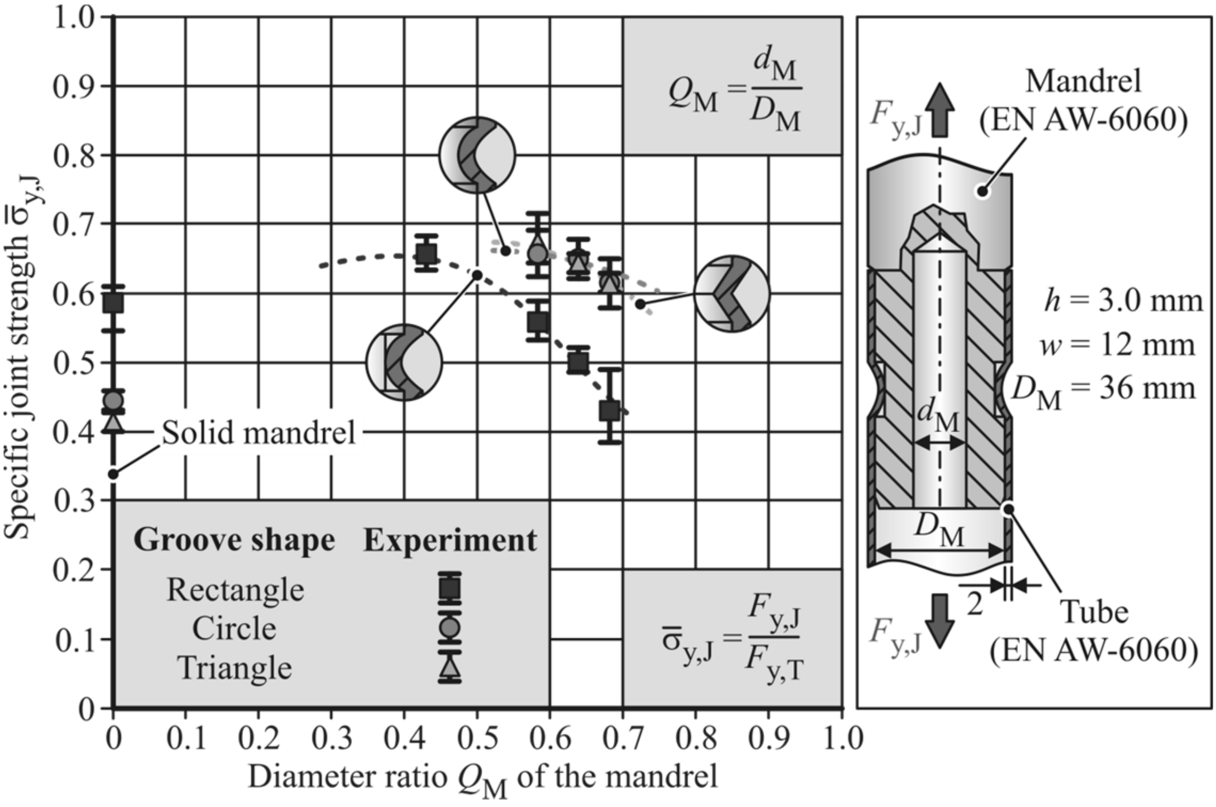

Figure 6-29: Groove shape influence on the strength of joints with hollow mandrels

Compared to the workpieces with rectangular grooves, the other two connection element shapes do not have such a drastic cross-sectional change of the mandrel at the groove edge. Therefore, they have a higher stiffness at this position and the full forming pressure does not act close to the section of the inner workpiece with the lowest compressive strength. This leads to a decreased deformation and thereby an increased specific joint strength.

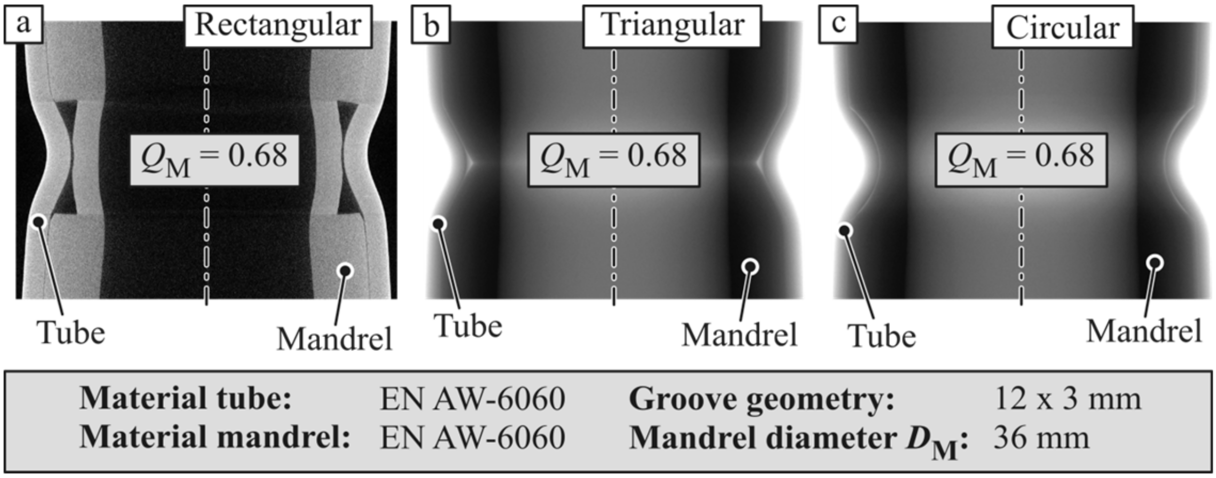
a
Rectangular
Q_M = 0.68
Tube
Mandrel
b
Triangular
Q_M = 0.68
Tube
Mandrel
c
Circular
Q_M = 0.68
Tube
Mandrel
Material tube: EN AW-6060
Material mandrel: EN AW-6060
Groove geometry: 12 x 3 mm
Mandrel diameter D_M: 36 mm

Figure 6-30: Deformations of hollow mandrels with different groove shapes

6.3.3 Influence of mandrel material

After the investigations regarding the influence of the geometrical mandrel properties on the specific strength, the effect of the yield strength of the mandrel on the joint quality is analyzed. The results of **Figure 6-31** show that an increasing yield strength leads to higher transferable loads. The maximum value is at about 85 % of the strength of the tube. This is almost double the strength of the connections with mandrels manufactured of EN AW-6060. At the same time, the mass beneath the groove is reduced up to about 70 % compared to solid mandrels. The significant strength increase of connections including mandrels with a higher yield strength can be explained by the following two effects. First, the compressive strength of the inner workpiece is increased. Hence, the deformation caused by the joining operation is decreased and the curvature changes of the tube wall in the joining zone are more distinct. Due to the higher bending forces, which result from these changes in contour during pull-out, the joint strength is increased.

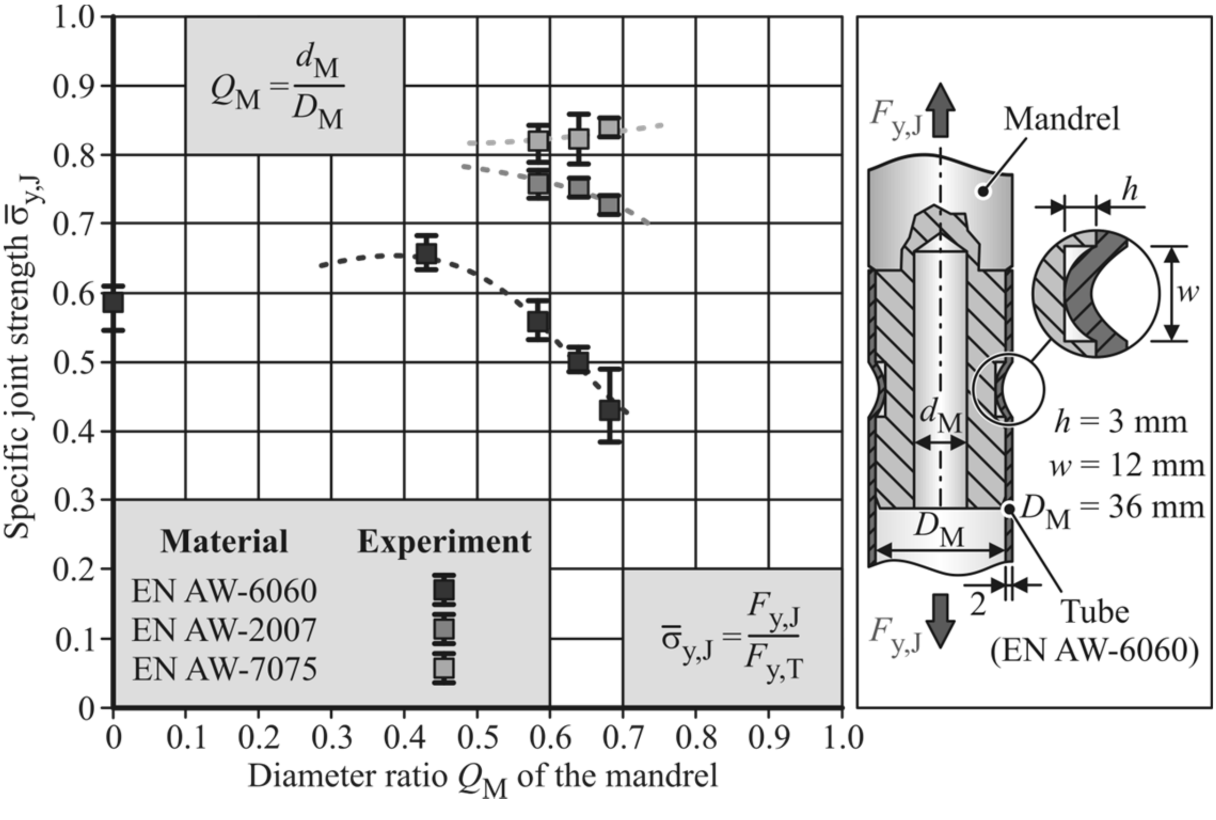

Figure 6-31: Effect of the mandrel material on the joint strength of hollow mandrels

The second effect causing the connection strength increase is based on the larger difference in elastic recovery of the joining partners resulting from the increased yield strength of the mandrel. Thus, the magnitude of the additional interference fit and that of the total connection strength are increased.

6.4 Summary and conclusion

In this chapter, an analytical model for the prediction of the achievable joint strength under quasi-static tensional loads is introduced. It is shown that this approach gives very accurate results for connections manufactured by compression and expansion with respect to different joining zone properties, such as groove dimensions and shapes. For all experiments together, a mean absolute percentage error between the calculated joint strengths and the experimentally determined ones of about 18 % is found. This implies that the model is well suited for the design process of form-fit connections. In addition, the analytical joint strength prediction provides a fundamental understanding of the load transfer of this joint type. For example, a comparison between expanded and compressed connections shows that the ones generated by compression are in general able to transfer higher loads. This can attributed to a different stress state in the tube during tensional loading.

For the validation of the analytical model and to analyze the influence of general joining zone parameters and process characteristics on the achievable joint strength, experimental investigations are performed. In terms of the groove dimensions it is observed that the transferable load increases with a decreasing width and an increasing depth of the form-fit feature. It is also found that the connection strength does not necessarily depend on the machined groove edge radius. Instead, it depends on the radius of the tube wall at this location, which is influenced by the manufacturing process and perhaps by the machined edge radius. Furthermore, the groove shape shows a significant influence on the specific joint strength. The highest strengths can be achieved by rectangular grooves. But this shape promotes shearing at the edge of the form-fit element. To avoid this, either triangular or circular grooves can be applied. Additionally, shearing can also be eliminated by a sufficiently large groove edge radius. Other options to influence the joint strength positively are the application of a charging energy higher than the level required to fill the groove and a specimen design which includes a joining gap between the workpieces. For all experiments, a relatively small statistical dispersion of the results is observed. This implies a high reproducibility of the process.

Subsequent to the experiments regarding the influence of the basic joining zone and process parameters, the effect of a mass reduction on the achievable connection strength is analyzed. For this purpose, joints with hollow mandrels are manufactured. The corresponding results show the existence of an optimal inner diameter d_M with respect to the transferable loads. For values of d_M smaller than the optimum, an additional interference fit is generated leading to the observed strength increase. If d_M exceeds the optimal diameter of the mandrel, the transferable load drops due to an increasing plastic deformation of the inner partner. It is also found that this deformation can be decreased by the application of triangular and circular grooves or by a higher strength mandrel material. By using such a material for the inner specimen, the additional interference fit becomes stronger as well and, hence, the joint strength can be increased further.

7 Manufacturing aspects for joints with hollow mandrels

The results of the previous chapter show that a target conflict between the reduction of mass and the joint strength exists. On the one hand, the inner diameter of the mandrel should be as large as possible to achieve a high mass reduction, but, on the other hand, this might lead to a significant decrease of the joint strength due to a plastic deformation of the mandrel during the joining operation. To achieve the highest possible mass reduction without a substantial decrease of the transferable load, two strategies for the manufacturing of form-fit connections with hollow mandrels are introduced in this chapter. In the first one, the inner partner is physically supported by an additional tooling element during the joining operation (Weddeling et al., 2010). Thus, the undesired inner workpiece deformation during electromagnetic crimping and the resulting strength reduction is avoided. In the second approach, to eliminate a joint strength decrease, the design of the mandrel is adapted to the applied forming pressure. For this purpose, an inner diameter d_M which leads to a compressive strength high enough to avoid a plastic deformation of the mandrel is selected. It is observed in **Section 6.3.2** that connections with rectangular grooves show the most distinctive mandrel deformation during the joining process. Therefore, the focus of these two strategies is on this groove shape.

Subsequent to the introduction of these two strategies, an exemplary connection design is conducted to reveal the potential of form-fit connections joined by electromagnetic crimping. In order to achieve this, the findings of this work are combined with the design recommendations from other researchers, as summarized in **Section 2.5.3**.

7.1 Joining with support mandrels

By placing a rigid support mandrel in the hole of the inner joining partner, its potential for being plastically deformed during joining is suppressed and the resulting connection strength decrease might be reduced (Weddeling et al., 2010). **Figure 7-1** shows the conventional setup of electromagnetic crimping of hollow mandrels compared to the usage of such an additional support. The gap between the inner joining partner and this tool has to be as small as possible to minimize the plastic deformation. Since the tooling element needs to be extracted from the inner workpiece after the generation of the connection, an interference fit between mandrel and support is undesirable and has to be avoided. Hence, the support tool has to exhibit a lower elastic recovery than the inner partner. This can be achieved by manufacturing the tool from a material with a higher Young's modulus than the mandrel material (Marré, 2009). A reduced elastic recovery of the support can also be achieved by using a material which has a lower yield strength than the material of the inner joining partner. But such a material selection for the support mandrel is not recommended because a too soft material is most likely to be deformed during the joining operation. This can lead to the formation of a gap between mandrel and tool. As a result the supporting effect of the tooling element is decreased and, thus, the strength of the joint might be reduced as well.

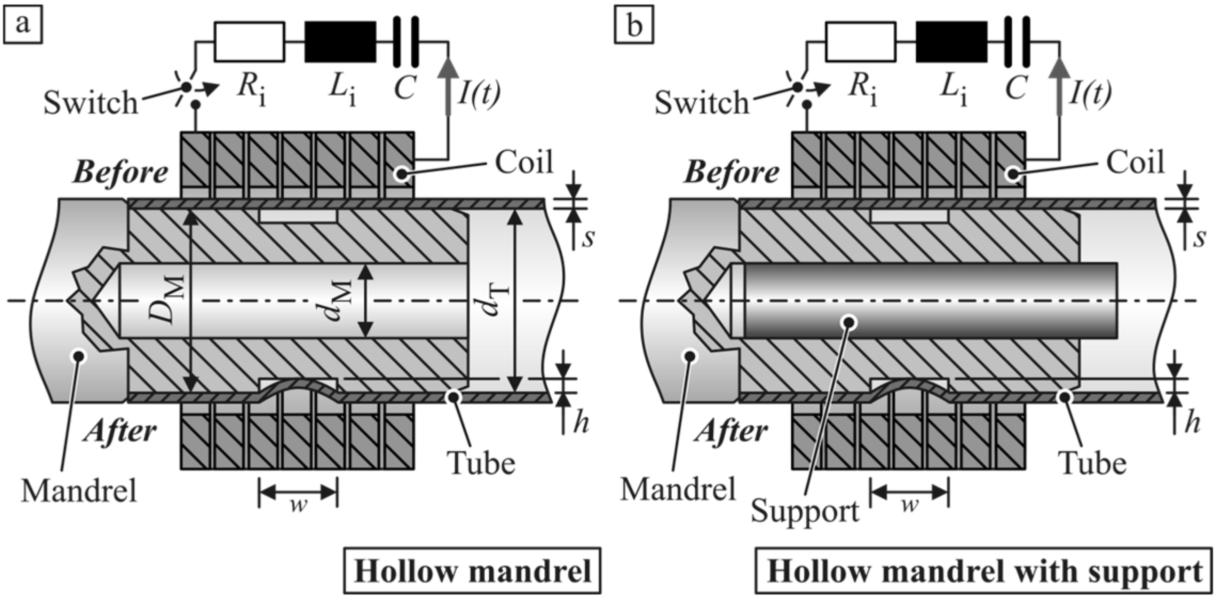
a
Switch
R_i
L_i
C
$I(t)$
Coil
Before
After
D_M
d_M
d_T
s
h
Mandrel
Tube
w
Hollow mandrel
b
Switch
R_i
L_i
C
$I(t)$
Coil
Before
After
s
h
Mandrel
Support
Tube
w
Hollow mandrel with support

Figure 7-1: Experimental setup joining hollow mandrels with and without support

In this investigation, a steel support with a Young's modulus three times higher than the workpiece material EN AW-6060 is used (Weddeling et al., 2010). To ensure the extractability of the additional tooling element, a thin film of Teflon grease is applied to its surface before it is inserted in the mandrel.

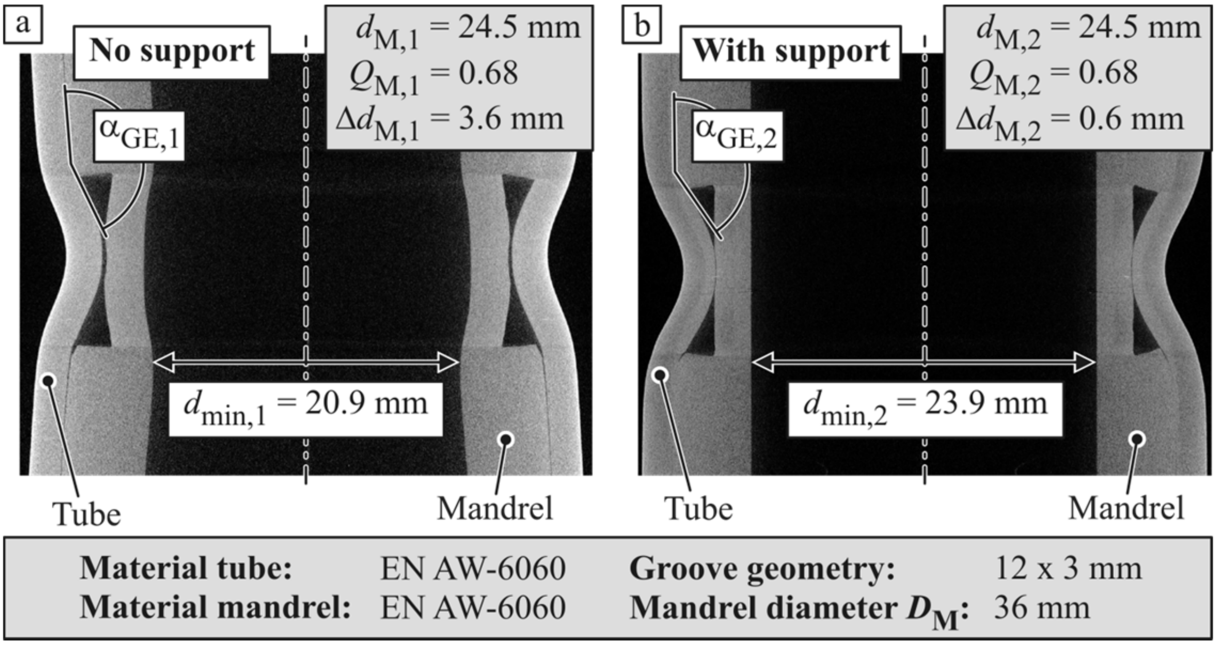
a
No support
$d_{\mathrm{M},1}$ = 24.5 mm
$Q_{\mathrm{M},1}$ = 0.68
$\Delta d_{\mathrm{M},1}$ = 3.6 mm
$\alpha_{\mathrm{GE},1}$
$d_{\mathrm{min},1}$ = 20.9 mm
Tube
Mandrel
b
With support
$d_{\mathrm{M},2}$ = 24.5 mm
$Q_{\mathrm{M},2}$ = 0.68
$\Delta d_{\mathrm{M},2}$ = 0.6 mm
$\alpha_{\mathrm{GE},2}$
$d_{\mathrm{min},2}$ = 23.9 mm
Tube
Mandrel
Material tube: EN AW-6060
Material mandrel: EN AW-6060
Groove geometry: 12 x 3 mm
Mandrel diameter D_M: 36 mm

Figure 7-2: Comparison of joining zone deformation of hollow mandrels joined with and without support

To examine the deformation behavior of the supported connections at joining, computer tomography images are taken. **Figure 7-2** shows the comparison of connections joined with and without supporting mandrel. Since both have the same groove geometry, the forming pressure level is identical for the two. The image in **Figure 7-2b** shows that the deformation of the inner joining partner is reduced substantially, which may be an explanation for the significant strength increase of the connections joined with an internal support. **Figure 7-3** shows that the transferable loads of these joints are up to 20 % higher compared to the strength of connections manufactured without additional tooling. This means that the pull-out strength level of the joints with solid mandrels is nearly reached.

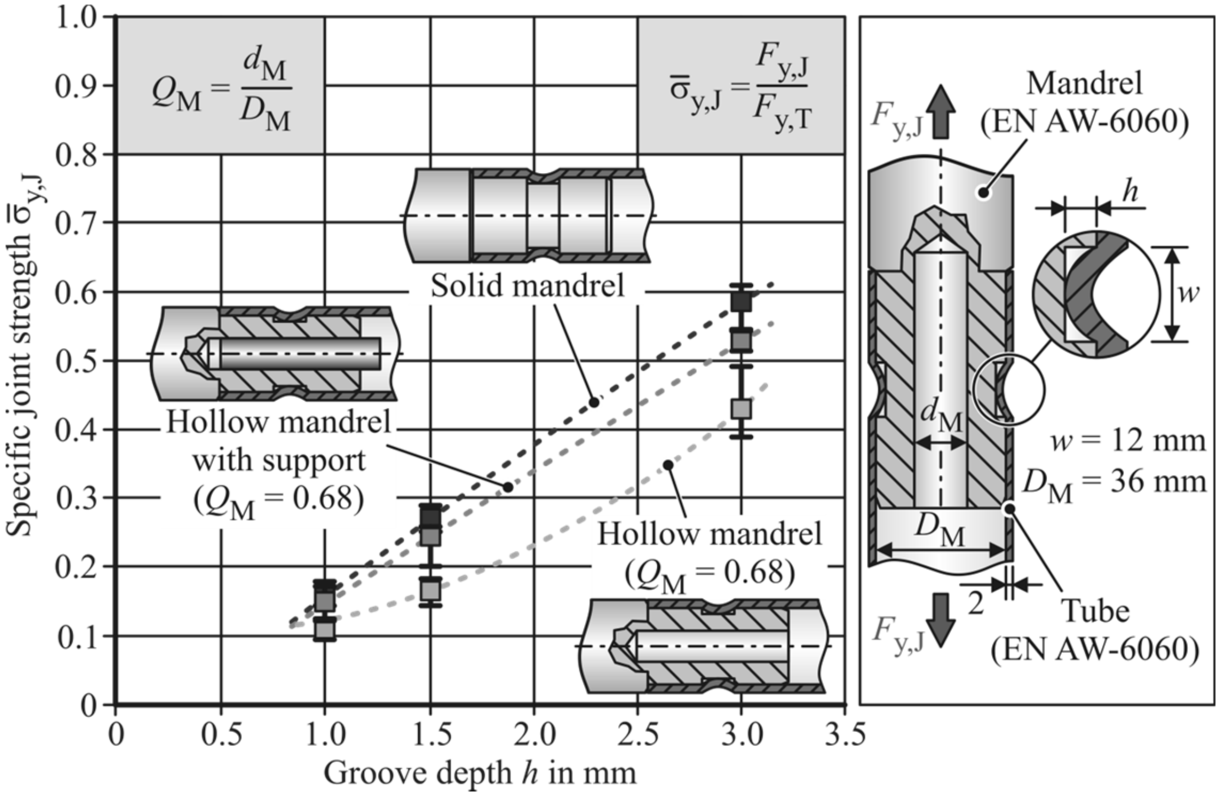

Figure 7-3: Specific joint strength of solid mandrels and hollow mandrels joined with and without support

The minor strength difference between the connections with solid inner joining partners and the ones including hollow mandrels, which are joined with an additional support, can be explained by the absence of shearing at the edge of the groove. Comparing the CT image in **Figure 7-2b** to **Figure 6-8a**, it can be observed that this effect is considerably reduced for the hollow mandrels joined with support. This can be attributed to the fact that despite a close adjustment of the diameter of the support to the inner diameter d_M of the mandrel, a gap between workpiece and tool cannot completely be prevented. Therefore, the inner joining partner slightly yields during the joining operation and shearing of the tube material at the edge of the groove is avoided or minimized.

Although this approach is well suited to manufacture connections featuring hollow mandrels without a significant drop of the joint strength, it has some critical disadvantages. The biggest handicap of this technique is that the accessibility necessary to extract the support tool from the inner joining partner does often not exist when manufacturing space frame structures. This approach also requires extra tooling, which increases the expenses of the process. Additionally, the generation of a supplementary interference fit is prevented by the support tool. Therefore, the full potential of the connection in terms of joint strength is not exploited.

The mass reduction of this technique is only limited by the requirement that the yield load $F_{\mathrm{y,M,GB}}$ of the smallest cross section of the mandrel has to be at least equal to the yield force $F_{\mathrm{y,T}}$ of the tube.

$$F_{y,M,GB} = F_{y,T} \tag{7.1}$$

If $F_{\mathrm{y,M,GB}}$ is smaller than the yield force of the tube, the mandrel becomes the weakest joining partner. Equation (7.1) takes the following form with the yield stresses of the joining partners, the cross-sectional area of the mandrel $A_{\mathrm{M,GB}}$ beneath the groove, and the cross section A_{T} of the tube:

$$\sigma_{y,M} \cdot A_{M,GB} = \sigma_{y,T} \cdot A_{y,T} \tag{7.2}$$

The smallest area $A_{\mathrm{M,GB}}$ of the mandrel can be determined from its inner diameter d_{M}, outer diameters D_{M}, and the groove depth h.

$$A_{M,GB} = \pi \left[\left(\frac{D_M}{2} - h \right)^2 - \left(\frac{d_M}{2} \right)^2 \right] \tag{7.3}$$

By combining Equation (7.2) and (7.3) with the term for the cross-sectional area of the tube and rearranging the resulting expression, the maximal inner diameter of the mandrel $d_{\mathrm{M,max}}$ is found.

$$d_{M,max} = \sqrt{4 \cdot \left(\frac{D_M}{2} - h \right)^2 - \left({D_T}^2 - {d_T}^2 \right) \frac{\sigma_{y,T}}{\sigma_{y,M}}} \tag{7.4}$$

Since the same material is used for both joining partners in this work, this diameter $d_{\mathrm{M,max}}$ depends only on the diameters of tube and mandrel.

$$d_{M,max} = \sqrt{4 \cdot \left(\frac{D_M}{2} - h \right)^2 - \left({D_T}^2 - {d_T}^2 \right)} \tag{7.5}$$

The area A_{T} is typically smaller than the cross section $A_{\mathrm{M,GB}}$ required to prevent the plastic deformation of the mandrel just by a high enough compressive strength of the inner workpiece. Hence, joining of connections featuring a hollow mandrel with an additional support mandrel allows usually the largest mass reduction with only a minor decrease of the transferable loads.

7.2 Threshold diameter ratio of the mandrels

By using mandrels with a compressive strength high enough to withstand a plastic deformation during joining, a significant strength reduction of joints with hollow mandrels can be prevented. The two major parameters affecting the compressive strength are the yield stress and the diameter ratio Q_{M} of the mandrel. Since the outer diameter of the inner joining partner is typically predefined by design requirements, the value of Q_{M} can only be adjusted by the selection of the inner diameter d_{M}. To ensure an adequate process design, the threshold value $d_{\mathrm{M,y}}$ of the inner diameter, at which the mandrel would become plastic, has to be determined. For this purpose, a simple analytical prediction of this value with respect to the acting forming pressure and the material properties of the inner workpiece is introduced in the following section.

As described above, electromagnetic form-fit joining of tubes is an impulse forming process. However, for the analytic calculations, a quasi-static and constant forming pressure p_{T} acting on the tube is assumed. The distribution of p_{T} is supposed to be uniform and an elastic ideal-plastic material behavior is assumed. If even the slightest gap between the joining partners is neglected, a contact or interference pressure between the workpieces is immediately generated when the tube is compressed. This interference pressure p_{M} acting on the mandrel leads to its deformation. In his work, Szabó (1964) develops the following expression to predict the value of p_{M} at which the elastic forming of the mandrel changes to an elastic-plastic deformation.

$$p_M = \sigma_{y,M} \cdot \frac{1 - {Q_{M,y}}^2}{2} \tag{7.6}$$

For a given material and contact pressure p_{M}, the diameter ratio $Q_{\mathrm{M,y}}$ causing this transformation of the deformation behavior can be determined by rearranging Equation (7.6):

$$Q_{M,y} = \sqrt{\left(1 - \frac{2 \cdot p_M}{\sigma_{y,M}}\right)} \tag{7.7}$$

While the contact pressure acts only on the mandrel, the tube experiences a loading from the outside by the applied forming pressure p_{T} and from the inside by the pressure p_{M}. Szabó (1964) gives the following relationship between the yield stress $\sigma_{\mathrm{y,T}}$ of the tube, its diameter ratio Q_{T}, and the acting pressures:

$$\sigma_{y,T} = \frac{1}{1 - {Q_T}^2} \cdot \sqrt{3 \cdot (p_M - p_T)^2 + \left(p_T - p_M \cdot {Q_T}^2\right)^2} \tag{7.8}$$

For a given forming pressure, the contact pressure p_{M} can be determined by the rearranged form of this equation.

$$p_M = \frac{1}{3 + {Q_T}^4}\left[3p_T + p_T {Q_T}^2 - \sqrt{\left({\sigma_{y,T}}^2 {Q_T}^4 - 3{p_T}^2 + 3{\sigma_{y,T}}^2\right)\left({Q_T}^2 - 1\right)}\right] \qquad (7.9)$$

With the combination of this expression and Equation (7.7), the threshold value $Q_{\mathrm{M,y}}$ of the diameter ratio for a given forming pressure p_{T} with respect to the workpiece properties can be predicted. To calculate this threshold value for connections joined by electromagnetic crimping, the forming pressure p_{T} is replaced by the amplitude of the acting magnetic pressure $p_{\mathrm{m,max}}$. In this work, the pressure amplitude is determined by the mechanical part of the analytical parameter prediction of **Section 5.1**. Since an analytical consideration of the sudden change in the cross-sectional area of the groove is extremely complex, the prediction of its effect on the compressive strength of the inner partner by the model is impossible. Additionally, it is mentioned in **Section 6.3** that the forming pressure only acts directly on the mandrel via the tube at the sections bordering the groove. In the area of the form-fit element, it just acts on the outer workpiece. Therefore, an inner workpiece without grooves is considered for the calculation of the threshold value $Q_{\mathrm{M,y}}$ of the mandrel and a decrease of the compressive strength of the inner partner due to a reduced cross-sectional area at the groove is neglected. Bühler and von Finckenstein (1968a) apply the same equations in their approach to determine the resulting interference pressure between electromagnetically crimped workpieces. This tool allows the strength prediction of interference-fit joints.

In **Figure 7-4**, the specific joint strength is plotted versus the diameter ratio of the mandrel. This relationship is shown for different groove depths in section **a)** of the diagram and for a variation of the width of the form-fit element in part **b)**. In addition, the calculated threshold values $Q_{\mathrm{M,y}}$ of this ratio are included in both diagrams. To improve the comprehensibility of the analytical results, the experimentally determined joint strengths of the connections with solid mandrels are included as horizontal lines. It can be observed that the analytical approach predicts the threshold diameter ratio at which the joint strength drops below the level of the connections with solid mandrels quite well. But the good agreement between model and experimental results decreases with an increase of the groove width. It can be seen in **Figure 7-4b** that the model overestimates the threshold value $Q_{\mathrm{M,y}}$ for the widest grooves of 20 mm. This observation can be attributed to the fact that at this width, the section with a reduced cross-sectional area takes up the largest proportion of the total joining zone among all investigated groove geometries. Since a reduced cross section causes a decrease of the compressive strength, the mandrels with this groove geometry are weakened the most.

Due to the fact that the analytically predicted threshold diameter ratios are in very good agreement with the experimentally determined results, the model is very suitable for the design of connections with hollow mandrels joined by electromagnetic crimping.

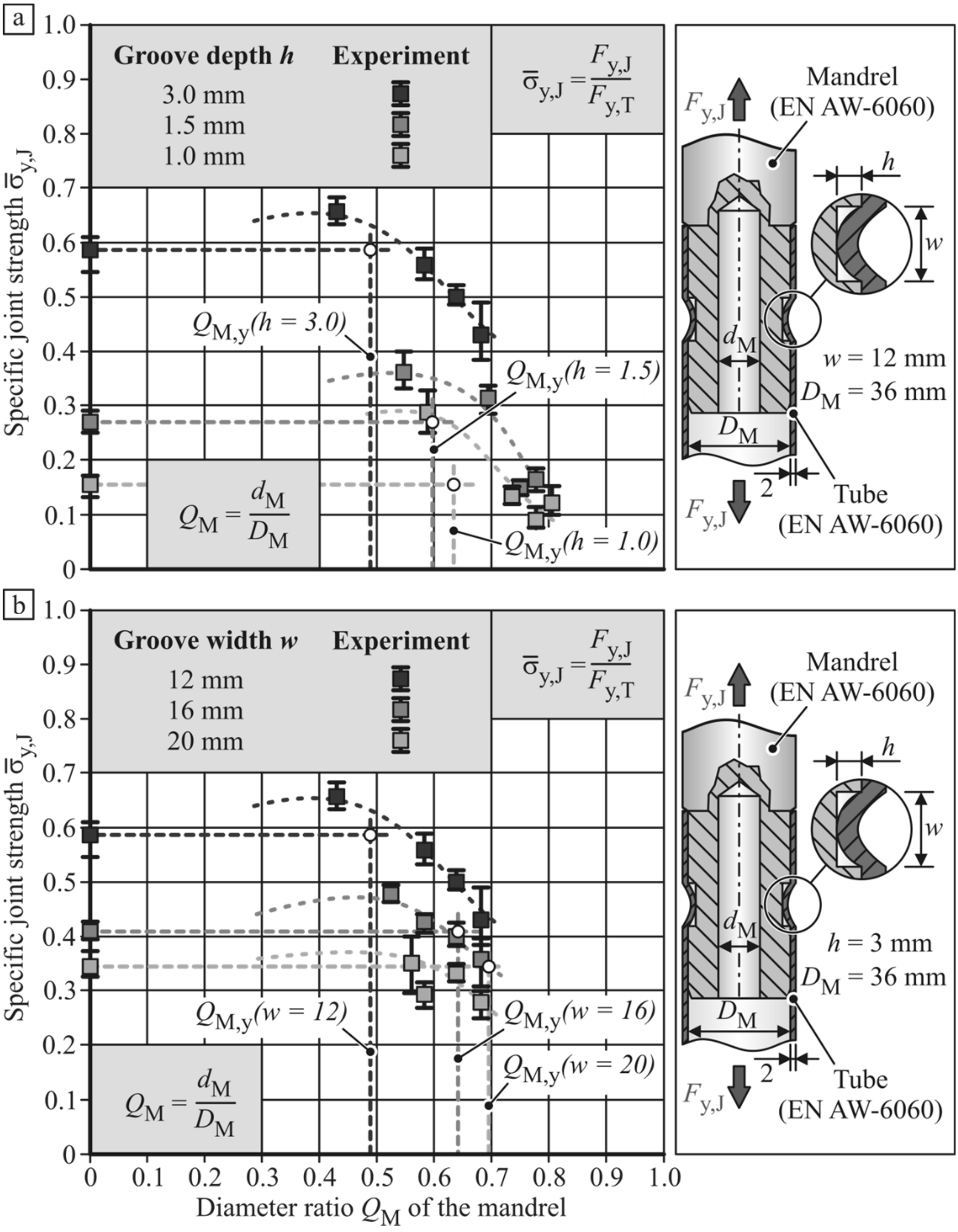

Figure 7-4: Specific joint strength versus diameter ratio including the threshold values of the $Q_{M,y}$, variation of groove a) depth and b) width

7.3 Deduction of a process window

To ease the design of connections featuring hollow mandrels, a method for setting up a process window for the manufacturing of such joints is introduced in the following. This window is based on the findings of **Section 7.1** and **7.2** in combination with the analytical models of **Section 5.1** and **6.1**. For the development of such a process window, either the groove depth h or its width w has to be appointed. This is necessary since a simultaneous variation of both values leads to a quite complex three dimensional diagram with reduced comprehensibility. The findings of **Section 6.2** and the design guidelines presented in **Section 2.5** can be used for the selection of a specific value for either w or h. In this section, the development of a process window for the joint design is shown taking the example of a groove depth of 3 mm as well as a 12 mm wide form-fit element. As mentioned above, the analytical joining process parameter prediction is used to determine the forming pressure acting on the workpieces with respect to different groove widths. These values are then used for the calculation of the threshold diameter ratios as described in **Section 7.2**.

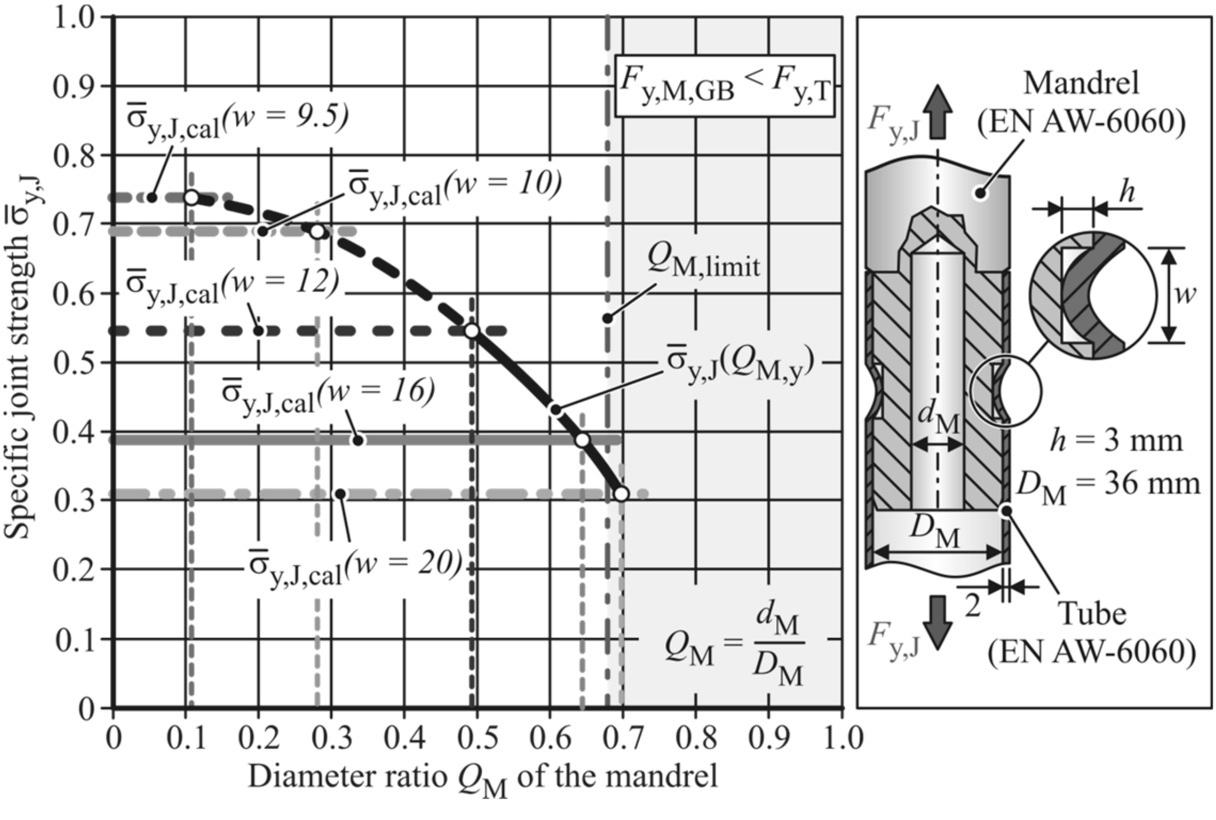

Figure 7-5: Development of a process window for compressive joining of hollow mandrels with a constant groove depth of h = 3.0 mm

In the next step, the joint strengths of the different geometries are predicted by Equation (6.41). As shown in **Figure 7-5**, the function $\bar{\sigma}_{y,J}(Q_{M,y})$ is generated by connecting the intersections of the calculated diameter ratios $Q_{M,y}$ and the predicted joint strengths. Every combination of strength and diameter ratio below this function can be joined without a significant decrease of the transferable load. To manufacture a combination above this curve and avoid a substantial strength drop at the same time, an additional support mandrel has to be applied to the joining zone as described in **Section 7.1**. Another boundary in **Figure 7-5** is the vertical line marked with $Q_{M,limit}$. At this diameter ratio, the force $F_{y,M,GB}$, at which the weakest section of the mandrel starts to yield, equals the yield force of the tube. Since the same material is used for both partners, the cross-sectional areas of the mandrel below the groove and the cross section of the tube are equal as well. If the diameter ratio Q_M of the mandrel is increased above this value, the inner joining partner becomes the weaker workpiece and, as a result, the total strength of the connection is decreased.

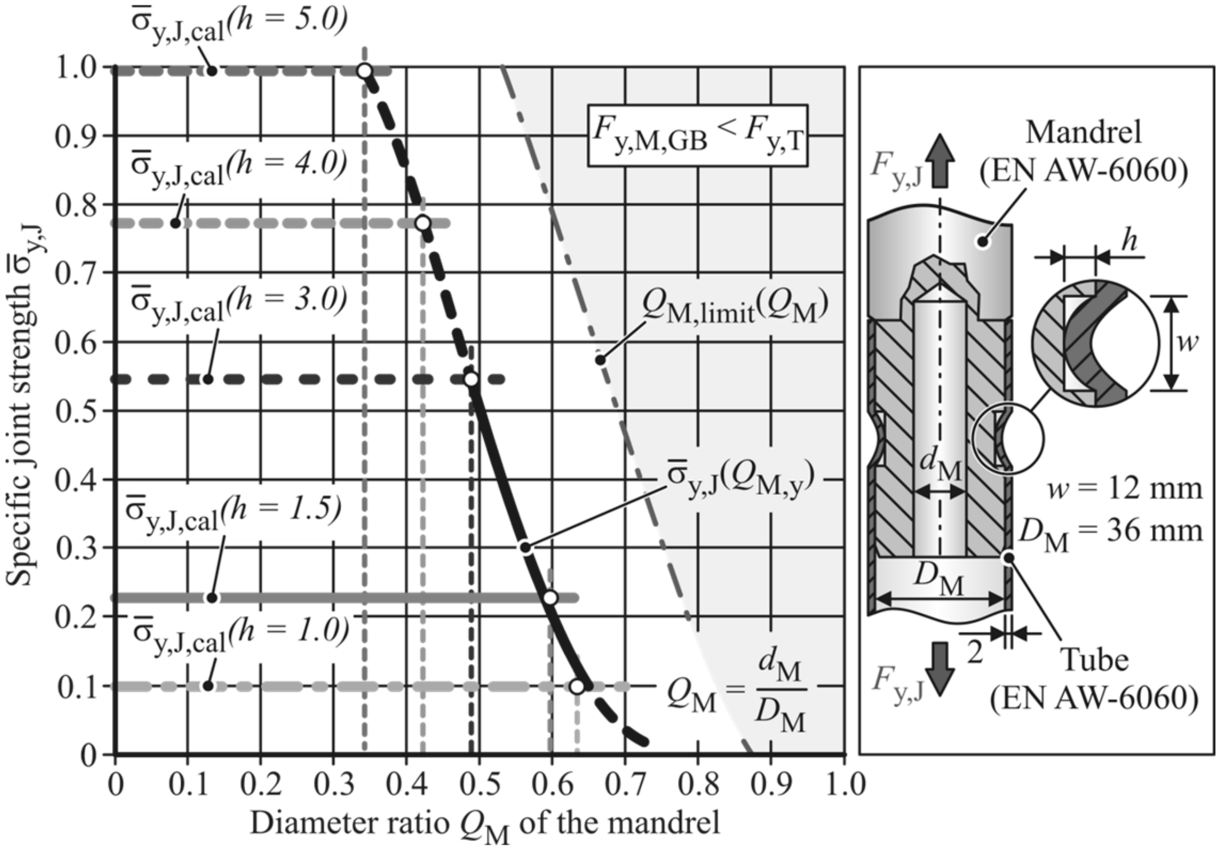

Figure 7-6: Development of a process window for compressive joining of hollow mandrels with a constant groove width of w = 12 mm

If a process window for a constant groove width and a varying depth is developed, the boundary $Q_{M,limit}$ does not come as a vertical line (see **Figure 7-6**). Since it depends on the radii of the mandrel in the groove area, it changes with a variation of the depth of the form-fit element. Therefore, it has to be presented in the diagram as a function of the diameter ratio as well. As shown in **Figure 7-6**, the boundary curve $\bar{\sigma}_{y,J}(Q_{M,y})$ for a process window with a constant width is also generated based on the analytical joint strength prediction and the values of $Q_{M,y}$ with respect to the forming pressure.

The mass reduction Δm_J of the mandrel below the groove and the joint, respectively, is evaluated by the following expression:

$$\Delta m_J = \frac{m_{M,s} - m_{M,h}}{m_{M,s}} \tag{7.10}$$

This value is calculated based on the mass of a solid mandrel

$$m_{M,s} = \rho \cdot w \cdot \pi \cdot \left(\frac{D_M - h}{2}\right)^2 \tag{7.11}$$

and the mass of the hollow inner joining partner

$$m_{M,h} = \rho \cdot w \cdot \pi \cdot \left(\left(\frac{D_M - h}{2}\right)^2 - \left(\frac{d_M}{2}\right)^2\right). \tag{7.12}$$

By combining the equations above, the following simple term for the value of Δm_J is found:

$$\Delta m_J = \frac{{d_M}^2}{(D_M - h)^2} \tag{7.13}$$

In **Figure 7-7** and **Figure 7-8**, the corresponding function $\Delta m_J(Q_M)$ of the mass reduction with respect to the diameter ratio is inserted.

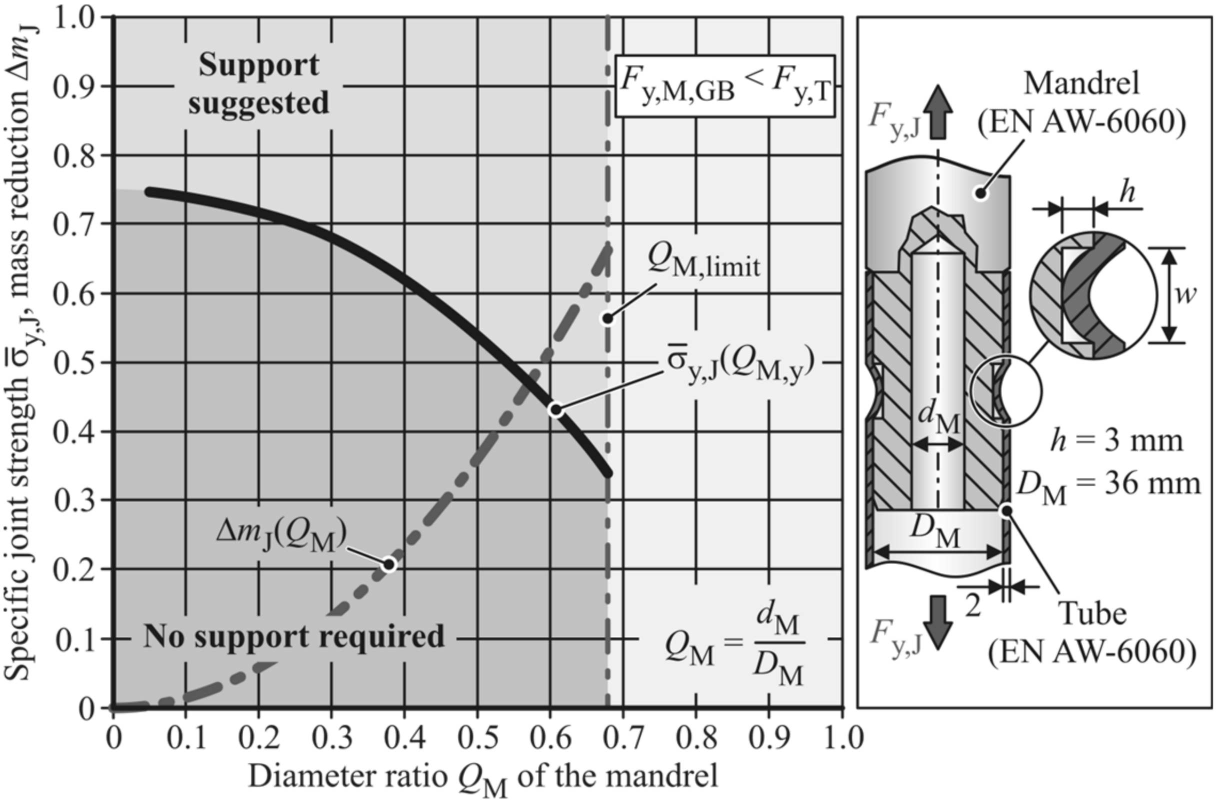

Figure 7-7: Process window for compressive joining of hollow mandrels with a constant groove depth of $h = 3.0$ mm

Figure 7-9 shows an example of the design process of a connection with a hollow mandrel based on the process window for a constant depth of 3 mm. In this example, a specific joint strength of 55 % shall be achieved. With Equation (6.41), it is found that for the given groove depth, the desired joint strength can be obtained with a form-fit element about 12 mm wide. The corresponding diameter ratio has to be at least 0.48 to withstand the forming pressure necessary to fill this groove geometry. It is illustrated by the function $\Delta m_J(Q_M)$ in **Figure 7-9** that a mass reduction of about 35 % can be achieved for this connection.

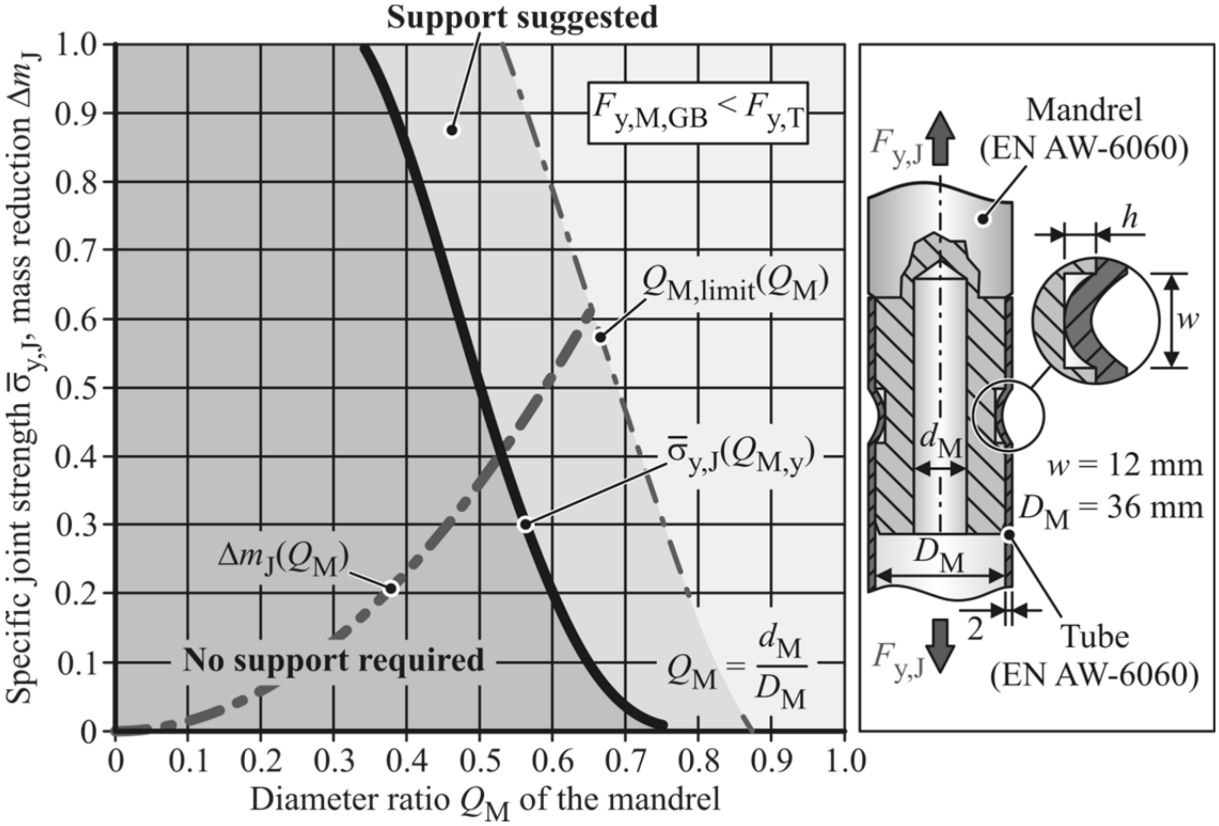

Figure 7-8: Process window for compressive joining of hollow mandrels with a constant groove width of w = 12 mm

It is not possible to manufacture a connection with a strength of 100 % and a reduced mass for the workpiece properties of the process window shown in **Figure 7-9**. Without the application of an additional support mandrel during the joining process, strength values above the maximum of about 75 % can be achieved by three alternative approaches. In the first one, the load is transferred by two or multiple grooves placed in a row (see **Section 2.5**). The disadvantage of this design is the additional mass resulting from the increased joining zone length. Another possibility is the application of a mandrel material with a higher yield strength than the tube material. In this way, the connection strength is increased due to a supplementary interference fit. Additionally, the inner workpiece can be manufactured with a thinner wall thickness leading to a reduction of its mass. The last approach to achieve a substantial mass reduction without a significant drop in strength is the application of mandrels with a circular or triangular groove shape (see **Section 6.3.2**).

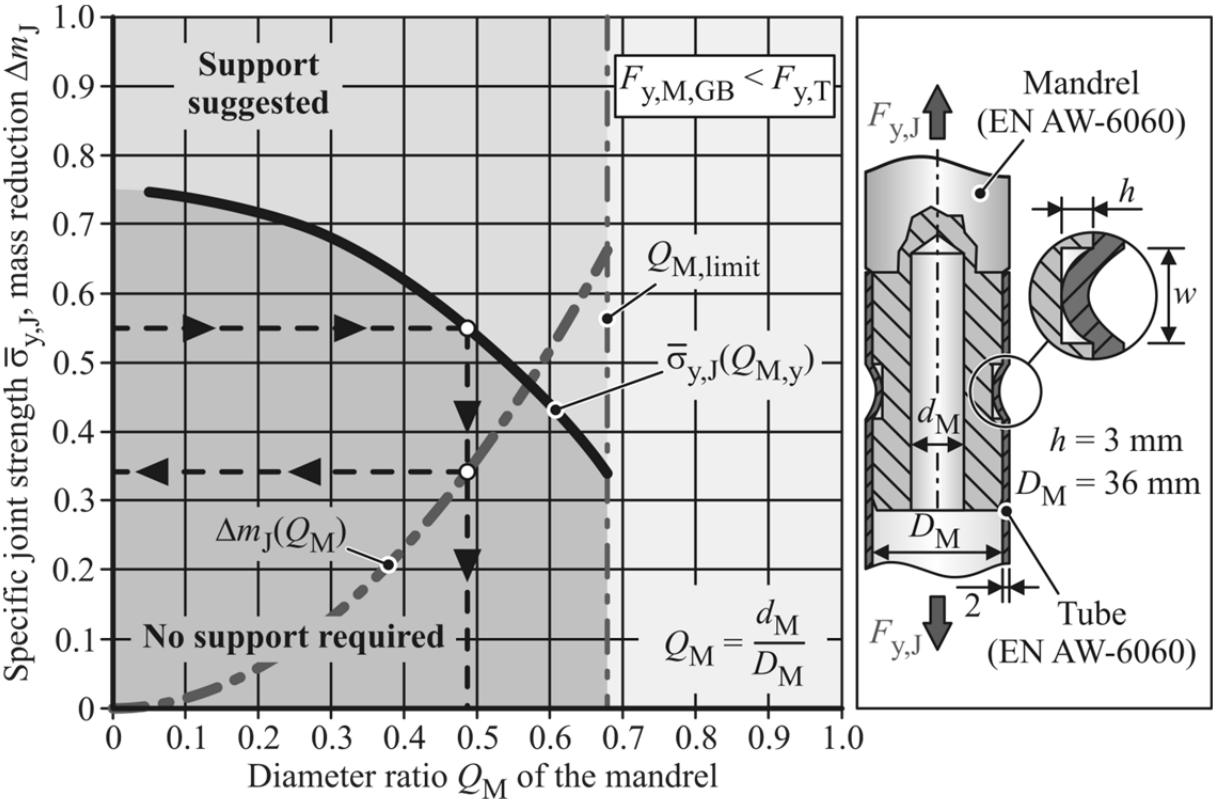

Figure 7-9: Example of a joint design featuring a hollow mandrel

7.4 Example joint design

To show the potential of electromagnetic form-fit joining, connections with optimized joining zone configurations are manufactured. The objective is to achieve a specific joint strength of about 100 % of the yield stress of the weakest partner, which in this case is the tube. A rectangular groove with a supplementary edge radius and a triangular geometry are selected since in **Section 6.2**, it is observed that shearing at the groove edges can be prevented by these two shapes. Park et al. (2005a) state that the thinning of the tube wall can decrease the total strength of electromagnetically crimped connections due to a stress concentration at the groove edge. Because it shows the lowest amount of thinning at the edge of the form-fit element, the triangular groove shape is chosen over the circular geometry (see **Section 6.2.1**). **Table 7-1** displays that 12 mm is selected as groove width and 3 mm is chosen as depth for both form-fit element types. To achieve the desired joint strength, two identical groove geometries with a distance of 12 mm between each other are placed in the joining zone. Based on **Figure 7-7**, an inner diameter d_M of 15.5 mm is selected for the inner workpieces with rectangular groove geometry. To ensure that a joint strength decrease due to a plastic deformation of the mandrel is avoided, this value also includes a safety factor of about 1.15. Since the rectangular geometry shows the largest mandrel deformation of all considered groove types (see **Figure 6-29**), the same value of d_M is applied to the inner partners with triangular grooves. In this way, a plastic deformation of the mandrel is avoided for this form-fit element shape as well. With an outer diameter of 36 mm, this value leads to a diameter ratio Q_M of 0.43 and a mass reduction of 27 %. The alloy EN AW-6060 is selected as tube and mandrel material for both joining zone geometries.

Table 7-1: Mandrel and joining zone characteristics

Material	**Temper condition**	**Groove shape**	**Groove dimensions w x h** (mm)	**Groove edge radius R_GE** (mm)	**Diameter ratio Q_M**
EN AW-6060	T6	rectangular	12 x 3	3	0.43
EN AW-6060	T6	triangular	12 x 3	-	0.43
EN AW-7075	T6	triangular	12 x 3	-	0.75

Golovashchenko (2001) gives the following equation for the determination of the total joint strength $\bar{\sigma}_\mathrm{y,J,tot}$ resulting from two form-fit elements in the joining zone:

$$\bar{\sigma}_{y,J,tot} = \sigma_{y,J,1} + \sigma_{y,J,2} \tag{7.14}$$

In this expression, $\bar{\sigma}_\mathrm{y,J,1}$ and $\bar{\sigma}_\mathrm{y,J,2}$ are the strength increments resulting from the first and the second groove. A joint prediction of the transferable loads with the analytical approach of **Section 6.1** in combination with Equation (7.14) gives an approximate specific strength of 100 % for the connections with the rectangular grooves. For the triangular form-fit elements, the model gives only a strength of 86 %.

A possibility to achieve also a strength of approximately 100 % for this shape is the generation of an additional interference fit. To produce this supplementary load transfer mechanism, another material combination with a significant yield stress difference is evaluated here. Therefore, additional mandrels of the aluminum alloy EN AW-7075, which has a yield stress of 460 MPa, are machined (see **Table 4-6**). In combination with EN AW-6060 as tube material, the desired substantial yield stress difference is achieved. For the determination of the inner diameter of the mandrels, the Equations (7.7) and (7.9) are used. The result of this calculation is a value of 29 mm for d_M which yields a diameter ratio of about 0.81. If this value is applied as inner diameter, the maximum load that can be transferred by the smallest cross-sectional area of the mandrel would be lower than the load which could be carried by the tube. As a result, the mandrel becomes the weaker joining partner and the total connection strength decreases. Therefore, a smaller inner diameter of 27 mm is selected. At this diameter, the smallest cross section can carry the same load as the tube. With this diameter ratio of 0.75, a mass reduction of 81 % is achieved.

The results of the pull-out tests of these example connections are displayed in **Figure 7-10**. Similar to the experimental data of **Chapter 6**, all results show a relatively small statistical dispersion, which implies high process stability. For the connections with two triangular grooves, an average specific strength of about 86 % is achieved. This is about double the strength of a joint with just one groove. The experimental connection strength and the analytically predicted strength are in very good agreement. For the joints with two rectangular grooves and rounded edges, a significant joint strength increase is also observed. Compared to the connections with just one form-fit element, a rise of the transferable load of about 32 % is achieved (compare **Section 6.2.1**).

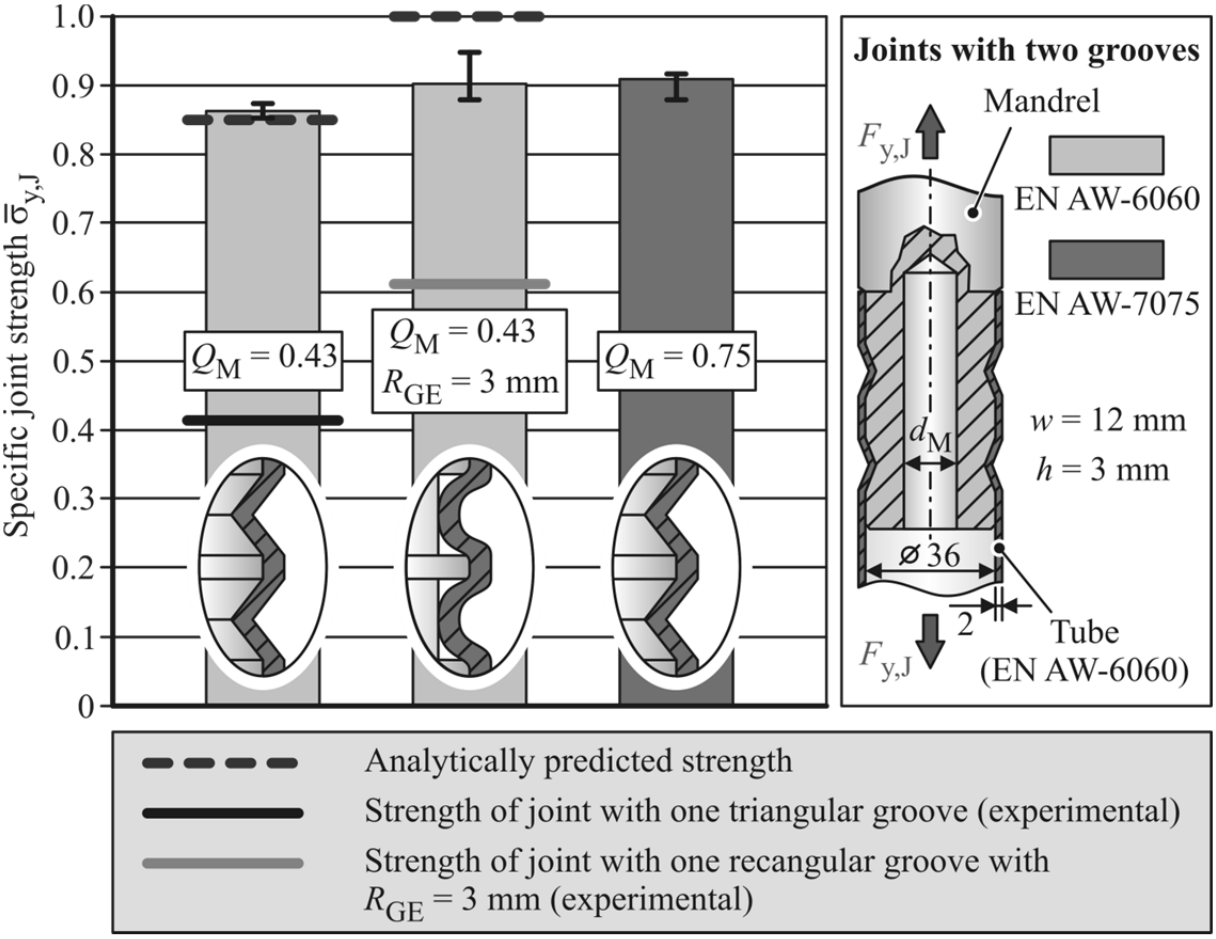

Figure 7-10: Connection strength of connections with two grooves

The connections with the EN AW-7075 mandrels and two triangular grooves failed at about 90 % of the yield stress of the tube as well. The fact that the predicted specific strength of 100 % is not achieved by all three example joints can be explained by superimposed tensions, which are induced by the grips of the universal tensile testing machine (Park et al., 2005a). This statement is also supported by the observed final joint failure for all specimens. By comparing **Figure 7-11** and **Figure 6-5a**, it can be seen that workpiece fracture occurs in a tube section outside the joining zone instead of at the groove edge as with some of the single form-fit element connections. Therefore, thinning or shearing at this edge can be excluded as an explanation of the joint failure below the yield strength of the tube material. In general, the results imply that it is possible to manufacture form-fit connections with reduced mass and transferable loads within the range of the strength of the base material by electromagnetic crimping.

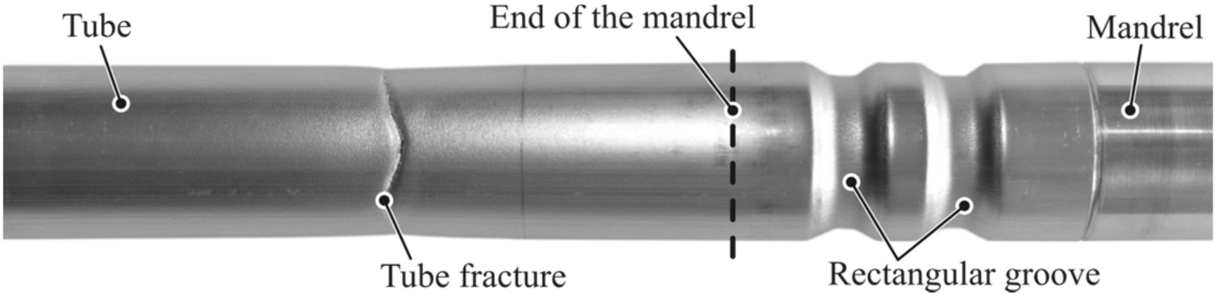

Figure 7-11: Example of the final joint failure by tube fracture

For metal inert gas (MIG) welding of EN AW-6060, the standard EN 1999-1-1 (N.N., 2014b) gives an achievable joint strength of about 43 % of the yield strength of the base material. For tungsten inert gas (TIG) welding of this aluminum alloy, the standard states a specific strength of about 34 %. These decreased values result from the heat-affected zone, which is formed during fusion welding. Barnes and Pashby (2000) state that strengths more closely approximating the base yield stress of the material can only be achieved by an additional post-welding heat treatment. In contrast to this, the connections manufactured by electromagnetic form-fit joining exceeded the strength of the welded joints by at least 100 %. Additionally, the generated form-fit connections require no subsequent process step to achieve their full strength and the process allows the manufacturing of multi-material components. Therefore, it is stated that electromagnetic form-fit joining is very suitable for manufacturing high strength joints for lightweight frame structures.

7.5 Summary and conclusion

Two approaches for electromagnetic crimping of form-fit connections with hollow mandrels are introduced in this chapter. The objective of these methods is the prevention of a plastic deformation of the mandrel during joining and thereby avoiding a significant drop in tensile strength. In the first approach, an additional support mandrel is placed inside the inner workpiece to suppress its deformation during crimping. It is shown that this is a feasible technique to prevent a substantial decrease of the transferable loads. But it also has some significant disadvantages, like the requirement of additional tooling and the need for a sufficient accessibility to extract the support after to the joining operation.

To counteract these disadvantages, a second approach is introduced. For this method, the inner workpiece is designed to have a high enough compressive strength to withstand a plastic deformation during joining. The factors influencing the resistance of the mandrel against plastic deformation are the inner and outer diameter of the workpiece and its yield stress. While the workpiece material and the outer diameter are often given by design restrictions, the inner diameter can be adjusted to generate a high enough compressive strength. To predict the inner diameter d_M necessary to prevent a plastic deformation of the mandrel, an analytical approach is developed. For this model, the acting forming pressure, the tube properties as well as the yield stress of the mandrel and its outer diameter are considered.

Based on this method and the analytical models of **Section 5.1** and **6.1**, a technique for setting up a process window is developed. This tool allows the design of a joint with respect to the achievable connection strength and the mass reduction of the joining zone. Regarding the manufacturing process, the process window also allows a statement on whether a support mandrel has to be used or not to meet the requirements in terms of joint strength and mass reduction.

Finally, the developed models are applied to design three example connections. An experimental determination of the transferable loads of these joints reveals that electromagnetic form-fit joining allows the manufacturing of connections with specific strengths within the range of the yield stress of the base material. The gained connection strengths are at least 100 % higher than the strengths of MIG or TIG welded joints without an additional post-welding heat treatment. Due to this fact and since electromagnetic crimping allows the generation of multi-material connections, it is stated that the process is well suited for the manufacturing of lightweight frame structures.

8 Summary and outlook

In modern lightweight design concepts, structures and components composed of multiple materials are being increasingly used like, for example, in the automotive industry. Space frame structures for low volume production of vehicles are also becoming more prevalent. Both of these concepts allow a significant reduction in the mass of a structure, but they are also extremely difficult to manufacture using common joining techniques, like welding or mechanical fastening. An innovative alternative to remedy the difficulties associated with conventional processes is joining by electromagnetic crimping. Form-fit connections, in particular, manufactured using this technique have great potential in replacing conventional joining processes for several applications. However, the drawbacks are that the process and joining zone design of electromagnetic crimping is quite complex and expensive. And in many cases, because of the intricate interactions between electromagnetic and mechanical mechanisms during the forming process, only sophisticated numerical calculations or extensive experimental studies lead to satisfying results.

To remedy this disadvantage associated with the joining method, a continuous analytical model for the process and joint design for electromagnetically crimped connections is developed in this research work. The first part of this approach allows the prediction of the required forming pressure and the respective charging energy needed to manufacture a specific form-fit joint by electromagnetic forming. For the determination of the transferable loads with respect to the workpiece and joining zone properties, the second part of the model is developed to approximate the strengths of compressed and expanded connections. The analytical comparison of these two joint types shows that a significantly higher strength can be achieved by compressed connections. Finally, both parts are used to develop a process window for the design of joints which feature hollow mandrels to reduce the mass of the connections. To validate the continuous model, experimental investigations are used. These studies show that the analytical values are in good agreement with the experimental results. In addition, numerical simulations are performed for the verification of the analytical process parameter prediction. These investigations are also in good agreement with the calculated process parameters. Hence, the introduced approach is well suited for the process and joining zone design of connections manufactured by electromagnetic crimping.

In addition to the validation of the developed analytical approach, the results of the experimental joint strength determination are also used to analyze the effects of the workpiece and joining zone characteristics on the achievable connection strength. A major finding of this investigation is the observed influence of the forming element shape on the specific strength. For connections with hollow mandrels, it is found that a mass reduction by inserting a hole in the center of the mandrel will lead to a decrease in compressive strength, which can negatively affect the joint strength. Based on this finding, a joining procedure that minimizes the strength decrease of connections with reduced mass is developed, in which the hollow inner workpiece is supported by an additional support mandrel during the joining operation. In this way, the hollow mandrel temporarily has a similar compressive strength to that of a solid workpiece and a substantial strength decrease is prevented. Finally, joints based on the findings of this work are manufactured to show the potential of electromagnetically crimped connections for lightweight frame structures. The specific strength of all joints is within the range of the yield stress of the base material and the maximal mass reduction of the joining zone is 81%. The experiments also prove to be highly reproducible and, together with the experimental results, they show how suitable electromagnetic form-fit joining is for the manufacturing of lightweight frame structures.

Since the joints in this work are only characterized in terms of their tensile strength, the load transfer of electromagnetically crimped connections has to be analyzed for additional load cases in future research works. For lightweight space frame structures, a combination of tension and torsional load as well as bending would be of particular interest. Investigations on how the connections behave under oscillating loads and in the case of a crash would also be important. Afterwards, the joint design can be improved based on the findings. For example, it is already evident that the circumferential grooves, which are studied in this work, are not able to carry a torsional load. Therefore, the combination of tension and torsion requires the application of joining partners with pockets or knurled surfaces (see **Figure 2-15**).

Besides an adjustment of the joining zone, it would also be very valuable to adapt the analytical approach for the process and the joint design for these different form-fit element types. By doing so, the need for complex numerical calculations and extensive experimental studies for the determination of the process parameters and the geometries of the form-fit elements can be minimized. Another useful modification of the joint strength prediction for connections with hollow mandrels is the development of an analytical approach to calculate the strength generated by an additional interference fit. If such a model is integrated in the strength determination introduced in this work, the transferable loads of connections with hollow mandrels can be evaluated much more accurately and it would especially help in the selection of material combinations for the joining partners and the joining zone design. It would also allow a more precise determination of the diameter ratio at which the joint strength drops below the strength of a connection with a similar groove geometry machined in a solid mandrel. This, in turn, facilitates a further reduction of mass in the joining zone.

To promote electromagnetic crimping and forming in industrial applications, it is also necessary to supply simple and manageable instruments that can determine the tool lifetime. So far, this is only possible by time consuming experimental studies or with the help of sophisticated numerical models. The tool design strategies have to be improved to increase the application of electromagnetic crimping for the manufacturing of lightweight space frames and for this, it is necessary to develop tools that are both lightweight and durable. The weight of the tool is important as to allow an easy manipulation within an automated production line, for example, at the end of an industrial robot arm. A promising approach for the fabrication of such tool coils is additive manufacturing, which permits the generation of coils with a geometry precisely adapted to the locally acting loads and the integration of cooling channels. Furthermore, with additive manufacturing, it could also be possible to engineer tools composed of dissimilar materials. For example, the coil winding could be manufactured of a conductive metal, like copper, in combination with high strength steel as reinforcement.

References

Al-Hassani, S. T. S., Duncan, J. L., Johnson, W., 1974. On the Parameters of the Magnetic Forming Process. Journal of Mechanical Engineering Science 16 (1), pp. 1 – 9.

Armstrong, J. S., 1985. Long-range forecasting: From Crystal Ball to Computer. Wiley, ISBN 978-0-4718-2360-5.

Balanethiram, V. S., Daehn, G. S., 1995. Hyperplasticity-increased forming limits at high workpiece velocity. Scripta Metallurgica et Materialia 30(4), pp. 515 – 520.

Barnes, T. A., Pashby, I. R., 2000. Joining techniques for aluminium spaceframes used in automobiles, Part I – Solid and liquid phase welding. Journal of Materials Processing Technology 99, pp. 62 – 71.

Barreiro, P., Schulze, V., Löhe, D., Marré, M., Beerwald, C., Homberg, W., Kleiner, M., 2006. Strength of Tubular Joints Made by Electromagnetic Compression at Quasi-static Cyclic Loading. Proceedings of the 2nd International Conference on High Speed Forming – ICHSF2006, March 20th – 21th, 2006, Dortmund, Germany, pp. 107 – 116, http://hdl.handle.net/2003/27068.

Bauer, D., 1965. Messung der Umformkraft und der Formänderung bei der Hochgeschwindigkeitsumformung rohrförmiger Werkstücke durch magnetische Kräfte. Bänder Bleche Rohre 6, pp. 575 – 577.

Bauer, D., 1967. Ein neuartiges Messverfahren zur Bestimmung der Kräfte, Arbeiten, Formänderungen, Formänderungsgeschwindigkeiten und Formänderungsfestigkeiten beim Aufweiten zylindrischer Werkstücke durch schnell veränderliche magnetische Felder. Dr.-Ing. Dissertation, Technische Hochschule Hannover.

Beerwald, C., 2005. Grundlagen der Prozessauslegung und -gestaltung bei der elektromagnetischen Umformung. Dr.-Ing. Dissertation, Universität Dortmund, ISBN 3-8322-4421-2.

Belyy, I. V., Fertik, S. M., Khimenko, L. T., 1977. Spravochnik Po Magnitno-impul' Snoy Obrabotke Metallov (Electromagnetic Metal Forming Handbook). English translation by Altynova, M. M., Dept. of Materials Science and Engineering, The Ohio State University, 1996.

Ben-Artzy, A., Stern, A., Frage, N., Shribman, V., Sadot, O., 2010. Wave Formation Mechanism in Magnetic Pulse Welding. International Journal of Impact Engineering 37(4), pp. 397 – 404.

Bertholdi, W., Daube, J., 1966. Die elektrohydraulische und die elektromagnetische Umformung von Metallen. Urania – Gesellschaft zur Verbreitung wissenschaftlicher Kenntnisse.

Birdsall, D., Ford, F., Furth, H. P., Riley, R., 1961. Magnetic Forming! What is it? American Machinist/Metalworking Manufacturing 105(6), 1961, pp. 117 – 121.

Brandes, K., 1998. Kraftschlüssige Welle-Nabe-Verbindungen mit hoher Tragfähigkeit durch Innenhochdruckumformen. Proceedings of "Welle-Nabe-Verbindungen. Systemkomponenten im Wandel, Tagung Fulda", VDI-Verlag, Düsseldorf, pp. 277 – 284.

Brosius, A., Kleiner, M., 2004. Determination of Material Characteristics using Electromagnetic Forming and Weak Coupled Finite Element Simulations. Proceedings of 1st International Conference on High Speed Forming – ICHSF2004, Dortmund, March 31st – April 1st, 2004, pp. 13 – 21, http://hdl.handle.net/2003/27054.

Bruno, E. J., 1968. High-Velocity Forming of Metals. American Society of Tool and Manufacturing Engineers, Dearborn.

Brown, W. F., Bandas, J., Olson, N. T., 1978. Pulsed magnetic welding of breeder reactor fuel pin and closures. Proceedings of the AWS 59th Annual Meeting, New Orleans, USA.

Bühler, H., Bauer, D., 1968. Ein Beitrag zur Magnetumformung rohrförmiger Werkstücke. Werkstatt und Betrieb 110(9), pp. 513 – 516.

Bühler, H., von Finckenstein, E., 1968a. Fügen durch Magnetumformung. Werkstatt und Betrieb 101 (4), pp. 209 – 215.

Bühler, H., von Finckenstein, E., 1968b. Fügen durch Magnetumformung – Lösekräfte von Sickenverbindungen aus Stahl. Werkstatt und Betrieb101 (11), pp. 671 – 676.

Bühler, H., von Finckenstein, E., 1971. Bemessung von Sickenverbindungen für ein Fügen durch Magnetumformung. Werkstatt und Betrieb 104, pp. 45 – 51.

Chatti, S., 2004. Production of Profiles for Lightweight Structures. Habilitation Thesis, University of Dortmund, Books on Demand GmbH, ISBN 3-8334-4929-2.

Cho, J. R., Song, J. I., Noh, K. T., Jeon, D. H., 2005. Nonlinear Finite Element Analysis of Swaging Process for Automobile Power Steering Hose. Journal of Materials Processing Technology 170(1–2), pp. 50 – 57.

Cho, J. R., Song, J. I., 2007. Swaging Process of Power Steering Hose, Its Finite Element Analysis Considering the Stress Relaxation. Journal of Materials Processing Technology 187–188, pp. 497 – 501.

Cowan, G., Bergmann, O., Holtzman, A., 1971. Mechanism of Bond Zone Wave Formation in Explosive-Clad Metals. Metallurgical Transactions 2, pp. 3145 – 3155.

Cowper, G. R., Symonds, P. S., 1957. Strain hardening and strain-rate effects in the impact loading of cantilever beams. Brown University Division of Applied Mathematics Report No. 28.

Daehn, G., 2011. Energy Field Methods and electromagnetic sheet metal forming. Intelligent energy field manufacturing: Interdisciplinary process innovations, pp. 471 – 504.

Daube, J., Götsch, A., Hänisch, H., 1966. Ausnutzung gespeicherter elektrischer Energie zur Magnetumformung von Metallen und Grenzen dieses Verfahrens. Fertigungstechnik und Betrieb 16(2), pp. 107 – 113.

Dietz, H., Lippmann, H. J., Schenk, H., 1967. Theorie des Magneform-Verfahrens: Erreichbarer Druck. Elektronische Zeitschrift ETZ-A 88(9), pp. 217 – 222.

Eguia, I., Zhang, P., Daehn, G. S., 2004. Crimped-joining of aluminum tubes onto mandrels with undulating surfaces. Proceedings of the 1st International Conference on High Speed Forming – ICHSF2004, Dortmund, March 31st – April 1st, 2004, pp. 161 – 170, https://eldorado.tu-dortmund.de/handle/2003/27041.

Friedrich, H. E., 2013. Leichtbau in der Fahrzeugtechnik. Springer-Vieweg, ISBN 978-3-8348-1467-8, DOI 10.1007/978-3-8348-2110-2.

Furth, H. P., Levine, M. A., Waniek, R. W., 1957. Production and use of high transient magnetic fields II. The Review of Scientific Instruments 28(11), pp. 949 – 958.

Garzke, M., 2001. Auslegung innenhochdruckgefügter Pressverbindungen unter Drehmomentbelastung. Dr.-Ing. Dissertation, TU Clausthal, VDI-Verlag, Düsseldorf. ISBN 3-18-335001-7.

Garzke, M., Geuss, M., 2007. Innenhochdruckfügen von Pressverbindungen mit geschwächten Naben. Proceedings of "Welle-Nabe-Verbindungen. Gestaltung - Fertigung – Anwendungen". Wiesloch bei Heidelberg, Germany, VDI-Verlag, Düsseldorf, pp. 359 – 374.

Gies, S., Weddeling, C., Marré, M., Kwiatkowski, L., Tekkaya, A. E., 2012. Analytic Prediction of the Process Parameters for Form-Fit Joining by Die-Less Hydroforming. Key Engineering Materials 504 – 506, Trans Tech Publications, pp. 393 – 398.

Gies, S., Weddeling, C., Kwiatkowski, L., Tekkaya, A. E., 2013. Groove Filling Characteristics and Strength of Form-Fit Joints produced by Die-Less Hydroforming. Key Engineering Materials 554-557, Trans Tech Publications, pp. 671 – 680.

Golovashchenko, S., 2001. Methodology of Design of Pulsed Electromagnetic Joining of Tubes. Proceedings of the TMS Symposium "Innovations in Processing and Manufacturing of Sheet Materials". New Orleans, Louisiana, United States of America, pp. 283 – 299.

Golovashchenko, S., Dmitriev, V., Sherman, A., 2005. An Apparatus for Electromagnetic Forming, Joining and Welding. US patent 6,875,946 B2.

Golovashchenko, S., 2006. Electromagnetic forming and joining for automotive applications. Proceedings of the 2nd International Conference on High Speed Forming – ICHSF2006, March 20th – 21st, 2006, Dortmund, pp. 201 – 206, https://eldorado.tu-dortmund.de/handle/2003/27060.

Goroncy, J., 2011. Offenes Reiseziel – Elektrifizierung der Antriebe bei Audi. Automobil Konstruktion 2, pp. 44 – 45.

Groche, P., Tibari, K., 2006. Fundamentals of angular joining by means of hydroforming. CIRP Annals – Manufacturing Technology 55 (1), pp. 259 – 262.

Groche, P., Wohletz, S., Brenneis, M., Pabst, C., Resch, F., 2014. Joining by forming – A review on joint mechanisms, applications and future trends. Journal of Materials Processing Technology 214 (10), pp. 1972 – 1994.

Grote, K. H., Antonsson, E. K., 2009. Springer Handbook of Mechanical Engineering, Springer. ISBN 978-3-540-49131-6.

Grünendick, T., 2002. Fester Presssitz durch "hydraulisches Aufweiten". Hochschulzeitschrift TU Clausthal 11, pp. 20 – 24.

Hagedorn M., 2005. Herstellung von Verbundbauteilen durch Einwalzen – Verfahrensentwicklung und experimentelle Grundlagen. Institute of Machining Technology, Dr.-Ing. Dissertation, TU Dortmund.

Haisler, W., 1986. Finite Element Analysis of hydraulic hose couplings. Proceedings of the Sixth International Conference on Vehicle Structural Mechanics, Warrendale, PA, USA, pp. 169 – 177.

Hammers, T., Marré, M., Rautenberg, J., Barreiro, P., Schulze, V., Biermann, D., Brosius, A., Tekkaya, A. E., 2009. Influence of Mandrel's Surface on the Mechanical Properties of Joints Produced by Electromagnetic Compression. Steel Research International 80 (5), pp. 366 – 375. DOI 10.2374/SRI08SP151.

Harvey, G. W., Brower, D. F., 1958. Metal Forming Device and Method. US-Patent Nr. 2976907.

Henselek, A., Beerwald, M., Beerwald, C., 2004. Design and Adaptation of EMF Equipment – From Direct Acting Multi-turn Coils to Separable Tool Coils for Electromagnetic Tube Compression. Proceedings of the 1st International Conference on High Speed Forming – ICHSF2004, Dortmund, Germany, March 31st – April 1st, 2004, pp. 275 – 184, http://hdl.handle.net/2003/22251.

Hisashi, S., Isao, S., Sherif, R., Hidekazu, M., 2009. Numerical study of joining process in magnetic pressure seam welding. Transactions of JWRI 38(1), pp. 63 – 68.

Hockauf, M., 2009. Fließspannungsverhalten ultrafeinkörniger Aluminiumwerkstoffe unter besonderer Berücksichtigung der Dehnrate. Dr.-Ing. Dissertation, Technische Hochschule Chemnitz.

Hodge, P. G., 1955. Impact Pressure Loading of Rigid-Plastic Cylindrical Shells. Journal of Mechanical Physics of Solids 3, pp. 176 – 188.

Hölzl, R., 1998. Beanspruchungssimulation an hydraulisch gefügten Rohr-Rohrplatten-Verbindungen. Dr.-Ing. Dissertation, TU München, Munich.

Homberg, W, Marré, M., Beerwald, C., Kleiner, M., 2006. Joining by Forming of Lightweight Frame Structures. Advanced Materials Research: Flexible Manufacture of Lightweight Frame Structures 10, pp. 89 – 100.

Jablonski, J., 1976. Analyse der elektromagnetischen Umformung rohrförmiger Werkstücke. Dr.-Ing. Dissertation, Akademie der Wissenschaften der DDR, Berlin.

Jablonski, J., Winkler, R., 1978. Analysis of the Electromagnetic Forming Process. International Journal of Mechanical Science 20, pp. 315 – 325.

Jantscha, R., 1929. Über das Einwalzen und Einpressen von Kessel- und Überhitzerrohren bei Verwendung verschiedener Werkstoffe. Dr.-Ing. Dissertation, Technische Hochschule Darmstadt.

Jones, N., 1997. Structural Impact. Cambridge University Press, ISBN 0-521-30180-7.

Johnson, W., 1970. Impact Strength of Materials, Edward Arnold, London.

Kazimierczuk, M., 2014. High Frequency Magnetic Components. 2nd Edition, John Wiley & Sons Ltd., ISBN 978-1-118-71779-0.

Kim, Y. B., Platner, E. D., 1959. Flux concentrator for high-intensity pulsed magnetic fields. The Review of Scientific Instruments 30(7), pp. 524 – 533.

Kleiner, M., Marré, M., Beerwald, C., Homberg, W., Löhe, D., Barreiro, P., and Schulze, V., 2006. Investigation on force-fit joints produced by electromagnetic tube compression. Annals of the German Academic Society for Production Engineering, WGP 13 (1), pp. 227 – 230.

Kore, S. D., Date, P. P., Kulkarni, S. V., 2007. Effect of process parameters on electromagnetic impact welding of aluminum sheets. International Journal of Impact Engineering 34(8), pp. 1327 – 1341.

Kore, S. D., Imbert, J., Worswick, M. J., Zhou, Y., 2009. Electromagnetic impact welding of Mg to Al sheets. Science and Technology of Welding and Joining 14(6), pp. 549 – 553.

Krips, M., Podhorsky, M., 1976. Hydraulisches Aufweiten - Ein neues Verfahren zur Befestigung von Rohren. VGB-Kraftwerkstechnik 56(7), pp 456 – 464.

Krips, H., Podhorsky, M., 1985. Vorrichtung zum hydraulischen Aufweiten von Rohrabschnitten. Patent application DE 35 32 499 C1.

Lamb, H., 1883. On Electrical Motions in a Spherical Conductor. Philosophical Transactions of the Royal Society of London 174, pp. 519 – 549.

Lange, K., 1993. Umformtechnik – Band 4: Sonderverfahren, Prozesssimulation, Werkzeugtechnik, Produktion. 2nd Edition, Springer, Berlin, ISBN 3-540-55939-6.

Lindholm, U. S., Bessey, R. L., Smith, G. V., 1971. Effect of strain rate on yield strength, tensile strength, and elongation of three aluminum alloys. Journal of Materials 6(1), pp. 119 – 133.

Lorentz, H. A., 1895. Versuch einer Theorie der elektrischen und optischen Erscheinungen in bewegten Körpern. E. J. Brill, Leiden.

Lysenko, D. N., Ermolaev, V. V., Dudin, A. A., 1970. Method of pressure welding. US Patent 3,520,049.

Marré, M., Barreiro, P., Schomäcker, M., Brosius, A., Schulze, V., Tekkaya, A. E., Löhe, D., 2007. Characteristics of composite extruded tubes for joining by electromagnetic compression. Proceedings of the International conference on new forming technologies — ICNFT, Bremen.

Marré, M., Brosius, A., Tekkaya, A. E., 2008. Joining by Compression and Expansion of (None-) Reinforced Profiles. Advanced Materials Research 43, pp. 57 – 68.

Marré, M., 2009. Grundlagen der Prozessgestaltung für das Fügen durch Weiten mit Innenhochdruck. Dr.-Ing. Dissertation, TU Dortmund, Shaker Verlag Aachen, ISBN 978-3-8322-8361-2.

Marré, M., Andreas, R., Heuse, R., Tekkaya, A. E., 2011. Verfahren zum lokalen Fügen und/oder zum lokalen Umformen von Hohlprofilen mittels Hochdruck. Patent application DE 10 2012 012 452 A1.

Marciniak, and Z., Duncan, J. L., 2002. Mechanics of Sheet Metal Forming. Butterworth Heinemann, Oxford.

Mori, K., Bay, N., Fratini, L., Fabrizio, M., Tekkaya, A. E., 2013. Joining by plastic deformation. CIRP Annals – Manufacturing Technology 62, pp. 673-694.

Mousavi, A., Sartangi, F., 2009. Experimental investigation of explosive welding of cp-titanium/AISI 304, Materials and Design 30(3), pp. 459 – 468.

Neugebauer, R., Mauermann, R., Grützner, R., 2005. Combination of Hydroforming and Joining. Steel Research International 76(12), pp. 939 – 944.

Neugebauer, R., 2007. Hydro-Umformung. Springer Verlag, Berlin, Heidelberg, ISBN 3540211713.

N.N., 2001. EN 10002-1, Metallic materials – Tensile testing – Part 1: Method of test at ambient temperature. Beuth Verlag, Berlin.

N.N., 2003. VDI Richtlinie 2230 – Systematische Berechnung hochbeanspruchter Schraubenverbindungen (Systematic calculation of high duty bolted joints). Beuth Verlag, Berlin.

N.N., 2009. Setting emission performance standards for new passenger cars as part of the Community's integrated approach to reduce CO_2 emissions from light-duty vehicles. Regulation (EC) No. 443/2009 of the European Parliament and of the council.

N.N., 2011. Nationale Plattform Elektromobilität: Zweiter Bericht der Nationalen Plattform Elektromobilität, Berlin.

N.N., 2014a. aluSELECT database. European Aluminium Association. http://aluminium.matter.org.uk/aluselect/default.asp, Date: May 25th, 2014.

N.N., 2014b. EN 1999-1-1, Design of aluminium structures – Part 1-1: General structural rules. Beuth Verlag, Berlin.

Okagawa, K., Aizawa, T., 2004. Impact seam welding with magnetic pressure for aluminum sheets. Material Science Forum 465–466, pp. 231 – 236.

Ostermann. F., 2007. Anwendungstechnologie Aluminium. 2. Auflage, Springer Verlag, Berlin, Heidelberg, New York, ISBN 978-3-540-71196-4.

Park, Y., Kim, H., Oh, S., 2005a. Design of axial/torque joint made by electromagnetic forming. Thin-Walled Structures 43, 826 – 844.

Park, Y., Kim, H., Oh, S., 2005b. Joining oft thin-walled Aluminum Tube by Electromagnetic Forming (EMF). International Journal of Automotive Technology 6 (5), pp. 519 – 527.

Podhorsky, M., Krips, H., 1990. Wärmetauscher. Aktuelle Probleme der Konstruktion und Berechnung. Vulkan-Verlag, Essen, ISBN 3-8027-2296-5.

Popow, E. A., 1977. Fundamentals in Sheet Metal Forming Theory. Mashinostroenie Moscow, USSR (in Russian).

Pryzybylski, W., Wojciechwski, J., Marré, M., Kleiner, M., 2007. Influence of design characteristics and manufacturing process parameters on the strength of tubular aluminium joints produced by hydroforming. Archiwum Technologii Maszyn i Automatyzacji 27(1), pp. 153 – 167.

Psyk, V., 2010. Prozesskette Krümmen – Elektromagnetisch Komprimieren – Innenhochdruckumformen für Rohre und profilförmige Bauteile. Dr.-Ing. Dissertation, TU Dortmund, Shaker Verlag Aachen, ISBN 978-3-8322-9026-9.

Psyk, V., Risch, D., Kinsey, B. L., Tekkaya, A. E., Kleiner, M., 2011. Electromagnetic forming – A review. Journal of Materials Processing Technology 211 (5), pp. 787 – 829.

Rasmussen, D., 1977. Evolution of the Crimped Hydraulic Hose Assembly. Hydraulic and Air Engineering 4(6), pp. 55 – 62.

Risch, D., 2009. Energietransfer und Analyse der Einflussparameter der formgebundenen elektromagnetischen Blechumformung. Dr.-Ing. Dissertation, TU Dortmund, Shaker Verlag Aachen.

Rowland, A., 1967. Metal forming by magnetic means. Proceedings of the Conference on Electrical Methods of Machining and Forming, pp. 192 – 197.

Sanderson, L., 1967. Magnetic pulse forming. The Journal of the Gage and Tool Industry 21, pp. 43 – 46.

Schmidt, M., Schneider, M., 2010. Kosteneinsparung durch Ressourceneffizienz in produzierenden Unternehmen. uwf – Umweltwirtschaftsforum 18 (3-4), Springer, pp. 153 – 164, DOI: 10.1007/s00550-010-0182-8.

Schürmann, H., 2007. Konstruieren mit Faser-Kunststoff-Verbunden. Berlin, Heidelberg, New York: Springer Verlag.

Shirgaokar, M., Cho, H., Ngaile, G., Altan, T., Yu, J.-H., Balconi, J., Rentfrow, R., Worrell, W. J., 2004a. Optimization of mechanical crimping to assemble tubular components. Journal of Materials Processing Technology 146(1), pp. 35 – 43.

Shirgaokar M., Ngaile G., Altan T., Yu J. H., Balconi J., Rentfrow R., Worrell W. J., 2004b. Hydraulic Crimping, Application to the Assembly of Tubular Components. Journal of Materials Processing Technology 146(1), pp. 44 – 51.

Shribman, V., Tomer, Y., 2006. Magnetic pulse technology for improved tube joining and forming. Tube & Pipe Technology, pp. 91–95.

Storoschew, M. W., Popow, E. A., 1968. Grundlagen der Umformtechnik. VEB Verlag Technik Berlin.

Strand, O. T., Berzins, L. V., Goosman, D. R., Kuhlow, W. W., Sargis, P.D., and Whitworth, T. L., 2004. Velocimetry Using Heterodyne Techniques. Proceedings of the 26th International Congress on High-Speed Photography and Photonics, Alexandria (USA), September 20th – 24th, 2004, pp. 593 – 599, ISBN 0-819-45530-X.

Szabó, I., 1964. Höhere Technische Mechanik. 4th Edition, Springer Verlag, Berlin.

Szabó, I., 2001. Höhere Technische Mechanik. 6th Edition, Springer Verlag, Berlin, Heidelberg, New York, ISBN 3-540-67653-8.

Tanimura, S., Higashi, K., Mukai, T., Kaizu, K., 1989. Influences of Strain Rate and Temperature on the Flow Stress and Ductility of Some Commercial Aluminium Alloys. In Advances in Plasticity 1989, Pergamon, Oxford, pp. 421 – 424, http://dx.doi.org/10.1016/B978-0-08-040182-9.50105-3.

Vivek, A., Weddeling, C., Hahn, M., Daehn, G. S., Tekkaya, A. E., 2014. Electrically Driven Plasma via Vaporization of Metallic Conductors: A Novel Tool for Joining Tubular Workpieces. Proceedings of the International Conference on Manufacture of Lightweight Components – ManuLight 2014, April 3rd – 4th, 2014, Dortmund, Germany, Procedia CIRP, Vol. 18, pp. 62 – 67, DOI: 10.1016/j.procir.2014.06.108.

Voce, E., 1948. The relationship between stress and strain for homogeneous deformations. J. Inst. Metals, Vol. 74, pp. 537 – 562.

Watanabe, M., Kumai, S., Aizawa, T., 2006. Interfacial microstructure of magnetic pressure seam welded Al–Fe, Al–Ni, and Al–Cu lap joints. Materials Science Forum 519–521, pp. 1145 – 1150.

Weddeling, C., Woodward, S. T., Marré, M., Nellesen, J., Psyk, V., Tekkaya, A. E., Tillman, W., 2010. Development of design principles for form-fit joints in lightweight frame structures. Proceedings of the 4th International Conference on High Speed Forming – ICHSF2010, Columbus, Ohio (USA), March 9th – 10th, 2012, pp. 137 – 148, http://hdl.handle.net/2003/27190.

Weddeling, C., Marré, M., Brosius, A., Tekkaya, A. E., 2011a. Umformtechnisches Fügen leichter Tragwerksstrukturen. Fortschrittsbericht VDI 2(678), pp. 169 – 191, ISBN 978-3-18-367802-0.

Weddeling, C., Woodward, S. T., Marré, M., Nellesen, J., Psyk, V., Tekkaya, A. E., Tillman, W., 2011b. Influence of groove characteristics on strength of form-fit joints. Journal of Materials Processing Technology 211 (5), pp. 925 – 935.

Weddeling, C., Gies, S., Nellesen, J., Kwiatkowski, L., Tillmann, W., Tekkaya, A. E., 2012. Influencing Factors on the Strength of Electromagnetically Produced Form-Fit Joints using Knurled Surfaces. Proceedings of the 5th International Conference on High Speed Forming – ICHSF2012, April 24th – 26th, 2012, Dortmund, Germany, pp. 243 – 254, http://hdl.handle.net/2003/29521.

Weddeling, C., Gies, S., Ben Khalifa, N., Tekkaya, A. E., 2014a. Proceedings of the ASME 2014 International Manufacturing Science and Engineering Conference – MSEC2014, June 9th – 13th, 2014, Detroit, Michigan, USA, DOI: 10.1115/MSEC2014-3955.

Weddeling, C., Hahn, M., Daehn, G. S., Tekkaya, A. E., 2014b. Uniform Pressure Electromagnetic Actuator – An innovative tool for magnetic pulse welding. Proceedings of the International Conference on Manufacture of Lightweight Components – ManuLight 2014, April 3rd – 4th, 2014, Dortmund, Germany, Procedia CIRP, Vol. 18, pp. 156 – 161, DOI: 10.1016/j.procir.2014.06.124.

Wegerdt, C., Thoms, V., Franke, R., Carstensen, H., 2000. Mechanische Fügetechnik – ein Beitrag zum Leichtbau. Stahl für moderne Fertigungsverfahren und innovative Produkte, 72. Tagung des wissenschaftlichen Rates de AiF, November 23rd, 1999, Düsseldorf. Verlag und Vertriebsgesellschaft mbH, Düsseldorf, pp. 6.1 – 6.20.

Winkler, R., 1973. Hochgeschwindigkeitsbearbeitung – Grundlagen und technische Anwendung elektrisch erzeugter Schockwellen und Impulsmagnetfelder. VEB Verlag Technik Berlin.

Yokell, S., 1990. A working guide to shell-and-tube heat exchangers. McGraw-Hill, New York, USA, ISBN 0-07-072281-1.

Yokell, S., 1992. Expanded and welded-and-expanded tube-to-tubesheet joints. Journal of Pressure Vessel Technology 114, pp. 157 – 165.

Youngdahl, C. K., 1970. Correlation Parameters for Eliminating the Effect of Pulse Shape on Dynamic Plastic Deformation. ASME Journal of Applied Mechanics 39, pp. 744 – 752.

Zäh, M. F., Trautmann, A., 2004. Vergleich des hybriden, bifokalen Laserschutzgasschweißens mit Laser MIG-Hybridverfahren. Aluminium – International Journal for Industry, Research and Application 80 (12), pp. 1387 – 1392.

Zhang, Y., Babu, S., Prothe, C., Blakely, M., Kwasegroch, J., LaHa, M., Daehn, G. S., 2010. Application of high velocity impact welding at varied different length scales. Journal of Materials Processing Technology 211(5), pp. 944 – 952.

Appendix

A. Mechanics of a fully clamped cylindrical element shell

(Appendix to **Section 5.1.1**)

Figure A-1 shows the loads and moments acting on a fully clamped cylindrical shell element, which is exposed to an axial-symmetric pressure pulse (Hodge, 1955). Here, N_θ and M_z are the circumferential stress resultant and axial bending stress resultant across the shell thickness. M_z is taken as positive if it corresponds to tensile stresses at the inner surface and N_θ is positive in tension.

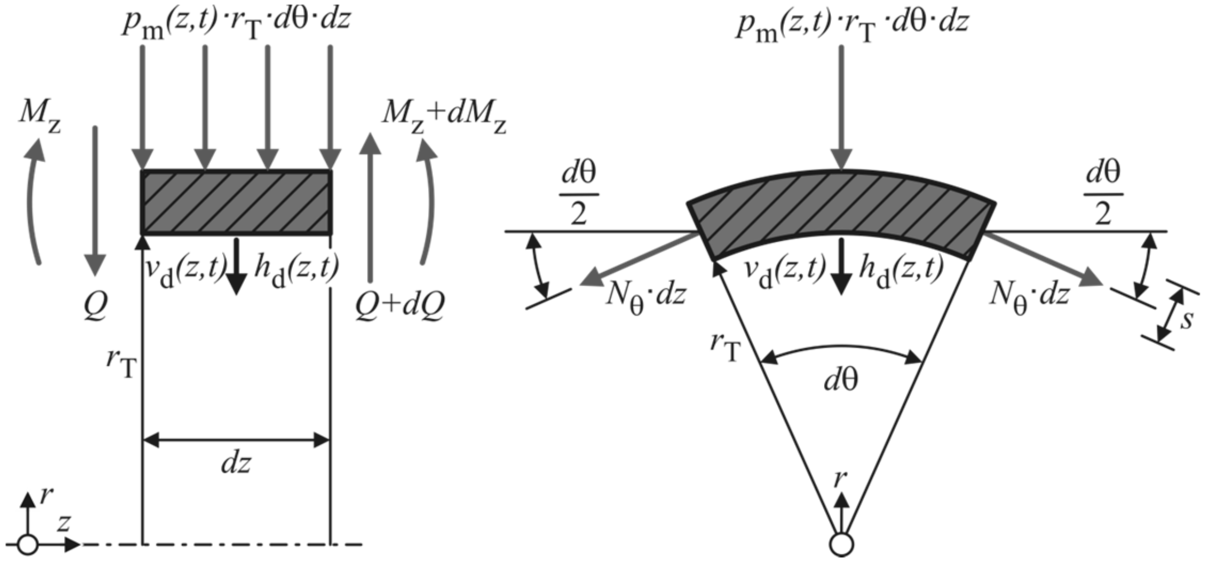
$p_m(z,t)\cdot r_T\cdot d\theta\cdot dz$
M_z
M_z+dM_z
$v_d(z,t)$
$h_d(z,t)$
Q
$Q+dQ$
r_T
dz
r
z
$p_m(z,t)\cdot r_T\cdot d\theta\cdot dz$
$\frac{d\theta}{2}$
$\frac{d\theta}{2}$
$N_\theta\cdot dz$
$v_d(z,t)$
$h_d(z,t)$
$N_\theta\cdot dz$
s
r_T
$d\theta$
r

Figure A-1: Load and moments acting on a cylindrical shell

For this differential shell element, Newton's second law takes the following form in the radial direction:

$$\frac{\partial Q_z(z,t)}{\partial z} r_T d\theta - N_\theta(z,t) d\theta dz - p(z,t) r_T d\theta dz = -\rho_A \frac{\partial^2 h_d(z,t)}{\partial t^2} r_T d\theta dz \qquad \text{(A.1)}$$

In this equation Q_z represents the shear force and ρ_A gives the surface density of the shell material. By canceling, the equilibrium can be reduced to the following form:

$$\frac{\partial Q_z(z,t)}{\partial z} - \frac{N_\theta(z,t)}{r_T} - p(z,t) = -\rho_A \frac{\partial^2 h_d(z,t)}{\partial t^2} \qquad \text{(A.2)}$$

To eliminate the shear force, the equilibrium of moments is established

$$\frac{\partial M(z,t)}{\partial z} = -Q(z,t) \qquad \text{(A.3)}$$

and inserted in Equation (A.1):

$$\frac{\partial^2 M_z(z,t)}{\partial z^2} + \frac{N_\theta(z,t)}{r_T} + p(z,t) - \rho_A \frac{\partial^2 h_d(z,t)}{\partial t^2} = 0 \tag{A.4}$$

To solve this differential equation, Hodge (1955) assumes an ideal plastic material behavior and applies a rectangular approximation of the yield domain (see **Figure A-2**). The yield regime of the cylindrical shell under compression lies on the line segment A-B (see **Figure 5-2b**) since M_z varies from its negative maximum at the groove edge to its positive maximum in the center of the shell. Due to the assumption of a constant pressure in axial direction, N_θ is also assumed to be constant over the length of the shell segment (Hodge, 1955).

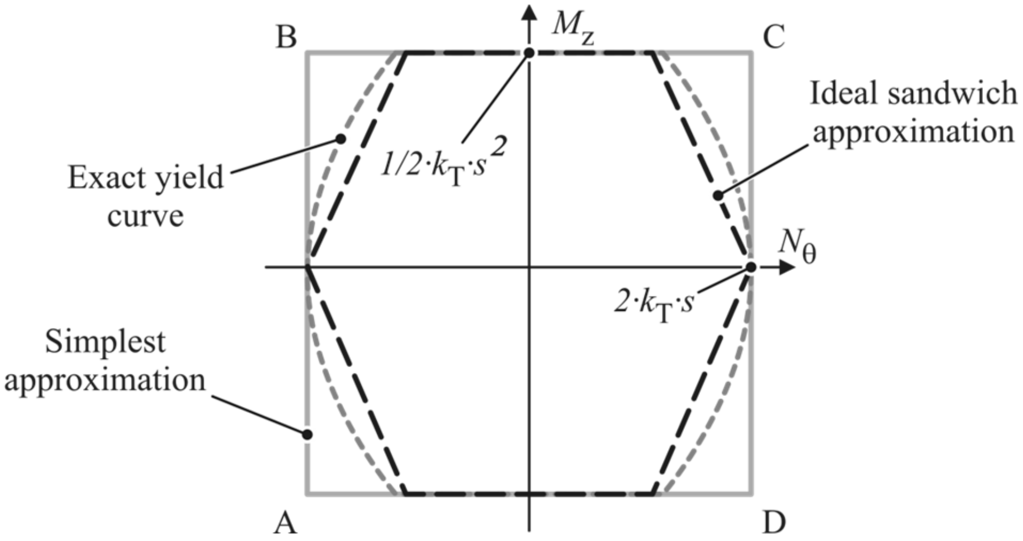

Figure A-2: Yield domains (Hodge, 1955)

As mentioned in **Section 5.1.1**, Hodge assumes a linear velocity field which implies the formation of plastic hinge bands (see **Figure 5-3a**). With this simplification, the workpiece velocity $v_d(z,t)$ with respect to the axial position z and time can be described by the following equation for $0 \leq z \leq w/2$:

$$v_d(z,t) = v_d(t) \cdot \frac{2 \cdot z}{w} \tag{A.5}$$

By applying the concepts of the formation of plastic hinge bands and a rectangular yield domain, Hodge (1955) finds the boundary conditions below:

$$\begin{aligned} N_\theta &= -2 \cdot k_T \cdot s, \\ M_z(0,t) &= -\frac{1}{2} \cdot k_T \cdot s^2 \\ M_z(w/2, t) &= \frac{1}{2} \cdot k_T \cdot s^2 \\ \frac{dM_z}{dz}(w/2, t) &= 0 \end{aligned} \tag{A.6}$$

With these boundary conditions, Hodge (1955) obtains the following solution for Equation (A.4):

$$\dot{v}_d(z,t) = \frac{3}{2 \cdot \rho_A} \left[p_m(\tau) - p_y \right] \cdot \frac{2 \cdot z}{w} \tag{A.7}$$

The functions of workpiece velocity $v_d(z,t)$ and deformation $h_d(z,t)$ with respect to the acting pressure p_m can be calculated from this expression of the acceleration of the shell element by integration (see **Section 5.1.1**). Hodge (1955) states that for all $0 \leq z \leq w/2$, the boundary condition

$$-\frac{1}{2} \cdot k_T \cdot s^2 \leq M_z(z,t) \leq \frac{1}{2} \cdot k_T \cdot s^2 \tag{A.8}$$

of Equation (A.6) is only valid if the acting pressure p_m is below the limit pressure p_b (see Equation (5.14)). To solve Equation (A.4) for pressures $p_m \geq p_b$, Hodge (1955) introduces a new velocity field (see **Figure 5-3b**). Since the derivation of the solution of Equation (A.4) for the velocity field with two moving hinge bands is quite extensive, it is not presented in this work. But a detailed description of this problem can be found in the work of Hodge (1955).

B. Additional meridional stress caused by bending

(Appendix to **Section 6.1**)

Popow (1977) developed an approach for the determination of a meridional stress increase $\Delta\sigma_\phi$ caused by bending due to a radius change of the curvature. The author assumes that the workpiece element shown in **Figure B-1** moves from position ① to ②. The following relationship can be established if the length of the centerline of the element is unchanged:

$$d\beta_a = \frac{R_{rb}}{R_{ra}} \cdot d\beta_b \tag{B.1}$$

The angle $d\gamma$ is perpendicular to the centerline during the transition from ① to ② and it can be expressed by

$$d\gamma = \frac{dl}{s/2}. \tag{B.2}$$

The following expression for the increment dl can be found based on the geometrical relationships in **Figure B-1**:

$$\begin{aligned} dl &= \left(R_{rb} + \frac{s}{2}\right) d\beta_b - \left(R_{ra} + \frac{s}{2}\right) d\beta_a = \left[R_{rb} + \frac{s}{2} - \left(R_{ra} + \frac{s}{2}\right)\frac{R_{rb}}{R_{ra}}\right] d\beta_b \\ &= \frac{s}{2}\left(1 - \frac{R_{rb}}{R_{ra}}\right) d\beta_b \end{aligned} \tag{B.3}$$

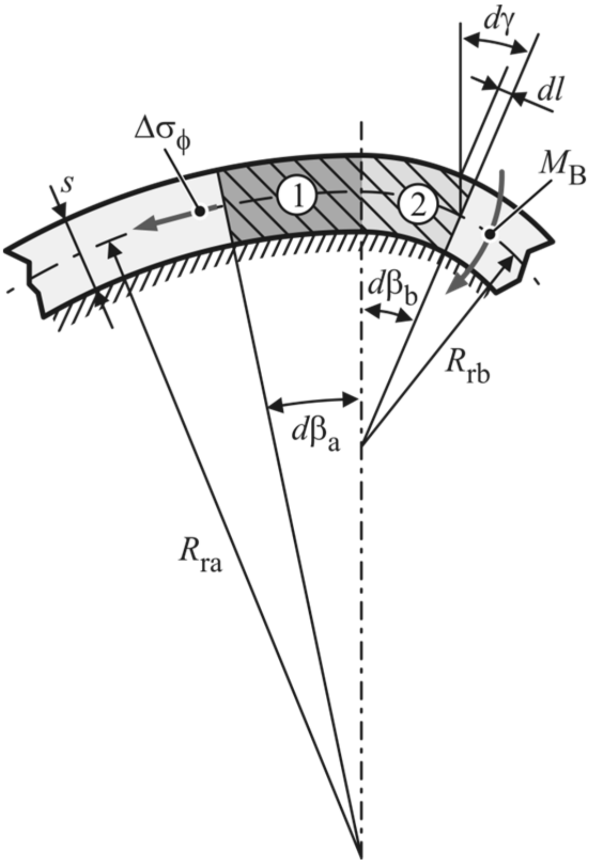

Figure B-1: Meridional stress increase $\Delta\sigma_\phi$ due to a change in curvature

Introducing Equation (B.3) in (B.2) yields to a description of the angle $d\gamma$ based on the curvature radii and $d\beta_b$.

$$d\gamma = \left(1 - \frac{R_{rb}}{R_{ra}}\right) d\beta_b \tag{B.4}$$

On the assumption of plane strain, Popow (1977) equates the work required for the element movement from position ① to ② with the deformation work which is necessary to bend a workpiece element around a rotation angle (see **Figure B-1**).

$$\Delta\sigma_\phi \cdot s \cdot R_{rb} \cdot d\beta_b = M_B \cdot d\gamma \tag{B.5}$$

The researcher also assumes ideal plastic material behavior. Therefore, the bending moment M_B is replaced by the fully plastic moment (Marciniak and Duncan, 2002) and Equation (B.5) takes the following form:

$$\Delta\sigma_\phi \cdot s \cdot R_{rb} \cdot d\beta_b = \frac{\sigma_{y,T}\, s^2}{4} d\gamma \tag{B.6}$$

By inserting Equation (B.4) in (B.6), the additional meridional stress resulting from the curvature change can be expressed as

$$\Delta\sigma_\phi = \frac{1}{4} \cdot \sigma_{y,T} \cdot s \cdot \left(\frac{1}{R_{rb}} - \frac{1}{R_{ra}}\right). \tag{B.7}$$

If the curvature radii R_{ra} and R_{rb} have different directions, the algebraic sign in the term in parentheses needs to be reversed.

C. Free bending of a shell element curved in two planes

(Appendix to **Section 6.1.1**)

During the manufacturing of form-fit connections by electromagnetic compression, the tube wall is bent freely at the edge of the groove. To determine the resulting bending radius R_{r2} at this location, Storoschew and Popow (1968) introduced the following approach. For their calculation of R_{r2}, the authors assume a shell element curved in two planes, which is exposed to pure bending (see **Figure C-1**).

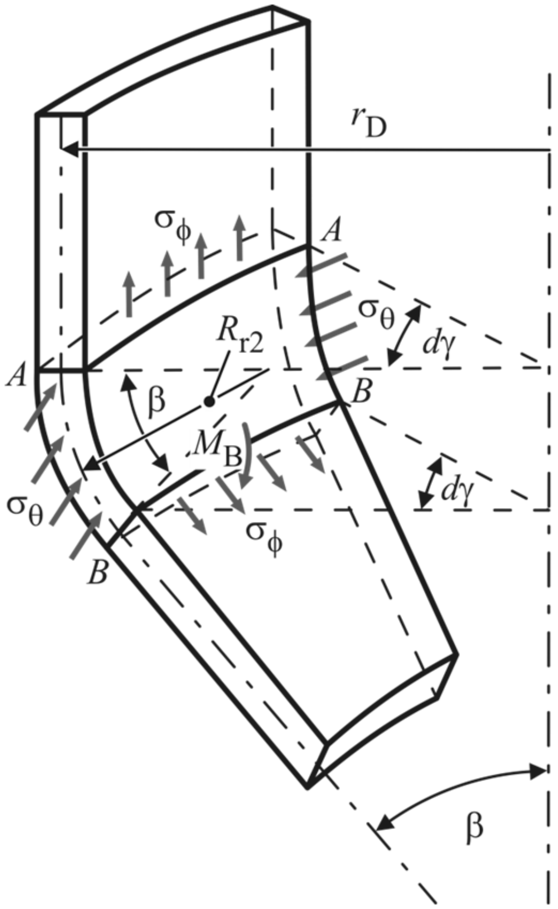

Figure C-1: Assumptions for the determination of the groove edge radius R_{r2} (Storoschew and Popow, 1968)

They also assumed that while in plane A-A no moment occurs, in plane B-B, the bending moment M_B acts. With the rotation axis in plane A-A, the following equilibrium of moments can be established:

$$\sigma_\phi r_D s\, d\gamma (1-\cos\beta) R_{r2} + \sigma_\theta s\, {R_{r2}}^2 \sin\beta\, d\gamma \frac{\sin\beta}{2} = M_B \tag{C.1}$$

Under the assumption of an ideal plastic material behavior, M_B can be expressed as follows (Marciniak and Duncan, 2002):

$$M_B = \frac{1}{4}\sigma_{y,T} s^2\, r_D d\gamma. \tag{C.2}$$

The equilibrium (C.1) is converted into a quadratic equation by canceling and rearranging.

$$\sigma_\theta \sin^2\beta\, {R_{r2}}^2 + 2\sigma_\phi r_D (1-\cos\beta)\, R_{r2} - \frac{1}{2}\sigma_{y,T} s\, r_D = 0 \tag{C.3}$$

By using the positive square root of the quadratic formula, the solution for R_{r2} is achieved.

$$R_{r2} = \frac{\sqrt{4\sigma_\phi^2 r_D^2 (1-\cos\beta)^2 + 2\sigma_\theta \sigma_{y,T} s\, r_D \sin^2\beta} - 2\sigma_\phi r_D (1-\cos\beta)}{2\sigma_\theta \sin^2\beta} \tag{C.4}$$

Since the groove edge radius R_{r2} originates from the joining process, its stress state at the groove edge has to be applied for the calculation of this bending radius. In case of tube compression, the circumferential stress σ_θ is compressive and the meridional stress σ_ϕ is tensile. It is assumed that σ_θ has its maximum value in the groove center and decreases towards the edges of the groove. Due to the support of the mandrel, the circumferential deformation is suppressed at the edge. Hence, the circumferential stress is supposed to be about zero at this position. Therefore, Equation (C.4) becomes indeterminate. By applying L'Hospital's rule, the following solution for R_{r2} in case of compression can be found (Storoschew and Popow, 1968).

$$R_{r2} = \frac{\sigma_{y,T} \cdot s}{4 \cdot \sigma_\phi \cdot (1-\cos\beta)} \tag{C.5}$$

With the Tresca yield criterion, the following expression is achieved for the determination of the principle radius at the groove edge:

$$R_{r2} = \frac{s}{4(1-\cos\beta)} \tag{C.6}$$

Curriculum vitae

Personal Information

Name:	Christian Weddeling
Date and Place of Birth	July 9th, 1981 in Vreden, Germany

Professional Experience

03/2013 – to date	Institute of Forming Technology and Lightweight Construction, *Head of Department of non-conventional forming processes*	Dortmund
11/2011 – 01/2012	The Ohio State University, *Visiting Scholar*	Columbus, OH
02/2009 – 03/2013	Institute of Forming Technology and Lightweight Construction, *Research Assistant*	Dortmund
04/2006 – 06/2008	Institute of Forming Technology and Lightweight Construction, *Student Assistant*	Dortmund
10/2005 – 04/2006	Airbus Germany GmbH, *Intern*	Bremen
11/2002 – 07/2003	Airline Training Center Arizona Inc., *Aircraft Mechanic*	Goodyear, AZ
09/1998 – 06/2001	15th German Army Aviators Regiment, *Apprenticeship as an Aircraft Mechanic*	Rheine

University Studies

06/2008 – 12/2008	The Ohio State University, *Visiting Scholar*	Columbus, OH
04/2006 – 01/2009	Technische Universität Dortmund, *Diploma in Industrial Engineering*	Dortmund
10/2003 – 04/2006	University of Paderborn, *Intermediate Diploma in Industrial Engineering*	Paderborn

Education

08/2001 – 07/2002	Pictorius Berufskolleg, *High School Diploma*	Coesfeld

Honors

06/2008 – 12/2008	Stipend of the Martin-Schmeißer-Stiftung
08/2002 – 07/2003	Stipend of the Congress-Bundestag Youth Exchange Program for Young Professionals

Aus der Dortmunder Umformtechnik sind im Shaker Verlag bisher erschienen:

A. Adelhof: Komponenten einer flexiblen Fertigung beim Profilrunden.
ISBN 3-86111-601-4

G. Reil: Prozeßregelung numerisch gesteuerter Umformmaschinen mit Fuzzy Logic. ISBN 3-86111-862-9

F. Maevus: Rechnerintegrierte Blechteilefertigung am Beispiel des Gesenkbiegens. ISBN 3-8265-0104-7

R. Warstat: Optimierung der Produktqualität und Steigerung der Flexibilität beim CNC-Schwenkbiegen. ISBN 3-8265-1170-0

H. Sulaiman: Erweiterung der Einsetzbarkeit von Gesenkbiegepressen durch die Entwicklung von Sonderwerkzeugen. ISBN 3-8265-1443-2

Ch. Smatloch: Entwicklung eines numerisch einstellbaren Werkzeugsystems für das Tief- und Streckziehen. ISBN 3-8265-1465-3

T. Straßmann: Prozeßführung für das Walzrunden auf der Basis Neuronaler Netze. ISBN 3-8265-1966-3

L. Keßler: Simulation der Umformung organisch beschichteter Feinbleche und Verbundwerkstoffe mit der FEM. ISBN 3-8265-2256-7

E. Szücs: Einsatz der Prozeßsimulation bei der Entwicklung eines neuen Umformverfahrens - der Hochdruckblechumformung. ISBN 3-8265-3119-1

S. Chatti: Optimierung der Fertigungsgenauigkeit beim Profilbiegen.
ISBN 3-8265-3534-0

F. Haase: Eigenspannungen an dünnwandigen Bauteilen und Schichtverbunden. ISBN 3-8265-4312-2

N. Austerhoff: Integrierte Produkt- und Prozeßgestaltung für die Herstellung von Blechbiegteilen. ISBN 3-8265-6613-0

D. Arendes: Direkte Fertigung gerundeter Aluminiumprofile beim Strangpressen. ISBN 3-8265-6442-1

R. Kolleck: Finite-Element-Simulation wirkmedienbasierter Blechumformverfahren als Teil einer virtuellen Fertigung. ISBN 3-8265-6566-5

T. Weidner: Untersuchungen zu Verfahren und Werkzeugsystemen der wirkmedienbasierten Blechumformung. ISBN 3-8265-6602-5

W. Homberg: Untersuchungen zur Hochdruckblechumformung und deren Verfahrenskomponenten. ISBN 3-8265-8684-0

M. Rohleder: Simulation rückfederungsbedingter Formabweichungen im Produktentstehungsprozess von Blechformteilen. ISBN 3-8265-9977-2

V. Hellinger: Untersuchungen zur Methodik der Berechnung und Herstellung von leichten Stützkernverbunden. ISBN 3-8322-0104-1

A. Klaus: Verbesserung der Fertigungsgenauigkeit und der Prozesssicherheit des Rundens beim Strangpressen. ISBN 3-8322-0208-0

B. Heller: Halbanalytische Prozess-Simulation des Freibiegens von Fein- und Grobblechen. ISBN 3-8322-0923-9

A. Wellendorf: Untersuchungen zum konventionellen und wirkmedienbasierten Umformen von komplexen Feinstblechbauteilen. ISBN 3-8322-2435-1

C. Klimmek: Statistisch unterstützte Methodenplanung für die Hochdruck-Blechumformung. ISBN 3-8322-2994-9

R. Krux: Herstellung eigenschaftsoptimierter Bauteile mit der Hochdruck-Blechumformung und Analyse der induzierten Eigenspannungen.
ISBN 3-8322-3551-5

S. Jadhav: Basic Investigations of the Incremental Sheet Metal Forming Process on a CNC Milling Machine. ISBN 3-8322-3732-1

C. Beerwald: Grundlagen der Prozessauslegung und -gestaltung bei der elektromagnetischen Umformung. ISBN 3-8322-4421-2

A. Brosius: Verfahren zur Ermittlung dehnratenabhängiger Fließkurven mittels elektromagnetischer Rohrumformung und iterativer Finite-Element-Analysen.
ISBN 3-8322-4835-8

R. Ewers: Prozessauslegung und Optimierung des CNC-gesteuerten Formdrückens. ISBN 3-8322-5177-4

T. Langhammer: Untersuchungen zu neuen Konzepten für PKW-Kraftstoffbehälter. ISBN 3-8322-5300-9

M. Schikorra: Modellierung und simulationsgestützte Analyse des Verbundstrangpressens. ISBN 3-8322-5506-0

M. Schomäcker: Verbundstrangpressen von Aluminiumprofilen mit endlosen metallischen Verstärkungselementen. ISBN 978-3-8322-6039-2

N. Ridane: FEM-gestützte Prozessregelung des Freibiegens.
ISBN 978-3-8322-7253-1

R. Shankar: Surface Reconstruction and Tool Path Strategies for Incremental Sheet Metal Forming. ISBN 978-3-8322-7314-9

U. Dirksen: Testumgebung für Prozessregelungen zum Drei-Rollen-Profilbiegen mit virtuellem und realem Biegeprozess.
ISBN 978-3-8322-7673-7

D. Risch: Energietransfer und Analyse der Einflussparameter der formgebundenen elektromagnetischen Blechumformung.
ISBN 978-3-8322-8360-5

M. Marré: Grundlagen der Prozessgestaltung für das Fügen durch Weiten mit Innenhochdruck. ISBN 978-3-8322-8361-2

D. Becker: Strangpressen 3D-gekrümmter Leichtmetallprofile.
ISBN 978-3-8322-8488-6

V. Psyk: Prozesskette Krümmen - Elektromagnetisch Komprimieren - Innenhochdruckumformen für Rohre und profilförmige Bauteile.
ISBN 978-3-8322-9026-9

M. Trompeter: Hochdruckblechumformung großflächiger Blechformteile.
ISBN 978-3-8322-9080-1

H. Karbasian: Formgenauigkeit und mechanische Eigenschaften pressgehärteter Bauteile. ISBN 978-3-8322-9250-8

M. J. Gösling: Metamodell unterstützte Simulation und Kompensation von Rückfederungen in der Blechumformung. ISBN 978-3-8322-9355-0

H. Pham: Process Design for the Forming of Organically Coated Sheet Metal.
ISBN 978-3-8440-0309-3

B. Rauscher: Formschlüssig verbundene Metall-Kunststoff-Hybridbauteile durch Integration von Blechumformung und Spritzgießen.
ISBN 978-3-8440-0655-1

T. Cwiekala: Entwicklung einer Simulationsmethode zur zeiteffizienten Berechnung von Tiefziehprozessen.
ISBN 978-3-8440-0701-5

M. Hermes: Neue Verfahren zum rollenbasierten 3D-Biegen von Profilen.
ISBN 978-3-8440-0793-0

N. Ben Khalifa: Strangpressen schraubenförmiger Profile am Beispiel von Schraubenrotoren.
ISBN 978-3-8440-0969-9

J. Kolbe: Thermisch beschichtete, faserverstärkte Polymerwerkzeuge für die Umformung höherfester Blechwerkstoffe.
ISBN 978-3-8440-1353-5

L. Kwiatkowski: Engen dünnwandiger Rohre mittels dornlosen Drückens.
ISBN 978-3-8440-1381-8

T. Kloppenborg: Analyse- und Optimierungsmethoden für das Verbundstrangpressen.
ISBN 978-3-8440-1384-9

A. Schuster: Charakterisierung des Faserverlaufs in umgeformten Stählen und dessen Auswirkung auf mechanische Eigenschaften.
ISBN 978-3-8440-1581-2

A. Jäger: Strangpressen von Aluminiumprofilen mit prozessintegrierter umformtechnischer Weiterverarbeitung.
ISBN 978-3-8440-1654-3

M. M. Hussain: Polymer Injection Sheet Metal Forming – Experiments and Modeling.
ISBN 978-3-8440-2041-0

M. S. Aydın: Efficient Parameter Characterization for Hardening and Yield Locus Models for Sheet Metals.
ISBN 978-3-8440-2118-9

A. Canpolat: Experimentelle und numerische Bewertung der Fließortbestimmung mittels Kreuzzugversuch.
ISBN 978-3-8440-2126-4

V. Güley: Recycling of Aluminum Chips by Hot Extrusion.
ISBN 978-3-8440-2476-0

D.Pietzka: Erweiterung des Verbundstrangpressens zu höheren Verstärkungsanteilen und funktionalen Verbunden.
ISBN 978-3-8440-2538-5

M. Haase: Mechanical Properties Improvement in Chip Extrusion with Integrated Equal Channel Angular Pressing.
ISBN 978-3-8440-2571-2

Q. Yin: Verfestigungs- und Schädigungsverhalten von Blechwerkstoffen im ebenen Torsionsversuch.
ISBN 978-3-8440-2839-3

C. Becker: Inkrementelles Rohrumformen von hochfesten Werkstoffen.
ISBN 978-3-8440-2947-5

R. Hölker: Additiv hergestellte Werkzeuge mit lokaler Innenkühlung zur Produktivitätssteigerung beim Aluminium-Strangpressen.
ISBN 978-3-8440-3149-2